Sustainable Catalytic Systems for Ammonia Synthesis

by

Zixuan Wang

A dissertation submitted in partial fulfillment
of the requirements for the degree of
Doctor of Philosophy
(Chemical Engineering)
in the University of Michigan
2021

Doctoral Committee:

Assistant Professor Bryan R. Goldsmith, Co-Chair
Assistant Professor Nirala Singh, Co-Chair
Assistant Professor Charles C. L. McCrory
Professor Johannes W. Schwank
Assistant Professor William A. Tarpeh, Stanford University

Zixuan Wang

zixuwang@umich.edu

ORCID iD: 0000-0002-5546-2056

Dedication

For my family.

Their unconditional love and sacrifices made this dissertation possible.

Acknowledgements

I would like to thank both my advisors Prof. Nirala Singh and Prof. Bryan Goldsmith for their incredible guidance and support throughout my time as a graduate student at the University of Michigan. Their combined expertise always provided me with high quality and timely feedback on my work. From them, I learned how to critically think about research problems, efficiently design impactful experiments, and thoroughly analyze data to extract meaningful trends. I would also like to thank the rest of my committee members: Prof. Johannes Schwank never fails to provide big-picture insights from his wealth of catalysis knowledge; Prof. Charles McCrory's curiosity always pushed the boundaries of my scientific knowledge; and Prof. William Tarpeh always made me feel like a research superstar even in the darkest of days.

It takes a village to finish a Ph.D., specifically Ann Arbor. From the beginning, I have had the honor of working with a group of very talented and intelligent individuals that I am also proud to call my friends. I would like to specially thank Shawn Eady, Trenton Wilke, Jennifer Jocz, Wei-Chung Wen, Sarah Carl, Elizabeth Wilson (Kezar), and Connor McGlothin. From them, I learned the fundamental skills to become a catalysis researcher, and more importantly, how to diagnose a broken GC. Additionally, I thank the members of the Singh and Goldsmith groups who welcomed me as one of their own. I have had to pleasure to work "alongside" (COVID-19) some incredible colleagues and friends these past three years: Benjamin Silcox, Danielle Richards, Harsh Agarwal, Cailin Buchanan, James Akinola, Jacques Esterhuizen, Frank Doherty, Isaiah Barth, and Samuel Young. Specifically, I would like to thank Danielle Richards, who helped me set up my first

electrochemical nitrate experiment. Also, we published a nitrate review paper together, which in research terms, means our friendship is cemented in writing. Many thanks to Harsh Agarwal, for always keeping me on my toes and never failing to provide lab assistance, and Samuel Young, for your computation viewpoint on alloys. I would also like to thank Evan Ortiz, my unicorn of an undergrad, for helping me screen catalysts at different operational conditions. I thank Kelly Raickovich, Susan Hamlin, Jennifer Downey, and Barbara Perry for all their administrative support and assistance. Lastly, I would like to acknowledge the National Defense Science and Engineering Graduate Fellowship for providing me four years of financial freedom in research.

I would also like that extend my appreciation to my wonderful group of friends I've make at the University of Michigan, who mentally, physically, and emotionally helped me push through the lows during this journey. Sarah Carl, Lisa Smith, Genesis Lopez, Hannah Chia, Danielle Richards, and etc., I thank you for laughing, baking, dancing, wining, and complaining with me. I can't list everyone in these two short pages, but for all the other friends, you know who you are, and you've been an integral part of this adventure.

Most importantly, I would like to thank my family for being a consistent source of love and support for the past (almost) 27 years of my life. Over 20 years ago, my parents decided to leave their family, friends, and culture behind and immigrate to a foreign country. Despite these circumstances, they taught me to pursue my goals and value a good education. I admire their tenacity and thank them for the sacrifices they made for me to be where I am today.

Lastly, I would like to thank my best friend and partner-in-life, Connor, whose unwavering support, punny jokes, and breakfast sandwiches have become such an integral part of my life. I'm grateful that you're always by my side to share my happiness, frustration, and love. Journey before destination, and I'm glad to be taking this journey with you.

Table of Contents

List of Tables

List of Figures

List of Schemes

List of Appendices

Abstract

The Haber-Bosch ammonia synthesis process is one of the most impactful catalytic reactions that sustains the global population. However, this reaction is extremely energy-intensive and emits excess CO_2 that is detrimental to the environment. Additionally, anthropogenic nitrogen fixation creates nitrate pollutants that contaminate water sources and becomes a health hazard for humans upon consumption. To address these problems, we explore catalysts and alternative reaction systems to reduce the environmental impact of fertilizer use for humans.

To improve upon the Haber-Bosch ammonia synthesis, we explored a series of metal (e.g., Fe, Co, and Ru) supported molybdenum carbides (Mo_2C) and nitrides (Mo_2N) that have previously been shown to be active for ammonia synthesis at ambient pressures (**Chapter 3**). We hypothesized that metal sites will break the nitrogen triple bond and support sites will perform the hydrogenation steps. This synergistic interaction will improve ammonia synthesis activity at ambient operating conditions. Kinetic experiments at 400 °C and 1 atm for supported Mo_2C and Mo_2N display little to no catalytic improvement beyond activity from the supports. Future in situ work is recommended to understand the role of nitrogen atoms in the nitride participating in the ammonia synthesis reaction via a Mars-van Krevelen mechanism.

Alternative catalytic systems that recycle nitrate to ammonia can be more environmentally friendly, and both thermocatalytic nitrate reduction reaction (TNO_3RR) and electrocatalytic nitrate reduction reaction (ENO_3RR) are explored in this work. Previous research from the Goldsmith Group predicts that a Pt_3Ru alloy could be active for ENO_3RR. To experimentally confirm these

results, different compositions of Pt_xRu_y/C (x = 48–100%) were synthesized, characterized, and tested for their activity and selectivity for nitrate reduction at different operating potentials (**Chapter 4**). The Pt_xRu_y/C alloys are more active than Pt/C, with $Pt_{78}Ru_{22}/C$ being six times more active than Pt/C at 0.1 V vs. RHE with 93–98% faradaic efficiencies towards ammonia. Experimental and computational results show similar qualitative trends, with the maximum catalytic activity occurring at Ru content of ~25 at%. This maximum is rationalized by an optimum in nitrate and hydrogen binding energies where there is a transition of the rate-determining step from nitrate dissociation to a new rate-determining step. This work confirms previous computational models and demonstrates how electrocatalyst activity can be optimized by changing the adsorption strength of reacting species through alloying, providing further insights for future catalyst design for optimal nitrate reduction and ammonia production.

By comparing ENO_3RR with TNO_3RR, we obtain additional mechanistic insights for the similarities and differences between the two reactions (**Chapter 5**). The results show that increasing the driving force of hydrogen (H_2 partial pressure for TNO_3RR and applied potential for ENO_3RR) and nitrate concentration increases the reaction activity. Additionally, the activity order of catalyst composition also remains the same. Despite these similarities, the effects of pH and the apparent activation energy have a different effect on PtRu/C for TNO_3RR and ENO_3RR activity, suggesting reaction effects and changes to the mechanism unique to ENO_3RR. Additional work to isolate pH effects on ENO_3RR, such as ionic strength, hydrogen equilibrium potential, the point of zero free charge, is important to understand nitrate reduction mechanisms. By comparing these reactions at similar conditions, this work allows us to evaluate TNO_3RR and ENO_3RR systems for industrial implementation.

Chapter 1

Introduction

1.1 Motivation

This section will provide an overview of the motivations for developing an environmentally sustainable ammonia synthesis process. **Section 1.1.1** will provide a background for the current Haber-Bosch process and offer insights on methods to improve upon operational challenges. **Section 1.1.2** will present a brief overview of problems that result from anthropogenic nitrogen fixation that needs to be considered to rebalance the nitrogen cycle.

1.1.1 Production of Ammonia via Sustainable Methods

The Haber-Bosch process is a revolutionary catalytic reaction that produces ammonia (NH_3) from nitrogen (N_2) and hydrogen (H_2). This process has facilitated the production of agricultural fertilizer on an industrial scale and increased global agricultural productivity.[1] Currently, more than 150 million tons of NH_3 are produced annually using the Haber-Bosch process and are projected to increase by 2.3% per year.[2] Approximately 80 – 90% of the product from this reaction is used as fertilizer, which supports a large fraction of the global population (**Figure 1.1**).[3] It is estimated that the number of humans supported per hectare of arable land has increased from 1.9 to 4.3 persons between 1908 to 2008,[4] and that 40% of the population since the end of the 20th century depends on fertilizer from the Haber-Bosch process.[5,6]

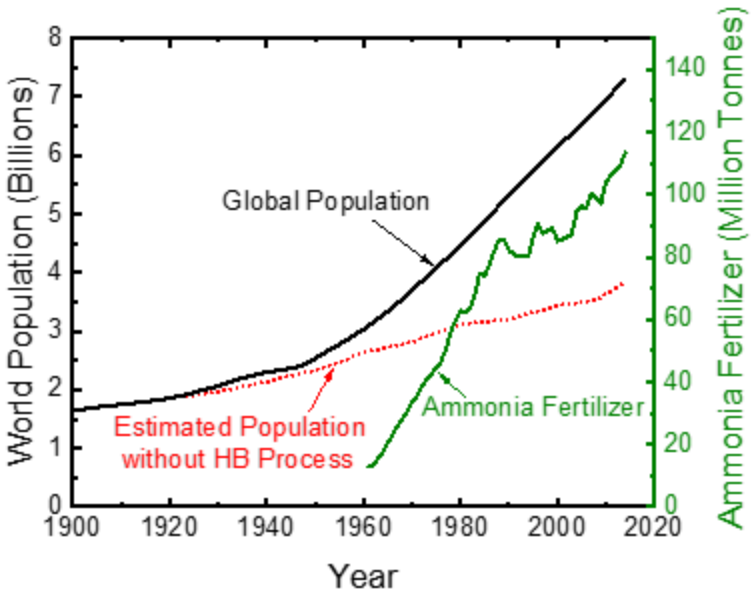

Figure 1.1. Correlation between the global population (billions) and annual ammonia fertilizer production rates (million tonnes) from 1900 to 2015. The dotted red line indicates estimated population without the innovation of the Haber-Bosch (HB) process. Data of world population and ammonia fertilizer production obtained from Ref. [7].

Despite the discovery of Haber-Bosch ammonia synthesis over a century ago, there have been no significant changes to current commercial plants that operate at high temperatures (400 – 500 °C) and pressures (150 – 300 bar). In the low-energy Kellogg ammonia plants developed in 1995, operations at high pressures attribute to 40% of the total energy consumption during the reaction.[8,9] At these operating conditions, the equilibrium conversion is ~15%, and reactants are recycled until the reaction reaches 97% conversion.[10,11] Additionally, the hydrogen gas used during this reaction is generated from fossil-fuel feedstock (e.g., methane, coal, oil) that emits vast quantities of CO_2 throughout the process (**Figure 1.2**). CO_2 emission from hydrogen production account for more than half of the CO_2 emitted during the entire ammonia synthesis process.[12] Post-production, additional CO_2 emissions are incurred from transporting ammonia from a large centralized plant.[13] Accounting for all these factors, ammonia synthesis accounts for 2% of the annual global energy consumption. Additionally, approximately 1.9 tonnes of CO_2 are emitted for

every tonne of NH_3 produced,[3] which represents 1.2% of the global anthropogenic CO_2 emissions.[14]

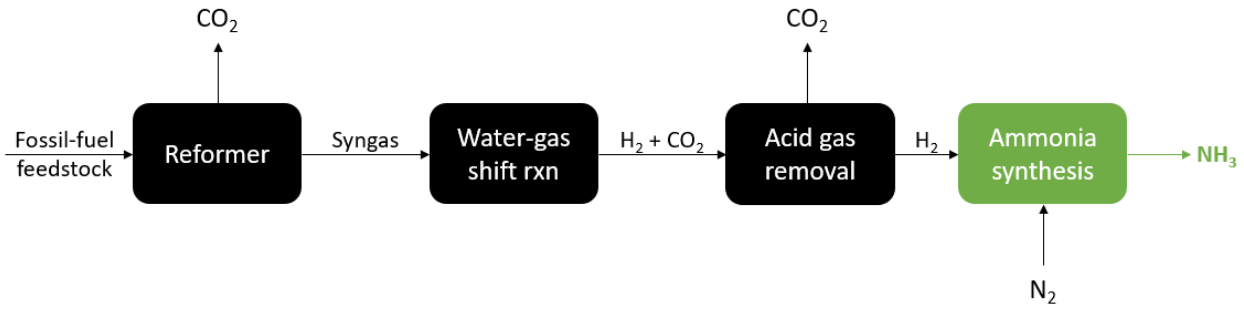

Figure 1.2. Current industrial process for ammonia synthesis involving multiple steps to generate hydrogen gas. In the first step, reformers are used to turn fossil-fuel feedstock (e.g., methane, coal, oil) into synthesis gas (syngas), which consists of H_2, CO_2, CO, and H_2O. A CO shift converter combines CO and H_2O to form CO_2 and H_2 before isolating the H_2 used for ammonia synthesis. Vast quantities of CO_2 are emitted throughout this process. Figure adapted from Ref. [12].

As a carbon- and energy-intensive process, there is a global urgency to make ammonia production more sustainable to feed the global population. There are many different scientific approaches to tackle this challenge: (1) lower operating pressures to reduce energy consumption during the reaction, (2) use renewable electricity to reduce greenhouse gas emissions for H_2 production, (3) enable decentralized ammonia production to minimize CO_2 emissions from transportation, and (4) rebalance the nitrogen cycle by reducing excess nitrate pollutants generated from anthropogenic nitrogen fixation. Thus, it is vital to rebalance the nitrogen cycle for long-term environmental sustainability. **Chapter 3** will examine catalysts for approach (1) and **Chapters 4** and **5** will explore alternative catalytic options for approaches (2 – 4).

Many engineering advancements explore using renewable energy and sustainable feedstock to make ammonia on a smaller scales. Companies are investigating the option of deriving hydrogen from electrolysis and alternative energy sources that can be implemented in the Haber-Bosch process for small-scale ammonia synthesis. By decentralizing N_2 fixation, local renewable energy source can also reduce CO_2 emissions and costs associated with NH_3 transportation,[13]

though exact emission values are difficult to obtain depending on different transportation infrastructures around the world. **Figure 1.3** provides an estimated overview of CO_2 emissions from both the traditional Haber-Bosch process that uses H_2 gas from a methane-fed and electrical system. By eliminating H_2 gas production from methane, the electrical system would ultimately reduce CO_2 emissions by over 70% for every tonne of NH_3.

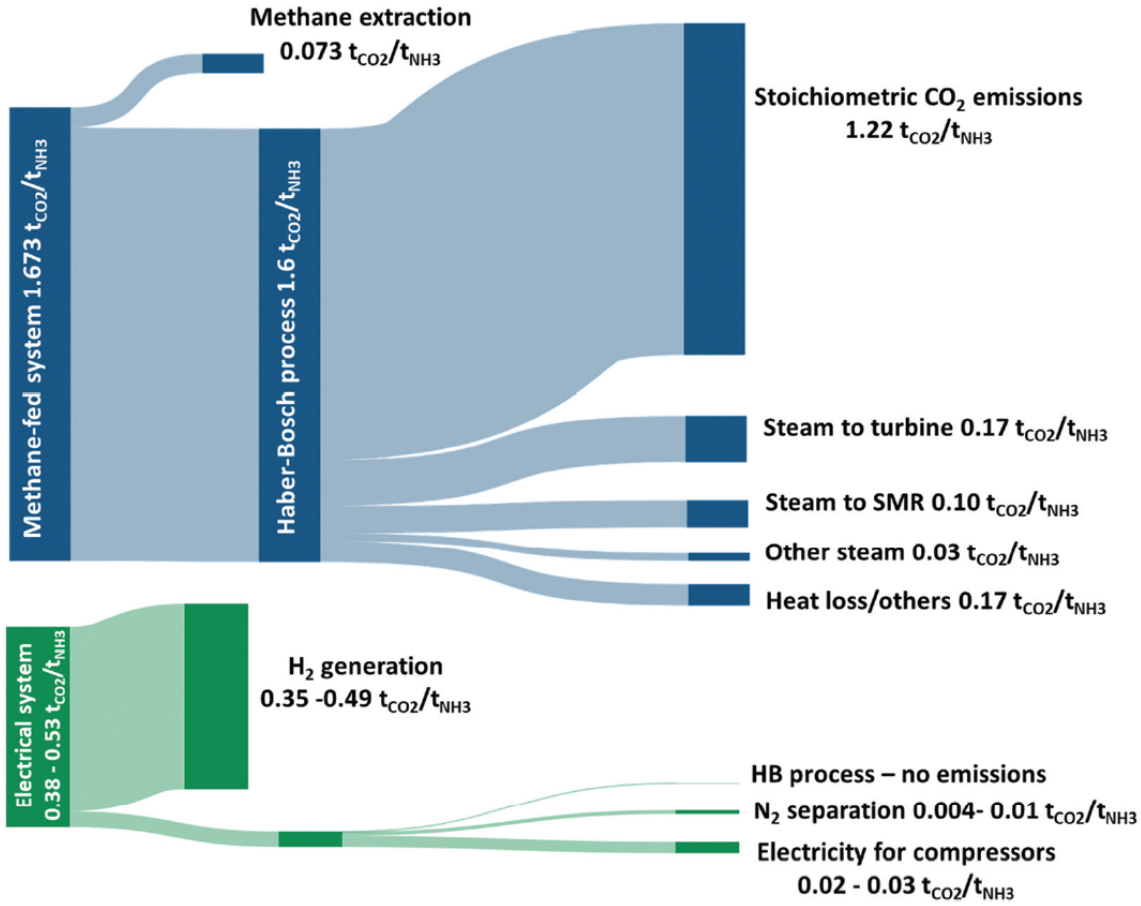

Figure 1.3. Sankey diagram of CO_2 emissions from methane-fed and electrically driven Haber-Bosch synthesis. The range of values in the electrical system depends on the size of the wind turbines. Image from Ref. [8].

At the forefront of this technological revolution is Japanese company JGC, which uses solar power to produce hydrogen through water electrolysis for the Haber-Bosch process using a ruthenium catalyst. JGC has constructed a demonstration plant, which is capable of producing 20 kg of ammonia per day.[15] Likewise, demonstration plants from Siemens in the UK use wind power

as the primary source of electricity to generate hydrogen and produce 20 – 30 kg of ammonia per day.[16] Despite reducing CO_2 emissions from producing H_2, these systems still use the Haber-Bosch process to synthesize ammonia, limiting the maximum production efficiency to ~50%.[12]

Researchers have also explored directly producing ammonia electrocatalytically from nitrogen as an alternative to the Haber-Bosch process. Nitrogen reduction reaction (NRR) uses electricity instead of hydrogen gas, thus reducing carbon emissions. This process also has the benefit of operating at low temperature and pressure, which further reduces energy consumption. In fact, technoeconomic analyses show that catalysts benchmarked at 62% efficiency for NRR would be 18% more economical than electrocatalytically producing hydrogen at 80% efficiency for the Haber-Bosch reaction.[17] However, despite the advantages of NRR, many kinetic limitations still limit this reaction to be scaled industrially, and recent research has focused on recycling nitrate as a reactant in place of nitrogen.[12]

1.1.2 Conversion of Nitrate Pollutants to Ammonia

Major alternatives to current Haber-Bosch ammonia synthesis include bypassing the use of nitrogen and using nitrate (NO_3^-) as the major reactant instead. Nitrate is the most oxidized nitrogen species and is a major pollutant in groundwater, rivers, and lakes, accumulating in all parts of the globe.[18,19] Leaching nitrate in water sources leads to negative environmental consequences, which include eutrophication, global acidification, climate change, and ozone loss in the stratosphere.[20] Consumption of nitrate-contaminated water also has detrimental health impacts, such as methemoglobinemia and cancer.[20]

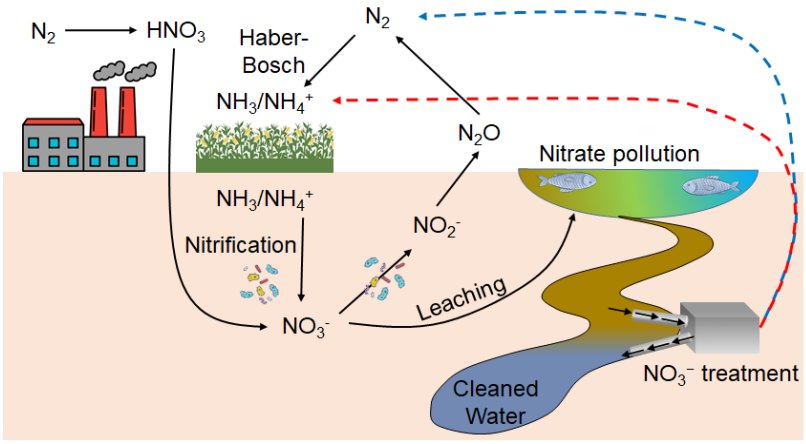

Figure 1.4. Simplified description of the nitrogen cycle including nitrogen fixation by Haber-Bosch and for crop cultivation, as well as from industrial processes. Adapted from images in Ref. [21], Ref. [22], and Ref. [23]. Certain bacteria convert ammonia to nitrate, and other bacteria convert nitrate to nitrite and back to N_2. Dominant nitrogen species pathways are shown by solid lines. Additional nitrate treatment is needed to prevent further accumulation of nitrate in water streams by converting nitrate to N_2 and NH_3/NH_4^+ as indicated by the blue and red dashed lines, respectively.[23]

As of 2020, the National Academy of Engineering identifies the management of the nitrogen cycle, through improved fertilization technologies and by capturing and recycling waste, as a grand challenge.[24] Large-scale anthropogenic nitrogen fixation (**Figure 1.4**) creates an imbalance in the nitrogen cycle that may pose an even more immediate threat or exacerbate challenges with the carbon cycle.[25] Fertilizer for food production through the Haber-Bosch process results in 10^8 metric tonnes of nitrogen being fixed per year.[18] An additional 2.5×10^7 metric tonnes of nitrogen is produced from the combustion of fossil fuels and 3.3×10^7 metric tonnes from the cultivation of crops that fix nitrogen through biological pathways.[20] Even though bacterial species naturally convert fixed nitrogen back to N_2, the continuously increasing nitrogen fixation rates to support the world's growing population are much higher. Due to the continued importance of anthropogenic nitrogen fixation for industry and food production, it is crucial to implement actions to rebalance the nitrogen cycle and maintain the environmental health of the Earth.[22] Using nitrate as a reactant for ammonia production has two major advantages: (1) this process can

rebalance the nitrogen cycle by removing nitrate contaminants from water sources, and (2) it can convert nitrate to ammonia to minimize the need for Haber-Bosch processes.

Even though the technology is promising, large-scale applications of denitrification have been limited due to a lack of research on long-term operational stability of the heterogeneous catalysts under practical conditions.[21] Additionally, a majority of prior research has focused on developing materials with high selectivity to N_2 as a method to treat nitrate contaminants, and only recently have studies focused on developing materials aimed at selectively reducing nitrate to ammonia.[26] Furthermore, there are no studies that compare electrocatalytic and thermal catalytic nitrate conversion to ammonia, despite research in both systems using similar catalysts. This is most likely because electrocatalytic systems operate at higher concentrations of nitrate at either very acidic or basic conditions while studies in thermal catalytic systems focus on lower concentrations at neutral conditions.

The current industrial Haber-Bosch process consumes almost 4 kWh per kg of ammonia produced.[27] By comparison, the most active and selective strained Ru catalyst for electrocatalytic nitrate reduction requires approximately 22 kWh per kg of ammonia (based on cell potential of 2 V and 100% faradaic efficiency (FE)).[28] To make this technology economically and industrially feasible, it is important to identify active and selective catalysts to convert nitrate to ammonia at lower overpotentials to reduce electricity costs.[23]

1.2 Reactions for Ammonia Synthesis

This section will provide an overview of different catalytic reaction mechanisms for ammonia synthesis. **Section 1.2.1** will focus on the industrial Haber-Bosch process, and **Sections 1.2.2** and **1.2.3** will explore electrocatalytic and thermocatalytic nitrate reduction reactions, respectively.

1.2.1 Haber-Bosch Synthesis

The Haber-Bosch process is one of the most successful and well-studied reactions that converts nitrogen and hydrogen to ammonia at high temperatures (400 – 500 °C) and pressures (150 – 300 bar). The major challenge of this reaction is the competition between synthesis rates and reaction equilibrium. For example, the iron-based catalysts need to operate at 400 °C to be effective in breaking the nitrogen triple bond. However, this reaction is exothermic, meaning that it would become more favorable for product formation at lower temperatures (equilibrium constant = 1 from 150 – 200 °C). Additionally, increasing the pressure will favor higher ammonia yields because there are 4 moles of reactant for every 2 moles of product. The reaction mechanism for Haber-Bosch ammonia synthesis is presented in the following elementary steps (**Equations 1.1-1.6**):

$$H_2(g) \rightleftharpoons 2H^* \tag{1.1}$$

$$N_2(g) \rightleftharpoons 2N^* \tag{1.2}$$

$$N^* + H^* \rightleftharpoons NH^* \tag{1.3}$$

$$NH^* + H^* \rightleftharpoons NH_2^* \tag{1.4}$$

$$NH_2^* + H^* \rightleftharpoons NH_3^* \tag{1.5}$$

$$NH_3^* \rightleftharpoons NH_3(\mathrm{g}) \tag{1.6}$$

Energy values for each individual step, derived experimentally and from estimated calculations, provide a potential energy diagram for the overall reaction (**Figure 1.5**). At industrial synthesis conditions, the dissociation of nitrogen is the rate-limiting step in the reaction. However, since the activation energy for nitrogen dissociation is less than its subsequent hydrogenation steps, the latter steps may become rate-limiting at low temperatures.

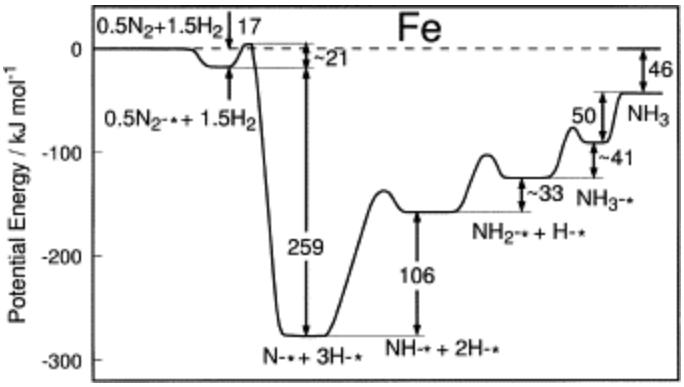

Figure 1.5. Potential energy diagram for ammonia synthesis on an iron surface. Energy values are provided in kJ/mol. Figure adapted from Ref. [29,30].

Due to the challenges and reaction condition limitations, industrial ammonia synthesis requires stoichiometric balances of hydrogen and nitrogen to pass over catalyst beds four times with intermittent cooling to maintain equilibrium. On each pass, only 15% conversion occurs and reactants are recycled until the reaction reaches an overall conversion of 97%.[31] Industrial Haber-Bosch ammonia synthesis is performed with promoted iron (Fe) catalysts. Al_2O_3 typically acts as the structural support, which prevents the iron particles from sintering under reaction conditions, but has no direct impact on the reaction chemistry. Potassium (K) is used as an electronic promoter to accelerate nitrogen dissociation (**Equation 1.2**). Once the nitrogen atoms form on K sites, they diffuse away to Fe sites where the reaction takes place.[29,32] At ambient pressures with N_2/H_2 flow, the surface of the catalyst shows an increased concentration of metallic iron. Under operating conditions at above 350 °C and at high pressures, there is low surface concentration of adsorbed N_2 and NH_3 since the reaction is equilibrium-limited. At higher NH_3 and H_2 partial pressures, bulk nitrides might form.[33]

1.2.2 Electrocatalytic Nitrate Reduction Reaction

This section provides an overview of the mechanism of electrocatalytic nitrate reduction reaction (ENO_3RR) (as adapted with permission from Ref. [34]), focusing on direct nitrate reduction

occurring at a catalyst surface rather than indirectly through formation of reactive species.[35] Direct ENO_3RR is the dominant mechanism at < 1 M nitrate without excess nitrite in solution and is the focus of the research presented in this dissertation.[35,36] Following the mechanistic discussions, the effect of different metal and alloy electrocatalyst on ENO_3RR will be discussed. This overview provides the technical background for the work in **Chapter 4**.

The mechanism for direct nitrate reduction begins with adsorption of the nitrate ion onto an electrocatalyst surface, as depicted in **Figure 1.6**. Adsorbed nitrate is reduced to adsorbed nitrite, and then subsequent steps lead to the formation of ammonia, nitrogen, and different nitrogen oxides. While the initial nitrate-to-nitrite step is common to all ENO_3RR pathways and often controls the overall reaction rate, the rates of the subsequent steps that diverge at NO* control the selectivity of the reaction. The general ENO_3RR pathway is also similar to that for catalytic (i.e., non-electrochemical) nitrate reduction.[21,37] H_2 often forms during ENO_3RR but is not explicitly discussed as it occurs in a separate mechanistic pathway that often lowers the ENO_3RR FE.

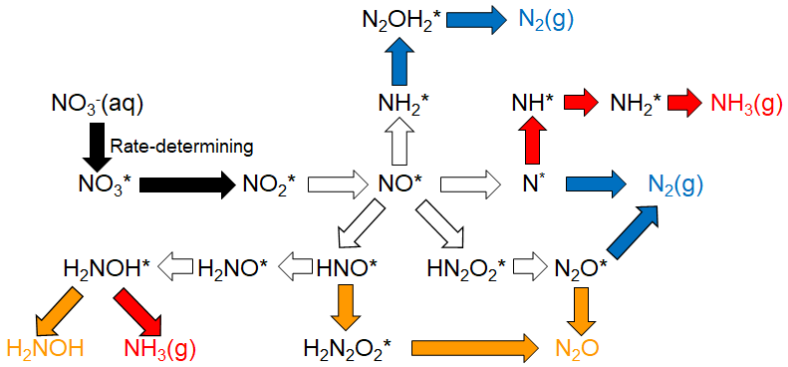

Figure 1.6. Electrocatalytic nitrate reduction reaction mechanism using reported mechanisms from Ref. [38] and Ref. [39]. Pathways to different products are labeled according to whether they form ammonia/ammonium (red), nitrogen (blue), or nitrogen oxides (orange). White colored arrows correspond to pathways that lead to different products, while black arrows are those steps commonly associated with the rate-determining step on transition metal surfaces. Species adsorbed onto the catalyst surface are noted by *, representing a catalyst surface site. Only the nitrogen species are included.

The work to understand the ENO_3RR mechanism has been primarily through kinetic studies that have identified reaction products and hypothesized pathways based on microkinetics. Additionally, in situ spectroscopy and computational work have been used to identify adsorbed intermediate species and test the microkinetic models. The effect of reaction environment (e.g., pH, concentration, anions) on reaction rates also gives valuable insight into the overall reaction mechanism. The combination of kinetic studies, spectroscopy, and computational work has improved the understanding of the first nitrate to nitrite step and the selectivity determining steps that control the product distribution.

1.2.2.1 *Nitrate Deoxygenation to Nitrite*

As discussed above, the first step in ENO_3RR is nitrate adsorption (**Equation 1.7**), and thus nitrate's adsorption energy and mode are expected to play a significant role in the overall reaction pathway. Here, nitrate adsorption is denoted as involving charge transfer as the electron is completely donated to the electrocatalyst surface. However, unlike protons or other anions such as chloride, there is no clear evidence about the valency of the adsorbed nitrate (i.e., whether it is NO_3* or NO_3^-*, where * represents a catalyst site). Regardless, the thermodynamics of nitrate adsorption depend on the applied potential and the adsorption free energy of nitrate. Surface-enhanced infrared-adsorption spectroscopy (SEIRAS) spectra of nitrate ion at Pt identified an O,O-bidentate adsorption mode.[38,40] Note that nitrate typically adsorbs onto two catalyst atoms, but it is denoted as adsorbing onto a single site here for simplicity. At very negative potentials, some proposed mechanisms involve the formation of nitrate radicals as an initial step.[41]

$$NO_3^-(aq) + * \rightleftharpoons NO_3 * + e^- \tag{1.7}$$

There are two series of elementary steps for adsorbed nitrate (NO_3*) to convert to NO_2* and water. In the first series of elementary steps, the NO_3*-to-NO_2* dissociation may occur by

protonation of NO_3* to form HNO_3*, followed by formation of NO_2* and H_2O.[42] In the second case, shown by **Equations 1.8-1.12**, the oxygen bond of NO_3* is cleaved to form NO_2* and O*. This O* group hydrogenates to form H_2O. H is generally believed to be supplied through adsorbed hydrogen (H*) from proton reduction[43] or electron transfer reduction. Hydrogen radicals have recently been proposed as an alternative H source formed from the tensile lattice strain of subsurface O in Ru.[28] The rate of the nitrate-to-nitrite step will depend on the rates of these individual elementary steps.

$$NO_3 * + * \longrightarrow NO_2 * + O * \tag{1.8}$$

$$H^+(aq) + e^- + * \rightleftarrows H * \tag{1.9}$$

$$O * + H * \longrightarrow OH * + * \tag{1.10}$$

$$OH * + H * \longrightarrow H_2O(l) + 2 * \tag{1.11}$$

$$NO_2 * \longrightarrow other\ species \tag{1.12}$$

The conversion of nitrate to nitrite is believed to be the rate-determining step (RDS) for ENO_3RR on transition metals, but it is not always clear which specific elementary step of the nitrate-to-nitrite process is rate-determining.[44–47] The reaction order in nitrate is 0.51 and 0.34 for Pt and Rh from 0.001 to 0.1 M NO_3^-, respectively, indicating that the RDS occurs after nitrate adsorption and that nitrate adsorption (**Equation 1.7**) is quasi-equilibrated.[44] On Pt,[35] the reaction order is positive at low nitrate concentrations (< 0.1 M) but becomes negative at high nitrate concentrations (> 0.1 M). Because of the observation of a negative reaction order in nitrate, other species (e.g., H*, O*, OH*) must also compete for surface sites under those reaction conditions in addition to nitrate. If the hydrogenation (removal of the cleaved oxygen, **Equations 1.10** and **1.11**) were sufficiently fast, the rate would be solely determined by the coverage of nitrate on the surface and the rate constant of deoxygenation. Thus, the coverage of nitrate is controlled by the adsorption

energies of nitrate (**Equation 1.7**) and any other species that may adsorb and compete for sites on the catalyst surface (e.g., hydrogen, other anions).

Some electrocatalysts display a maximum in activity with potential rather than a monotonically increasing activity with more negative potential, most commonly seen for Pt.[21,38] This activity maximum can be explained by the competition between hydrogen and nitrogen species on the electrocatalyst surface.[45,48] Nitrate adsorption is more favorable at positive potentials while hydrogen adsorption is more favorable at negative potentials. Other possible elementary steps that would control the rate might be the hydrogenation of the adsorbed oxygen, but typically this step is assumed to be fast compared to nitrate deoxygenation such that it can be assumed to be at quasi-equilibrium.

The observations that nitrate deoxygenation controls the rate means that active ENO_3RR catalysts must adsorb nitrate strongly enough to maintain high surface coverages under reaction conditions. Vibrational spectroscopy of nitrate adsorption on Pt(110) identified that the difference in ENO_3RR activity on different sites is attributed to structure sensitivity of the adsorption.[48,49] The nitrate adsorption energy trend also explains the order of platinum group metals activity (Rh > Ru > Ir > Pd ≈ Pt).[44]

Measurements of the H and nitrate coverage under reaction conditions support that the RDS involves H* and NO_3* and that the activity is related to the nitrate adsorption energy. X-ray absorption near edge spectroscopy (XANES) showed that adsorbed hydrogen competes with and can block nitrate from adsorbing at more negative potentials.[38] This rationalizes the observation that nitrate reduction activity on platinum reaches a maximum and then decreases at more negative potentials. Computational studies of the mechanism and the degree of rate control[50,51] also support the hypothesis that nitrate deoxygenation is the RDS for most single metals.[38] It is important to

note, however, that at different potentials and for new catalysts (particularly those that may bind nitrate very strongly), other elementary steps may be rate-determining.

1.2.2.2 *Nitrate to Ammonia Pathways*

Following nitrate conversion to nitrite, the products formed will differ based on the electrolyte conditions and electrocatalyst. This dissertation will focus on the reaction mechanism to convert nitrate to ammonia, a valuable product used as fertilizer, fuels, cleaners, and chemical precursors.[4] Ammonia production from ENO_3RR is kinetically more feasible than breaking the nitrogen triple bond as required in the Haber-Bosch process, and would provide a less energy-intensive approach for decentralized fertilizer production using renewable electricity. Thus, recent ENO_3RR literature have focused more on producing ammonia as the desired product.

Nitrate reduction to ammonia (E^0 = 0.82 V vs. RHE) typically proceeds by sequential hydrogenation steps using 8 electrons. Following the formation of adsorbed nitrite, further reduction leads to NO*. From the adsorbed NO, there are two major pathways to produce ammonia. One potential pathway is the conversion of NO* to hydroxylamine (NH_2OH), then reduction of hydroxylamine to ammonia, as proposed by Kuwabata et al. (**Equations 1.13-1.16**).[52] This pathway is supported by product quantification measurements that detect hydroxylamine as a byproduct of ammonia production on various Cu-based catalysts.[53,54]

$$NO* + H^+(aq) + e^- \rightleftarrows HNO* \tag{1.13}$$

$$HNO* + H^+(aq) + e^- \rightarrow H_2NO* \tag{1.14}$$

$$H_2NO* + H^+(aq) + e^- \rightarrow H_2NOH* \tag{1.15}$$

$$H_2NOH* + 2H^+(aq) + 2e^- \rightarrow NH_3(g) + H_2O(l) + * \tag{1.16}$$

Another ammonia pathway is NO* reacting with adsorbed hydrogen atoms in a strong reducing environment to produce NH_3 (**Equations 1.17-1.20**). In the special case of the strained Ru nanoclusters,[28] an optimal tensile lattice strain in the material creates hydrogen radicals that act as the dominant species to accelerate the conversion from nitrate to ammonia. The intrinsic electrocatalytic nitrate reduction rate is the highest reported to date in literature, producing 1.17 ± 0.04 mmol h^{-1} cm^{-2} of ammonia.[28]

$$NO* + 2H* \rightarrow N* + H_2O(l) + 2* \quad (1.17)$$

$$N* + H* \rightarrow NH* + * \quad (1.18)$$

$$NH* + H* \rightarrow NH_2* + * \quad (1.19)$$

$$NH_2* + H* \rightarrow NH_3(g) + 2* \quad (1.20)$$

Fourier transform infrared (FTIR) spectroscopy studies on Cu(100) and Cu(111) (**Figure 1.7a**) at different applied potentials show nitrate consumption in the solution and ammonia production on both surfaces in acidic media.[55] The change in the band at 1370 cm^{-1} indicates the consumption of nitrate as the overpotential increases. NO* is indicated by the N-O stretching bands that occur at 1627 cm^{-1} and 1617 cm^{-1} for Cu(111) and Cu(100), respectively. Both copper surfaces show an increase in the signal from the peak at 1460 cm^{-1} with increasing overpotential, corresponding to the formation of NH_3. The absence of nitrite peaks at 1231 cm^{-1} indicates a fast conversion of nitrite into NO, and subsequently from NO to NH_3 in acidic media on both Cu facets (**Figure 1.7b**). However, in basic conditions, both Cu surfaces indicate the presence of nitrite, and Cu(100) produces hydroxylamine, indicating a change in reaction mechanism with electrolyte conditions.[55]

Ammonia production is most commonly believed to proceed via sequential hydrogenation on platinum group metals.[56] In the case of Pt[48] and Pd[56], the metal active sites typically provide

the adsorbed hydrogen atoms required for the hydrogenation reaction. A recent study on Rh in basic electrolyte with SEIRAS and differential electrochemical mass spectrometry (DEMS) detect N=N bond stretching at 2020 cm^{-1}. This finding implies an electrochemical process with a two-electron transfer to form N_2H_2 (**Figure 1.7c**) which subsequently decomposes into NH_3.[57] A recent study that focuses on investigating different compositions of PtRu alloys also shows that regardless of the metal composition, all the alloys reached above 93% FE towards ammonia throughout a 7-hour reaction.[58]

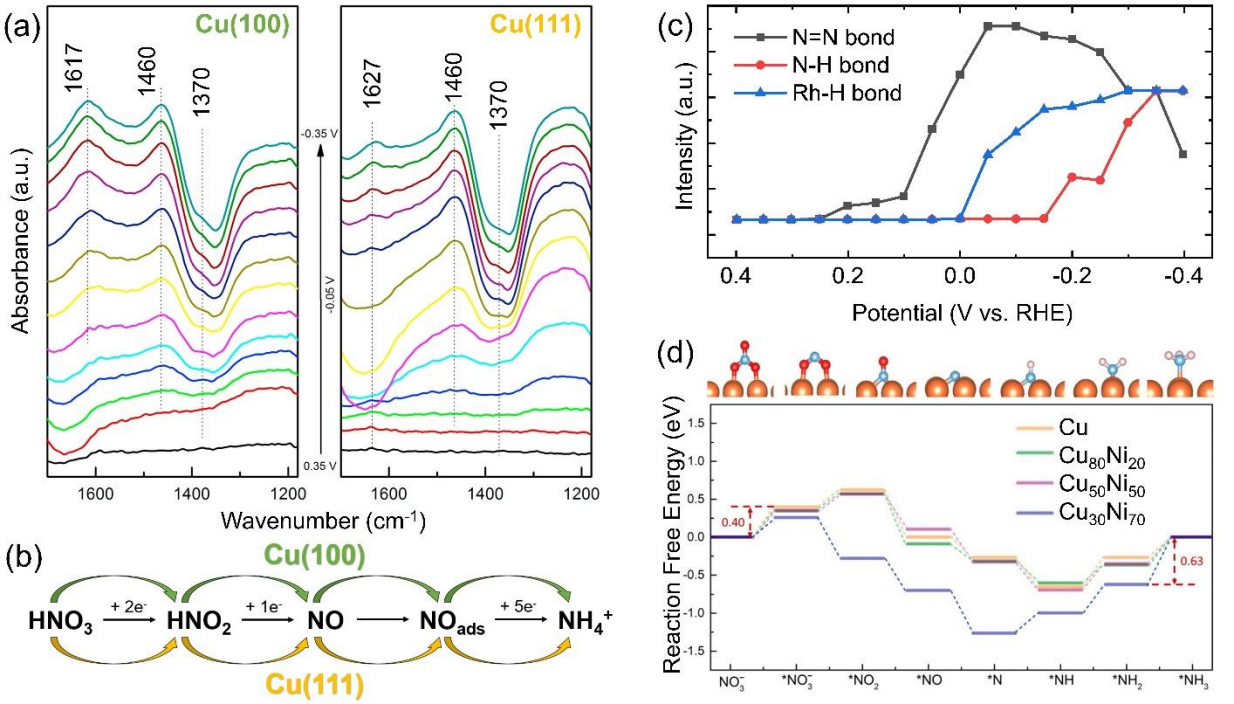

Figure 1.7. Evidence for different possible ammonia formation mechanisms. **(a)** Fourier transform infrared spectroscopy (FTIR) on Cu(100) and Cu(111) surfaces in 0.1 M $HClO_4$ + 10 mM $NaNO_3$ at applied potentials from 0.35 V vs. RHE to −0.35 V vs. RHE. See text for peak assignments. Adapted from Ref. [55]. **(b)** Hydrogenation mechanism proposed from nitrate to ammonia on Cu(100) and Cu(111) surfaces in acidic media. Adapted from Ref. [55]. **(c)** FTIR band intensities as a function of potential on Rh. The N=N stretching vibration, hydrogen adsorbed on Rh, and N–H bending vibration are represented in black squares, red circles, and blue triangles, respectively. Adapted from Ref. [57]. **(d)** Reaction free energy diagram for each hydrogenation step from nitrate to ammonia. As the Ni content increases in the alloy, the rate-determining step shifts from the conversion of nitrate to nitrite step to hydrogenation of NH_2* to NH_3*. Adapted from Ref. [59].

For most, but not all, metals, more acidic conditions result in high selectivity towards ammonia.[60] For example, Sn, Bi, Pb, Al, Zn, and In operating in a pH range of 0 to 4 correspond to a higher fraction of ammonia formed.[61] On Ti, strongly acidic (0.77) pH and moderate to high nitrate concentration (0.1 to 0.6 M NO_3^-) promote the highest selectivity toward ammonia synthesis.[60] This is attributed to a higher proton availability to form NH_4^+/NH_3. An outlier to the general trend of ammonia production at lower pH is the family of CuNi alloys, which display above 95% FE towards ammonia in basic conditions (pH of 8.5 to 14).[59,62–64] When exploring different compositions of Cu and Ni, Wang et al. found $Cu_{50}Ni_{50}$ to have the optimal activity and selectivity towards ammonia (**Figure 1.7d**). As the Ni content in the alloy increases, the free energy of reaction from the initial nitrate conversion to nitrite decreases. However, at 70% Ni, the free energy for the hydrogenation step from NH_2* to NH_3* becomes the limiting factor. These results show that CuNi alloys are promising to investigate for the conversion of nitrate to ammonia in wastewater of high pH.

1.2.3 Thermal Catalytic Nitrate Hydrogenation

For comparison, **Chapter 5** will focus on exploring the differences between thermal catalytic nitrate reduction (TNO_3RR) and ENO_3RR and evaluate which system is more favorable for ammonia production. TNO_3RR is very similar to ENO_3RR and follows a stepwise reaction (**Figure 1.8**) with nitrate reduction to nitrite as the rate-determining step in the reaction.[65] Like ENO_3RR, the NO hydrogenation step determines the product selectivity and depends on catalysts and reaction conditions. Major differences between the two reaction mechanisms have not been explored extensively.

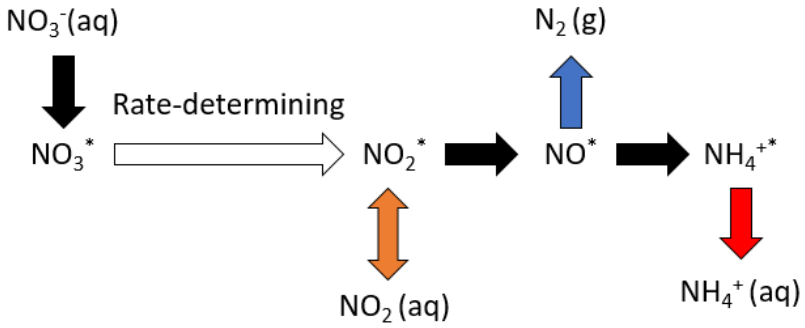

Figure 1.8. Schematic of stepwise thermal catalytic nitrate reduction reaction (TNO_3RR) mechanism from Ref. [65]. Pathways to different products are labeled as ammonia/ammonium (red), nitrogen (blue), and nitrite (orange). White colored arrow corresponds to the rate-determining step. Species adsorbed onto the catalyst surface are noted by *, representing a catalyst surface site.

Major investigations into this mechanism focus on identifying the active sites at each step of the reaction. In the bifunctional mechanism on supported Pt-Cu alloys, nitrate hydrogenation occurs on Cu promoter sites while Pt sites help to maintain the Cu in metallic state and improve selectivity towards N_2.[66] Similarly, this bifunctional mechanism also applies to supported Pd-Cu alloys for NH_3 production.[67,68] Yoshinaga et al. further suggested that the products are directly related to the site identity (**Figure 1.9**). Nitrite reduction in the flat terrace sites of Pd results in nitrogen formation whereas edge sites tend to favor ammonia production.[69] Additionally, the selectivity depends on the different concentrations of Cu and Pd sites available on the surface, indicating that the metal ratios also play a key role in the catalytic performance.

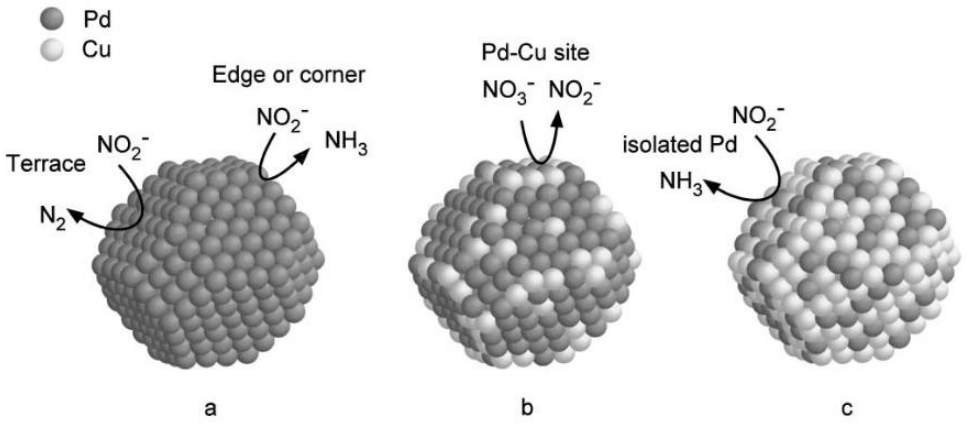

Figure 1.9. Proposed models of Pd and Pd-Cu particles for nitrite hydrogenation. **(a)** 5 wt% Pd, **(b)** 5 wt% Pd-0.6 wt% Cu, **(c)** 5 wt% Pd-3 wt% Cu. Adapted with permission from Ref. [69].

1.3 Catalysts for Ammonia Synthesis

In this section, many different types of catalysts used for Haber-Bosch synthesis, ENO_3RR, TNO_3RR will be evaluated. **Section 1.3.1** focuses on traditional ammonia synthesis catalysts and supported molybdenum carbides (Mo_2C) and nitrides (Mo_2N) that are active at ambient operating pressure. The specific activity, defined as the rate of ammonia normalized by the surface area, is primarily used to evaluate the catalyst performance. **Section 1.3.2** provides an overview of both monometallic and bimetallic catalysts that have previously been studied for ENO_3RR, and **Section 1.3.3** will expand upon similar materials, but for TNO_3RR. In the latter two sections, the catalyst performance is determined by the turnover frequency, selectivity, and FE, as defined in **Equations 1.21 – 1.23**.

$$Turnover\ frequency\ (TOF) = \frac{moles\ of\ desired\ product}{moles\ of\ active\ sites\ \times\ time\ of\ rxn} \tag{1.21}$$

$$Selectivity\ of\ product\ x = \frac{[x]_t}{[NO_3^-]_{t0} - [NO_3^-]_t} \times 100\% \tag{1.22}$$

$$Faradaic\ efficiency\ (FE)\ of\ x = \frac{charge\ for\ product\ x}{total\ charge} \quad (1.23)$$

1.3.1 Gas-Phase Ammonia Synthesis Catalysts

1.3.1.1 *Industrial Ammonia Synthesis Catalysts*

Iron (Fe) is cheap, abundant, and is the most effective known catalyst for ammonia synthesis when supported on aluminum oxide (Al_2O_3) and potassium oxide (K_2O).[70,71] As previously mentioned in **Section 1.2.1**, Al_2O_3 typically acts as structural support to prevent Fe sintering while potassium is responsible for the electronic promotion that improves nitrogen dissociation. Currently, a substitute commercial process (Kellogg Advanced Ammonia Process) uses a ruthenium-based catalyst that reports activities 10–20 times greater than that of commercial Fe catalysts while operating at approximately 2 bar compared to commercial pressures at above 150 bar.[72] Despite these advancements, **Figure 1.10** shows that compressors used to operate the reaction at high pressures still represent the single highest energy cost of the overall ammonia synthesis process. Therefore, it is necessary to find cheap alternative catalysts that achieve higher activity at lower operating temperatures and pressures.

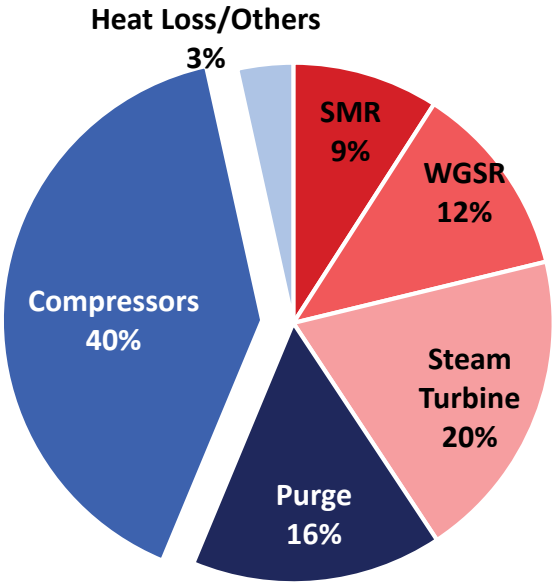

Figure 1.10. Breakdown of the energy consumption for the 1995 low-energy process that uses a Ru-based catalyst. The red and blue shadings represent energy consumption during the H_2 production and ammonia synthesis process, respectively. SMR represents steam methane reforming and WGSR stands for the water-gas shift reaction. Adapted from Refs. [8,9].

1.3.1.2 *Carbides and Nitrides for Ambient Pressure Ammonia Synthesis*

The research introduced in **Chapter 3** will explore using early transition metal carbides and nitrides for ammonia synthesis, as these materials are more active than the commercial Ru catalyst under atmospheric pressure for NH_3 synthesis.[73] Early transition metal carbides and nitrides are produced by inserting carbon or nitrogen atoms interstitially into the lattice of the bulk metal. These materials possess physical properties that are similar to those of ceramics, which makes them ideal to withstand the harsh conditions of ammonia synthesis, while their electronic and magnetic properties are more closely aligned to those of metals. Thus, carbides and nitrides are ideal candidates for a multitude of heterogeneous catalytic applications, and are active for reactions including but not limited to selective hydrogenations,[74–76] Fischer-Tropsch synthesis,[77,78] methanol steam reforming,[79,80] water-gas shift,[81,82] and hydrogen oxidation reactions.[83]

Common temperature-programmed synthesis methods for high surface area early transition metal carbides and nitrides were first developed by the Boudart group and consist of treating a precursor in a reactive gas stream while changing the temperature uniformly in a packed bed flow reactor.[84–86] With this technique, it is possible to directly transform the precursor to carbide or nitride while bypassing the metallic state, which limits the surface area of the product.[73,87] A related temperature-programmed synthesis procedure has been developed by the Thompson group which maximizes the surface area of the catalysts by using ammonium paramolybdate ($(NH_4)_6Mo_7O_{24}\cdot 4H_2O$) as the precursor under different gas flow conditions (see methods in **Chapter 2**).[88]

Many earlier works explored a variety of binary nitrides that were identified to be active for NH_3 synthesis, including molybdenum (Mo_2N),[89–91] uranium (U_2N_3),[92,93] vanadium (VN),[94,95] rhenium(RhN_3),[96,97] and cerium (CeN)[98] nitrides. Using U_2N_3 and VN for NH_3 synthesis gave promising results, but high pressures (25 – 30 bar) were still required to obtain activities comparable to commercial Fe catalysts. CeN exhibits lower NH_3 synthesis rates compared to the commercial Fe catalyst at 50-100 bars. At atmospheric pressure, only Mo_2N and RhN_3 catalysts displayed high activity for NH_3 production. When normalized by the BET surface area, Mo_2N displayed significantly higher specific activity.[96] Thus, Mo_2N was concluded to be a promising catalyst for NH_3 synthesis at atmospheric pressure.

More current work conducted in the past decade focuses on altering the nitride supports to improve catalytic activity and investigating carbides for ammonia synthesis. Kojima and Aika also compared the ammonia synthesis rates between α-MoC_{1-x}, β-Mo_2C, and γ-Mo_2N, which were synthesized by using a temperature-programmed reaction with NH_3 for the nitride and 20% CH_4/H_2 gas for the carbides. α-MoC_{1-x} was synthesized by carburizing γ-Mo_2N while β-Mo_2C was

carburized directly from the oxide precursor. To evaluate the performance of each catalyst, the materials were pretreated for 1 hour at 600 °C with a stoichiometric balance of H_2/N_2 (3:1) at 60 mL/min. The rate of NH_3 production was evaluated at 400 °C and atmospheric pressure. The results, shown in **Table 1.1**, confirmed that NH_3 production rates were higher with both the α-Mo_2C_{1-x} and β-Mo_2C compared to the γ-Mo_2N.

Table 1.1. Ammonia synthesis rates at 400 °C under atmospheric pressure, BET surface areas, and specific activities of two different phases of molybdenum carbides and a molybdenum nitride catalyst.[90]

Catalyst	Rate (μmol h^{-1} g^{-1})	Surface Area (m^2 g^{-1})	Specific Activity (μmol h^{-1} m^{-2})
γ-Mo_2N	48	152	0.3
α-MoC_{1-x}	284	78	3.6
β-Mo_2C	489	24	20.4

In addition to the binary molybdenum carbides and nitrides, there have also been studies conducted on selective ternary metal nitrides. Jacobsen and Nørskov have rationalized the activity of bimetallic cobalt molybdenum nitride (Co_3Mo_3N) in terms of the N_2 binding energy as determined by a density functional theory (DFT) study.[99] As shown in the volcano plot in **Figure 1.11**, Ru and Os are predicted as two of the best catalysts for ammonia synthesis in industrial conditions. However, these materials are expensive and less attractive for commercial applications compared to the traditional Fe catalyst. An approach to solving this problem is to engineer a surface with a combination of strongly bonding and weakly bonding active sites, such as CoMo, to optimize NH_3 production activities.

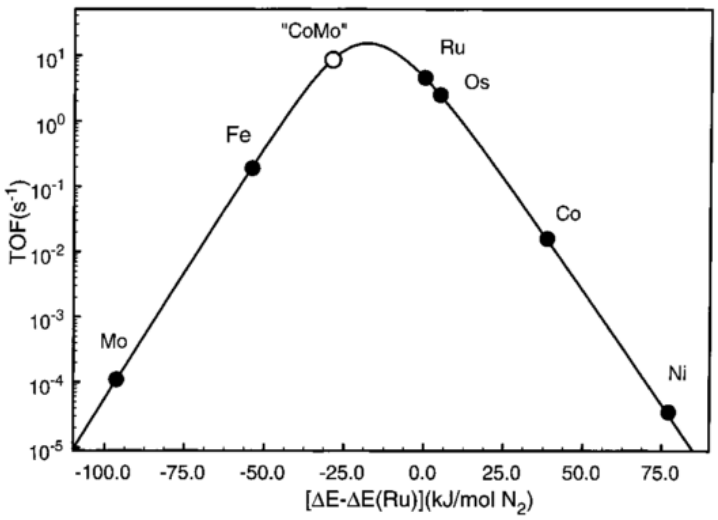

Figure 1.11. Volcano plot displaying the turnover frequency for ammonia as a function of the adsorption energy of nitrogen. The conditions of the microkinetic modeling is at 400 °C, 50 bar, and 3:1 ratio of hydrogen to nitrogen. Adapted from Ref.[99].

This computationally inspired hypothesis was experimentally confirmed by Aika and Kojima when they synthesized Co_3Mo_3N and a Co-promoted molybdenum nitride (Mo_2N-Co) and compared the NH_3 activity rates of those catalysts with those of a commercial doubly-promoted Fe catalyst (Fe-K_2O-Al_2O_3).[100–102] Mo_2N-Co was produced by using a solution of cobalt nitrate to impregnate the molybdenum precursor (MoO_3) and Co_3Mo_3N from a cobalt molybdate hydrate precursor ($CoMoO_4 \cdot nH_2O$). These different high-surface area nitride catalysts were synthesized by subjecting the oxide precursors to a temperature programmed reaction as previously prescribed from literature.[100]

Ammonia synthesis was performed at 400 °C under atmospheric pressure with a flow rate of 60 mL/min (25% N_2, 75% H_2) and the catalytic performance of the materials was compared. Initially, the Mo_2N-Co catalyst displayed the highest rate of ammonia production; however, as the reaction proceeded beyond the first 20 minutes, the Co_3Mo_3N increased from 179 to 239 μmol h^{-1} g^{-1}, making it the most active catalyst. **Table 1.2** provides the rates, surface area, and specific activity of each of the catalysts.

Table 1.2. Ammonia synthesis rates at 400 °C under atmospheric pressure, surface areas, and specific activities of three types of molybdenum nitride catalysts before and after the first 20 min of synthesis.[100]

Catalyst	Rate (μmol h^{-1} g^{-1})		Surface Area (m^2 g^{-1})		Specific Activity (μmol h^{-1} m^{-2})	
	Before	After	Before	After	Before	After
Mo_2N	35	10	186	181	0.2	0.1
Mo_2N-Co	210	114	194	190	1.1	0.6
Co_3Mo_3N	179	239	52	33	3	7

1.3.2 Materials for Electrocatalytic Conversion of Nitrate to Ammonia

The electrocatalyst material has a significant effect on the ENO_3RR rates and selectivity. This section will briefly summarize the recently studied single metals and alloys for this reaction, as adopted with permission from Wang et al.[103] Although the general nitrate reduction pathway is believed to be the same for these different classes,[21] the way that these different materials control the reaction and their active sites may differ. Further exploration of alloys for ENO_3RR is presented in **Chapter 4**.

1.3.2.1 *Metal Electrocatalysts*

Although the platinum group metals and copper are the most studied single metal electrocatalysts, the range of other metals that have been studied has given a sense of how different electrocatalyst properties affect activity and selectivity. Cu is a commonly studied metal because its strong nitrate adsorption energy makes it highly active for ENO_3RR.[104,105] Similarly, platinum group metal activities ($Rh > Ru > Ir > Pd \approx Pt$)[44] follow the trend of their nitrate adsorption strength shown computationally by DFT and experimentally via cyclic voltammetry.[38] Of the range of other metals studied, it is difficult to make uniform comparisons because experiments are typically conducted at different overpotentials and under different reaction conditions. Thus, the differences between metals can stem from the large difference in potential rather than the different interaction of the metal electrocatalyst with the nitrate species.

Typically, metals have a single type of active site that participates in the reaction. As ENO_3RR is a site-dependent reaction, which site nitrate adsorbs onto (e.g., the metal facet) controls activity and selectivity.[106] For example, the product distribution is different on Cu(111) and Cu(100) sites where the formation of hydroxylamine is more prevalent on Cu(100) than Cu(111) in basic media.[55] Step sites are typically more active for single metals.[21] Because metals often only have one type of active site, this site must adsorb both nitrate and hydrogen with the optimal adsorption energy to have high ENO_3RR activity. It is unlikely that a single site will adsorb all ENO_3RR intermediates with the ideal adsorption strength. Thus, the activity of metals for ENO_3RR is limited, similar to the limitations shown for many other electrocatalytic reactions involving multiple mechanistic steps on a single type of catalyst site (e.g., oxygen reduction).[107]

Identifying the electrocatalyst structure and adsorbates *under reaction conditions* is important for determining physical and electronic properties that influence the reaction rates. For example, Ti under ENO_3RR reaction conditions may form titanium hydride, which will exhibit different performance for ENO_3RR than metallic Ti.[60] Despite the low Raman cross-section of nitrogen compounds,[21] the technique is still useful for ENO_3RR and has been used to distinguish the structure between Cu and Cu_2O.[108] As discussed previously, X-ray absorption has been used to detect adsorbed species as a function of potential,[38] and also can be used to characterize electrocatalyst structure.

1.3.2.1.1 Nitrate reduction products formed on metals

To meet the engineering challenges of closing the nitrogen cycle, metals that can produce N_2 or NH_3 from ENO_3RR are of considerable environmental interest and are highlighted in **Figure 1.12**. Sn is highly active for nitrate reduction and displays 92% selectivity towards N_2 production in neutral electrolytes.[109] Bi is less activity than Sn but still reaches between 58% and 65%

selectivity for N_2 under basic conditions.[110] Despite low ENO_3RR rates, Fe is a cheap metal that is highly selective towards N_2[39] because of its strong nitrate adsorption energy.[38] Fe in carbon microspheres were shown to have high N_2 selectivity and maintain high surface areas.[111] Al, In, Zn, and Pb also produce N_2 selectively with minor co-production of ammonia (<20% selectivity) and N_2O (>20% only for In and Zn).[61] In basic environments, Pt has been reported to produce N_2 if sufficient nitrite ions are present.[112]

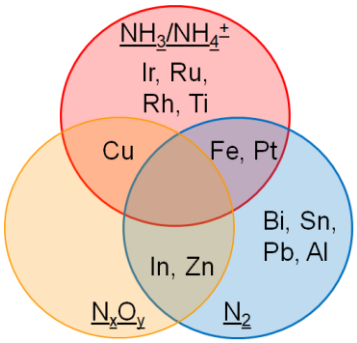

Figure 1.12. Distribution of dominant products (> 20% selectivity) formed for different pure metals. Red, blue, and orange circles represent selectivity towards NH_3/NH_4^+, N_2, and N_xO_y, respectively. Overlap regions indicate different product formations under various reaction conditions (e.g., acid vs. base) or a mixture of reaction products.

Ammonia is produced on the platinum group metals at voltages positive of 0 V vs. RHE[28,44,113] and certain base metals at higher overpotentials (**Figure 1.12**). Even though the platinum group metals form ammonia at positive potentials, they typically are too selective towards hydrogen evolution below 0 V vs. RHE to form ENO_3RR products at high FE. Ti produces ammonia with 82% FE in acidic pH at −1 V vs. RHE.[114] Cu, depending on reaction conditions, forms ammonia or nitrogen oxides such as hydroxylamine.[55] Fe operated at constant current density also forms ammonia and small concentrations of nitrite in neutral $NaNO_3/Na_2SO_4$ solutions.[115] There are no metals that solely make nitrogen oxides, typical side reaction products or intermediates for ammonia and N_2 production.

1.3.2.1.2 Techniques to enhance single metal performance

Ir nanotubes are reported to have higher conversions per mass of catalyst than Ir nanoparticles for ENO_3RR. However, it is unclear whether this is due to higher specific surface area or an increase in the per site catalytic activity.[113] Because the H_{upd} charge for Ir nanotubes is greater than the nanocrystals, the nanotubes have a higher surface area, indicating that some of the activity enhancement is due to an increase in the active surface area.

As discussed above, strained Ru clusters[28] enhance ENO_3RR reaction rates by inducing tensile strain from subsurface oxygen species embedded in the Ru lattice. This tensile strain enabled hydrogen radicals to form, which lower the reaction barrier for hydrogenation and increase the ammonia formation rate. The authors normalized the activity to the electrochemically active surface area based on double layer capacitance, showing that the enhancement is not merely due to an increase in surface area.[28]

A Cu electrocatalyst loaded in an organic molecular solid was the most active for ENO_3RR compared to other metals tested.[116] The organic molecular solid controlled the proton and electron transport to the Cu active sites while the electronic structure of the Cu controlled the competitive hydrogen evolution reaction. The synergy of the Cu in the organic solid resulted in 85.9% FE towards ammonia at −0.4 V vs. RHE,[116] where hydrogen evolution dominates on Cu without the organic solid.[55]

Metals are the most studied and well-understood surfaces for ENO_3RR, and many spectroscopic techniques have been used to elucidate the electrocatalyst structure and reaction mechanisms. Different metals can produce different ENO_3RR products, but typically not at the rates necessary for commercial applications. This prompts studies in methods to enhance reaction

rates. In addition to modification techniques performed on single metals, alloying metals can be used to enhance the activity and selectivity, as discussed in the next section.

1.3.2.2 *ENO_3RR on Alloys*

A major advantage of alloys is the ability to enhance the activity and selectivity of pure metals. Additionally, alloying can be used to lower the amount of expensive metal required in a catalyst, which can reduce the overall cost of the working electrode for industrial ENO_3RR. This section aims to summarize recent results on alloys for nitrate reduction and focus on the role that alloys play in improving the reaction rate and selectivity. The naming conventions used in this review will be the same as in the corresponding peer-reviewed articles.

There are two major ways in which alloys function to improve the activity of ENO_3RR. One effect is tuning the adsorption energy of nitrate and other intermediate species on the surface. Examples of this include CuNi alloys,[59] PtRu alloys,[58] and Au/Ag alloys,[117] where optimal alloy compositions were used to increase the ENO_3RR rate. Additionally, alloys often exhibit bifunctional effects, where two adjacent sites contribute to different steps of the mechanism. For example, synergistic effects between Pd and Cu create active sites for nitrate to reduce to nitrite and further conversion to nitrogen.[118]

Alloys can also be used to increase the selectivity towards a desired product or shift the selectivity towards other compounds. For example, Bi[110] and Sn[109] have previously been studied to be selective towards N_2. The alloy of these two metals, $Bi_{60}Sn_{40}$, exhibited improved activity relative to pure Bi or Sn and displayed over 50% selectivity towards nitrogen.[119] For PtSn alloys, even though pure Pt tends to produce NH_3,[35] the addition of Sn shifts the selectivity towards hydroxylamine.[120]

A major consideration for industrializing the ENO_3RR process is the cost of the metals used for the ENO_3RR alloys. **Table 1.3** provides the cost of the metals for alloys that have been examined in this section, and should be considered when determining the cost of the working electrode for the conversion of NO_3^-. This means that even though some platinum group metals might be more active for ENO_3RR, their high costs might outweigh the benefits. Instead, a slightly less active, but significantly less expensive metal or alloy may be preferred.

Table 1.3. Cost per mole of different metals that have been studied for ENO_3RR. Based on prices from Daily Metal Prices, 2020.[121]

Metals	Cost ($ mol^{-1})
Platinum (Pt)	$6,020.00
Palladium (Pd)	$7,930.00
Rhodium (Rh)	$40,400.00
Iridium (Ir)	$10,200.00
Ruthenium (Ru)	$877.00
Cobalt (Co)	$1.94
Copper (Cu)	$0.43
Nickel (Ni)	$0.90
Iron (Fe)	$0.01
Zinc (Zn)	$0.17
Bismuth (Bi)	$1.24
Tin (Sn)	$2.11

Recent studies of alloys for ENO_3RR can be divided into two sub-categories: (1) improving upon alloying platinum group metals that have traditionally displayed high activity towards nitrate reduction and (2) incorporating the use of cheap but active coinage metals such as Cu.

1.3.2.2.1 Platinum group metal alloys

Alloys have been used in many instances to improve the activity of their pure metal counterparts. For example, at 21–42% Pt content, PtRh and PtIr in acid have been shown to lower the onset overpotential for nitrate reduction compared to pure Pt, Rh, and Ir.[122] This observation can be rationalized by the change adsorption energy of the material, which shifts the optimal potential for nitrate adsorption and hydrogen desorption on the surface.

Apart from using alloy composition to tune the adsorption energy and improve ENO_3RR activity, the properties of different metal sites can also lead to bifunctional catalysts. Pd-Cu alloys have improved nitrate removal and selectivity to N_2, where Cu is reported to promote the reduction of nitrate to nitrite while Pd improves the conversion of nitrite to N_2.[118] Sn-modified Pd catalysts have also displayed increased activity for nitrate reduction in acidic media. Similar to Cu, Sn is active in catalyzing the reaction from nitrate to nitrite.[123] Unlike Pd-Cu alloy, PdSn is selective towards N_2O.[123] In another report, depositing PdSn (1:4 Sn:Pd ratio) on a stainless steel mesh achieved nitrogen selectivity of 89%.[124] The synergistic composition between the Pd and Sn likely influences the availability of surface hydrogen on the material. DFT calculations also indicate high N_2 yield for $Sn_3Pd(420)$, which is likely due to a favorable arrangement of active sites for nitrate adsorption.[124] The discrepancies between the products for different PdSn alloys are likely due to different supports and reaction conditions between the various reports.

Similarly, Kato et al. investigated the effect on nitrate reduction by modifying Pt, Pd, and PtPd with Sn. Each of the electrode surfaces was prepared with the (111) or (100) facet of each Pt material before Sn deposition.[125] As stated before, Sn was believed to enhance the reduction of nitrate to nitrite. Cyclic voltammetry confirmed that the trimetallic Sn/PtPd had the highest activities compared to Sn/Pt and Sn/Pd. Additionally, higher activities were achieved on (100) facets in both acidic and neutral solutions.[125]

Siriwatcharapiboon et al. investigated the effects of alloying Sn with Rh.[47] Even though Rh is the most active metal for ENO_3RR, its activity and selectivity can be even further enhanced with Sn modification. In this case, Sn is believed to supply highly oxophilic sites. Thus, the activity enhancement is likely due to nitrate adsorption on active sites consisting of Rh and $Sn(OH)_x$ species. While ammonia is the main ENO_3RR product on Rh/C, SnRh/C displayed selectivity

towards both ammonia and hydroxylamine. Because Rh has a strong tendency to cleave the N–O bond, it is hypothesized that the addition of Sn is suppressing the N–O cleavage.

1.3.2.2.2 Copper-based alloys

Cu alloys have been widely investigated as an electrocatalytic cathode material because Cu is cheap and has high ENO_3RR activity. Many studies focus on alloying different metals with Cu to improve activity and selectivity towards desired products. CuNi alloys have been reported to have higher activity than either pure Cu or pure Ni.[59,63,64] In basic solutions, a Cu/Ni alloy displayed higher activity than Cu and over 55% selectivity towards N_2.[62] Cu/Ni/Zn alloys,[126] CuZn,[127] Cu-Pd,[128] and Cu underpotentially deposited on Pd:Au[129] have been shown to be more active than pure Cu and selective towards ammonia. Cu-Bi alloys[130] are also interesting because they display high activity of nitrate removal at a neutral pH.

In many cases, there are also studies investigating different Cu-based alloys on novel supports. For example, bimetallic Cu-Rh nanoparticles were dispersed in benzenethiol-grafted high-surface-area graphite powders.[131] Without changing the metal composition, this grafting technique is able to enhance the dispersion of Cu and Rh particles on the support, and thus increase the rate of NO_3RR. Shen et al. tested the performance of Cu/Pd electrodeposited on Ni foam, a conductive and porous substrate that can provide more active sites.[132] Cu/Pd on Ni foam was tested in both a controlled electrolyte and municipal wastewater treatment plant effluent. In wastewater, it reached over 96% FE for nitrate removal and over 65% selectivity towards N_2.[132]

1.3.2.2.3 Other metal alloys

There are many instances where alloys can be used to enhance the selectivity of nitrate reduction at lower overpotentials. Sn has previously been shown to be very active in converting nitrate to ammonia. However, electrodes often operate at very negative potentials, which increases

the operating electrical input and subjects the material to be subjected to cathodic corrosion. Bi is active at lower overpotentials but is less active and selective towards N_2. By alloying these two metals together, Bi-Sn nanoparticles[119] can enhance the activity and selectivity due to synergistic effects. As previously stated, $Bi_{60}Sn_{40}$ has shown above 50% FE towards N_2 production.

The adsorption energy of nitrate on various surface facets of Au, Ag, and their surface alloys has been studied with DFT calculations. Because the adsorption of nitrate is the rate-limiting step on transition metals during ENO_3RR, systematic trends in the calculations can provide insight for the most active surface. These predictions were supported with experimental results confirming that nitrate reduction reaction reached peak activity at 2/3 surface coverage of Ag on Au.[133]

1.3.3 Thermal Catalytic Nitrate Reduction Catalysts

Unlike ENO_3RR, the TNO_3RR uses hydrogen gas to convert nitrate and is commonly studied for water sources with low nitrate concentrations (<0.1 M NO_3^-). Catalysts used for TNO_3RR are very similar to those investigated for ENO_3RR. In particular, most studies focus on bimetallic catalysts, which were originally tested by Vorlop and Tacke,[134] and monometallic catalysts composed of Pd or Pt on reducible supports and zero valent iron (ZVI).

1.3.3.1 *Bimetallic Catalysts*

Vorlop and Tacke pioneered the work to remove nitrate from water by testing a bimetallic system composed of precious metals (e.g., Pt or Pd) and a promoter (e.g., Cu, Ni, Fe, Sn, In, Ag), which was responsible to catalyze the reduction from nitrate to nitrite.[65] Since then, different combinations of metals have been tested to improve the nitrate reduction activity and selectivity towards desired products. In general, Pd outperforms Pt for nitrate conversion,[135] while Sn is the best promoter for high nitrogen selectivity.[136]

Bimetallic catalyst performance depends on both the metal composition and the proximity and interaction between the metals. For Pd-Cu catalysts, an optimal 1:1 Pd:Cu ratio resulted in the highest activity.[137] As implied from the bifunctional mechanism for this reaction, this indicates an optimal concentration of surface sites that allow for nitrate reduction to nitrite, and from nitrite to desired products. Additionally, the proximity of the noble metal is essential to stabilize the promoter metal via hydrogen spill-over. When comparing the performance of phase-pure Pd-Cu catalysts and phase-segregated (non-alloyed) Pd-Cu, results show that phase-segregated materials had higher selectivity towards nitrogen production while alloys had higher overall activity for nitrate reduction.[138]

Supports also play an important role in determining nitrate reduction activity and selectivity. Al_2O_3 is the most commonly investigated support for TNO_3RR.[139–141] However, metals supported on activated carbon display higher selectivity towards nitrogen than other supports (e.g., SiO_2, TiO_2, Al_2O_3) due to the fact that there is higher metal dispersion on the surface of the support.[69,142] In general, ideal supports for TNO_3RR should be stable under reaction conditions, adsorb nitrates, and ensure high metal dispersion on the surface.

Since TNO_3RR occurs in two steps on bimetallic catalysts, many have investigated the use of two batch reactors in series: the first to convert nitrates to nitrites, followed by hydrogenation to desired products under optimal conditions. Initial results have shown improve activity and selectivity for nitrogen by using a batch reactor at low pH with Pd-Cu catalyst to initially convert nitrate to nitrite, and then hydrogenate nitrite to nitrogen at even neutral pH with Pd.[143] Though the two-reactor configuration demands more capital and operating costs, it enables more precise control of optimal catalysts and reaction conditions for desired products.

1.3.3.2 *Monometallic Catalysts*

In contrast to ENO_3RR, monometallic catalysts for TNO_3RR have not been as extensively studied. The two major sub-groups of materials explored in this area are noble metals (e.g., Pt or Pd) on reducible supports and ZVI. Previous investigation of Pd supported on CeO_2 and TiO_2 showed that the catalyst was very active, but not as selective towards N_2 production.[144] The material also performed better at lower pH, but the CO_2 that was used as the acidic buffer in the system poisoned the catalyst over time. Even though the selectivity trends between Pd/CeO_2 and Pd/TiO_2 were similar, the activity correlated with the increase in oxide sites of the supports.[145] Recent studies have also compared the activity of Pd to Ru. Results indicate that Ru has higher nitrate TOF without the presence of promoter metals and that the selectivity is almost exclusively towards ammonia production, regardless of the solution pH.[146]

The second sub-class of monometallic catalyst is ZVI, which primarily uses the iron redox couple to convert nitrate without a H_2 supply. Studies proposed that metallic iron (Fe^0) oxidized in the presence of nitrates to form Fe^{2+}/Fe^{3+}, nitrites, ammonia, and nitrogen.[147–149] Under acidic conditions with pH between 2 – 4.5, the reaction is accelerated, indicating that H^+ ions directly participate in the redox reaction towards ammonia.[150] The major advantage of this reaction is that ZVI catalysts are very cheap and are not toxic for nitrate treatment applications that involve directly injecting the catalyst into the soil. However, the major disadvantage of ZVI is the need for another reducing source to convert Fe^{2+}/Fe^{3+} back to metallic iron to complete the catalytic cycle.

1.4 Research Goals

Even though the production process of ammonia is over a century old, there are many engineering challenges that need to be addressed to reduce the energy demand and CO_2 emission for the current process. The overall goal of the research presented in this dissertation is to elucidate

the mechanism and reactivity of catalysts and alternative reaction conditions that would be able to produce ammonia under more environmentally sustainable conditions. Thus, four main objectives are formulated:

1. Design supported metal catalysts for different ammonia production reactions.

2. Carefully characterize the material to determine active sites and the role of compositional effects.

3. Elucidate reaction kinetics and mechanisms.

4. Explore and evaluate the most sustainable ammonia synthesis reaction reactions.

The dissertation is divided into six chapters as outlined below:

Chapter 1: Introduction and Background

This chapter explores the engineering challenges for ammonia synthesis and the overall motivations for exploring alternative ammonia synthesis systems. Details regarding the reaction mechanisms and the common catalysts for each system are also presented.

Chapter 2: Experimental Techniques

This chapter presents a broad overview of all the experimental techniques that are used to obtain the data in this dissertation. The first half covers a series of synthesis techniques and detailed descriptions of characterization experiments. The latter half provides detailed kinetic experimental protocols and basic models used to evaluate the system. The information in this chapter serves to provide researchers an in-depth guide to a variety of experimental techniques to effectively reproduce the work in this dissertation.

Chapter 3: Supported Mo_2C and Mo_2N for Ambient Pressure Ammonia Synthesis

This chapter details the work initially completed with Prof. Levi Thompson, which explored using a series of supported Mo_2C and Mo_2N catalysts for gas-phase ammonia synthesis

at ambient pressures. The key hypothesis presented in this chapter is that a bifunctional mechanism would allow metal sites to break the nitrogen triple bond while support sites would enhance subsequent hydrogenation steps in the reaction. This synergistic effect would lead to increased ammonia synthesis activity at milder reaction conditions. Major results from this work did not support our key hypothesis. Thus, this work serves as a pivot away from traditional gas-phase reactions for ammonia production.

Chapter 4: Pt_xRu_y/C for Electrocatalytic Nitrate Conversion to Ammonia

This chapter focuses on exploring alloys for electrocatalytically converting nitrate to ammonia. As a sustainable alternative to the traditional Haber-Bosch process, ENO_3RR has the capability to use renewable electricity to reduce nitrate contaminants in water to ammonia at low operating potentials. In this study, we report the surface-area normalized activity of platinum-ruthenium (Pt_xRu_y/C) catalysts of different compositions (x = 48–100%) for electrocatalytic nitrate reduction, chosen based on screening using a computational activity volcano plot. Results indicate that the Pt_xRu_y/C alloys are more active than Pt/C, with $Pt_{78}Ru_{22}$/C six times more active than Pt/C at 0.1 V vs. RHE, and ammonia faradaic efficiencies of 93–98%. Density functional theory calculations predict maximum activity at 25 at% Ru, consistent with experiments. This study demonstrates how electrocatalyst performance is tunable by changing the adsorption strength of reacting species through alloying.

Chapter 5: Comparison between Electrocatalytic and Thermal Catalytic Nitrate Reduction

This chapter will further expand upon the work from **Chapter 4** by comparing the kinetic similarities and differences between TNO_3RR and ENO_3RR on Pt_xRu_y/C catalysts under different reaction conditions. We identify similarities in both reactions that show increasing activity with increasing the hydrogen driving potential (i.e., H_2 partial pressure for TNO_3RR and applied

potential for ENO_3RR) and nitrate concentration. However, we also identify differences between E_a and pH effects for TNO_3RR and ENO_3RR, indicating reaction effects from electrochemical processes that are exclusive to ENO_3RR. Future work by isolating the pH effects can further improve our understanding of nitrate reduction mechanism. By testing Pt_xRu_y/C under similar reaction conditions, we are able to evaluate the prospects of TNO_3RR and ENO_3RR for nitrate reduction applications.

Chapter 6: Conclusions, Future Recommended Works, and Outlooks

This chapter summarizes the key findings from my research and relates these results to the overall motivation of the work. Based on the findings, I suggest potential extensions of the current project and propose new thrusts to advance scientific understanding of ammonia production reactions and mechanisms. Additionally, a series of policy recommendations to enable technological implementation and improve regulation of water contaminants are provided.

1.5 References

(1) Stewart, W. M.; Dibb, D. W.; Johnston, A. E.; Smyth, T. J. The Contribution of Commercial Fertilizer Nutrients to Food Production. *Agronomy Journal* **2005**, *97* (1), 1–6. https://doi.org/10.2134/agronj2005.0001.

(2) Food and Agriculture Organization of the United Nations. *World Fertilizer Trends and Outlook to 2022.*; Food & Agriculture Org: S.l., 2019.

(3) Nørskov, J.; Contacts, B.; Miranda, R.; Fitzsimmons, T.; Stack, R.; Singh, A.; Rohr, B.; University, S.; Goldstein, J. Sustainable Ammonia Synthesis Exploring the Scientific Challenges Associated with Discovering Alternative, Sustainable Processes for Ammonia Production DOE Roundtable Report SUSTAINABLE AMMONIA SYNTHESIS Marriott Dulles Airport Suites Hotel, 45020 Aviatio. **2016**.

(4) Erisman, J. W.; Sutton, M. A.; Galloway, J.; Klimont, Z.; Winiwarter, W. How a Century of Ammonia Synthesis Changed the World. *Nature Geoscience* **2008**, *1* (10), 636–639. https://doi.org/10.1038/ngeo325.

(5) Smil, V. Nitrogen and Food Production: Proteins for Human Diets. *ambi* **2002**, *31* (2), 126–131. https://doi.org/10.1579/0044-7447-31.2.126.

(6) Smil, V. *Enriching the Earth: Fritz Haber, Carl Bosch, and the Transformation of World Food Production*; MIT Press, 2001.

(7) Roser, M.; Ritchie, H. Fertilizers. *Our World in Data* **2013**.

(8) Smith, C.; Hill, A. K.; Torrente-Murciano, L. Current and Future Role of Haber–Bosch Ammonia in a Carbon-Free Energy Landscape. *Energy Environ. Sci.* **2020**, *13* (2), 331–344. https://doi.org/10.1039/C9EE02873K.

(9) Nielsen, A. *Ammonia: Catalysis and Manufacture*; Springer Berlin Heidelberg: Berlin, Heidelberg, 1995.

(10) Back, S.; Jung, Yousung. On the Mechanism of Electrochemical Ammonia Synthesis on the Ru Catalyst. *Physical Chemistry Chemical Physics* **2016**, *18* (13), 9161–9166. https://doi.org/10.1039/C5CP07363D.

(11) Tanabe, Y.; Nishibayashi, Y. Developing More Sustainable Processes for Ammonia Synthesis. *Coordination Chemistry Reviews* **2013**, *257*, 2551–2564. https://doi.org/10.1016/j.ccr.2013.02.010.

(12) Boerner, L. K. Industrial ammonia production emits more CO2 than any other chemical-making reaction. Chemists want to change that https://cen.acs.org/environment/green-chemistry/Industrial-ammonia-production-emits-CO2/97/i24 (accessed Apr 26, 2021).

(13) Renner, J. N.; Greenlee, L. F.; Herring, A. M.; Ayers, K. E. Electrochemical Synthesis of Ammonia: A Low Pressure, Low Temperature Approach. *The Electrochemical Society Interface* **2015**, 8.

(14) Liu, X.; Elgowainy, A.; Wang, M. Life Cycle Energy Use and Greenhouse Gas Emissions of Ammonia Production from Renewable Resources and Industrial By-Products. *Green Chem.* **2020**, *22* (17), 5751–5761. https://doi.org/10.1039/D0GC02301A.

(15) CO2-Free Ammonia Synthesis - CO2-Free Energy Carrier https://www.jgc.com/en/business/tech-innovation/environment/co2-free.html (accessed Apr 27, 2021).

(16) Brown, T. Green Ammonia Demonstration Plants Now Operational, in Oxford and Fukushima. *Ammonia Energy Association*, 2018.

(17) Hochman, G.; Goldman, A. S.; Felder, F. A.; Mayer, J. M.; Miller, A. J. M.; Holland, P. L.; Goldman, L. A.; Manocha, P.; Song, Z.; Aleti, S. Potential Economic Feasibility of Direct Electrochemical Nitrogen Reduction as a Route to Ammonia. *ACS Sustainable Chem. Eng.* **2020**, *8* (24), 8938–8948. https://doi.org/10.1021/acssuschemeng.0c01206.
(18) Fields, S. Global Nitrogen: Cycling out of Control. *Environmental Health Perspectives* **2004**, *112* (10), 556–563. https://doi.org/10.1289/ehp.112-a556.
(19) Zhang, W. L.; Tian, Z. X.; Zhang, N.; Li, X. Q. Nitrate Pollution of Groundwater in Northern China. *Agriculture, Ecosystems and Environment* **1996**, *59* (3), 223–231. https://doi.org/10.1016/0167-8809(96)01052-3.
(20) Galloway, J. N.; Aber, J. D.; Erisman, J. W.; Seitzinger, S. P.; Howarth, R. W.; Cowling, E. B.; Cosby, B. J. The Nitrogen Cascade. *BioScience* **2003**, *53* (4), 341–356. https://doi.org/10.1641/0006-3568(2003)053[0341:tnc]2.0.co;2.
(21) Duca, M.; Koper, M. T. M. Powering Denitrification: The Perspectives of Electrocatalytic Nitrate Reduction. *Energy & Environmental Science* **2012**, *5*, 9726–9742. https://doi.org/10.1039/c2ee23062c.
(22) Lehnert, N.; Dong, H. T.; Harland, J. B.; Hunt, A. P.; White, C. J. Reversing Nitrogen Fixation. *Nature Reviews Chemistry* **2018**, *2* (10), 278–289. https://doi.org/10.1038/s41570-018-0041-7.
(23) Singh, N.; Goldsmith, B. R. Role of Electrocatalysis in the Remediation of Water Pollutants. *ACS Catalysis* **2020**, *10*, 3365–3371. https://doi.org/10.1021/acscatal.9b04167.
(24) National Academy of Engineering. National Academy of Engineering Grand Challenges For Engineers. **2017**, 19–22.
(25) Gruber, N.; Galloway, J. N. An Earth-System Perspective of the Global Nitrogen Cycle. *Nature* **2008**, *451* (7176), 293–296. https://doi.org/10.1038/nature06592.
(26) van Langevelde, P. H.; Katsounaros, I.; Koper, M. T. M. Electrocatalytic Nitrate Reduction for Sustainable Ammonia Production. *Joule* **2021**, *5* (2), 290–294. https://doi.org/10.1016/j.joule.2020.12.025.
(27) Kyriakou, V.; Garagounis, I.; Vourros, A.; Vasileiou, E.; Stoukides, M. An Electrochemical Haber-Bosch Process. *Joule* **2020**, *4* (1), 142–158. https://doi.org/10.1016/j.joule.2019.10.006.
(28) Li, J.; Zhan, G.; Yang, J.; Quan, F.; Mao, C.; Liu, Y.; Lei, F.; Li, L.; Chan, A. W. M.; Xu, L.; Shi, Y.; Du, Y.; Wong, P. K.; Wang, J.; Dou, S.; Zhang, L.; Yu, J. C. Efficient Ammonia Electrosynthesis from Nitrate on Strained Ruthenium Nanoclusters. *Journal of American Chemical Society* **2020**, *142* (15), 7036–7046. https://doi.org/10.1021/jacs.0c00418.
(29) Ertl, G. Surface Science and Catalysis—Studies on the Mechanism of Ammonia Synthesis: The P. H. Emmett Award Address. *Catalysis Reviews* **1980**, *21* (2), 201–223. https://doi.org/10.1080/03602458008067533.
(30) Hinrichsen, O. Kinetic Simulation of Ammonia Synthesis Catalyzed by Ruthenium. *Catalysis Today* **1999**, *53* (2), 177–188. https://doi.org/10.1016/S0920-5861(99)00115-7.
(31) Appl, M. *Ullmann's Encyclopedia of Industrial Chemistry*; Wiley-VCH Verlag GmbH & Co. KGaA, 2006.
(32) Ertl, G.; Thiele, N. XPS Studies with Ammonia Synthesis Catalysts. *Applications of Surface Science* **1979**, *3* (1), 99–112. https://doi.org/10.1016/0378-5963(79)90064-3.
(33) Ertl, G.; Huber, M.; Thiele, N. Formation and Decomposition of Nitrides on Iron Surfaces. *Zeitschrift für Naturforschung A* **1979**, *34* (1), 30–39. https://doi.org/10.1515/zna-1979-0106.

(34) Wang, Z.; Richards, D.; Singh, N. Recent Discoveries in the Reaction Mechanism of Heterogeneous Electrocatalytic Nitrate Reduction. *Catal. Sci. Technol.* **2021**, *11* (3), 705–725. https://doi.org/10.1039/D0CY02025G.

(35) De Groot, M. T.; Koper, M. T. M. The Influence of Nitrate Concentration and Acidity on the Electrocatalytic Reduction of Nitrate on Platinum. *Journal of Electroanalytical Chemistry* **2004**, *562* (1), 81–94. https://doi.org/10.1016/j.jelechem.2003.08.011.

(36) Garcia-Segura, S.; Lanzarini-Lopes, M.; Hristovski, K.; Westerhoff, P. Electrocatalytic Reduction of Nitrate: Fundamentals to Full-Scale Water Treatment Applications. *Applied Catalysis B: Environmental* **2018**, *236* (March), 546–568. https://doi.org/10.1016/j.apcatb.2018.05.041.

(37) Barrabés, N.; Sá, J. Catalytic Nitrate Removal from Water, Past, Present and Future Perspectives. *Applied Catalysis B: Environmental* **2011**, *104* (1–2), 1–5. https://doi.org/10.1016/j.apcatb.2011.03.011.

(38) Liu, J.-X.; Richards, D.; Singh, N.; Goldsmith, B. R. Activity and Selectivity Trends in Electrocatalytic Nitrate Reduction on Transition Metals. *ACS Catalysis* **2019**, *9*, 7052–7064. https://doi.org/10.1021/acscatal.9b02179.

(39) Martínez, J.; Ortiz, A.; Ortiz, I. State-of-the-Art and Perspectives of the Catalytic and Electrocatalytic Reduction of Aqueous Nitrates. *Applied Catalysis B: Environmental* **2017**, *207*, 42–59. https://doi.org/10.1016/j.apcatb.2017.02.016.

(40) Nakata, K.; Kayama, Y.; Shimazu, K.; Yamakata, A.; Ye, S.; Osawa, M. Surface-Enhanced Infrared Absorption Spectroscopic Studies of Adsorbed Nitrate, Nitric Oxide, and Related Compounds 2: Nitrate Ion Adsorption at a Platinum Electrode. *Langmuir* **2008**, *24* (8), 4358–4363. https://doi.org/10.1021/la703476m.

(41) Cook, A. R.; Dimitrijevic, N.; Dreyfus, B. W.; Meisel, D.; Curtiss, L. A.; Camaioni, D. M. Reducing Radicals in Nitrate Solutions. The NO32- System Revisited. *Journal of Physical Chemistry A* **2001**, *105* (14), 3658–3666. https://doi.org/10.1021/jp0038052.

(42) Jia, R.; Wang, Y.; Wang, C.; Ling, Y.; Yu, Y.; Zhang, B. Boosting Selective Nitrate Electroreduction to Ammonium by Constructing Oxygen Vacancies in TiO2. *ACS Catalysis* **2020**, *10*, 3533–3540. https://doi.org/10.1021/acscatal.9b05260.

(43) Taguchi, S.; Feliu, J. M. Kinetic Study of Nitrate Reduction on Pt(1 1 0) Electrode in Perchloric Acid Solution. *Electrochimica Acta* **2008**, *53* (10), 3626–3634. https://doi.org/10.1016/j.electacta.2007.12.032.

(44) Dima, G. E.; De Vooys, A. C. A.; Koper, M. T. M. Electrocatalytic Reduction of Nitrate at Low Concentration on Coinage and Transition-Metal Electrodes in Acid Solutions. *Journal of Electroanalytical Chemistry* **2003**, *554–555* (1), 15–23. https://doi.org/10.1016/S0022-0728(02)01443-2.

(45) Gootzen, J. F. E.; Lefferts, L.; Van Veen, J. A. R. Electrocatalytic Nitrate Reduction on Palladium Based Catalysts Activated with Germanium. *Applied Catalysis A: General* **1999**, *188* (1–2), 127–136. https://doi.org/10.1016/S0926-860X(99)00221-5.

(46) Shimazu, K.; Goto, R.; Piao, S.; Kayama, R.; Nakata, K.; Yoshinaga, Y. Reduction of Nitrate Ions on Tin-Modified Palladium Thin Film Electrodes. *Journal of Electroanalytical Chemistry* **2007**, *601* (1–2), 161–168. https://doi.org/10.1016/j.jelechem.2006.11.005.

(47) Siriwatcharapiboon, W.; Kwon, Y.; Yang, J.; Chantry, R. L.; Li, Z.; Horswell, S. L.; Koper, M. T. M. Promotion Effects of Sn on the Electrocatalytic Reduction of Nitrate at Rh

Nanoparticles. *ChemElectroChem* **2014**, *1* (1), 172–179. https://doi.org/10.1002/celc.201300135.
(48) Dima, G. E.; Beltramo, G. L.; Koper, M. T. M. Nitrate Reduction on Single-Crystal Platinum Electrodes. *Electrochimica Acta* **2005**, *50* (21), 4318–4326. https://doi.org/10.1016/j.electacta.2005.02.093.
(49) Rosca, V.; Beltramo, G. L.; Koper, M. T. M. Reduction of NO Adlayers on Pt(110) and Pt(111) in Acidic Media: Evidence for Adsorption Site-Specific Reduction. *Langmuir* **2005**, *21* (4), 1448–1456. https://doi.org/10.1021/la0475831.
(50) Campbell, C. T. The Degree of Rate Control: A Powerful Tool for Catalysis Research. *ACS Catalysis* **2017**, *7* (4), 2770–2779. https://doi.org/10.1021/acscatal.7b00115.
(51) Campbell, C. T. Micro- and Macro-Kinetics: Their Relationship in Heterogeneous Catalysis. *Topics in Catalysis* **1994**, *1*, 353–366. https://doi.org/10.1007/BF01492288.
(52) Kuwabata, S.; Uezumi, S.; Tanaka, K.; Tanaka, T. Assimilatory and Dissimilatory Reduction of NO3- and NO2- with an (n-Bu4N)3[Mo2Fe6S8(SPh)9] Modified Glassy-Carbon Electrode in Water. *Inorganic Chemistry* **1986**, *25* (17), 3018–3022. https://doi.org/10.1021/ic00237a019.
(53) Reyter, D.; Bélanger, D.; Roué, L. Elaboration of Cu-Pd Films by Coelectrodeposition: Application to Nitrate Electroreduction. *Journal of Physical Chemistry C* **2009**, *113* (1), 290–297. https://doi.org/10.1021/jp805484t.
(54) Reyter, D.; Bélanger, D.; Roué, L. Elaboration by High-Energy Ball Milling of Copper/Palladium Composite Materials - Characterization and Electrocatalytic Activity for the Reduction of Nitrate in Alkaline Medium. *Journal of Electroanalytical Chemistry* **2008**, *622* (1), 64–72. https://doi.org/10.1016/j.jelechem.2008.05.002.
(55) Pérez-Gallent, E.; Figueiredo, M. C.; Katsounaros, I.; Koper, M. T. M. Electrocatalytic Reduction of Nitrate on Copper Single Crystals in Acidic and Alkaline Solutions. *Electrochimica Acta* **2017**, *227*, 77–84. https://doi.org/10.1016/j.electacta.2016.12.147.
(56) Petrii, O. A.; Akbaeva, Y. A.; Safonova, T. Y.; Kondrasheva, V. S.; Kolosov, E. N.; Tsirlina, G. A.; Gryaznov, V. M. Intensification of the Nitrate Anion Reduction on a Membrane Palladium Electrode. *Russian Journal of Electrochemistry* **2002**, *38* (2), 220–223. https://doi.org/10.1023/A:1016884718990.
(57) Yao, Y.; Zhu, S.; Wang, H.; Li, H.; Shao, M. A Spectroscopic Study of Nitrogen and Nitrate Electrochemical Reduction on Rhodium Surfaces. *Angewandte Chemie International Edition* **2020**. https://doi.org/10.1002/anie.202003071.
(58) Wang, Z.; Young, S. D.; Goldsmith, B. R.; Singh, N. Increasing Electrocatalytic Nitrate Reduction Activity by Controlling Adsorption through PtRu Alloying. *Submitted* **2020**.
(59) Wang, Y.; Xu, A.; Wang, Z.; Huang, L.; Li, J.; Li, F.; Luo, M.; Nam, D.; Tan, C.; Ding, Y.; Wu, J.; Dinh, C.; Sinton, D.; Zheng, G.; Sargent, E. H. Enhanced Nitrate-to-Ammonia Activity on Copper- Nickel Alloys via Tuning of Intermediate Adsorption. *Journal of the American Chemical Society* **2020**, *142* (12), 5702–5708. https://doi.org/10.1021/jacs.9b13347.
(60) McEnaney, J. M.; Blair, S. J.; Nielander, A. C.; Schwalbe, J. A.; Koshy, D. M.; Cargnello, M.; Jaramillo, T. F. Electrolyte Engineering for Efficient Electrochemical Nitrate Reduction to Ammonia on a Titanium Electrode. *ACS Sustainable Chemistry & Engineering* **2020**, *8* (7), 2672–2681. https://doi.org/10.1021/acssuschemeng.9b05983.
(61) Dortsiou, M.; Katsounaros, I.; Polatides, C.; Kyriacou, G. Influence of the Electrode and the PH on the Rate and the Product Distribution of the Electrochemical Removal of Nitrate.

Environmental Technology (United Kingdom) **2013**, *34* (3), 373–381. https://doi.org/10.1080/09593330.2012.696722.

(62) Shih, Y. J.; Wu, Z. L.; Huang, Y. H.; Huang, C. P. Electrochemical Nitrate Reduction as Affected by the Crystal Morphology and Facet of Copper Nanoparticles Supported on Nickel Foam Electrodes (Cu/Ni). *Chemical Engineering Journal* **2020**, *383* (October 2019), 123157. https://doi.org/10.1016/j.cej.2019.123157.

(63) Mattarozzi, L.; Cattarin, S.; Comisso, N.; Gambirasi, A.; Guerriero, P.; Musiani, M.; Vázquez-Gómez, L.; Verlato, E. Hydrogen Evolution Assisted Electrodeposition of Porous Cu-Ni Alloy Electrodes and Their Use for Nitrate Reduction in Alkali. *Electrochimica Acta* **2014**, *140*, 337–344. https://doi.org/10.1016/j.electacta.2014.04.048.

(64) Reyter, D.; Bélanger, D.; Roué, L. Optimization of the Cathode Material for Nitrate Removal by a Paired Electrolysis Process. *Journal of Hazardous Materials* **2011**, *192* (2), 507–513. https://doi.org/10.1016/j.jhazmat.2011.05.054.

(65) Barrabés, N.; Sá, J. Catalytic Nitrate Removal from Water, Past, Present and Future Perspectives. *Applied Catalysis B: Environmental* **2011**, *104* (1–2), 1–5. https://doi.org/10.1016/j.apcatb.2011.03.011.

(66) Epron, F.; Gauthard, F.; Pinéda, C.; Barbier, J. Catalytic Reduction of Nitrate and Nitrite on Pt–Cu/Al2O3 Catalysts in Aqueous Solution: Role of the Interaction between Copper and Platinum in the Reaction. *Journal of Catalysis* **2001**, *198* (2), 309–318. https://doi.org/10.1006/jcat.2000.3138.

(67) Wang, Q.; Wang, W.; Yan, B.; Shi, W.; Cui, F.; Wang, C. Well-Dispersed Pd-Cu Bimetals in TiO2 Nanofiber Matrix with Enhanced Activity and Selectivity for Nitrate Catalytic Reduction. *Chemical Engineering Journal* **2017**, *326*, 182–191. https://doi.org/10.1016/j.cej.2017.05.110.

(68) Jung, S.; Bae, S.; Lee, W. Development of Pd–Cu/Hematite Catalyst for Selective Nitrate Reduction. *Environ. Sci. Technol.* **2014**, *48* (16), 9651–9658. https://doi.org/10.1021/es502263p.

(69) Yoshinaga, Y.; Akita, T.; Mikami, I.; Okuhara, T. Hydrogenation of Nitrate in Water to Nitrogen over Pd–Cu Supported on Active Carbon. *Journal of Catalysis* **2002**, *207* (1), 37–45. https://doi.org/10.1006/jcat.2002.3529.

(70) Hargreaves, J. S. J. Nitrides as Ammonia Synthesis Catalysts and as Potential Nitrogen Transfer Reagents. *Applied Petrochemical Research* **2014**, *4* (1), 3–10. https://doi.org/10.1007/s13203-014-0049-y.

(71) Logadottir, A.; Rod, T. H.; Nørskov, J. K.; Hammer, B.; Dahl, S.; Jacobsen, C. J. H. The Brønsted–Evans–Polanyi Relation and the Volcano Plot for Ammonia Synthesis over Transition Metal Catalysts. *Journal of Catalysis* **2001**, *197*, 229–231. https://doi.org/10.1006/jcat.2000.3087.

(72) Rhodes, A. K. New Ammonia Process, Catalyst Proven in Canadian Plant. *Oil and Gas journal* **1996**, *94* (47), 37–41.

(73) Oyama, S. T. Preparation and Catalytic Properties of Transition Metal Carbides and Nitrides. *Catalysis Today* **1992**, *15* (2), 179–200. https://doi.org/10.1016/0920-5861(92)80175-M.

(74) Shou, H.; Davis, R. J. Reactivity and in Situ X-Ray Absorption Spectroscopy of Rb-Promoted Mo 2 C/MgO Catalysts for Higher Alcohol Synthesis. *Journal of Catalysis* **2011**, *282*, 83–93. https://doi.org/10.1016/j.jcat.2011.05.028.

(75) Xiang, M.; Li, D.; Xiao, H.; Zhang, J.; Li, W.; Zhong, B.; Sun, Y. K/Ni/b-Mo 2 C: A Highly Active and Selective Catalyst for Higher Alcohols Synthesis from CO Hydrogenation. **2007**. https://doi.org/10.1016/j.cattod.2007.10.083.

(76) Perret, N.; Wang, X.; Delannoy, L.; Potvin, C.; Louis, C.; Keane, M. A. Enhanced Selective Nitroarene Hydrogenation over Au Supported on Î²-Mo2C and Î²-Mo2C/Al2O3. *Journal of Catalysis* **2012**, *286*, 172–183. https://doi.org/10.1016/j.jcat.2011.10.026.

(77) Griboval-Constant, A.; Giraudon, J.-M.; Twagishema, I.; Leclercq, G.; Rivas, M. E.; Alvarez, J.; Pérez-Zurita, M. J.; Goldwasser, M. R. Characterization of New Co and Ru on ⎵-WC Catalysts for Fischer-Tropsch Reaction Influence of the Carbide Surface State. *Journal of Molecular Catalysis A: Chemical* **2006**, *259*, 187–196. https://doi.org/10.1016/j.molcata.2006.06.015.

(78) Griboval-Constant, A.; Giraudon, J.-M.; Leclercq, G.; Leclercq, L. Catalytic Behaviour of Cobalt or Ruthenium Supported Molybdenum Carbide Catalysts for FT Reaction. *Applied Catalysis A: General* **2004**, *260*, 35–45. https://doi.org/10.1016/j.apcata.2003.10.031.

(79) Setthapun, W.; Bej, S. K.; Thompson, L. T. Carbide and Nitride Supported Methanol Steam Reforming Catalysts: Parallel Synthesis and High Throughput Screening. https://doi.org/10.1007/s11244-008-9070-7.

(80) Schaidle, J. A.; Lausche, A. C.; Thompson, L. T. Effects of Sulfur on Mo2C and Pt/Mo2C Catalysts: Water Gas Shift Reaction. *Journal of Catalysis* **2010**, *272* (2), 235–245. https://doi.org/10.1016/j.jcat.2010.04.004.

(81) Schaidle, J. A.; Schweitzer, N. M.; Ajenifujah, O. T.; Thompson, L. T. On the Preparation of Molybdenum Carbide-Supported Metal Catalysts. *Journal of Catalysis* **2012**, *289*, 210–217. https://doi.org/10.1016/j.jcat.2012.02.012.

(82) Schweitzer, N. M.; Schaidle, J. A.; Ezekoye, O. K.; Pan, X.; Linic, S.; Thompson, L. T. High Activity Carbide Supported Catalysts for Water Gas Shift. *J. Am. Chem. Soc* **2011**, *133*, 2378–2381. https://doi.org/10.1021/ja110705a.

(83) Venkataraman, R.; Kunz, H. R.; Fenton, J. M. Development of New CO Tolerant Ternary Anode Catalysts for Proton Exchange Membrane Fuel Cells. *Journal of The Electrochemical Society* **2003**, *150* (3), A278. https://doi.org/10.1149/1.1543567.

(84) Volpe, L.; Boudart, M. Compounds of Molybdenum and Tungsten with High Specific Surface Area: I. Nitrides. *JOURNAL OF SOLID STATE CHEMISTRY* **1985**, *59*, 332–347.

(85) Volpe, L.; Boudart, M. Compounds of Molybdenum and Tungsten with High Specific Surface Area: II. Carbides. *JOURNAL OF SOLID STATE CHEMISTRY* **1985**, *59*, 348–356.

(86) Wrobleskil, J. T.; Boudart, M. Preparation of Solid Catalysis: An Appraisal. *Catalysis Today* **1992**, *15*, 349–360.

(87) Oyama, S. T. *The Chemistry of Transition Metal Carbides and Nitrides*; 1996. https://doi.org/10.1007/978-94-009-1565-7.

(88) Patt, J. J. Carbide and Nitride Catalysts for the Water Gas Shift Reaction, University of Michigan, 2003.

(89) Volpe, L.; Boudart, M. Ammonia Synthesis on Molybdenum Nitride. *Journal of Physical Chemistry* **1986**, *90* (20), 4874–4877. https://doi.org/10.1021/j100411a031.

(90) Kojima, R.; Aika, K. I. Molybdenum Nitride and Carbide Catalysts for Ammonia Synthesis. *Applied Catalysis A: General* **2001**, *219* (1–2), 141–147. https://doi.org/10.1016/S0926-860X(01)00676-7.

(91) Mckay, D.; Hargreaves, J. S. J.; Rico, J. L.; Rivera, J. L.; Sun, X. L. The Influence of Phase and Morphology of Molybdenum Nitrides on Ammonia Synthesis Activity and Reduction Characteristics. *Journal of Solid State Chemistry* **2008**, *181* (2), 325–333. https://doi.org/10.1016/j.jssc.2007.12.001.
(92) Segal, N.; Sebba, F. Ammonia Synthesis Catalyzed by Uranium Nitride I. The Reaction Mechanism. *Journal of Catalysis* **1967**, *8*, 105–112.
(93) Segal, N. Sebba, F. Ammonia Synthesis Catalyzed by Uranium Nitride II. The Transient Behavior. *Journal of Catalysis* **1967**, No. 8, 113–119.
(94) D. A. King, F. S. The Catalytic Synthesis of Ammonia over Vanadium Nitride Containing Oxygen. *Journal of Catalysis* **1965**, *94*, 1–6.
(95) King, D. A.; Sebba, F. The Catalytic Synthesis of Ammonia over Vanadium Nitride Containing Oxygen I. The Reaction Mechanism. *JOURNAL OF CATALYSIS* **1965**, *4*, 253–259.
(96) Kojima, R.; Aika, K.-I. Rhenium Containing Binary Catalysts for Ammonia Synthesis. *Applied Catalysis A: General* **2001**, *209*, 317–325.
(97) Kojima, R.; Enomoto, H.; Muhler, M.; Aika, K.-I. Cesium-Promoted Rhenium Catalysts Supported on Alumina for Ammonia Synthesis. *Applied Catalysis A: General* **2003**, *246*, 311–322. https://doi.org/10.1016/S0926-860X(03)00062-0.
(98) Panov, G. I.; Kharitonov, A. S. Catalytic Properties of Nitrides in Ammonia Synthesis. *React. Kinet. Catal. Lett* **1985**, *29* (1), 267–274.
(99) Jacobsen, C. J. H.; Dahl, S.; Clausen, B. G. S.; Bahn, S.; Logadottir, A.; Nørskov, J. K. Catalyst Design by Interpolation in the Periodic Table: Bimetallic Ammonia Synthesis Catalysts [2]. *Journal of the American Chemical Society* **2001**, *123* (34), 8404–8405. https://doi.org/10.1021/ja010963d.
(100) Kojima, R.; Aika, K. ichi. Cobalt Molybdenum Bimetallic Nitride Catalysts for Ammonia Synthesis: Part 2. Kinetic Study. *Applied Catalysis A: General* **2001**, *218* (1–2), 121–128. https://doi.org/10.1016/S0926-860X(01)00626-3.
(101) Kojima, R.; Aika, K.-I. Cobalt Molybdenum Bimetallic Nitride Catalysts for Ammonia Synthesis Part 1. Preparation and Characterization. *Applied Catalysis A: General* **2001**, *215*, 149–160.
(102) Kojima, R.; Aika, K.-I. Cobalt Molybdenum Bimetallic Nitride Catalysts for Ammonia Synthesis Part 3. Reactant Gas Treatment. *Applied Catalysis A: General* **2001**, *219*, 157–170.
(103) Wang, Z.; Richards, D.; Singh, N. Recent Discoveries in the Reaction Mechanism of Heterogeneous Electrocatalytic Nitrate Reduction. *Catal. Sci. Technol.* **2021**, 10.1039.D0CY02025G. https://doi.org/10.1039/D0CY02025G.
(104) Butcher, D. P.; Gewirth, A. A. Nitrate Reduction Pathways on Cu Single Crystal Surfaces: Effect of Oxide and Cl−. *Nano Energy* **2016**, *29*, 457–465. https://doi.org/10.1016/j.nanoen.2016.06.024.
(105) Bae, S. E.; Stewart, K. L.; Gewirth, A. A. Nitrate Adsorption and Reduction on Cu(100) in Acidic Solution. *Journal of the American Chemical Society* **2007**, *129* (33), 10171–10180. https://doi.org/10.1021/ja071330n.
(106) Katsounaros, I.; Figueiredo, M. C.; Chen, X.; Calle-Vallejo, F.; Koper, M. T. M. Interconversions of Nitrogen-Containing Species on Pt(100) and Pt(111) Electrodes in Acidic Solutions Containing Nitrate. *Electrochimica Acta* **2018**, *271*, 77–83. https://doi.org/10.1016/j.electacta.2018.03.126.

(107) Kulkarni, A.; Siahrostami, S.; Patel, A.; Nørskov, J. K. Understanding Catalytic Activity Trends in the Oxygen Reduction Reaction. *Chemical Reviews* **2018**, *118* (5), 2302–2312. https://doi.org/10.1021/acs.chemrev.7b00488.

(108) Wang, Y.; Zhou, W.; Jia, R.; Yu, Y.; Zhang, B. Unveiling the Activity Origin of a Copper-based Electrocatalyst for Selective Nitrate Reduction to Ammonia. *Angewandte Chemie* **2020**, 1–6. https://doi.org/10.1002/ange.201915992.

(109) Katsounaros, I.; Ipsakis, D.; Polatides, C.; Kyriacou, G. Efficient Electrochemical Reduction of Nitrate to Nitrogen on Tin Cathode at Very High Cathodic Potentials. *Electrochimica Acta* **2006**, *52* (3), 1329–1338. https://doi.org/10.1016/j.electacta.2006.07.034.

(110) Dortsiou, M.; Kyriacou, G. Electrochemical Reduction of Nitrate on Bismuth Cathodes. *Journal of Electroanalytical Chemistry* **2009**, *630* (1–2), 69–74. https://doi.org/10.1016/j.jelechem.2009.02.019.

(111) Su, L.; Han, D.; Zhu, G.; Xu, H.; Luo, W.; Wang, L.; Jiang, W.; Dong, A.; Yang, J. Tailoring the Assembly of Iron Nanoparticles in Carbon Microspheres toward High-Performance Electrocatalytic Denitrification. *Nano Letters* **2019**, *19* (8), 5423–5430. https://doi.org/10.1021/acs.nanolett.9b01925.

(112) Horányi, G.; Rizmayer, E. M. Electrocatalytic Reduction of NO2- and NO3- Ions at a Platinized Platinum Electrode in Alkaline Medium. *Journal of Electroanalytical Chemistry* **1985**, *189* (1), 265–272. https://doi.org/10.1016/0368-1874(85)85644-6.

(113) Zhu, J. Y.; Xue, Q.; Xue, Y. Y.; Ding, Y.; Li, F. M.; Jin, P.; Chen, P.; Chen, Y. Iridium Nanotubes as Bifunctional Electrocatalysts for Oxygen Evolution and Nitrate Reduction Reactions. *ACS Applied Materials and Interfaces* **2020**, *12* (12), 14064–14070. https://doi.org/10.1021/acsami.0c01937.

(114) Ma, X.; Li, M.; Feng, C.; Hu, W.; Wang, L.; Liu, X. Development and Reaction Mechanism of Efficient Nano Titanium Electrode: Reconstructed Nanostructure and Enhanced Nitrate Removal Efficiency. *Journal of Electroanalytical Chemistry* **2016**, *782*, 270–277. https://doi.org/10.1016/j.jelechem.2016.10.047.

(115) Li, M.; Feng, C.; Zhang, Z.; Yang, S.; Sugiura, N. Treatment of Nitrate Contaminated Water Using an Electrochemical Method. *Bioresource Technology* **2010**, *101* (16), 6553–6557. https://doi.org/10.1016/j.biortech.2010.03.076.

(116) Chen, G. F.; Yuan, Y.; Jiang, H.; Ren, S. Y.; Ding, L. X.; Ma, L.; Wu, T.; Lu, J.; Wang, H. Electrochemical Reduction of Nitrate to Ammonia via Direct Eight-Electron Transfer Using a Copper–Molecular Solid Catalyst. *Nature Energy* **2020**, *5*, 605–613. https://doi.org/10.1038/s41560-020-0654-1.

(117) Calle-Vallejo, F.; Huang, M.; Henry, J. B.; Koper, M. T. M.; Bandarenka, A. S. Theoretical Design and Experimental Implementation of Ag/Au Electrodes for the Electrochemical Reduction of Nitrate. *Physical Chemistry Chemical Physics* **2013**, *15* (9), 3196. https://doi.org/10.1039/c2cp44620k.

(118) Zhang, Z.; Xu, Y.; Shi, W.; Wang, W.; Zhang, R.; Bao, X.; Zhang, B.; Li, L.; Cui, F. Electrochemical-Catalytic Reduction of Nitrate over Pd-Cu/ΓAl2O3 Catalyst in Cathode Chamber: Enhanced Removal Efficiency and N2 Selectivity. *Chemical Engineering Journal* **2016**, *290*, 201–208. https://doi.org/10.1016/j.cej.2016.01.063.

(119) Sanjuàn, I.; García-Cruz, L.; Solla-Gullón, J.; Expósito, E.; Montiel, V. Bi-Sn Nanoparticles for Electrochemical Denitrification: Activity and Selectivity towards N2

Formation. *Electrochimica Acta* **2020**, *340*, 135914. https://doi.org/10.1016/j.electacta.2020.135914.
(120) Yang, J.; Kwon, Y.; Duca, M.; Koper, M. T. M. Combining Voltammetry and Ion Chromatography: Application to the Selective Reduction of Nitrate on Pt and PtSn Electrodes. *Analytical Chemistry* **2013**, *85* (16), 7645–7649. https://doi.org/10.1021/ac401571w.
(121) Daily Metal Prices https://www.dailymetalprice.com (accessed Oct 10, 2020).
(122) Duca, M.; Sacré, N.; Wang, A.; Garbarino, S.; Guay, D. Enhanced Electrocatalytic Nitrate Reduction by Preferentially-Oriented (100) PtRh and PtIr Alloys: The Hidden Treasures of the 'Miscibility Gap.' *Applied Catalysis B: Environmental* **2018**, *221* (August 2017), 86–96. https://doi.org/10.1016/j.apcatb.2017.08.081.
(123) Birdja, Y. Y.; Yang, J.; Koper, M. T. M. Electrocatalytic Reduction of Nitrate on Tin-Modified Palladium Electrodes. *Electrochimica Acta* **2014**, *140*, 518–524. https://doi.org/10.1016/j.electacta.2014.06.011.
(124) Su, J. F.; Kuan, W.-F.; Chen, C.-L.; Huang, C.-P. Enhancing Electrochemical Nitrate Reduction toward Dinitrogen Selectivity on Sn-Pd Bimetallic Electrodes by Surface Structure Design. *Applied Catalysis A, General* **2020**, 117809. https://doi.org/10.1016/j.apcata.2020.117809.
(125) Kato, M.; Okui, M.; Taguchi, S.; Yagi, I. Electrocatalytic Nitrate Reduction on Well-Defined Surfaces of Tin-Modified Platinum, Palladium and Platinum-Palladium Single Crystalline Electrodes in Acidic and Neutral Media. *Journal of Electroanalytical Chemistry* **2017**, *800* (2), 46–53. https://doi.org/10.1016/j.jelechem.2017.01.020.
(126) Zhang, L.; Yin, D.; Zhai, S.; Liu, Y.; Dou, C.; Chen, P.; Huang, G. Electrochemical Behaviors and Influence Factors of Copper and Copper Alloys Cathode for Electrocatalytic Nitrate Removal. *Water Environment Research* **2019**, *91* (12), 1589–1599. https://doi.org/10.1002/wer.1151.
(127) Mattarozzi, L.; Cattarin, S.; Comisso, N.; Gerbasi, R.; Guerriero, P.; Musiani, M.; Vázquez-Gómez, L.; Verlato, E. Electrodeposition of Compact and Porous Cu-Zn Alloy Electrodes and Their Use in the Cathodic Reduction of Nitrate. *Journal of The Electrochemical Society* **2015**, *162* (6), D236–D241. https://doi.org/10.1149/2.1041506jes.
(128) Mattarozzi, L.; Cattarin, S.; Comisso, N.; Gerbasi, R.; Guerriero, P.; Musiani, M.; Verlato, E. Electrodeposition of Compact and Porous Cu-Pd Alloy Layers and Their Application to Nitrate Reduction in Alkali. *Electrochimica Acta* **2017**, *230*, 365–372. https://doi.org/10.1016/j.electacta.2017.02.012.
(129) Han, Q.; Jebaraj, A. J. J.; Solla-Gullón, J.; Feliu, J.; Scherson, D. Rational Design of Electrocatalytic Interfaces: Cd UPD Mediated Nitrate Reduction on Pd: Au Bimetallic Surfaces. *Journal of The Electrochemical Society* **2019**, *166* (13), H640–H643. https://doi.org/10.1149/2.0921913jes.
(130) Gao, W.; Gao, L.; Li, D.; Huang, K.; Cui, L.; Meng, J.; Liang, J. Removal of Nitrate from Water by the Electrocatalytic Denitrification on the Cu-Bi Electrode. *Journal of Electroanalytical Chemistry* **2018**, *817* (August 2017), 202–209. https://doi.org/10.1016/j.jelechem.2018.04.006.
(131) Mirzaei, P.; Bastide, S.; Aghajani, A.; Bourgon, J.; Leroy, É.; Zhang, J.; Snoussi, Y.; Bensghaier, A.; Hamouma, O.; Chehimi, M. M.; Cachet-Vivier, C. Bimetallic Cu-Rh Nanoparticles on Diazonium-Modified Carbon Powders for the Electrocatalytic Reduction

of Nitrates. *Langmuir* **2019**, *35* (45), 14428–14436. https://doi.org/10.1021/acs.langmuir.9b01911.

(132) Shen, Z.; Liu, D.; Peng, G.; Ma, Y.; Li, J.; Shi, J.; Peng, J.; Ding, L. Electrocatalytic Reduction of Nitrate in Water Using Cu/Pd Modified Ni Foam Cathode: High Nitrate Removal Efficiency and N2-Selectivity. *Separation and Purification Technology* **2020**, *241* (October 2019). https://doi.org/10.1016/j.seppur.2020.116743.

(133) Calle-Vallejo, F.; Huang, M.; Henry, J. B.; Koper, M. T. M.; Bandarenka, A. S. Theoretical Design and Experimental Implementation of Ag/Au Electrodes for the Electrochemical Reduction of Nitrate. *Physical Chemistry Chemical Physics* **2013**, *15* (9), 3196. https://doi.org/10.1039/c2cp44620k.

(134) Vorlop, K.-D.; Tacke, T. Erste Schritte Auf Dem Weg Zur Edelmetallkatalysierten Nitrat-Und Nitrit-Entfernung Aus Trinkwasser. *Chemie Ingenieur Technik* **1989**, *61* (10), 836–837. https://doi.org/10.1002/cite.330611023.

(135) Marchesini, F. A.; Irusta, S.; Querini, C.; Miró, E. Spectroscopic and Catalytic Characterization of Pd–In and Pt–In Supported on Al2O3 and SiO2, Active Catalysts for Nitrate Hydrogenation. *Applied Catalysis A: General* **2008**, *348* (1), 60–70. https://doi.org/10.1016/j.apcata.2008.06.026.

(136) Prüsse, U.; Hähnlein, M.; Daum, J.; Vorlop, K.-D. Improving the Catalytic Nitrate Reduction. *Catalysis Today* **2000**, *55* (1–2), 79–90. https://doi.org/10.1016/S0920-5861(99)00228-X.

(137) Gauthard, F. Palladium and Platinum-Based Catalysts in the Catalytic Reduction of Nitrate in Water: Effect of Copper, Silver, or Gold Addition. *Journal of Catalysis* **2003**, *220* (1), 182–191. https://doi.org/10.1016/S0021-9517(03)00252-5.

(138) Deganello, F.; Liotta, L. F.; Macaluso, A.; Venezia, A. M.; Deganello, G. Catalytic Reduction of Nitrates and Nitrites in Water Solution on Pumice-Supported Pd–Cu Catalysts. *Applied Catalysis B: Environmental* **2000**, *24* (3), 265–273. https://doi.org/10.1016/S0926-3373(99)00109-5.

(139) Batista, J.; Pintar, A.; Gomilšek, J. P.; Kodre, A.; Bornette, F. On the Structural Characteristics of γ-Alumina-Supported Pd–Cu Bimetallic Catalysts. *Applied Catalysis A: General* **2001**, *217* (1), 55–68. https://doi.org/10.1016/S0926-860X(01)00580-4.

(140) Pintar, A.; Batista, J.; Arčon, I.; Kodre, A. Characterization of γ-Al2O3 Supported Pd-Cu Bimetallic Catalysts by EXAFS, AES and Kinetic Measurements. In *Studies in Surface Science and Catalysis*; Delmon, B., Jacobs, P. A., Maggi, R., Martens, J. A., Grange, P., Poncelet, G., Eds.; Preparation of Catalysts VII; Elsevier, 1998; Vol. 118, pp 127–136. https://doi.org/10.1016/S0167-2991(98)80175-4.

(141) Batista, J.; Pintar, A.; Mandrino, D.; Jenko, M.; Martin, V. XPS and TPR Examinations of γ-Alumina-Supported Pd-Cu Catalysts. *Applied Catalysis A: General* **2001**, *206* (1), 113–124. https://doi.org/10.1016/S0926-860X(00)00589-5.

(142) Matatov-Meytal, U.; Sheintuch, M. Activated Carbon Cloth-Supported Pd–Cu Catalyst: Application for Continuous Water Denitrification. *Catalysis Today* **2005**, *102–103*, 121–127. https://doi.org/10.1016/j.cattod.2005.02.015.

(143) Pintar, A.; Batista, J. Catalytic Stepwise Nitrate Hydrogenation in Batch-Recycle Fixed-Bed Reactors. *Journal of Hazardous Materials* **2007**, *149* (2), 387–398. https://doi.org/10.1016/j.jhazmat.2007.04.004.

(144) Epron, F.; Gauthard, F.; Barbier, J. Catalytic Reduction of Nitrate in Water on a Monometallic Pd/CeO2 Catalyst. *Journal of Catalysis* **2002**, *206* (2), 363–367. https://doi.org/10.1006/jcat.2001.3498.
(145) Sá, J.; Berger, T.; Föttinger, K.; Riss, A.; Anderson, J. A.; Vinek, H. Can TiO2 Promote the Reduction of Nitrates in Water? *Journal of Catalysis* **2005**, *234* (2), 282–291. https://doi.org/10.1016/j.jcat.2005.06.015.
(146) Huo, X.; Van Hoomissen, D. J.; Liu, J.; Vyas, S.; Strathmann, T. J. Hydrogenation of Aqueous Nitrate and Nitrite with Ruthenium Catalysts. *Applied Catalysis B: Environmental* **2017**, *211*, 188–198. https://doi.org/10.1016/j.apcatb.2017.04.045.
(147) Chen, S.-S.; Hsu, H.-D.; Li, C.-W. A New Method to Produce Nanoscale Iron for Nitrate Removal. *J Nanopart Res* **2004**, *6* (6), 639–647. https://doi.org/10.1007/s11051-004-6672-2.
(148) Chew, C. F.; Zhang, T. C. In-Situ Remediation of Nitrate-Contaminated Ground Water by Electrokinetics/Iron Wall Processes. *Water Science and Technology* **1998**, *38* (7), 135–142. https://doi.org/10.1016/S0273-1223(98)00615-5.
(149) Westerhoff, P.; James, J. Nitrate Removal in Zero-Valent Iron Packed Columns. *Water Research* **2003**, *37* (8), 1818–1830. https://doi.org/10.1016/S0043-1354(02)00539-0.
(150) Huang, Y. H.; Zhang, T. C. Effects of Low PH on Nitrate Reduction by Iron Powder. *Water Research* **2004**, *38* (11), 2631–2642. https://doi.org/10.1016/j.watres.2004.03.015.

Chapter 2

Research Design and Methods

2.1 Introduction

This chapter provides a description of experimental techniques used in this dissertation. **Section 2.2** details major techniques used to synthesize catalysts for ammonia synthesis, electrocatalytic nitrate reduction, and thermocatalytic nitrate reduction reactions. **Section 2.3** covers the characterization techniques and **Section 2.4** gives an overview of how each of the catalysts were evaluated for their catalytic activity and selectivity. The information in the chapter provides a structure for incoming Ph.D. students to design experiments and select appropriate techniques. Additionally, it serves as a tool for researchers who wish to replicate the experimental work conducted in this dissertation.

2.2 Synthesis Techniques

2.2.1 Temperature Programmed Synthesis

The work in **Chapter 3** focuses on studying molybdenum carbides and nitrides for ammonia synthesis, which are traditionally synthesized via temperature-programmed reactions.[1–3] Ammonium paramolybdate (AM) precursor was first crushed and sieved to particle sizes between 125 – 250 μm before loading into a quartz flow-reactor supported by a bed of quartz wool, and secured in a heated furnace. Depending on the desired support (e.g., Mo_2C or Mo_2N), different

temperatures, ramp rates, soak times, and gas compositions were used to synthesize the catalyst (**Figure 2.1**).

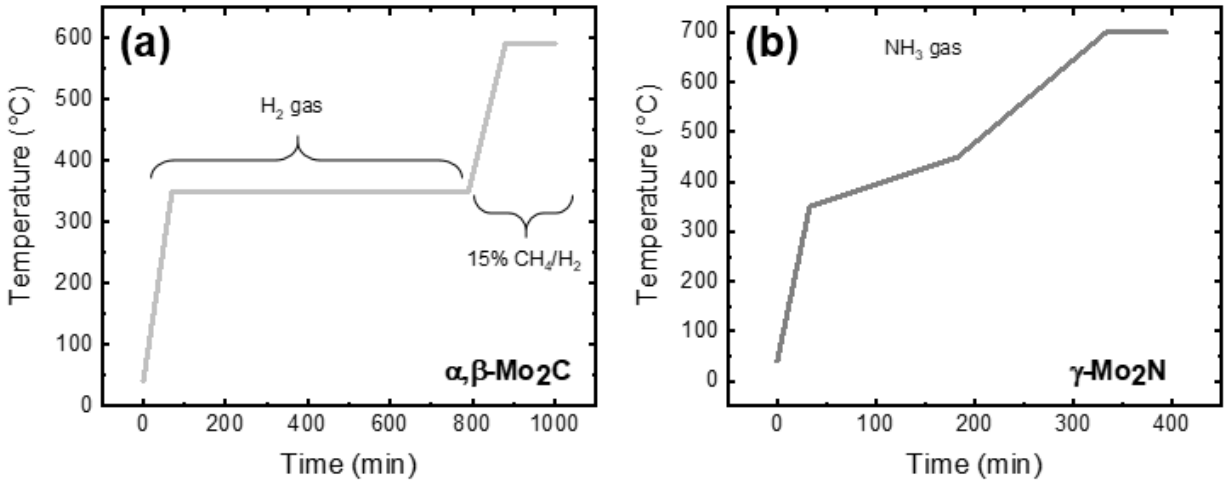

Figure 2.1. Temperature-programmed reaction protocols to synthesize **(a)** α,β-Mo_2C and **(b)** γ-Mo_2N.

To synthesize α,β-Mo_2C, 1.3 g of AM was heated from 40 °C to 350 °C in 70 min followed by a 720 min soak in H_2 to reduce the oxide in the precursor. After switching the gas to 15% CH_4/H_2, the temperature was ramped to 590 °C in 90 min followed by a 120 min soak to carbonize the material. For γ-Mo_2N, 1.5 g of AM is heated to 350 °C in 33 min, 450 °C in 150 min, and 700 °C in 150 min before final soak for 60 min in NH_3.

Following the temperature-programmed synthesis reactions, the materials were cooled to room temperature by removing the reactor from the furnace. After reaching room temperature (15 – 30 min), the material was exposed to 1% O_2/He at 20 mL min^{-1} for at least 5 hrs to passivate the surface and prevent bulk oxidation upon exposure to air. The synthesized materials were stored under vacuum in an argon-filled glove box to limit exposure to oxygen.

2.2.2 Impregnation

Two common methods of impregnation are used to synthesize a variety of heterogeneous catalysts throughout this dissertation. In incipient-wetness impregnation ("capillary impregnation"), the active metal precursor is dissolved in an aqueous or organic solution and added to a catalyst support containing the same pore volume as the volume of the solution added. This method uses capillary action to ensure that all the metal solution is drawn into the pores of the support, so that no excess solution remains outside the pore space (**Figure 2.2a**). Thus, the weight loading of the metal deposited should be equal to the initial to target deposition value.

Wet impregnation is implemented under optimal diffusion conditions in combination with conventional stirring. In this case, both the active metal precursor and the support are immersed in excess solution. If there is a strong interaction between the support and the precursor, diffusion will allow the metal to be deposited on the surface of the support (**Figure 2.2b**).

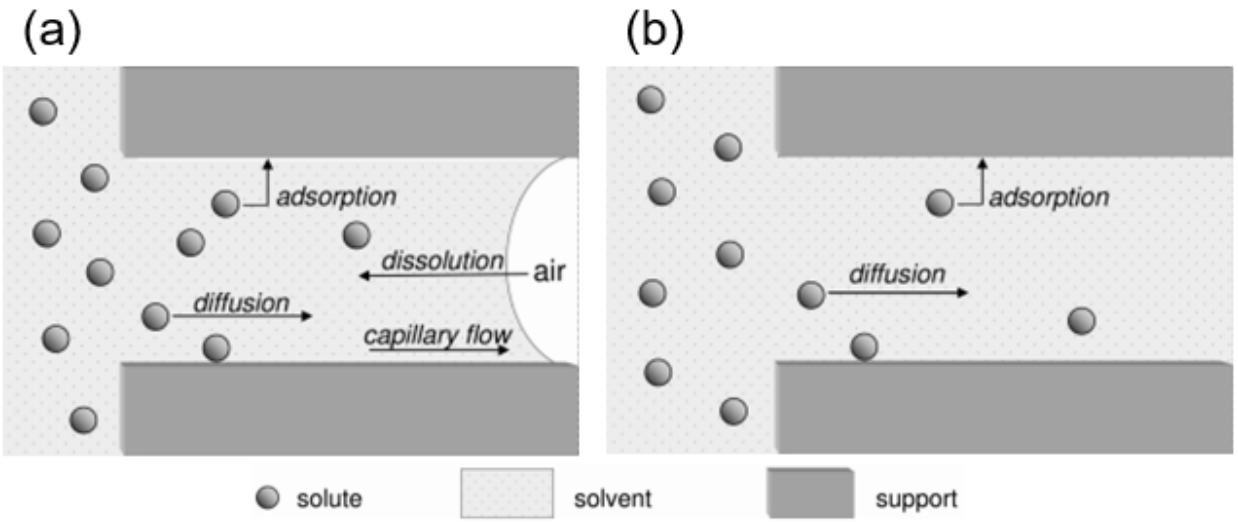

Figure 2.2. Schematic of transport phenomena in **(a)** incipient-wetness impregnation and **(b)** wet impregnation as adapted from Ref.[4]. The solute (left) migrates into the pore of the support (right).

Following impregnation of the metal, a drying step is needed to remove the solvent from the material and deposit the metal on the support surface. Typically, this involves heating up the

material in an oven up to the boiling point of the solvent. The maximum loading in either of these impregnation techniques depends on the solubility of the metal precursor in the solution.

In **Chapter 3**, incipient-wetness impregnation was primarily used to deposit Fe, Ru, and Co onto the surface of active Mo_2C and Mo_2N supports. The porosity of Mo_2C and Mo_2N was first measured by using N_2-physisorption (additional details in **Section 2.3.2**) with the Horváth-Kawazoe (HK)[5] and Barrett-Joyner-Halenda (BJH)[6] methods. Desired concentrations of $Fe(NO_3)_3$ (14% Fe; Sigma Aldrich), $RuCl_3$ (38% Ru; Sigma Aldrich), and $Co(NO_3)_2$ (20% Co; Sigma Aldrich) dissolved in Millipore water (18.2 MΩcm, Millipore MilliQ system) were added dropwise to the support with continuous stirring and mixing in between each addition of solution. Following the deposition, the catalysts were transferred into a quartz reactor to be reduced at 110 °C in H_2 for 2 hrs.

2.2.3 Chemical Reduction

Chemical reduction is another common method of synthesizing metal nanoparticles by introducing a chemical reducing agent into the metal precursor solution. Typically, stronger reducing agents (e.g., sodium borohydride) yield smaller particle sizes while weaker reducing agents (e.g., citrate) produce larger particles.[7] For the work in **Chapter 4** and **5**, all of the platinum-ruthenium alloys were synthesized using a modified sodium borohydride reducing agent on a Vulcan carbon support (**Figure 2.3**).[8]

A suspension of 25 mg of carbon black (Vulcan XC 72; Fuel Cell Store) was pretreated in H_2 at 400 °C for 2 hrs to remove impurities from the surface. After, the support was suspended in 15 mL of Millipore water and sonicated for 15 min to ensure adequate dispersion. Measured concentrations of $RuCl_3$ (38% Ru; Alfa Aesar) and H_2PtCl_6 (38–40% Pt; Sigma Aldrich) in Millipore water were added to the solution in which the support was suspended, and stirred for 15

min. 40 mg of $NaBH_4$ (Sigma Aldrich) dissolved in 25 mL of Millipore water was then introduced to reduce the metal precursors. This solution was stirred for 2 hrs before being centrifuged and washed 3 times at 3000 rpm for 8 min with Millipore water. The recovered solid was dried overnight in an oven at 80 °C.

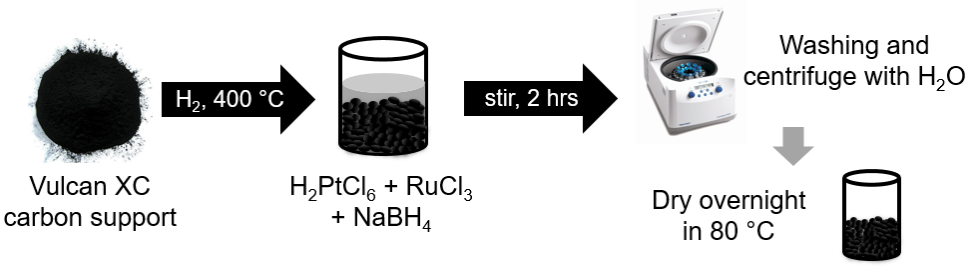

Figure 2.3. Overview of $NaBH_4$ synthesis procedure to make Pt_xRu_y/C catalysts. Different concentrations of H_2PtCl_6 and $RuCl_3$ were used to vary the composition of the alloys in the $NaBH_4$ solution. After stirring the solution for 2 hrs, the remaining catalyst was centrifuged at 3000 rpm for 8 min before washing with Millipore water. The recovered material was dried overnight at 80 °C in ambient air.

2.2.4 Electrode Ink Preparation

After synthesizing a variety of powdered catalysts, electrode inks were prepared to load the catalyst onto an electrode for electrochemical measurements.[9,10] The catalyst ink was prepared by adding 3 mg of the supported catalyst in 5 mL of water and isopropanol mixture (1:1 molar ratio). 17.5 µL of Nafion solution (5% in 95% isopropanol, Sigma Aldrich) was added to the solution to act as a binder and sonicated for at least 120 min. A glassy carbon disk (5 mm in diameter) was cleaned by polishing with 0.05 µm alumina suspension, followed by rinsing, and then sonicated in Millipore water to remove trace surface contaminants for 30 min. The prepared catalyst ink was sonicated for at least 30 min before depositing on the electrode surface. 8 µL of this sonicated ink is deposited onto the surface of the clean glassy carbon electrode. The deposition was kept in closed containment as the ink dried and a second 8 µL of the ink was deposited unto the dried ink surface to give a total catalyst loading of 9.6 µg, including carbon.

2.2.5 Electrode Felt Synthesis

In many cases, the catalysts are loaded onto high surface area electrode felts to yield high enough currents to allow for product quantification in electrochemical measurements. There are two major ways to load the catalysts on carbon felts: (1) synthesize nanoparticles directly on the felts via concentrated precursor solution, and (2) deposit synthesized powder catalysts onto the carbon felt via wet impregnation. For our studies of Pt_xRu_y alloys in **Chapter 4**, we used the first technique. Desired concentrations of Pt and Ru precursors were deposited via the same $NaBH_4$ reduction method (**Section 2.2.3**) on 2.5×2.5 cm^2 pieces of carbon felt (6.35 mm thick, 99.0%, Alfa Aesar). Briefly, the carbon felts are submerged in Millipore water before adding desired concentrations of precursor. The solution is stirred for 15 min before adding $NaBH_4$ to reduce the metals onto the support. In the second technique, supported catalysts can also be deposited on carbon felts through diffusion of the powder catalysts onto the surface of the felt under highly reducing conditions. In **Chapter 5**, 10 mg of PtRu/C powder catalyst is dispersed in 40 mL of 1 M H_2SO_4. The carbon felt was suspended in the solution with bubbling H_2 at 80 °C to accelerate the deposition process. In both cases, the carbon felts were rinsed with Millipore water before immediate use or air-dried Depending on the catalyst for deposition, it is recommended to pretreat the felt (e.g., plasma, thermal, chemical, etc.) to further improve the interactions between the felt and the powder catalysts.[11]

2.3 Material Characterization Techniques

Various characterization techniques have been used in this dissertation to further understand different physical and chemical properties of the materials before performance evaluation. This section first provides a general description of each technique followed by specific descriptions of the equipment and conditions implemented in this work.

2.3.1 X-ray Diffraction

X-ray Diffraction (XRD) is a materials characterization technique that uses X-ray beams to analyze the structure of crystalline samples. The penetration depth of Cu Kα ranges from 1 μm for gold to 500 μm for graphite, and thus is not a surface sensitive technique.[12] Diffraction occurs when beams of X-rays with wavelengths comparable to interatomic distances interact with the periodic array of molecules. The positions of the atoms in the unit cell determine the position of the diffracted beams with respect to the incident X-ray beam.[12,13] When the unit cells in the sample have perfect three-dimensional periodicity, then the diffraction corresponds to a series of refracted beams that satisfy Bragg's law for constructive interference (**Equation 2.1**):

$$n\lambda = 2d\sin\theta \tag{2.1}$$

where n is a positive integer, λ is the wavelength of the X-ray, d is the spacing between atomic planes with equal electron density, and θ is the incidence and reflection angle. In a conventional XRD measurement, the θ-2θ scan shows the planes that contribute to diffraction peaks parallel to the surface.[12] These spectra can be further processed and analyzed in JADE software and compared to standards from the International Centre for Diffraction Data database to identify materials. Additionally, the measured peak width is inversely proportional to the crystal thickness measured perpendicular to the reflecting planes, also known as the Scherrer's equation (**Equation 2.2**):

$$\tau = \frac{K\lambda}{\beta\cos\theta} \tag{2.2}$$

where τ is the average size of the crystalline particles, K is the shape factor (0.89), λ is the wavelength of the X-ray (1.54056 Å), β is the full width of the peak at half maximum, and θ is the Bragg angle of the peak (in degrees). Note that the Scherrer formula is limited to nano-scale crystallites and cannot be applied to particle sizes larger than 0.2 μm.[12]

XRD has been used to characterize all the catalysts synthesized in this dissertation and have been conducted using a Rigaku Miniflex with Cu Kα radiation and a Ni filter (k = 1.5418 Å). 10 – 25 mg of the catalyst is loaded and packed into a zero-background sample holder. The voltage and current from the X-ray tube are set at 40 kV and 15 mA, respectively, before starting the experiment. The 2θ range ($10° < 2\theta < 90°$) was scanned at a rate of 5°/min with a 0.02° step size. Increasing the sample size and reducing the scan rate can further improve resolution of XRD measurements.

2.3.2 X-ray Photoelectron Spectroscopy

X-ray photoelectron spectroscopy (XPS) is a technique used to analyze the surface chemistry of a material. XPS experiments are collected by irradiating solid surfaces with X-rays while detectors measure the kinetic energy of electrons emitted.[14] A photoelectron spectrum is recorded by counting the number of electrons ejected over a range of kinetic energies. The peaks that appear in the spectrum are characteristic of specific materials, which allows for identification and quantification of surface elements. Further analysis and deconvolution of the spectra allow users to identify surface elemental composition, chemical state, and overall electronic structure and density of electronic states in the material. Depending on instrument sensitivity and X-ray source, this technique can penetrate surfaces ranging from ~2 to 10 nm, and can detect all elements except hydrogen and helium.[14] When analyzing and deconvoluting the XPS spectra for information about the electronic state of materials, it is important to produce accurate physical interpretations rather than the perfect mathematical fit from the software.

For the experiments in **Chapter 4**, XPS was conducted using a Kratos Axis Ultra X-ray photoelectron spectrometer. Powder catalysts were loaded onto the sample holder with copper tape. While keeping the analysis chamber at 1×10^{-9} Torr, a monochromatic Al X-ray source (10

mA and 12 kV) was used with a pass energy of 12 eV and step size of 1 eV. Collected spectra were calibrated by positioning the C(1s) peak at 248.8 eV. Survey scans ranged from 600 – 0 eV while the narrow scans were performed between 370 – 300 eV and 510 – 450 eV for Pt 4*d* and Ru 3*p*, respectively (**Figure. 2.4**). The resulting Pt 4*d* and Ru 3*p* peaks were fitted with the Shirley-type background with the CasaXPS software.[15] The relative compositions were determined by integrating the peaks and normalized by the relative sensitivity factor of the instrument for Pt 4*d* and Ru 3*p*.

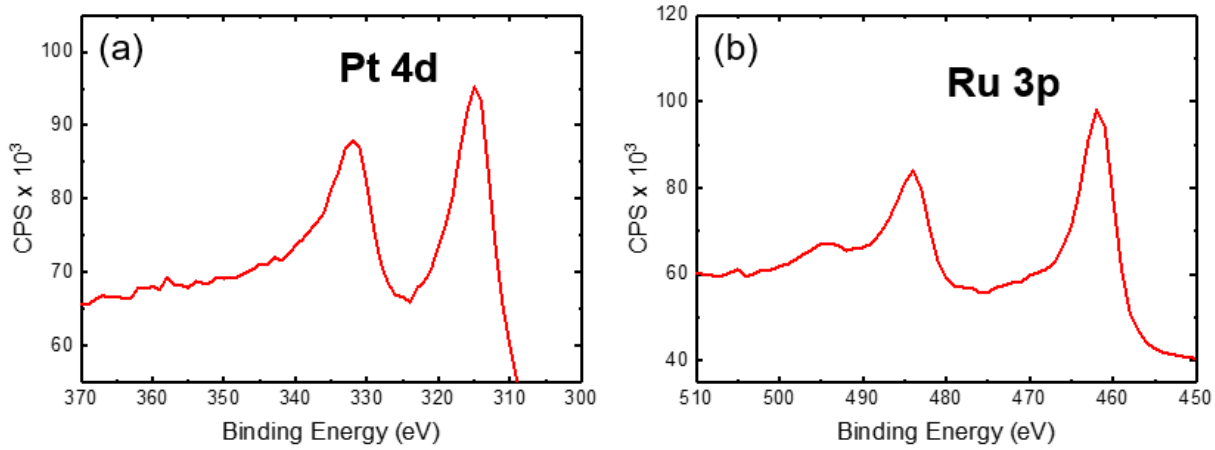

Figure 2.4. X-ray photoelectron spectra shown for **(a)** Pt/C and **(b)** Ru/C. The signal intensity from these regions represent the amount of Pt and Ru on the surface of the material.

2.3.3 X-ray Absorption Fine Structure

X-ray absorption fine structure (XAFS) is a technique primarily used to obtain information about the formal oxidation state, coordination chemistry, and the distances, coordination number, and species of neighboring atoms. These experiments require an energy-tunable X-ray that are primarily performed with synchrotron radiation sources at particular stations. Thus, this technique is less commonly used than many other spectroscopic methods due to its lack of access. In a typical experiment, an incident X-ray with energy equal to the binding energy of a core-level electron

irradiates the sample. The photoelectric effect occurs, in which the core-level electron is promoted out of the atom into the continuum and an X-ray is absorbed (**Figure 2.5**).[16]

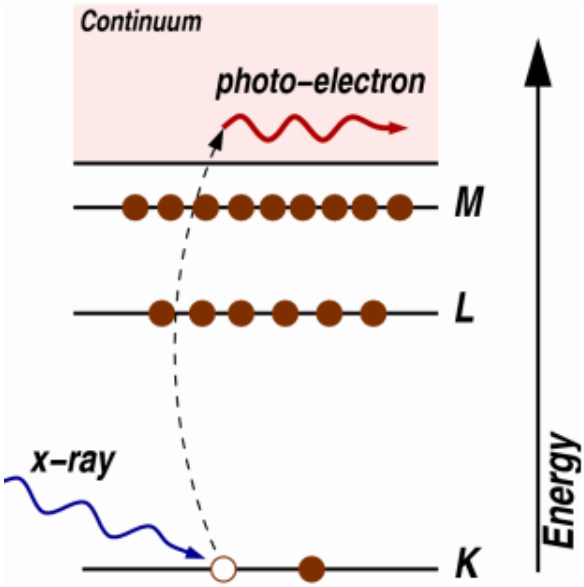

Figure 2.5. Schematic of the photoelectric effect where an X-ray is absorbed and a core-level electron is promoted out of the atom into the continuum. Image from Ref.[17].

Following absorption, the atom in the excited state will decay within a few femtoseconds via two primary mechanism: (1) X-ray fluorescence, where a higher energy electron fills the core hole and ejecting a characteristic X-ray, (2) Auger effect, where a higher energy electron fills the core hole and a second electron is emitted into the continuum. X-ray fluorescence is more likely to occur until X-ray absorption energies are below 2 keV.[17] There are two different types of XAFS measurements: transmission and fluorescence. Transmission measurements require uniform samples with elemental concentrations above 10%, but do not require well-aligned beam on the sample.[17] Florescence measurements are typically for materials with lower elemental concentrations and require well-aligned beams to avoid noisy spectra. The X-ray absorption spectrum is divided into two energy regimes: X-ray absorption near edge structure (XANES) and extended X-ray absorption fine structure (EXAFS). XANES provides information on the oxidation

state and coordination chemistry of absorbing atoms, while processing EXAFS data can be used to determine the distances, coordination number, and identity of atoms in the surrounding environment.[16] Though these measurements are straightforward, accurate and precise data analysis from the iterative fitting process can be very challenging.

In **Chapter 4**, XANES and EXAFS measurements were taken at the Sector 20 bending-magnet beamline of the Advanced Photon Source at Argonne National Laboratory. Catalyst samples were loaded into 1.5 mm glass capillaries for measurement in transmission mode at the Pt L_3-edge. To measure the spectra at the Ru K-edge, the catalyst samples were also tested in the glass capillaries using transmission mode, except for the lowest Ru weight loading sample, for which the sample was filled into a Kapton tube to allow a longer path distance to increase the signal to noise ratio. All measurements were taken of samples exposed to air (ex situ). Two 14-min scans were taken for each sample at each edge and co-added to generate the spectrum. Pt and Ru reference foils were located downstream and taken concurrently with the sample for energy calibration and to verify monochromatic stability.

The data was processed using ATHENA software with a Fourier cutoff of R_{bkg} = 1.0 Å and a k range of 3 to 16 $Å^{-1}$.[18] First, the edge onset energy (E_0) was defined for the Pt foil and set accordingly for spectra of all alloy catalysts. Next, the background signal for the data was removed by fitting the pre-edge and post-edge data to a linear function and subtracting it out. After processing the data, fitting paths were generated using FEFF9 theoretical standards[19] and structure coordinates from Materials Project. For improved convergence and optimization tests in FEFF9, the COREHOLE card was varied during XANES calculations. The default setting is based off of the Final State Rule (FSR), which may over overestimate the strength of the core-hole interaction and exclude the core-hole mixing effect for L-shell metals.[20,21] To overcome this problem, the

random phase approximation (RPA) was used in the XANES calculations of the Pt-Pt, Pt-O, and Pt-Ru paths. The use of RPA over FSR improved the fit in the first shell and χ error. The final structural parameters were derived by using FEFF9 fitting were set as inputs to the ARTEMIS software package.[18,22] Fits included first Pt-Pt or Pt-Ru and Pt-O paths including the third cumulant to account for asymmetry.

2.3.4 N_2-Physisorption

N_2-physisorption isotherms are effective in evaluating the surface area and porosity of materials. Brunner-Emmett-Teller (BET) gas adsorption theory is the most commonly used method to estimate the surface area of materials from the monolayer volume of adsorbed N_2 at different partial pressures of N_2.[23] The micropore and mesopore size distributions can also be obtained via the Horváth-Kawazoe (HK)[5] and Barrett-Joyner-Halenda (BJH)[6] methods, respectively. While this technique is non-destructive and relatively easily to perform, the analysis provides the bulk surface area of the material and does not distinguish between metal or support surface areas. Additionally, the detection limit for using N_2 as the adsorptive gas is ~10 m^2 g^{-1}. For materials with expected surface area below 0.01 m^2 g^{-1}, it is recommended to perform the experiment with krypton (Kr) as an adsorptive gas. However, use of Kr is limited because of high cost and less reliability to achieve accurate porosity measurements.

For the work in **Chapter 3**, N_2-physisorption experiments were performed using Micrometrics ASAP 2020 with the BET, HK, and BJH methods to estimate surface area and pore size distribution. To perform this experiment, the weight of an empty, bulb-shaped, glass sample tube with a filler tube is measured and recorded. The filler tube is used to ensure accuracy in low total surface area of samples less than 100 m^2 g^{-1} (e.g., supported carbides and nitrides, carbon felts) by reducing the free-volume space and preventing adsorption of physisorption gas to internal

glass surface. For higher surface area materials (e.g., powder carbon catalysts), the filler tube is unnecessary.

In a typical run for supported carbides and nitrides, ~100 mg of the sample was loaded into the sample tube after recording weight measurements. The sample was degassed by heating the material to 350 °C under vacuum (<5 mm Hg) for four hrs. This process was necessary to ensure the removal of adsorbed species from the sample surface that directly affects the results of analysis. After degassing, the weight of the tube and catalyst was measured and recorded before exposing the sample to discrete nitrogen partial pressures relative to the saturation pressure.

The experimental procedure for carbon-based materials was similar, but minor adjustments were made to the degas conditions to ensure the removal of adsorbed species from higher surface areas. 40 – 50 mg of material was loaded into the sample tube after recording weight measurements. For carbon powder, the catalyst was funneled directly to the bottom of the tube before quickly sonicating the sample tube in water to ensure that the entire sample is at the bottom of the glass bulb. For carbon felts, the material was cut into smaller pieces so that it can fit through the neck of the tube. The carbon-based material were degassed by heating to 150 °C under vacuum (<5 mm Hg) for 12 hrs before analysis.

2.3.5 Electron Microscopy

2.3.5.1 *Scanning Electron Microscopy*

Scanning electron microscopy (SEM) is a technique used to obtain magnified images of samples that reveal information about the size, shape, topography, and other physical and chemical properties of the sample. This technique uses a finely focused beam of energetic electrons emitted from an electron source that typically ranges from 0.2 to 40 keV. Apertures, lenses, and electromagnetic coils modify the electron beam, which ultimately reduces the diameter of the beam

to raster across sample surfaces.[24] At each location, the interaction between the incident electron beam and sample produces both backscattered electrons (BSEs) and secondary electrons (SEs).

BSEs result from high-energy elastic collisions of incident electrons with atoms. Because penetration depths are large, BSEs have lower resolution than SEs.[25] However, the average atomic number of the sample is proportional to the brightness of the image and can provide insights on the material composition. In contrast, SEs originate from the surface or the near-surface of the sample as a result of inelastic interactions between the primary electron bean and the sample.[25] SEs tend to have lower kinetic energy than BSEs and provide higher quality topographic images.

In **Chapter 5**, SEM images of samples were obtained using Nova 200 Nanolab (Thermo Fisher) coupled with energy-dispersive X-ray spectroscopy (SEM/EDX). Samples were prepared on pin stub mounts using carbon tape and silicon wafers (Ted Pella). Prior to analysis in SEM chambers, the samples were cleaned with plasma to remove surface organic contaminants. Images were collected at accelerating voltage of 10 keV and working distances of 5 mm for maximum resolution. Elemental analyses were obtained using Energy Dispersive X-ray Spectroscopy (EDX), as discussed in **Section 2.3.6**.

2.3.5.2 *Transmission Electron Microscopy*

Similar to SEM, transmission electron microscopy (TEM) uses accelerated beams of electron to observe structures and morphology of samples. Electrons interact with atoms via elastic and inelastic scattering, so samples must be thin (between 5 nm to 0.5 μm), depending on the density and elemental composition of the material and the desired resolution.[26] TEM typically operates by accelerating electron beams to high speeds using electromagnetic coils with voltage between 40 and 300 keV. By using a series of condenser lenses, the electron beam is focused into a thin, small beam, which irradiates the sample. Parts of the beam are diffracted, and the

transmitted electron beams are focused by an objective lens to form an image. Intermediate and projector lenses magnify the image onto a phosphor screen or electron camera. Alternatively, objective apertures are used to improve the contrast by reducing lens aberrations.[27] TEM is conducted in vacuum to ensure that electrons do not collide with gas atoms.

In **Chapter 4**, TEM was performed on a JEOL 2010F electron microscope operating with 200 keV accelerating voltage. The samples were made by adding 1 mg of catalyst into isopropanol. One drop of this suspension was deposited on a gold grid. The isopropanol was dried before imaging of the sample. The uniformity, distribution, and average size of the nanoparticles were calculated by using ImageJ software.

2.3.6 Energy Dispersive X-ray Spectroscopy

Energy dispersive X-ray spectroscopy (EDX/EDS) is a technique that uses electron beams to identify and quantify elements present in a sample. This technique is typically used in conjunction with other electron microscopy techniques (e.g., SEM or TEM). Once a high-energy electron decays, it produces a characteristic X-ray with energies that correspond to specific elements. EDX detectors can measure spectra with energies ranging from 0.4 to 30 keV, and an analytical software is used to assign spectral peaks to specific elements.[24] This technique determines the relative bulk composition within the beam-excited interaction volume, but excludes H and He, which do not emit X-rays.[24] Depending on the applications, the interaction volume for EDX can be used for spot analyses, line scan analyses, or elemental mapping. In spot analyses, the beam is focused on a specific point in the sample to determine the composition. Line scan analyses the composition along a line drawn through the sample. This option is frequently used to obtain compositions of core-shell materials. Elemental mapping is used to obtain the composition over a

rectangular scanning area. By overlapping different elemental compositions over the sample, this option shows the relative distribution in the target area.

In **Chapter 5**, EDX measurements were obtained in the Nova 200 Nanolab (Thermo Fisher) with the Genesis Microanalysis Software. Accelerating voltage was adjusted to range between 10 – 18 keV at 5.1 mm working distance to maximize detection signal, and the detector was switched to EDS mode before collecting elemental data.

2.3.7 Bulk Elemental Analysis

After synthesis, it is important to perform elemental analysis to determine the accurate compositions of catalysts as compared to the target loading. Catalyst compositions were determined through elemental analysis using Inductively Coupled Plasma-Optical Emission Spectroscopy (ICP-OES), Inductively Coupled Plasma-Mass Spectrometry (ICP-MS), and Microwave Plasma-Atomic Emission Spectroscopy (MP-AES). In ICP-OES, a plasma source is created from argon. When samples are introduced to the plasma, the electrons become excited to higher energy states. Upon relaxation, these electrons will return to their initial ground state and emit electromagnetic radiation that possess characteristic wavelengths for elemental analysis.[28] MP-AES offers a cheaper and more environmentally sustainable alternative to ICP-OES by using nitrogen gas to generate a microwave plasma source.[29] ICP-MS has similar operations to typical mass spectrometer (**Section 2.4.2**) and uses inductively coupled plasma to ionize samples. This technique is effective in isotope labeling and provides the highest levels of sensitivity at lower concentrations.[30]

For analysis, catalysts are first dissolved in aqua regia (3:1 molar HCl:HNO_3). In **Chapter 3**, 15 mg of the metals supported on carbides and nitrides was dissolved in 3 mL of aqua regia for at least 24 hrs. Then, 1 mL of the solution was diluted with 13 mL of deionized water before

analysis in a Varian 710-ES ICP-OES. The measured concentrations were compared to standard calibrations of Mo, Fe, Ru, and Co.

In **Chapter 4**, the final Pt and Ru loadings were determined by using a PerkinElmer NexION 2000 ICP-MS after digesting 1 mg of the catalyst in aqua regia (3:1 molar HCl:HNO_3). Since ICP-MS had higher levels of sensitivity, 1 mL of the solution was diluted with 100 mL of Millipore water before analysis. The sample solutions were co-fed along with a 20-ppb bismuth internal standard, and concentrations were compared to known concentrations of Pt and Ru. Likewise, the Pt and Ru loading were determined by using an Agilent 4210 MP-AES in **Chapter 5**. Since MP-AES had lower levels of sensitivity, 1 mL of the metal solution was diluted with 20 mL of Millipore water.

2.3.8 Thermal Gravimetric Analysis

Thermal gravimetric analysis (TGA) is an experimental technique that measures the mass of a sample over time with changing temperature under a controlled environment. The atmosphere used during the experiment can be reactive, oxidizing, or inert, depending on applications.[31] As the temperature increases, mass losses occur when the sample interacts with the surrounding atmosphere. Water loss and chemical reactions that occur (e.g., combustion) result in a loss in mass while physical changes (e.g., melting) have no effect on mass.[31]

In **Chapter 5**, the final bulk metal loadings of carbon-supported catalysts were determined by using thermogravimetric analysis on a Shimadzu TGA-50H in a quartz pan. The quartz pan was first placed into the instrument after cleaning for calibration before loading 40 – 60 mg of catalyst samples. The materials were first pretreated under He at 100 °C for 30 min to remove surface contaminants and adsorbed water mass. Samples were heated to 700 °C at 10°C/min in air to oxidize the Vulcan carbon support and ensure no mass change with increased temperature.[32,33] The

final metal loading weight % was determined by dividing the final mass by the initial mass after pretreatment.

2.3.9 Double-layer Capacitance Surface Areas

Double-layer capacitance uses the capacitance of the electrochemical double layer to estimate the surface area of the electrode in contact with the electrolyte. The capacitance is typically measured by plotting cyclic voltammograms as a function of scan rate in a non-Faradaic region or using electrochemical impedance spectroscopy. Although this technique is relatively easy to incorporate into experimental protocol, it becomes harder to deconvolute for catalysts that are synthesized on supports due to the inability to distinguish between the capacitance of the support and of the catalyst itself. Additionally, the technique requires specific capacitance values to calculate electrochemically active surface area (ECSA), which might not be available in literature and varies with the electrolyte and material.[34]

In **Chapter 4** and **5**, the double-layer capacitance technique was used to measure the surface area of treated and untreated carbon felts. The felts were submerged in 0.5 M H_2SO_4 (Sigma-Aldrich, 98%) solution and cyclic voltammetry (CV) measurements were conducted at scan rates that ranged from 10 to 100 $mV \cdot s^{-1}$. The non-Faradaic currents were plotted against the scan rates to extract the double layer capacitance, which was used to calculate the surface area assuming the specific capacitance of carbon felts to be 40 $\mu F \cdot cm^{-2}$.[35]

2.3.10 Coulometric Techniques

There are different coulometric techniques that have been incorporated to probe the ECSA for electrocatalytic reactions. These techniques electrochemically or chemically deposit a monolayer of a certain species onto the catalyst surface and then quantify the charge associated with stripping the deposited monolayer to determine the ECSA. Unlike double layer capacitance

(**Section 2.3.9**), these techniques can deconvolute between surface sites such as metals and supports (e.g., carbon), and thus have significant advantages for supported catalysts. Hydrogen underpotential deposition (H_{upd}) has been used predominantly for counting surface sites on certain platinum group metals to obtain normalized activity.[36] CO stripping and copper underpotential deposition (Cu_{upd}) techniques have also been used to detect active surface site of metals and alloys where H_{upd} might be less accurate. For example, the current densities used to evaluate a series of PtRh and PtIr catalysts were normalized to areas measured from CO stripping,[37] while the area from Cu_{upd} was used to evaluate and compare activities for different compositions of PtRu alloys.[38]

In both **Chapter 4** and **5**, various coulometric techniques were used to obtain the electrochemically active surface area (ECSA) for rate normalization. After compensating for 85% of the solution resistance using electrochemical impedance spectroscopy (EIS), H_{upd} in the hydrogen desorption region was used as one method to determine the ECSA of the Pt_xRu_y/C alloys. The average charge density of Pt (210 $\mu C \cdot cm^{-2}$) was employed to calculate the ECSA. A slanted baseline, representing the double-layer charging current, was taken by subtracting half of the double-layer charging current measured at 0.35 V vs. RHE.[39] All Cu_{upd} experiments were conducted in 0.1 M H_2SO_4 for an initial H_{upd} baseline before adding 2 mM $CuSO_4$ into the solution. The electrodes were polarized at 1.0 V vs. RHE for 2 min to ensure no Cu ions adsorbed to the surface of the electrode. Deposition potentials from 0.28–0.48 V vs. RHE were applied for 100 s to deposit a monolayer of Cu^{2+} on the surface of the catalyst. After, a linear voltammetric scan was performed at 100 $mV \cdot s^{-1}$ from the applied potential to 1.0 V vs. RHE, in which all the underpotential-deposited copper has been oxidized. Charges obtained from the copper stripping were corrected by subtracting the double-layer charge obtained in the absence of cupric ions in the solution.

2.4 Performance Evaluations

One of the biggest challenges in working with the nitrogen-based species is the ability to quantify intermediates and products to elucidate the reaction mechanism and activity trends. This section provides an overview of all the methods used in this dissertation to quantify gas-phase and liquid-phase intermediates and products for ammonia synthesis and nitrate reduction reactions.

2.4.1 Chromatography

Chromatography is a technique used to separate, identify, and purify components of a mixture for qualitative or quantitative analysis. These techniques operate with a mobile and stationary phase that interact with each other. The mobile phase typically consists of an inert carrier gas or liquid with the sample while the stationary phase is always composed of a solid or a layer of liquid adsorbed on the surface of a solid support. As the mobile phase moves through the stationary phase, different affinities and interaction between the two phases cause different species to move through the medium at different velocities. Based on a molecule's partition coefficient, there are different retention times upon interaction with the stationary phase, and thus affecting overall separation.[40] Depending on the column, overlaps in signal for different reactants and products can make deconvolution and quantification of specific species difficult. Careful selection of column, carrier eluent, split ratio, injection dilutions and volume, and other operating parameters can improve signal identification and deconvolution.[41]

2.4.1.1 *Gas Chromatography*

Gas chromatography (GC) is primarily used to identify and quantify molecules in gaseous form. This technique contain samples in the mobile phase that interact with columns in the stationary phase. After separation from the columns, the quantity of molecules is measured via two major types of detectors in GC instruments: thermal conductivity detector (TCD) or flame

ionization detector (FID). The detector outputs the signal via specialized software to spectral peaks that are integrated for accurate product quantification. The FID is a destructive, mass-sensitive detector which operates by measuring ions formed during the combustion of organic compounds and a flame produced from hydrogen and air.[42] This system is ideal to analyze hydrocarbon compounds, and is not utilized in this work with nitrogen-based molecules. The TCD is a non-destructive universal detector that can measure mostly all compounds. This technology uses a Wheatstone bridge circuit to detect changes in the thermal conductivity in comparison to a reference gas.[43]

For part of the work in **Chapter 3**, a natural gas analyzer GC (SRI Instruments; 8610-3070) with an Rtx-Volatile Amine column (Restek; 18076) was used to optimize separation for nitrogen-based species. A TCD with He carrier gas was used to measure and quantify nitrogen and ammonia. Prior to experiments, the GC was calibrated by using standard gas mixtures (Cal Gas Direct Inc.) that created a linear calibration curve between the ammonia concentrations and integrated peak areas.

2.4.1.2 *Ion Chromatography*

Ion chromatography (IC) can be used to quantify a variety of liquid-phase ions in solution (e.g., NO_3^-, NO_2^-, NH_4^+, and NH_3OH^+).[41,44–46] Small volumes of sample are passed through a column containing a stationary phased charged opposite to the measured species. For example, anion columns are used for positively charged ions such as NH_4^+ and cation columns are used for negatively charged ions such as NO_3^-. Once separated, either the conductivity or UV-Vis absorbance of the effluent is used for detection and quantification.[41]

In **Chapter 4**, an ion chromatography (Agilent), equipped with AS9-HC column (Dionex) with 9 mM sodium carbonate eluent was used to quantify the amount of nitrate and nitrite in the

electrolyte solution. For anion measurements, sodium nitrate (Sigma Aldrich, 99.0%) and sodium nitrite (Sigma Aldrich, 99.999% trace metal basis) were used to prepare the standard solutions for the calibration curve. To prevent oversaturating the system with anions, 0.1 mL of the electrolyte solution was extracted every hour and diluted by a factor of ten with Millipore water to measure the change in nitrate concentration. Separately, 0.5 mL of the electrolyte solution was extracted and neutralized with 0.1 M NaOH (Sigma Aldrich, 99.99%) to inhibit the decomposition of nitrite in acidic media.[47] However, the measured values of the nitrite concentration may be lower than the actual values due to the decomposition of nitrite during the extraction of the reactor aliquots. Both nitrate and nitrite were calibrated before measurements with known concentrations of $NaNO_3$ and $NaNO_2$ in solution.

2.4.2 Mass Spectrometry

Mass spectrometry (MS) is an analytical tool used to measure the mass-to-charge ratio (m/z) of sample molecules. Typically, MS is used to identify, quantify, and determine structure and chemical properties of samples via molecular weight. There are three major components in every MS equipment: (1) ionization source, (2) mass analyzer, and (3) ion detection system.[48] The ionization source (e.g., electron or chemical ionization, electrospray source) is first used to convert sample molecules to gas-phase ions. Once ionized, a mass analyzer (most commonly quadrupoles and ion traps) is used to separate the ions by m/z ratios. The separated ions are then measured in an ion detection system where the m/z ratios are reported along with their relative abundance. The final MS spectrum consists of the m/z ratios of the ions present in the sample plotted against their relative intensities

To extract quantitative information about product yields for multiple products in a sample, it is important to account for differences in ionization efficiencies, mass spectrometer gain, mass

fraction transmission, and the cracking of the parent molecule when deconvoluting overlapping fragmentation patterns.[49] The ionization efficiency (*I*) is primarily dependent on the number of electrons per molecule and can be calculated in **Equation 2.3**:

$$I = 0.6\frac{number\ of\ electrons}{14} + 0.4 \tag{2.3}$$

The gain of the electron multiplier (G_m) is a function of the ion mass and can be approximated in **Equation 2.4**:

$$G_m = (\frac{28}{MW})^{0.5} \tag{2.4}$$

where *MW* is the molecular weight of the species of interest. The transmission (T_m) of an electron through the quadrupole filter is also dependent on the ion mass as shown in **Equation 2.5**:

$$T_m = \begin{cases} 10^{(30-MW)/155} & MW > 30 \\ 1 & MW < 30 \end{cases} \tag{2.5}$$

The correlation factor (*C*) for a product spectrum is the summation over all mass fragments for the product species (**Equation 2.6**):

$$C = \frac{1}{F_m}\frac{1}{I}\sum_{fragments}\frac{F_m}{G_m \times T_m} \tag{2.6}$$

In **Chapter 3**, the catalyst performance was evaluated using a Micromeritics Autochem 2920 equipped with a thermal conductivity detector and a Pfeiffer Vacuum Quadstar GSD-301 mass spectrometer. ~100 mg of the catalyst was loaded into a U-shape quartz tube reactor, supported on a bed of quartz wool. The carbide-based materials were pretreated with 15% CH_4/H_2 gas mixture at 590 °C while the nitrides were pretreated with 25% N_2/H_2 mixture for at 600 °C.[50,51] Then, the system was purged with He at a temperature 10 °C higher than the pretreatment

temperature for 2 hrs. The material was exposed to a stoichiometric balance of 25% N_2 and 75% H_2 at different temperatures for kinetic data. Each temperature was held for 2 hrs with 15 min ramp in between. Measured ammonia concentrations from the mass spectrometer were deconvoluted, and the rates for each temperature was determined by averaging the last 30 min.

2.4.3 Ultraviolet-Visible Spectroscopy

Ultraviolet-visible (UV-Vis) spectroscopy is used to obtain the electromagnetic absorbance spectra, which excites electrons from the ground to the excited state of a compound in solution. Planck's equation shows that the less energy needed to excite the electrons, the longer the wavelength of the absorption band.[52] Thus, the absorption bands will provide insights on the molecular structure of the sample and will shift in wavelength and intensity depending on the interactions with environmental conditions. The principle behind absorbance spectroscopy resides in the Beer-Lambert Law, which measures the transmittance or amount of light transmitted through a sample (**Equation 2.7**):

$$A = \varepsilon cL = \log_{10}(\frac{I_0}{I}) \tag{2.7}$$

where A is the measured absorbance, I_0 is the intensity of the incident light at a given wavelength, I is the transmitted intensity, L is the path length through the sample, c is the concentration of the absorbing species, and ε is the extinction coefficient. For practical implications, this law states that the concentration of species is proportional to the absorbance, and is limited to concentrations below 10 mM.[53]

For the work in **Chapters 4** and **5**, nitrate and select liquid-phase products (i.e., NO_2 and NH_3) were measured using UV-Vis spectrometry (Thermo Fischer, Evolution 350). NO_3 was quantified using standard spectrometry techniques after dilution. 10 μL from the sample aliquot

was acquired and diluted to 2 mL using Millipore water. After, 1 mL of the resulting, well-mixed solution was further diluted to 3 mL in a quartz cuvette (Fisher Scientific, Azzota Corp 10 mm). UV-Vis measurements were taken between 190 – 300 nm, and the nitrate concentrations were calculated via the adsorption peak at 220 nm.[54] Millipore water was used as the background and subtracted from the sample spectra, and a calibration curve was created using known concentrations of $NaNO_3$ (Sigma Aldrich) in solution.

Nitrite was quantified via a modified Griess diazotization reaction.[54,55] 0.3 mL of the extracted sample aliquot was diluted to 1 mL and neutralized with 1 M NaOH. 40 μL of the Griess color reagent, which consisted of 2% sulfanilamide (Fischer Scientific, ≥98%) and 0.2% N-(1-napthyl)-ethylenediamine (Sigma Aldrich, ≥98%) in phosphoric acid (Acros Organics; 85%) diluted to 0.1 M, was added. A fresh electrolyte baseline solution was prepared with the same method and used as the background that was subtracted from the sample spectra. The resulting solution was left in the dark for 30 min before measuring absorbances at 543 nm.[52] Known concentration of calibration standards were made from $NaNO_2$ (Sigma Aldrich).

Ammonia was quantified by using the indophenol blue test,[56,57] where ammonia and hypochlorite react to form indophenol with a UV-Vis peak between 600 – 700 nm. 1 mL of the sample aliquot is extracted from the reactor. 1 M NaOH (Sigma Aldrich, 99.99%) was added to the solution sample to neutralize the acid to a pH of 12. After, 122 μL of sodium salicylate (Sigma Aldrich, >99.5%), 27.3 μL of sodium nitroprusside dihydrate (Sigma Aldrich, >99%), and 40 μL of sodium hypochlorite solution (Sigma Aldrich, 4.00 – 4.99%) were sequentially added to the electrolyte solution and manually stirred together. The solution was covered and left for 40 min. The indophenol peak was identified as the maximum absorbance between 600 – 700 nm. Similar to nitrite spectral measurements, a background was created with fresh electrolyte solution and

subtracted from the sample spectra. If the concentration of NH_3 was too high and oversaturated the detector, the solution was diluted and retested. A calibration curve was created using known concentrations of NH_4Cl (Sigma Aldrich) and unknown NH_3 concentrations were calculated using the Beer-Lambert law.

2.5 References

(1) Wise, R. S.; Markel, E. J. Catalytic NH3 Decomposition by Topotactic Molybdenum Oxides and Nitrides: Effect on Temperature Programmed γ-Mo2N Synthesis. *Journal of Catalysis* **1994**, *145* (2), 335–343. https://doi.org/10.1006/jcat.1994.1042.

(2) Claridge, J. B.; York, A. P. E.; Brungs, A. J.; Green, M. L. H. Study of the Temperature-Programmed Reaction Synthesis of Early Transition Metal Carbide and Nitride Catalyst Materials from Oxide Precursors. *Chem. Mater.* **2000**, *12* (1), 132–142. https://doi.org/10.1021/cm9911060.

(3) Pande, P.; Rasmussen, P. G.; Thompson, L. T. Charge Storage on Nanostructured Early Transition Metal Nitrides and Carbides. *Journal of Power Sources* **2012**, *207*, 212–215. https://doi.org/10.1016/j.jpowsour.2012.01.028.

(4) Jong, K. P. de. *Synthesis of Solid Catalysts*, 1st ed.; John Wiley & Sons, Ltd, 2009. https://doi.org/10.1002/9783527626854.

(5) Barrett, E. P.; Joyner, L. G.; Halenda, P. P. The Determination of Pore Volume and Area Distributions in Porous Substances. I. Computations from Nitrogen Isotherms. *J. Am. Chem. Soc.* **1951**, *73* (1), 373–380. https://doi.org/10.1021/ja01145a126.

(6) Horváth, G.; Kawazoe, K. Method for the Calculation of Effective Pore Size Distribution in Molecular Sieve Carbon. *Journal of Chemical Engineering of Japan* **1983**, *16* (6), 470–475. https://doi.org/10.1252/jcej.16.470.

(7) Martínez-Abad, A. 13 - Silver-Based Antimicrobial Polymers for Food Packaging. In *Multifunctional and Nanoreinforced Polymers for Food Packaging*; Lagarón, J.-M., Ed.; Woodhead Publishing, 2011; pp 347–367. https://doi.org/10.1533/9780857092786.3.347.

(8) Deivaraj, T. C.; Lee, J. Y. Preparation of Carbon-Supported PtRu Nanoparticles for Direct Methanol Fuel Cell Applications – a Comparative Study. *Journal of Power Sources* **2005**, *142* (1–2), 43–49. https://doi.org/10.1016/j.jpowsour.2004.10.010.

(9) Masud, J.; Nguyen, T. V.; Singh, N.; McFarland, E.; Ikenberry, M.; Hohn, K.; Pan, C.-J.; Hwang, B.-J. A RhxSy/C Catalyst for the Hydrogen Oxidation and Hydrogen Evolution Reactions in HBr. *J. Electrochem. Soc.* **2015**, *162* (4), F455. https://doi.org/10.1149/2.0901504jes.

(10) Wang, Z.; Young, S. D.; Goldsmith, B. R.; Singh, N. Increasing Electrocatalytic Nitrate Reduction Activity by Controlling Adsorption through PtRu Alloying. *Journal of Catalysis* **2021**. https://doi.org/10.1016/j.jcat.2020.12.031.

(11) Huong Le, T. X.; Bechelany, M.; Cretin, M. Carbon Felt Based-Electrodes for Energy and Environmental Applications: A Review. *Carbon* **2017**, *122*, 564–591. https://doi.org/10.1016/j.carbon.2017.06.078.

(12) Lee, M. *X-Ray Diffraction for Materials Research : From Fundamentals to Applications*; Apple Academic Press, 2017. https://doi.org/10.1201/b19936.

(13) Kim, S. H.; Lee, C. M.; Kafle, K. Characterization of Crystalline Cellulose in Biomass: Basic Principles, Applications, and Limitations of XRD, NMR, IR, Raman, and SFG. *Korean J. Chem. Eng.* **2013**, *30* (12), 2127–2141. https://doi.org/10.1007/s11814-013-0162-0.

(14) Baer, D. R.; Thevuthasan, S. Chapter 16 - Characterization of Thin Films and Coatings. In *Handbook of Deposition Technologies for Films and Coatings (Third Edition)*; Martin, P. M., Ed.; William Andrew Publishing: Boston, 2010; pp 749–864. https://doi.org/10.1016/B978-0-8155-2031-3.00016-8.

(15) Végh, J. The Analytical Form of the Shirley-Type Background. *Journal of Electron Spectroscopy and Related Phenomena* **1988**, *46* (2), 411–417. https://doi.org/10.1016/0368-2048(88)85038-2.
(16) Newville, M. Fundamentals of XAFS. *Reviews in Mineralogy and Geochemistry* **2014**, *78* (1), 33–74. https://doi.org/10.2138/rmg.2014.78.2.
(17) Newville, M. Fundamentals of XAFS. University of Chicago July 22, 2004.
(18) Ravel, B.; Newville, M. ATHENA, ARTEMIS, HEPHAESTUS: Data Analysis for X-Ray Absorption Spectroscopy Using IFEFFIT. *Journal of Synchrotron Radiation* **2005**, *12* (4), 537–541. https://doi.org/10.1107/S0909049505012719.
(19) J. Rehr, J.; J. Kas, J.; D. Vila, F.; P. Prange, M.; Jorissen, K. Parameter-Free Calculations of X-Ray Spectra with FEFF9. *Physical Chemistry Chemical Physics* **2010**, *12* (21), 5503–5513. https://doi.org/10.1039/B926434E.
(20) Rehr, J. J.; Soininen, J. A.; Shirley, E. L. Final-State Rule vs the Bethe-Salpeter Equation for Deep-Core x-Ray Absorption Spectra. *Phys. Scr.* **2005**, *2005* (T115), 207. https://doi.org/10.1238/Physica.Topical.115a00207.
(21) Mathew, K.; Zheng, C.; Winston, D.; Chen, C.; Dozier, A.; Rehr, J. J.; Ong, S. P.; Persson, K. A. High-Throughput Computational X-Ray Absorption Spectroscopy. *Scientific Data* **2018**, *5* (1), 1–8. https://doi.org/10.1038/sdata.2018.151.
(22) Newville, M. IFEFFIT : Interactive XAFS Analysis and FEFF Fitting. *Journal of Synchrotron Radiation* **2001**, *8* (2), 322–324. https://doi.org/10.1107/S0909049500016964.
(23) Brunauer, S.; Emmett, P. H.; Teller, E. Adsorption of Gases in Multimolecular Layers. *J. Am. Chem. Soc.* **1938**, *60* (2), 309–319. https://doi.org/10.1021/ja01269a023.
(24) Goldstein, J. I.; Newbury, D. E.; Michael, J. R.; Ritchie, N. W. M.; Scott, J. H. J.; Joy, D. C. *Scanning Electron Microscopy and X-Ray Microanalysis*; Springer New York: New York, NY, 2018. https://doi.org/10.1007/978-1-4939-6676-9.
(25) Reimer, L. *Scanning Electron Microscopy*; Hawkes, P. W., Lotsch, H. K. V., Series Eds.; Springer Series in Optical Sciences; Springer Berlin Heidelberg: Berlin, Heidelberg, 1998; Vol. 45. https://doi.org/10.1007/978-3-540-38967-5.
(26) Reimer, L. *Transmission Electron Microscopy: Physics of Image Formation and Microanalysis*; Springer, 2013.
(27) Zuo, J. M.; Spence, J. C. H. *Advanced Transmission Electron Microscopy*; Springer New York: New York, NY, 2017. https://doi.org/10.1007/978-1-4939-6607-3.
(28) Manard, B. T.; Metzger, S. C.; Quarles, C. D.; Rogers, K. T.; Ticknor, B. W.; Bostick, D. A.; McBay, E. H.; Hexel, C. R. Evaluation and Specifications for In-Line Uranium Separations Using Inductively Coupled Plasma Optical Emission Spectroscopy (ICP-OES) Detection for Trace Elemental Analysis. *Appl Spectrosc* **2019**, *73* (8), 927–935. https://doi.org/10.1177/0003702819837650.
(29) Balaram, V. Microwave Plasma Atomic Emission Spectrometry (MP-AES) and Its Applications – A Critical Review. *Microchemical Journal* **2020**, *159*, 105483. https://doi.org/10.1016/j.microc.2020.105483.
(30) Poirier, L.; Nelson, J.; Leong, D.; Berhane, L.; Hajdu, P.; Lopez-Linares, F. Application of ICP-MS and ICP-OES on the Determination of Nickel, Vanadium, Iron, and Calcium in Petroleum Crude Oils via Direct Dilution. *Energy Fuels* **2016**, *30* (5), 3783–3790. https://doi.org/10.1021/acs.energyfuels.5b02997.

(31) Bottom, R. Thermogravimetric Analysis. In *Principles and Applications of Thermal Analysis*; John Wiley & Sons, Ltd, 2008; pp 87–118. https://doi.org/10.1002/9780470697702.ch3.
(32) Baturina, O. A.; Aubuchon, S. R.; Wynne, K. J. Thermal Stability in Air of Pt/C Catalysts and PEM Fuel Cell Catalyst Layers. *Chem. Mater.* **2006**, *18* (6), 1498–1504. https://doi.org/10.1021/cm052660e.
(33) Pinchuk, O. A.; Aubuchon, S. R.; Marks, C.; Dominey, R.; Dundar, F.; Deniz, O. F.; Ata, A.; Wynne, K. J. Thermally Pretreated 46% Pt/Vulcan XC72: Characterisation by TGA/DSC/TEM and Cyclic Voltammetry. *Fuel Cells* **2009**, *9* (5), 554–561. https://doi.org/10.1002/fuce.200800183.
(34) McCrory, C. C. L.; Jung, S.; Ferrer, I. M.; Chatman, S. M.; Peters, J. C.; Jaramillo, T. F. Benchmarking Hydrogen Evolving Reaction and Oxygen Evolving Reaction Electrocatalysts for Solar Water Splitting Devices. *J. Am. Chem. Soc.* **2015**, *137* (13), 4347–4357. https://doi.org/10.1021/ja510442p.
(35) Wang, G.; Wang, H.; Lu, X.; Ling, Y.; Yu, M.; Zhai, T.; Tong, Y.; Li, Y. Solid-State Supercapacitor Based on Activated Carbon Cloths Exhibits Excellent Rate Capability. *Advanced Materials* **2014**, *26* (17), 2676–2682. https://doi.org/10.1002/adma.201304756.
(36) Liu, J.-X.; Richards, D.; Singh, N.; Goldsmith, B. R. Activity and Selectivity Trends in Electrocatalytic Nitrate Reduction on Transition Metals. *ACS Catalysis* **2019**, *9*, 7052–7064. https://doi.org/10.1021/acscatal.9b02179.
(37) Duca, M.; Sacré, N.; Wang, A.; Garbarino, S.; Guay, D. Enhanced Electrocatalytic Nitrate Reduction by Preferentially-Oriented (100) PtRh and PtIr Alloys: The Hidden Treasures of the 'Miscibility Gap.' *Applied Catalysis B: Environmental* **2018**, *221* (August 2017), 86–96. https://doi.org/10.1016/j.apcatb.2017.08.081.
(38) Wang, Z.; Young, S. D.; Goldsmith, B. R.; Singh, N. Increasing Electrocatalytic Nitrate Reduction Activity by Controlling Adsorption through PtRu Alloying. *Submitted* **2020**.
(39) Moniri, S.; Van Cleve, T.; Linic, S. Pitfalls and Best Practices in Measurements of the Electrochemical Surface Area of Platinum-Based Nanostructured Electro-Catalysts. *Journal of Catalysis* **2017**, *345*, 1–10. https://doi.org/10.1016/j.jcat.2016.11.018.
(40) Coskun, O. Separation Techniques: Chromatography. *North Clin Istanb* **2016**, *3* (2), 156–160. https://doi.org/10.14744/nci.2016.32757.
(41) Michalski, R.; Kurzyca, I. Determination of Nitrogen Species (Nitrate , Nitrite and Ammonia Ions) in Environmental Samples by Ion Chromatography. *Polish Journal of Environmental Studies* **2006**, *15*, 5–18.
(42) Skoog, D. A.; Holler, F. J.; Crouch, S. R. *Principles of Instrumental Analysis*; Cengage Learning, 2017.
(43) Uyanik, A. Anaesthetic Mixtures: Gas Chromotography. In *Encyclopedia of Separation Science*; Wilson, I. D., Ed.; Academic Press: Oxford, 2000; pp 2047–2053. https://doi.org/10.1016/B0-12-226770-2/02501-1.
(44) Yang, J.; Kwon, Y.; Duca, M.; Koper, M. T. M. Combining Voltammetry and Ion Chromatography: Application to the Selective Reduction of Nitrate on Pt and PtSn Electrodes. *Analytical Chemistry* **2013**, *85* (16), 7645–7649. https://doi.org/10.1021/ac401571w.
(45) Rice, E. W.; Baird, R. B.; Eaton, A. D. *Standard Methods for the Examination of Water and Wastewater*; 2017.

(46) Gao, W.; Gao, L.; Li, D.; Huang, K.; Cui, L.; Meng, J.; Liang, J. Removal of Nitrate from Water by the Electrocatalytic Denitrification on the Cu-Bi Electrode. *Journal of Electroanalytical Chemistry* **2018**, *817* (August 2017), 202–209. https://doi.org/10.1016/j.jelechem.2018.04.006.

(47) Yang, J.; Kwon, Y.; Duca, M.; Koper, M. T. M. Combining Voltammetry and Ion Chromatography: Application to the Selective Reduction of Nitrate on Pt and PtSn Electrodes. *Analytical Chemistry* **2013**, *85* (16), 7645–7649. https://doi.org/10.1021/ac401571w.

(48) Hoffmann, E. de. Mass Spectrometry. In *Kirk-Othmer Encyclopedia of Chemical Technology*; American Cancer Society, 2005. https://doi.org/10.1002/0471238961.1301191913151518.a01.pub2.

(49) Ko, E. I.; Benziger, J. B.; Madix, R. J. Reactions of Methanol on W(100) and W(100)-(5 × 1)C Surfaces. *Journal of Catalysis* **1980**, *62* (2), 264–274. https://doi.org/10.1016/0021-9517(80)90454-6.

(50) Schaidle, J. A.; Schweitzer, N. M.; Ajenifujah, O. T.; Thompson, L. T. On the Preparation of Molybdenum Carbide-Supported Metal Catalysts. *Journal of Catalysis* **2012**, *289*, 210–217. https://doi.org/10.1016/j.jcat.2012.02.012.

(51) Kojima, R.; Aika, K. I. Molybdenum Nitride and Carbide Catalysts for Ammonia Synthesis. *Applied Catalysis A: General* **2001**, *219* (1–2), 141–147. https://doi.org/10.1016/S0926-860X(01)00676-7.

(52) Perkampus, H.-H. *UV-VIS Spectroscopy and Its Applications*; Springer Berlin Heidelberg: Berlin, Heidelberg, 1992. https://doi.org/10.1007/978-3-642-77477-5.

(53) Skoog, D. A.; West, D. M.; Holler, F. J.; Crouch, S. R. *Fundamentals of Analytical Chemistry*; Cengage Learning, 2013.

(54) Singh, P.; Singh, M. K.; Beg, Y. R.; Nishad, G. R. A Review on Spectroscopic Methods for Determination of Nitrite and Nitrate in Environmental Samples. *Talanta* **2019**, *191* (August 2018), 364–381. https://doi.org/10.1016/j.talanta.2018.08.028.

(55) Kurniawati, P.; Gusrianti, R.; Dwisiwi, B. B.; Purbaningtias, T. E.; Wiyantoko, B. Verification of Spectrophotometric Method for Nitrate Analysis in Water Samples. *AIP Conference Proceedings* **2017**, *1911*, 020012. https://doi.org/10.1063/1.5016005.

(56) McEnaney, J. M.; Blair, S. J.; Nielander, A. C.; Schwalbe, J. A.; Koshy, D. M.; Cargnello, M.; Jaramillo, T. F. Electrolyte Engineering for Efficient Electrochemical Nitrate Reduction to Ammonia on a Titanium Electrode. *ACS Sustainable Chem. Eng.* **2020**, *8* (7), 2672–2681. https://doi.org/10.1021/acssuschemeng.9b05983.

(57) Zhu, D.; Zhang, L.; Ruther, R. E.; Hamers, R. J. Photo-Illuminated Diamond as a Solid-State Source of Solvated Electrons in Water for Nitrogen Reduction. *Nature Materials* **2013**, *12* (9), 836–841. https://doi.org/10.1038/nmat3696.

Chapter 3

Supported Mo_2C and Mo_2N for Ammonia Synthesis

3.1 Introduction

In this chapter, we will explore improving upon the Haber-Bosch process by using metal supported Mo_2C and Mo_2N for ambient-pressure ammonia synthesis. As previously discussed in **Chapter 1**, the Haber-Bosch process is a revolutionary catalytic reaction to produce ammonia that supports the global agricultural industry, as well as multiple industrial and household chemicals. However, the high energy consumption and CO_2 emissions of the Haber-Bosch process are unsustainable. Although most CO_2 emissions result from methane-fed production of the reactant H_2,[1,2] a majority of energy consumption is driven by compressors needed to reach the necessary high reaction pressures (150 – 300 bar).[3] Despite significant scientific advancements in the thermochemical process for ammonia production, alternative catalysts and reaction pathways to enhance the synthesis of NH_3 at lower temperatures and pressures are still desired. These developments would be able to reduce the amount of energy consumed and make this process more environmentally sustainable. In this research, we study a variety of metal carbide and nitride supported catalysts that can catalyze ammonia production under ambient conditions.

Previous investigations showed that Mo_2C and Mo_2N are active for a multitude of hydrogenation reactions including Fischer-Tropsch synthesis,[4,5] methanol steam reforming,[6,7]

water-gas shift,[8,9] and hydrogen oxidation reactions.[10] Importantly, these materials have also been active for ammonia synthesis at ambient pressure.[11,12] By adding promoter metals, the ammonia activities are enhanced, with Co_3Mo_3N displaying the highest activity among the bimetallic materials investigated.[13–15] Depositing cesium (Cs) or potassium (K) on Co_3Mo_3N increases the activity by almost two-fold. More recent works have focused on exploring the structural properties of catalyst under reaction conditions that utilize N-sites from nitrides to catalyze NH_3 via the Mars-van Krevelen mechanism.[16]

Despite confirming the high ammonia synthesis activity of α-MoC_{1-x}, β-Mo_2C, and the bimetallic Co_3Mo_3N at ambient pressure, there is still a gap in literature for exploring metal supported carbide and nitride for ammonia synthesis.[11,14] Most prior work has focused on altering the bulk structure of the material to optimize the catalyst performance, but there is limited experimental work that fine-tunes the bifunctional properties of the metal and the support. Supports are known to facilitate dispersion of the active phase and alter the electronic structure of the catalyst.[9,17] Previous experiments conducted for water gas shift reactions attributed the high activity of Pt/Mo_2C to the interaction at the interface between Pt and the Mo_2C support, where Pt sites effectively adsorb CO while the support and metal-support interface decompose H_2O to provide O_2.[18] However, the enhanced activity may be attributed to the synergistic effects by the strong metal-support interactions, which induces surface electronic perturbations and create special sites at the perimeter of the metal particles.[19,20] It is important to deconvolute these two effects and determine structure-function relationships of catalysts for NH_3 synthesis, where the metal and support can have different functional sites and interaction effects.

In this research, the metal will be directly deposited on the unpassivated Mo_2C which allows for stronger interaction between the metal and the supporting carbide or nitride and

improved dispersion of the metal.[17] We hypothesize that the bifunctional properties of the catalysts will enhance NH_3 synthesis activities at less energy-intensive reaction conditions. The metal domains will activate N_2 bond dissociation while the support sites will be favorable for nitrogen hydrogenation. The synergy between the metal and support will allow supported metal Mo_2C and Mo_2N catalysts to be highly active for low-temperature and low-pressure ammonia synthesis.

The primary objectives of the research described here are: (1) synthesize and characterize a series of metal support Mo_2C and Mo_2N, (2) test and identify catalyst designs that lead to high NH_3 synthesis activity at reduced temperatures and pressures. These results provide a fundamental understanding of the catalytic activity of transition metal carbides and nitride supported catalysts and how the properties can be fine-tuned to optimize NH_3 synthesis at ambient conditions.

3.2 Experimental Methods

3.2.1 Catalyst Synthesis

A mixed-phase molybdenum carbide (α,β-Mo_2C) and molybdenum nitride (γ-Mo_2N) were synthesized via a temperature-programmed reaction.[8,9,21] Ammonium paramolybdate (AM) precursor was first crushed and sieved to particle size between 125 – 250 μm before loaded into a quartz flow-reactor supported by a bed of quartz wool, and secured in a heated furnace. Depending on the desired support, different temperatures, ramp rates, soak times, and gas compositions were used to synthesize the catalyst (**Chapter 2**). Upon completion of the reaction, the reactor was removed from the furnace and quenched to room temperature before passivating with 1% O_2/He for at least 5 hours to prevent bulk oxidation upon contact with air.

To synthesize metal supported Mo_2C and Mo_2N, unpassivated catalysts are transferred into a water-tolerant, oxygen-free glove box. Incipient-wetness impregnation was primarily used to deposit Fe, Ru, and Co onto the surface of active Mo_2C and Mo_2N supports. Fe, Ru, and Co were

selected for metal deposition on the carbide and nitride supports due to their high activity levels for NH_3 production.[3,16,22,23] A solution of the metal precursor ($Fe(NO_3)_3$ (14% Fe; Sigma Alrich), $RuCl_3$ (38% Ru; Sigma Alrich), $Co(NO_3)_2$ (20% Co; Sigma Alrich)) dissolved in de-aerated Millipore water was added in dropwise increments onto the active powder and was stirred extensively between each addition. The nominal surface coverages of metals were 0.5 monolayers based on 10^{19} site/m^2. Following the incipient wetness impregnation process, the excess water was removed by drying at ~100 °C in the glove box. Following the deposition, the dried material was then transferred placed back into the quartz tube reactor, reduced in H_2 at 110 °C for 2 hrs, and passivated in 1% O_2/He at room temperature.

3.2.2 Material Characterization

The crystalline phases were determined by X-ray diffraction (XRD) using a Rigaku Miniflex equipped with a Cu Kα (λ = 0.15404) radiation source (40 kV, 15 mA) and a Ni filter. The catalyst samples were crushed and loaded on a zero-background sample holder. All scans were conducted from $10° < 2\theta < 90°$ at a rate of 5°/min with 0.02° step size and collected XRD spectra were analyzed using the JADE software.

The catalyst surface areas and porosity were measured by N_2-physisorption isotherm and Brunauer-Emmett-Teller (BET) method a using Micromeritics ASAP 2020 Analyzer. Approximately 100 mg of catalyst was degassed at 350 °C for 5 hrs under vaccine (<5 mm Hg) before analysis via exposure to different N_2 partial pressures relative to the saturation pressure.

Bulk metal weight loading was determined using Inductively Coupled Plasma-Optical Emission Spectroscopy (ICP-EOS) with a Varian 710-ES. For each sample, ~15 mg of catalyst was dissolved in 3 mL of aqua regia (3:1 $HCl:HNO_3$) for at least 24 hrs. 1 mL of the solution was

diluted with 13 mL of Millipore water before analysis. Resulting concentrations were compared to diluted ICP standards of 5% metal (e.g., Mo, Fe, Ru, and Co) in HCl.

3.2.3 Activity Measurements

The catalyst performance was evaluated using a Micromeritics Autochem 2920 equipped with a thermal conductivity detector and a Pfeiffer Vacuum Quadstar GSD-301 mass spectrometer. ~100 mg of the catalyst was loaded into a U-shape quartz tube reactor, supported on a bed of quartz wool. The carbide-based materials were pretreated with 15% CH_4/H_2 gas mixture at 590 °C while the nitrides were pretreated with 25% N_2/H_2 mixture at 600 °C.[8,11] Then, the system was purged with He at 10 °C higher than the pretreatment temperature for 2 hrs. The material was exposed to a stoichiometric balance of 25% N_2 and 75% H_2 at different temperatures for kinetic data. Each temperature was held for 2 hrs with a 15 min ramp in between. Measured ammonia concentrations from the mass spectrometer were deconvoluted and rates for each temperature was determined by averaging the last 30 min.

3.3 Results and Discussion

3.3.1 Synthesis and Bulk Characterization

X-ray diffraction patterns for the synthesized material are consistent with α,β-Mo_2C and γ-Mo_2N (**Figure 3.1**).[24] No peaks were observed for oxide phases, indicating complete bulk nitridation and carburization of the oxide precursor and that the amount of oxygen on the surface layer from passivation was below XRD detection limits. Diffraction patterns for the catalysts with metals deposited on the carbide and nitride supports were also obtained. However, due to the high metal dispersion from synthesis, the promoter metal peaks are not detected, consistent with previous findings.[8]

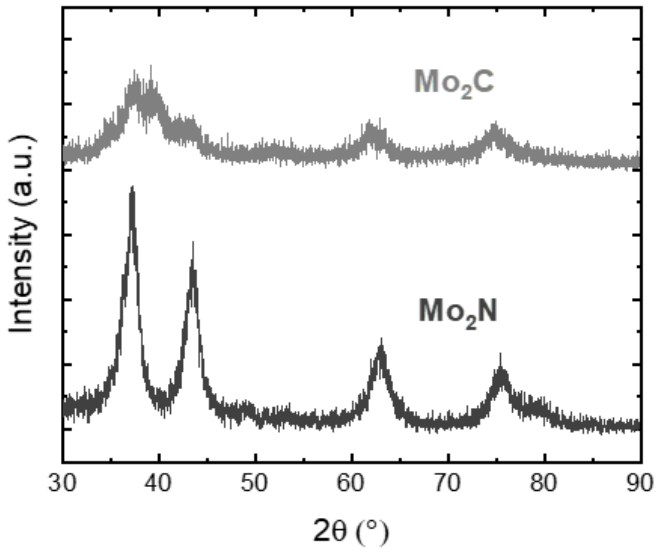

Figure 3.1. X-ray diffraction spectra of Mo_2C (gray) and Mo_2N (black) catalysts.

Surface areas calculated from N_2-physiorption and metal loadings determined from ICP-OES for all synthesized catalysts are listed in the **Table 3.1**. Metals deposited on nitrides (M/Mo_2N) catalysts tended to have higher surface areas compared to that of the metals deposited on carbide (M/Mo_2C) catalysts. Depositing metal onto the surface of the carbide and nitrides supports decreased the surface area,[17,24] but still allowed the catalyst to retain its high surface area properties.

Table 3.1. Surface areas as determined by N_2-physisorption metal loading from ICP-OES for supported Mo_2C and Mo_2N.

Catalyst	SA (m^2 g^{-1})	SA % decrease	Metal Loading (wt%)
Mo_2C	91	-	-
Fe/Mo_2C	65	29%	4.2
Ru/Mo_2C	65	29%	7.6
Co/Mo_2C	85	7%	4.5
Mo_2N	159	-	-
Fe/Mo_2N	117	26%	7.0
Ru/Mo_2N	126	21%	12.6
Co/Mo_2N	132	17%	7.3

3.3.2 Supported Mo_2C and Mo_2N Performance for Ammonia Synthesis

The specific ammonia production activities for metal supported Mo_2C and Mo_2N at 400 °C and 1 atm, as normalized by measured surface areas, are presented in **Figure 3.2**. Baseline experiments were conducted to ensure no detectable NH_3 production under identical conditions without a catalyst present in the reactor. Compared to the catalysts Kojima et al. tested for ammonia synthesis under the same conditions, our catalysts displayed 1.3 times higher activity for Mo_2C and 14.3 times higher activity for Mo_2N. This difference in activity of Mo_2C can be attributed to the different phases of the catalysts. In Kojima's proposed synthesis, β-Mo_2C is the majority phase. However, our synthesis displays a mixture of α,β-Mo_2C from XRD, potentially providing different types of active sites involved in adsorbing and breaking the nitrogen bond at ambient pressure.

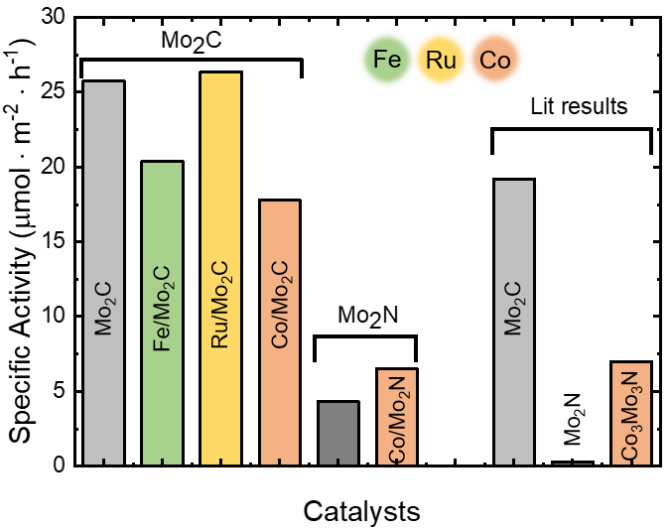

Figure 3.2. Specific ammonia synthesis activity of supported Mo_2C and Mo_2N at 400 °C under stoichiometrically balanced flow of N_2/H_2 for 2 hours. Results are compared to Mo_2C and Mo_2N from Ref. [11] and Co/Mo_2C from Ref. [13]. Mo_2C-based catalysts are pretreated with 15% CH_4/H_2 at 590 °C, while Mo_2N-based catalysts were pretreated with 25% N_2/H_2 mixture at 600 °C All activities are normalized by surface areas measured from N_2-physisorption.

Comparing the activity of Mo_2N, Kojima's temperature programmed synthesis of Mo_2N is significantly shorter at much lower temperatures. From their XRD results, there was evidence that an oxide phase of molybdenum was present in the catalyst, indicating that the precursor was not fully reduced to the desired Mo_2N. The activities of Mo_2N with a Co promoter are similar, despite different synthesis conditions. In both cases, adding Co to the Mo_2N improved the ammonia synthesis activity. We rationalize this trend as the synergistic effect of combining Mo, a metal strongly bound to nitrogen, and Co, a metal weakly bound to nitrogen.[25] The production of ammonia should be maximized where there is optimal adsorption and desorption of reactant species for the rate-determining step on the surface. The specific activity of all supported Mo_2C were higher than Mo_2N at 400 °C at 1 atm, which agrees with previous literature results.[11]

Addition of metal promoters does not increase the specific activity of Mo_2C-based catalysts. In fact, adding Fe and Co to Mo_2C reduced the specific activity by 20% and 31%, respectively. Prior results have indicated that the addition of Co to either α-Mo_2C or β-Mo_2C

decreases ammonia production activity,[11] which agree with our observed trends. Additionally, there is evidence that the structural interaction of CoMo-based materials has an effect on the ammonia synthesis.[16] It is possible that the decrease in activity can be attributed to unfavorable interaction of depositing Co on Mo_2C instead of incorporating Co into Mo before carbonization. Unlike Co, which has an optimal nitrogen adsorption energy when alloyed with Mo for ammonia production, Fe has stronger N_2 adsorption energy. Thus, the adsorption energy of Fe/Mo_2C might be too strong for effective ammonia production. Out of the three metal promoters, only Ru/Mo_2C showed a 3% increase in specific activity compared to Mo_2C. Typically, Ru-based catalysts are more active for ammonia synthesis than traditional iron-based catalysts at lower pressure.[23,26] In this case, it improved the activity of Mo_2C at ambient pressure.

The Arrhenius plots and derived apparent activation energy (E_a) of the metal supported Mo_2C and Mo_2N are presented in **Figure 3.3**. We also tested Fe/Al_2O_3 as an industrial ammonia synthesis standard. As confirmed previously, all the Mo_2C-based catalysts displayed higher activities than Mo_2N-based material between 300 – 400 °C at 1 atm. At these conditions, little to no activity was observed for the Fe/Al_2O_3 catalyst. The E_a for all the supported Mo_2C catalysts and Co/Mo_2N are reported to be between 20 – 23 kJ/mol at 1 atm. For comparison, similar materials tested at 30 atm showed E_a around 50 kJ/mol.[11,27] In many of these cases, the activity of the material improve without changing E_a, indicating that the rate-determining step does not change between catalysts. Mo_2N is the only catalyst that had a very low apparent activation energy of 7 kJ/mol. We believe that the experimental setup might be either equilibrium or diffusion limited.

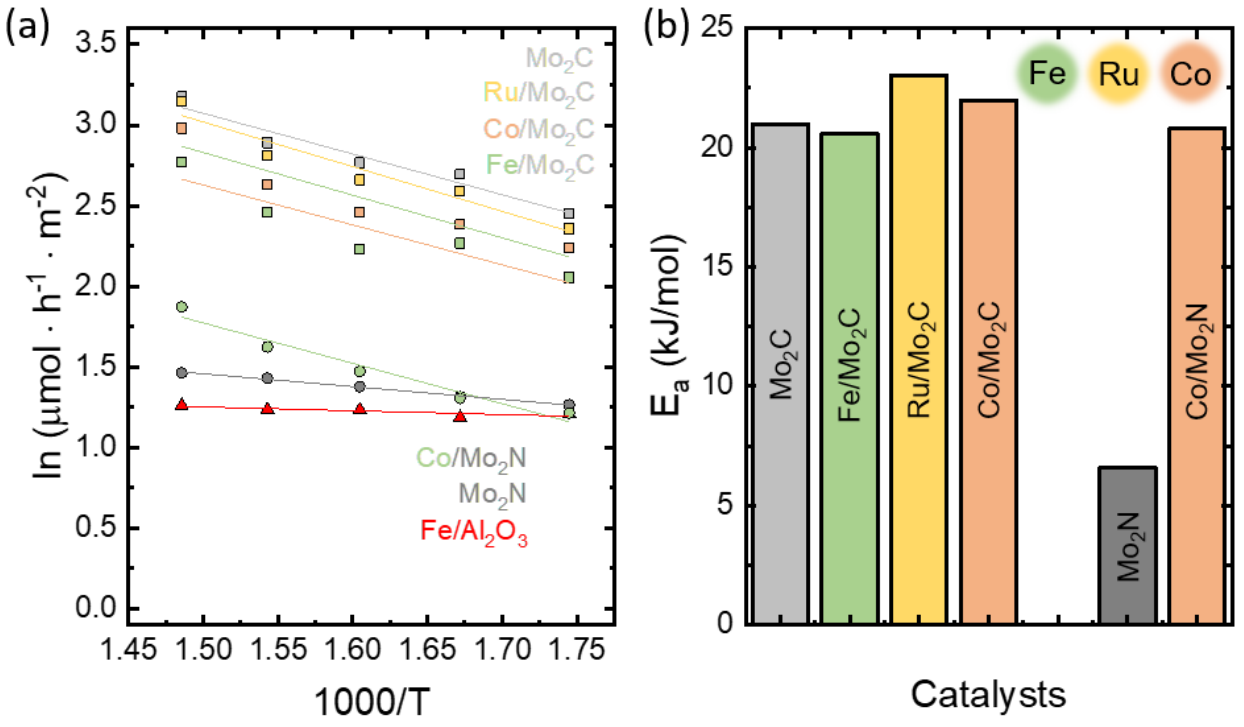

Figure 3.3. (a) Arrhenius plots of ammonia production rates for supported metal Mo_2C and Mo_2N catalysts. Fe/Al_2O_3 (red) was also tested as an industrial baseline catalyst. **(b)** Comparison of E_a across different catalysts.

3.3.3 Pretreatment Effect on Mo_2N Performance

To improve Mo_2N ammonia synthesis activities, we explored four different pretreatment methods to activate and remove the passivation layer from the catalyst. The first method used a stoichiometric balance of 25% N_2/H_2, which has most prevalently been cited in literature for nitride materials in ammonia applications.[13,16] The second and third method involved simply reducing the passivation layer on the surface the catalyst with H_2 at 450 °C and 600 °C. The final method activates Mo_2N with the same gas used to synthesize the material during the temperature programmed reaction. The rationale behind the last pretreatment condition was because Mo_2C-based materials were pretreated under the same conditions as their respective synthesis gas mixture.

The mass spectrometry measurements of ammonia levels during the reaction on Mo_2N under various pretreatment conditions are presented in **Figure 3.4**. Pretreatment of Mo_2N in H_2 at 600 °C yield no ammonia during the reaction and is excluded. Ammonia synthesis rates over the course of two hours are the highest with NH_3 pretreatment, followed by H_2 at 450 °C and 25% N_2/H_2. Both NH_3 and H_2 pretreatment effectively remove the passivation layer and sustain a level of ammonia activity similar to Mo_2C. However, slight decreases in the measurement over the course of ~2 hrs indicate that the surface might be changing under reaction conditions. 25% N_2/H_2 pretreatment at 450 °C removes the passivation layer, but the ammonia signal increases throughout the experiment. This finding could indicate that the longer pretreatment times were required to fully activate the catalyst. It is also possible that under reaction conditions, lattice N from Mo_2N react with H_2 to form NH_3 via the Mars-van Krevelen mechanism.[28,29]

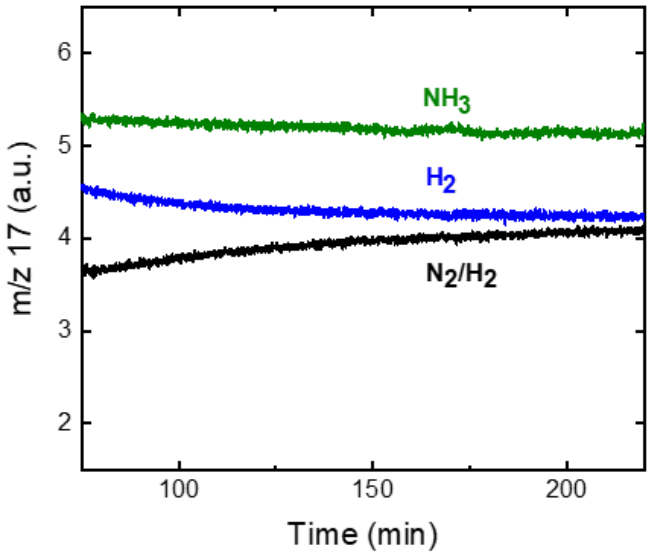

Figure 3.4. Deconvoluted mass spectrometry measurements at m/z 17 (ammonia production) for Mo_2N for three different pretreatment procedures. Black line represents traditional pretreatment of nitrides by using 25%N_2/H_2 at 600 °C. Blue line represents H_2 pretreatment at 450 °C. Green line represents NH_3 pretreatment at 450 °C.

3.3.4 Low-Temperature Ammonia Synthesis

Upon ensuring that metal supported Mo_2C and Mo_2N were active for ammonia synthesis at ambient pressure, we wanted to investigate their performance at low-temperature between 100 – 400 °C. **Figure 3.5** shows the deconvoluted mass spectrometry measurements at m/z 17 (ammonia) for a Co/Mo_2N catalyst. Even though Co/Mo_2N did not exhibit the highest activity among the catalysts, it has been most frequently cited for low temperature investigation for the electrochemical nitrogen reduction reaction.[30–32]

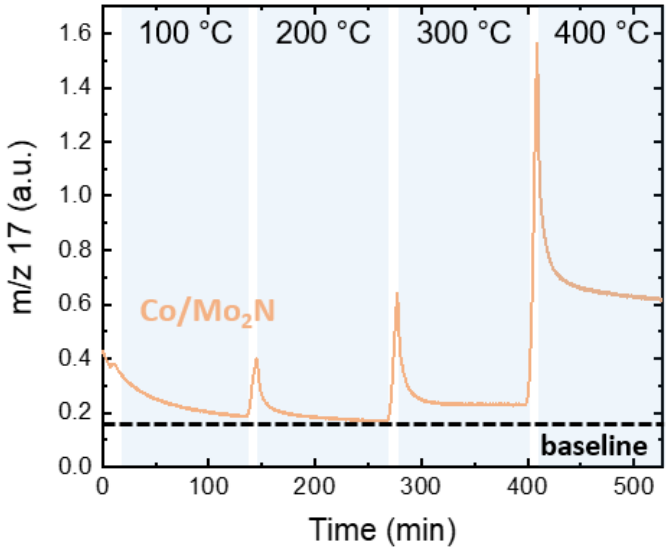

Figure 3.5. Deconvoluted mass spectrometry measurements at m/z 17 (ammonia production) for Co/Mo_2N at 100 °C, 200 °C, 300 °C, and 400 °C under 25% N_2/H_2. The ammonia level at each temperature is recorded over the course of 2 hrs, and the dashed black line indicates the baseline level for measurements with no activity.

During the first 2 hrs of the reaction at 100 °C, there is a downward slope in ammonia levels towards the baseline from remnants during the purging process after sample pretreatment. As the temperature is ramped, transient NH_3 is detected, most likely from bound surface species desorbing from the catalyst. At 300 °C and 400 °C, steady-state catalytic NH_3 production is recorded, indicating that low-temperature ammonia synthesis (<300 °C) is not feasible in this catalytic system.

3.4 Conclusions

Ammonia synthesis activities were evaluated for a series of metal supported Mo_2C and Mo_2N from 300 – 400 °C at 1 atm. Compared to the Fe/Al_2O_3 industrial standard, these catalysts displayed promising activities at ambient operating pressure. The Mo_2C-based materials showed more activity than their Mo_2N-based counterparts and improved overall activity compared to literature. However, there was little to no improvement upon depositing metal promoters on the carbide and nitride supports. Co/Mo_2N showed higher ammonia synthesis activity than Mo_2N, but also higher apparent activation energy. Both Fe/Mo_2C and Co/Mo_2C had lower activity than Mo_2C, while Ru/Mo_2C improved the ammonia production rates compared to Mo_2C by 3%. We also investigated the influence of four different pretreatment conditions on the ammonia synthesis activity for Mo_2N. Preliminary results show that NH_3 pretreatment resulted in levels of sustained ammonia production at similar levels to Mo_2C. Future work for the Mo_2C and Mo_2N-based materials should focus on different synthesis techniques that could improve reaction rates. This includes alloying the metals before carbonization and nitridation or including alkali promoters such as Cs and K to enhance catalytic activity. *In situ* EXAFS and isotopic N_2 labeling could also be used to further understand the surface chemistry of Mo_2N under different pretreatment conditions and the potential effect of the Mars-van Krevelen mechanism on the reaction.

3.5 References

(1) Boerner, L. K. Industrial ammonia production emits more CO2 than any other chemical-making reaction. Chemists want to change that https://cen.acs.org/environment/green-chemistry/Industrial-ammonia-production-emits-CO2/97/i24 (accessed Apr 26, 2021).

(2) Capdevila-Cortada, M. Electrifying the Haber–Bosch. *Nature Catalysis* **2019**, *2* (12), 1055–1055. https://doi.org/10.1038/s41929-019-0414-4.

(3) Smith, C.; Hill, A. K.; Torrente-Murciano, L. Current and Future Role of Haber–Bosch Ammonia in a Carbon-Free Energy Landscape. *Energy Environ. Sci.* **2020**, *13* (2), 331–344. https://doi.org/10.1039/C9EE02873K.

(4) Griboval-Constant, A.; Giraudon, J.-M.; Twagishema, I.; Leclercq, G.; Rivas, M. E.; Alvarez, J.; Pérez-Zurita, M. J.; Goldwasser, M. R. Characterization of New Co and Ru on ⎵-WC Catalysts for Fischer-Tropsch Reaction Influence of the Carbide Surface State. *Journal of Molecular Catalysis A: Chemical* **2006**, *259*, 187–196. https://doi.org/10.1016/j.molcata.2006.06.015.

(5) Griboval-Constant, A.; Giraudon, J.-M.; Leclercq, G.; Leclercq, L. Catalytic Behaviour of Cobalt or Ruthenium Supported Molybdenum Carbide Catalysts for FT Reaction. *Applied Catalysis A: General* **2004**, *260*, 35–45. https://doi.org/10.1016/j.apcata.2003.10.031.

(6) Setthapun, W.; Bej, S. K.; Thompson, L. T. Carbide and Nitride Supported Methanol Steam Reforming Catalysts: Parallel Synthesis and High Throughput Screening. https://doi.org/10.1007/s11244-008-9070-7.

(7) Schaidle, J. A.; Lausche, A. C.; Thompson, L. T. Effects of Sulfur on Mo2C and Pt/Mo2C Catalysts: Water Gas Shift Reaction. *Journal of Catalysis* **2010**, *272* (2), 235–245. https://doi.org/10.1016/j.jcat.2010.04.004.

(8) Schaidle, J. A.; Schweitzer, N. M.; Ajenifujah, O. T.; Thompson, L. T. On the Preparation of Molybdenum Carbide-Supported Metal Catalysts. *Journal of Catalysis* **2012**, *289*, 210–217. https://doi.org/10.1016/j.jcat.2012.02.012.

(9) Schweitzer, N. M.; Schaidle, J. A.; Ezekoye, O. K.; Pan, X.; Linic, S.; Thompson, L. T. High Activity Carbide Supported Catalysts for Water Gas Shift. *J. Am. Chem. Soc* **2011**, *133*, 2378–2381. https://doi.org/10.1021/ja110705a.

(10) Venkataraman, R.; Kunz, H. R.; Fenton, J. M. Development of New CO Tolerant Ternary Anode Catalysts for Proton Exchange Membrane Fuel Cells. *Journal of The Electrochemical Society* **2003**, *150* (3), A278. https://doi.org/10.1149/1.1543567.

(11) Kojima, R.; Aika, K. I. Molybdenum Nitride and Carbide Catalysts for Ammonia Synthesis. *Applied Catalysis A: General* **2001**, *219* (1–2), 141–147. https://doi.org/10.1016/S0926-860X(01)00676-7.

(12) Hargreaves, J. S. J. Nitrides as Ammonia Synthesis Catalysts and as Potential Nitrogen Transfer Reagents. *Appl Petrochem Res* **2014**, *4* (1), 3–10. https://doi.org/10.1007/s13203-014-0049-y.

(13) Kojima, R.; Aika, K. Cobalt Molybdenum Bimetallic Nitride Catalysts for Ammonia Synthesis: Part 1. Preparation and Characterization. *Applied Catalysis A: General* **2001**, *215* (1), 149–160. https://doi.org/10.1016/S0926-860X(01)00529-4.

(14) Kojima, R.; Aika, K.-I. Cobalt Molybdenum Bimetallic Nitride Catalysts for Ammonia Synthesis Part 2. Kinetic Study. *Applied Catalysis A: General* **2001**, *218*, 121–128.

(15) Kojima, R.; Aika, K. Cobalt Molybdenum Bimetallic Nitride Catalysts for Ammonia Synthesis: Part 3. Reactant Gas Treatment. *Applied Catalysis A: General* **2001**, *219* (1), 157–170. https://doi.org/10.1016/S0926-860X(01)00678-0.
(16) AlShibane, I.; Daisley, A.; Hargreaves, J. S. J.; Hector, A. L.; Laassiri, S.; Rico, J. L.; Smith, R. I. The Role of Composition for Cobalt Molybdenum Carbide in Ammonia Synthesis. **2017**, 9.
(17) Wyvratt, B. M.; Gaudet, J. R.; Thompson, L. T. Effects of Passivation on Synthesis, Structure and Composition of Molybdenum Carbide Supported Platinum Water-Gas Shift Catalysts. *Journal of Catalysis* **2015**, *330*, 280–287. https://doi.org/10.1016/j.jcat.2015.07.023.
(18) Schweitzer, N. M.; Schaidle, J. A.; Ezekoye, O. K.; Pan, X.; Linic, S.; Thompson, L. T. High Activity Carbide Supported Catalysts for Water Gas Shift. *Journal of the American Chemical Society* **2011**, *133* (8), 2378–2381. https://doi.org/10.1021/ja110705a.
(19) Kotobuki, M.; Leppelt, R.; Hansgen, D. A.; Widmann, D.; Behm, R. J. Reactive Oxygen on a Au/TiO2 Supported Catalyst. *Journal of Catalysis* **2009**, *264* (1), 67–76. https://doi.org/10.1016/j.jcat.2009.03.013.
(20) Tauster, S. J.; Fung, S. C.; Baker, R. T. K.; Horsley, J. A. Strong Interactions in Supported-Metal Catalysts. *Science* **1981**, *211* (4487), 1121–1125. https://doi.org/10.1126/science.211.4487.1121.
(21) Schaidle, J. A.; Lausche, A. C.; Thompson, L. T. Effects of Sulfur on Mo 2 C and Pt/Mo 2 C Catalysts: Water Gas Shift Reaction. *Journal of Catalysis* **2010**, *272*, 235–245. https://doi.org/10.1016/j.jcat.2010.04.004.
(22) Hochman, G.; Goldman, A. S.; Felder, F. A.; Mayer, J. M.; Miller, A. J. M.; Holland, P. L.; Goldman, L. A.; Manocha, P.; Song, Z.; Aleti, S. Potential Economic Feasibility of Direct Electrochemical Nitrogen Reduction as a Route to Ammonia. *ACS Sustainable Chem. Eng.* **2020**, *8* (24), 8938–8948. https://doi.org/10.1021/acssuschemeng.0c01206.
(23) Manaka, Y.; Nagata, Y.; Kobayashi, K.; Kobayashi, D.; Nanba, T. The Effect of a Ruthenium Precursor on the Low-Temperature Ammonia Synthesis Activity over Ru/CeO 2. *Dalton Transactions* **2020**, *49* (47), 17143–17146. https://doi.org/10.1039/D0DT01974G.
(24) Wyvratt, B. M.; Gaudet, J. R.; Pardue, D. B.; Marton, A.; Rudić, S.; Mader, E. A.; Cundari, T. R.; Mayer, J. M.; Thompson, L. T. Reactivity of Hydrogen on and in Nanostructured Molybdenum Nitride: Crotonaldehyde Hydrogenation. *ACS Catalysis* **2016**, 5797–5806. https://doi.org/10.1021/acscatal.6b00936.
(25) Jacobsen, C. J. H.; Dahl, S.; Clausen, B. S.; Bahn, S.; Logadottir, A.; Nørskov, J. K. Catalyst Design by Interpolation in the Periodic Table: Bimetallic Ammonia Synthesis Catalysts. *J. Am. Chem. Soc.* **2001**, *123* (34), 8404–8405. https://doi.org/10.1021/ja010963d.
(26) Saadatjou, N.; Jafari, A.; Sahebdelfar, S. Ruthenium Nanocatalysts for Ammonia Synthesis: A Review. *Chemical Engineering Communications* **2015**, *202* (4), 420–448. https://doi.org/10.1080/00986445.2014.923995.
(27) Kojima, R.; Aika, K. Cobalt Molybdenum Bimetallic Nitride Catalysts for Ammonia Synthesis: Part 2. Kinetic Study. *Applied Catalysis A: General* **2001**, *218* (1), 121–128. https://doi.org/10.1016/S0926-860X(01)00626-3.
(28) Abghoui, Y.; Garden, A. L.; Howalt, J. G.; Vegge, T.; Skúlason, E. Electroreduction of N2 to Ammonia at Ambient Conditions on Mononitrides of Zr, Nb, Cr, and V: A DFT Guide

for Experiments. *ACS Catal.* **2016**, *6* (2), 635–646. https://doi.org/10.1021/acscatal.5b01918.

(29) Abghoui, Y.; Skúlason, E. Electrochemical Synthesis of Ammonia via Mars-van Krevelen Mechanism on the (111) Facets of Group III–VII Transition Metal Mononitrides. *Catalysis Today* **2017**, *286*, 78–84. https://doi.org/10.1016/j.cattod.2016.06.009.

(30) Zhang, J.; Tian, X.; Liu, M.; Guo, H.; Zhou, J.; Fang, Q.; Liu, Z.; Wu, Q.; Lou, J. Cobalt-Modulated Molybdenum–Dinitrogen Interaction in MoS2 for Catalyzing Ammonia Synthesis. *J. Am. Chem. Soc.* **2019**, *141* (49), 19269–19275. https://doi.org/10.1021/jacs.9b02501.

(31) Li, Q.; He, L.; Sun, C.; Zhang, X. Computational Study of MoN2 Monolayer as Electrochemical Catalysts for Nitrogen Reduction. *J. Phys. Chem. C* **2017**, *121* (49), 27563–27568. https://doi.org/10.1021/acs.jpcc.7b10522.

(32) Amar, I. A.; Lan, R.; Petit, C. T. G.; Tao, S. Electrochemical Synthesis of Ammonia Based on Co3Mo3N Catalyst and LiAlO2–(Li,Na,K)2CO3 Composite Electrolyte. *Electrocatalysis* **2015**, *6* (3), 286–294. https://doi.org/10.1007/s12678-014-0242-x.

Chapter 4

Pt_xRu_y/C for Electrocatalytic Nitrate Conversion to Ammonia

This chapter was adapted from Wang, Zixuan, et al. "Increasing electrocatalytic nitrate reduction activity by controlling adsorption through PtRu alloying." *Journal of Catalysis* 395 (2021): 143-154.

4.1 Introduction

Nitrate is among the world's most widespread water pollutants, and its accumulation leads to adverse health effects and environmental damage through algal blooms and dead zone formation.[1,2] Multiple approaches have been explored to manage nitrate contamination of water, including physical separation,[3,4] biological denitrification,[5–7] chemical reduction,[8] catalytic hydrogenation,[9,10] and electrocatalytic reduction.[11,12] Each of these approaches has drawbacks for industrial applications. Physical separation can result in fast and large-scale water treatment but produces a concentrated secondary stream that requires further processing. Biological denitrification is currently the most cost-effective method.[13,14] However, biological approaches are ineffective for treating harsh waste streams (e.g., acidic or containing heavy metals and halides) because these conditions deactivate or kill the bacteria.[15,16] Chemical reduction and catalytic hydrogenation require continuous external reducing agents, creating hazards in storage, transportation, and utilization, in addition to high cost.[17]

A promising, less-explored route to remediate nitrate is electrocatalytic reduction.[16,18] The electrocatalytic nitrate reduction reaction (ENO_3RR) uses protons and electrons, which removes the need for an external H_2 stream and can be powered via renewable electricity.[19] ENO_3RR converts aqueous NO_3^- to NO_2^- and then to products such as HNO_2, NO, NH_2OH, NH_3, N_2O, and N_2 (**Scheme 4.1**). Preferential selectivity towards N_2 or NH_3 is often the target in literature.[20–22] N_2 is a benign, easily separable, and the most stable nitrate reduction product with a standard redox potential (E^0) of 1.25 V vs. RHE. NH_3 is a commodity chemical that would, in principle, reduce the reliance on the Haber-Bosch process for ammonia production if made from ENO_3RR (E^0 = 0.82 V vs. RHE). Producing NH_3 from NO_3^- is kinetically more accessible than breaking the N_2 triple bond, and ENO_3RR may enable decentralized ammonia production using renewable electricity.

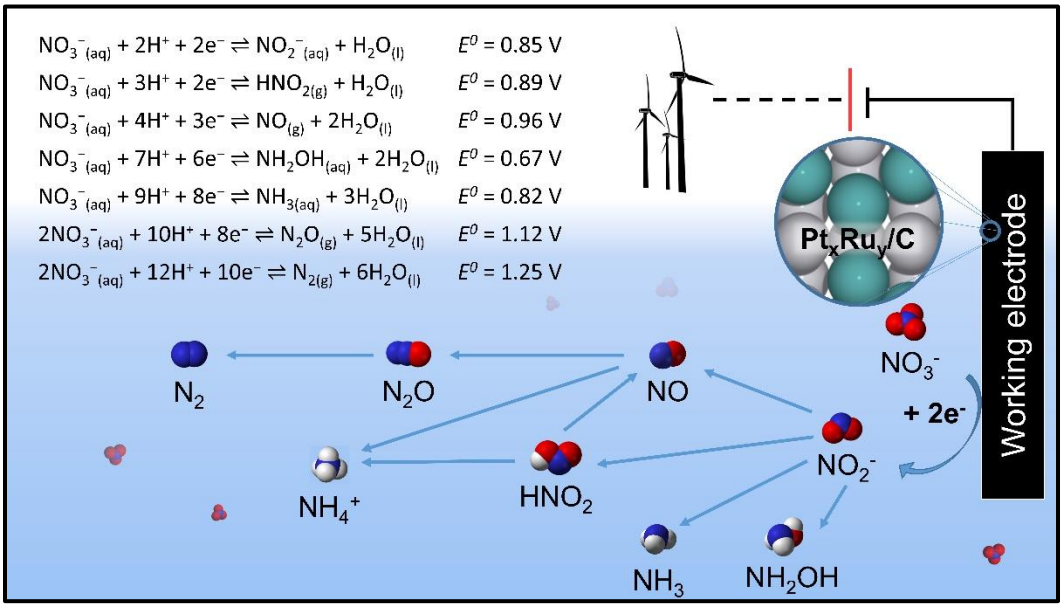

Scheme 4.1. Renewable electricity can drive the electrocatalytic reduction of nitrate to products such as NO_2^-, NH_2OH, NH_3, and N_2.[18] The standard redox potentials vs. RHE for typical nitrate reduction reactions are provided inset. Alloys, such as the Pt_xRu_y/C electrocatalyst reported herein, often have better performance than their pure metal constituents. Color legend: O atom = red; N atom = blue; H atom = gray. Oxidation reactions on the counter electrode are not pictured.

Despite ongoing research in electrocatalytic denitrification, there lacks a sufficiently inexpensive, active, selective (i.e., high faradiac efficiency (FE) towards N_2 or NH_3), and stable catalyst that would enable widespread application of this technology in acidic media.[23] Rh is currently the most active and selective pure metal for nitrate reduction towards NH_3 in acidic media at low overpotentials.[24] On Rh, nitrate adsorbs strong enough to maintain considerable surface coverages relative to hydrogen. The higher nitrate coverage promotes high rates of nitrate dissociation, which is often the rate-determining step for ENO_3RR.[25] However, Rh is extremely expensive, costing over $8,200/oz.[26] Besides the catalyst cost, another significant cost in an electrochemical process is electricity, typically accounting for 33% of commodity chemical production.[19,27] To reduce operating costs in the system, catalysts need to be active at low overpotentials. Finding an inexpensive, stable electrocatalyst with activity and selectivity comparable to those of Rh at low overpotentials is a major challenge for widespread commercial denitrification.

Determining optimal alloy compositions is important because the alloy composition determines the catalyst cost and the catalyst activity and selectivity. **Table 4.1** shows a summary of different alloys previously investigated for ENO_3RR.[20–22,28–33] For PtSn alloys, the addition of Sn enhanced the rate-determining step of nitrate reduction to nitrite and altered the selectivity from ammonia toward hydroxylamine.[34] More recently, $Cu_{50}Ni_{50}$ alloy catalysts were demonstrated to have a six-fold increase in activity compared to pure Cu at 0 V vs. RHE.[33] Alloying Cu with Ni raises the *d*-band center relative to the Fermi level and increases the adsorption strength of key intermediates such as $*NO_3$, $*NO_2$, and $*NH_2$. However, Ni composition greater than 50% increases the $*NH_2 \rightarrow *NH_3$ reaction free energy, which decreases the overall NH_3 production.

Consequently, a volcano-like relationship exists between catalyst composition and selectivity towards NH_3.

Table 4.1. Summary of different alloys previously investigated for ENO_3RR. Only catalysts with normalized current densities measured are reported.

Alloys[a]	Conditions	Current Density	Normalization Technique	Faradaic Efficiencies	Reference
$Cu_{50}Ni_{50}$	−0.1 V vs. RHE in 1 M KOH + 0.1 M KNO_3	−80 mA/cm^2	Capacitance	>95% NH_3	*J. Am. Chem. Soc.* **2020**, 142, 5702
Cu-Zn	*ca.* −0.6 V vs. SHE in 1 M KOH + 0.1 M $NaNO_3$	−3 mA/cm^2	Geometric	92–97% NH_3	*J. Electrochem Soc.*, **2015**, 162, 236
PtRh	0.155 V vs. RHE in 0.5 M H_2SO_4 + 0.01 M NO_3^-	−115 μA/cm^2	H_{upd} and CO stripping	N/A	*Appl. Catal. B*, **2018**, 221, 86
Sn-modified Pt, Pd, Pt-Pd	0.01 V vs. RHE in 0.1 M $HClO_4$ + 0.1 M $NaNO_3$	−32 mA/cm^2	H_{upd}	N/A	*J. Electroanal. Chem.* **2017**, 800, 46
Ag/Au	*ca.* −0.25 V vs. SHE in 0.1 M $HClO_4$ + 5 mM $NaNO_3$	−1 mA/cm^2	Geometric	N/A	*Phys. Chem. Chem. Phys.*, **2013**, 15, 3196
$Pt_{78}Ru_{22}$	0.05 V vs. RHE in 1 M H_2SO_4 + 1 M $NaNO_3$	−55 μA/cm^2	H_{upd} and Cu_{upd}	93–98% NH_3	This work

[a] Naming convention for each alloy reported based on how it is written in the original reference.

Computational catalysis has emerged as a powerful tool to understand and design electrocatalysts for wastewater treatment.[35] Our recent computational work using density functional theory (DFT) modeling identified the binding energies of atomic O and N as simple thermodynamic descriptors that correlate with the activity and selectivity of metal ENO_3RR catalysts.[25] These two descriptors were used with mean-field microkinetic modeling to generate theoretical volcano activity plots at different applied potentials. The descriptors reliably predict ENO_3RR activity trends on metals through adsorbate scaling and Brønsted-Evans-Polanyi relations. Based on these volcano plots, Pt_3Ru was predicted to be more active than Pt and among the most active alloys considered. Nevertheless, it is unclear whether the descriptors and microkinetic model for single metals can be applied to bimetallic alloys. This work will focus on

experimentally validating such descriptors and the volcano plot for alloys, which would create avenues for rapidly screening ENO_3RR catalysts.

In this chapter, we report the activity and selectivity for ENO_3RR on well-characterized Pt_xRu_y/C alloys (x = 48–100%) to test our computational hypothesis that platinum-ruthenium alloys are more active than Pt. Our synthesis method results in 3–6 nm Pt_xRu_y alloy nanoparticles on carbon without significant phase or surface segregation. We use hydrogen underpotential deposition (H_{upd}) and copper underpotential deposition (Cu_{upd}) to measure the electrochemically active surface area (ECSA) and report normalized steady-state current densities for ENO_3RR. Pt nanoparticles supported on carbon (Pt_{100}/C) have lower activity than all five Pt_xRu_y/C catalysts in the potential range 0.05–0.40 V vs. RHE. The activity increases with the Ru content to a maximum at $Pt_{78}Ru_{22}/C$, followed by a decrease in activity with higher Ru content. The experimental maximum in activity with Ru at% (atomic %) qualitatively matches predictions from our DFT calculations over the same range of Ru compositions. We attribute the change in activity with Ru content to changing the adsorption strength of nitrate, hydrogen, and intermediates by alloying. Our results support that the activity volcano plot previously developed for pure metals is applicable to bimetallic alloys. This finding suggests that simple thermodynamic descriptors, such as N and O binding energies, can be used to screen alloy catalysts for ENO_3RR. This work also gives insight into synthesizing more active ENO_3RR catalysts by tuning the adsorption strength of intermediates through alloying, further aiding the conversion of nitrate to benign or value-added products.

4.2 Methods

4.2.1 Catalyst Preparation

A $NaBH_4$ reduction synthesis was used for catalyst synthesis, as detailed in **Chapter 2, Section 2.2.3**. A suspension of 25 mg of carbon black (Vulcan XC 72; Fuel Cell Store) was

pretreated in H_2 at 400 °C for 2 hrs to remove impurities from the surface. After, the support was suspended in 15 mL of Millipore water (18.2 MΩcm, Millipore MilliQ system) and sonicated for 15 min. Measured concentrations of $RuCl_3$ (38% Ru; Alfa Aesar) and H_2PtCl_6 (38–40% Pt; Sigma Aldrich) in Millipore water were added to the solution and stirred. After, 40 mg of $NaBH_4$ (Sigma Aldrich) dissolved in 25 mL of Millipore water was introduced. This solution was stirred for 2 hrs before being centrifuged 3 times at 3000 rpm for 8 min and washed with Millipore water. The recovered solid was dried overnight in an oven at 80 °C. The final Pt and Ru loadings were determined by using a PerkinElmer NexION 2000 ICP-MS after digesting 1 mg of the catalyst in aqua regia (3:1 molar HCl:HNO_3). The sample solutions were co-fed along with a 20-ppb bismuth internal standard. X-ray diffraction (XRD) analysis indicated the presence of a separate Ru hexagonal phase instead of the bimetallic phase for Ru compositions above 60 at%.[36] Therefore, for the purpose of exploring only Pt_xRu_y alloys, we investigated bulk Ru concentrations of 0–52 at%. Commercial 30 wt% Pt/C, 30 wt% $Pt_{50}Ru_{50}$/C, and 20 wt% Rh/C were also purchased from Fuel Cell Store for comparison.

4.2.2 Material Characterization

X-ray absorption near edge structure (XANES) and extended X-ray absorption fine structure (EXAFS) measurements were taken at the Sector 20 bending-magnet beamline of the Advanced Photon Source at Argonne National Laboratory. Catalyst samples were loaded into 1.5 mm glass capillaries for measurement in transmission mode at the Pt L_3-edge. To take the spectra at the Ru K-edge, the catalyst samples were also measured in the glass capillaries using transmission mode, except for the lowest Ru weight loading sample, for which the sample was filled into a Kapton tube to allow a longer path distance to increase the signal to noise ratio. All measurements were taken of samples exposed to air (ex situ). Two 14-min scans were taken for

each sample at each edge and co-added to generate the spectrum. Pt and Ru reference foils were located downstream and taken concurrently with the sample for energy calibration and to verify monochromator stability. The data was processed using ATHENA software with a Fourier cutoff of R_{bkg} = 1.0 Å and a *k* range of 3 to 16 $Å^{-1}$.[37] Structural parameters were derived from the experimental data by fitting using FEFF9 theoretical standards[38] as inputs to the ARTEMIS software package.[37,39] Fits included first Pt-Pt or Pt-Ru and Pt-O paths including the 3rd cumulant to account for asymmetry.

XRD analysis was conducted using a Rigaku Miniflex XRD with Cu Kα radiation and a Ni filter (λ = 1.5418 Å). The 2θ range (10° < 2θ < 90°) was scanned at a rate of 5°/min with a 0.02° step size. Crystallite sizes were estimated using the Scherrer equation, as described in **Chapter 2, Section 2.3.1**. Pt and Ru peaks are referenced to #04-0802 and #06-0663, respectively.

Transmission electron microscopy (TEM) was performed on a JEOL 2010F electron microscope operating with 200 kV accelerating voltage. The samples were made by adding 1 mg of catalyst into isopropanol. One drop of this suspension was deposited on a gold grid. The isopropanol was dried before imaging of the sample.

X-ray photoelectron spectroscopy (XPS) was conducted using a Kratos Axis Ultra X-ray photoelectron spectrometer. While keeping the analysis chamber at 1×10^{-9} Torr, a monochromatic Al X-ray source (10 mA and 12 kV) was used with a pass energy of 12 eV and step size of 1 eV. Collected spectra were calibrated by positioning the C(1s) peak at 248.8 eV. The resulting Pt 4d and Ru 3p peaks were fitted with the Shirley-type background with the CasaXPS software.[40]

4.2.3 Electrode Preparation

The catalyst ink was prepared by adding 3 mg of the supported catalyst in 5 mL of water and isopropanol (1:1 molar ratio). 17.5 μL of Nafion (5% in 95% isopropanol, Sigma Aldrich) was

added to the solution to act as a binder and sonicated for at least 120 min. A glassy carbon rotating disk electrode (5 mm in diameter) was polished with 0.05 μm alumina suspensions before sonication in Millipore water to remove trace surface contaminants. The catalyst ink was sonicated for at least 30 min before depositing 8 μL of the ink onto the surface of the clean glassy carbon electrode. The deposition was kept in closed containment as the ink dried and repeated once more. The total loading was 9.6 μg of catalyst, including carbon. These prepared electrodes were placed into the electrolyte solution and cycled from hydrogen evolution to Pt oxidation potentials (−0.17 to 1.23 V vs. RHE) at least 50 times at 100 mV s^{-1} before conducting electrochemical measurements. ICP-MS experiments of the solution before and after the electrocatalyst pretreatment process for a commercial PtRu/C show ~8% of Pt and Ru in the electrolyte solution. We attribute this amount to catalyst powder that is not adequately bound to the surface of the glassy carbon. Following this pretreatment, we obtain stable CVs for all reported Pt_xRu_y/C, implying no further loss of catalyst.

4.2.4 Electrochemical Measurements

The electrochemical experiments were conducted in either a single compartment, three-electrode glass electrochemical cell (for steady-state activity measurements) or a two-compartment, three-electrode cell (to enable product quantification for selectivity measurements) using a VSP potentiostat (Bio-Logic Science Inst.). All measurements were taken at room temperature (23.3 °C). A graphite rod (AGKSP grade, ultra “F” purity, Alfa Aesar) and Ag/AgCl (4 M KCl, Pine Research Inst., Inc.) were used as the counter and the reference electrode, respectively. Before electrochemical experiments, the Ag/AgCl reference electrode was calibrated against a Pt wire with 1 bar H_2 in the electrolyte solution. All reported potentials are referenced to RHE. The sulfuric acid electrolyte was prepared by adding concentrated H_2SO_4 (99.999%, Sigma

Aldrich) to Millipore water. Before electrochemical measurements, N_2 gas (Ultra-high purity grade, 99.999%, Cryogenic Gases) was sparged through the electrolyte for at least 45 min to remove dissolved O_2 from the solution. Throughout the experiment, N_2 also blanketed the electrolyte solution to prevent O_2 from reaching the electrolyte.

4.2.5 Underpotential Deposition

After compensating for 85% of the solution resistance using electrochemical impedance spectroscopy (EIS), H_{upd} in the hydrogen desorption region was used as one method to determine the ECSA of the Pt_xRu_y/C alloys. The average charge density of Pt (210 μC cm^{-2}) was employed to calculate the ECSA. A slanted baseline, representing the double-layer charging current, was taken by subtracting half of the double-layer charging current measured at 0.35 V vs. RHE.[41]

All Cu_{upd} experiments were conducted in 0.1 M H_2SO_4 for an initial H_{upd} baseline before adding 2 mM $CuSO_4$ into the solution. The electrodes were polarized at 1.0 V vs. RHE for 2 min to ensure no Cu ions adsorbed to the surface of the electrode. Deposition potentials from 0.28–0.48 V vs. RHE were applied for 100 s to deposit a monolayer of Cu^{2+} on the surface of the catalyst. After, a linear voltammetric scan was performed at 100 mV s^{-1} from the applied potential to 1.0 V vs. RHE, in which all the underpotential-deposited copper has been oxidized. Charges obtained from the copper stripping were corrected by subtracting the double-layer charge obtained in the absence of cupric ions in the solution.

4.2.6 Steady-State Current Measurements for Nitrate Reduction

H_{upd} and baseline chronoamperometric measurements were performed in 100 mL of 1 M H_2SO_4 solution. The rotating disk electrode (RDE) was held at each potential for 5 min while rotating at 2500 rpm to eliminate mass transfer limitations. The absence of external mass transfer limitations was confirmed by verifying that the current densities were independent of rotation rate

at 2500 rpm or above. The film drop-cast method was used to deposit a thin layer of catalyst onto the glassy carbon electrode to avoid sources of internal diffusion limitations. The measured currents in the last 20 s were averaged and reported accordingly. After adding 20 mL of 6 M $NaNO_3$ (Sigma Aldrich, 99.0%) to reach 1 M nitrate, the electrolyte solution was sparged with N_2 for 15 min to remove trace oxygen. The chronoamperometric measurements were repeated with nitrate in the solution.

4.2.7 Selectivity Measurements

Measurements using solely catalyst deposited on glassy carbon did not give high enough currents to allow product quantification. To enable sufficient generation of ENO_3RR products in the electrochemical cell for product quantification, minor changes to the experimental setup were made to increase the catalyst amount. To increase the catalyst loading, Pt and Ru precursors were deposited via the same $NaBH_4$ reduction method on 2.52.5 cm^2 pieces of carbon felt (6.35 mm thick, 99.0%, Alfa Aesar). These carbon felts (CFs) were attached to a graphite rod (AGKSP grade, ultra "F" purity, Alfa Aesar) for use as the working electrode. Before electrochemical measurements, N_2 (Ultra-high purity grade, 99.999%, Cryogenic Gases) was sparged through the electrolyte for at least 45 min to remove O_2 from the solution. Throughout the experiment, N_2 blanketed the electrolyte solution to prevent O_2 from reaching the electrolyte. The carbon felt was treated in 1 M H_2SO_4 solution by cycling from hydrogen evolution to Pt oxidation (−0.17 to 1.23 V vs. RHE) at least 35 times at 100 mV s^{-1} to remove oxygenated species from the surface of the metal nanoparticles. H_{upd} experiments were conducted after compensating for 85% of the solution resistance. The Pt_xRu_y/CF (Pt and Ru alloys supported on carbon felt) was transferred to a two-compartment, three-electrode glass electrochemical cell with 150 mL of 0.1 M HNO_3 (sparged with N_2) as the electrolyte solution in the cathodic compartment. The electrolyte for selectivity

measurements was 0.1 M HNO_3 (rather than 1 M H_2SO_4 and 1 M $NaNO_3$) to avoid issues of sodium and sulfate interference in the ion chromatograph used for product quantification. Again, 85% of the solution resistance was compensated using EIS before running a 4-hr steady-state measurement at 0.1 V vs. RHE. Only 85% was directly compensated to avoid instability of the potentiostat controller.

An ion chromatography (Agilent), equipped with AS9-HC column (Dionex) with 9 mM sodium carbonate eluent, was used to quantify the amount of nitrate and nitrite in the electrolyte solution. For anion measurements, sodium nitrate (Sigma Aldrich, 99.0%) and sodium nitrite (Sigma Aldrich, 99.999% trace metal basis) were used to prepare the standard solutions for the calibration curve. To prevent oversaturating the system with anions, 0.1 mL of the electrolyte solution was extracted every hour and diluted by a factor of ten with Millipore water to measure the change in nitrate concentration. Separately, 0.5 mL of the electrolyte solution was extracted and neutralized with 0.1 M NaOH (Sigma Aldrich, 99.99%) to inhibit the decomposition of nitrite in acidic media.[34] However, we emphasize that the measured values of the nitrite concentration may be lower than the actual values due to the decomposition of nitrite during the extraction of the reactor aliquots.

NH_3 was quantified by using the indophenol blue test.[21,42] An aliquot of 1 mL of electrolyte solution was extracted from the cathodic side of the two-compartment cell every hour. 1 M NaOH (Sigma Aldrich, 99.99%) was added to the electrolyte solution to neutralize the acid to a pH of 12. After, 122 μL of sodium salicylate (Sigma Aldrich, >99.5%), 27.3 μL of sodium nitroprusside dihydrate (Sigma Aldrich, >99%), and 40 μL of sodium hypochlorite solution (Sigma Aldrich, 4.00–4.99%) were sequentially added to the electrolyte solution and manually stirred together. The solution was covered and left for 40 min. Afterward, a UV-vis spectrometer (Thermo Fischer,

Evolution 350) was used to obtain spectra between 400–1000 nm. The indophenol peak was identified as the maximum absorbance between 650–700 nm. A fresh 0.1 M HNO_3 electrolyte solution prepared with the indophenol blue method was used as the background and subtracted from the sample spectra. If the concentration of NH_3 was too high and oversaturated the detector, the solution was diluted and retested. A calibration curve was created using known concentrations of NH_4Cl (Sigma Aldrich) in 0.1 M HNO_3, and unknown NH_3 concentrations were calculated using the Beer-Lambert law. The FE was calculated by dividing the charge required to form the total NH_3 measured by the total charge passed during the steady-state experiments. The total charge passed was calculated by integrating the reduction current over the duration of the experiment and the charge required from NH_3 was calculated by assuming that eight electrons are required to form one molecule of NH_3 from one molecule of nitrate.

4.3 Results and Discussion

4.3.1 Synthesis and Bulk Characterization of the Supported Pt_xRu_y Alloys

We synthesize Pt_xRu_y (x = 48–100%) nanoparticles supported on Vulcan carbon via a modified $NaBH_4$ reduction method using different concentrations of H_2PtCl_6 and $RuCl_3$ precursors to vary the Pt:Ru ratio.[43] ICP-MS measurements determined the bulk weight and atomic loading of Pt and Ru in the alloys. The data in **Table 4.2** shows that a smaller wt% (weight %) of Ru than intended is incorporated into the catalyst. The deviations between the target and actual composition are likely due to the precision of the weighing scale and different reactivities of the two types of precursors upon reduction with $NaBH_4$.[36] We use the ICP-MS measured actual atomic percentage of Ru (with the balance Pt) for the naming convention of the catalysts. Additional characterization details, data processing, and results are in **Appendix A**.

Table 4.2. Atomic and weight percent loading of Ru in Pt_xRu_y/C (x = 48–100%) catalysts from ICP-MS. Target Ru wt% reflects the calculated amount of $RuCl_3$ precursor added during synthesis. All values are with respect to the total metal loading, not including carbon, such that the balance is Pt. The total target metal loading on carbon was 30 wt%.

Catalysts	Target Ru wt%	Actual Ru wt%	Actual Ru at%
Pt_{100}/C	0	0	0
$Pt_{90}Ru_{10}/C$	12.5	6	10
$Pt_{78}Ru_{22}/C$	25	13	22
$Pt_{63}Ru_{37}/C$	37.5	23	37
$Pt_{48}Ru_{52}/C$	50	36	52

To confirm that Pt_xRu_y/C alloys are synthesized, ex-situ EXAFS is employed to measure the local coordination of Pt and Ru atoms. The EXAFS spectra of the Pt L_3-edge for Pt_xRu_y/C in real space are shown in **Figure 4.1a**, and the corresponding Pt L_3-edge EXAFS in *k*-space and the imaginary components are shown in **Figure A1**. Both the Pt foil and Pt_{100}/C show a single peak between 2.5–3.0 Å (**Figure 4.1a**), which can be attributed to first shell Pt-Pt scattering. The Pt foil is scaled by a factor of 0.5 to aid visual comparison to the spectra of the nanoparticle catalysts, where the Pt-Pt coordination numbers and thus EXAFS amplitudes are smaller. The larger peak amplitude at lower *R* for the Pt_{100}/C compared to Pt foil is attributed to Pt-O scattering. The inclusion of Ru during the catalyst synthesis causes a second peak to manifest between 2.5–3.0 Å, which corresponds to Pt-Ru scattering paths.

By fitting the EXAFS data using Pt-Pt, Pt-O, and Pt-Ru paths, we extract the Pt-Pt and Pt-Ru coordination numbers and bond distances. The presence of Pt-Ru first-shell coordination by EXAFS indicates these materials are alloys, rather than separate phases of Pt and Ru. Because there is less Ru than Pt in the alloys, the Ru K-edge EXAFS data had low signal and is too noisy to accurately fit. The data in **Figure 4.1b** and **Figure 4.1c** show the XANES of Pt L_3- and Ru K-edges for the catalyst samples, respectively. The increase in the white line intensity for the Pt_xRu_y/C samples compared to bulk metallic Pt and Ru foils reveal that these samples are slightly

oxidized ex-situ. This slight oxidation is expected for small metal nanoparticles and typically is attributed to surface oxides that will be reduced electrochemically during pretreatment prior to reaction. The oxidized nature of the Pt_xRu_y/C samples from XANES is consistent with the observation of Pt-O scattering from EXAFS in **Figure 4.1a**.

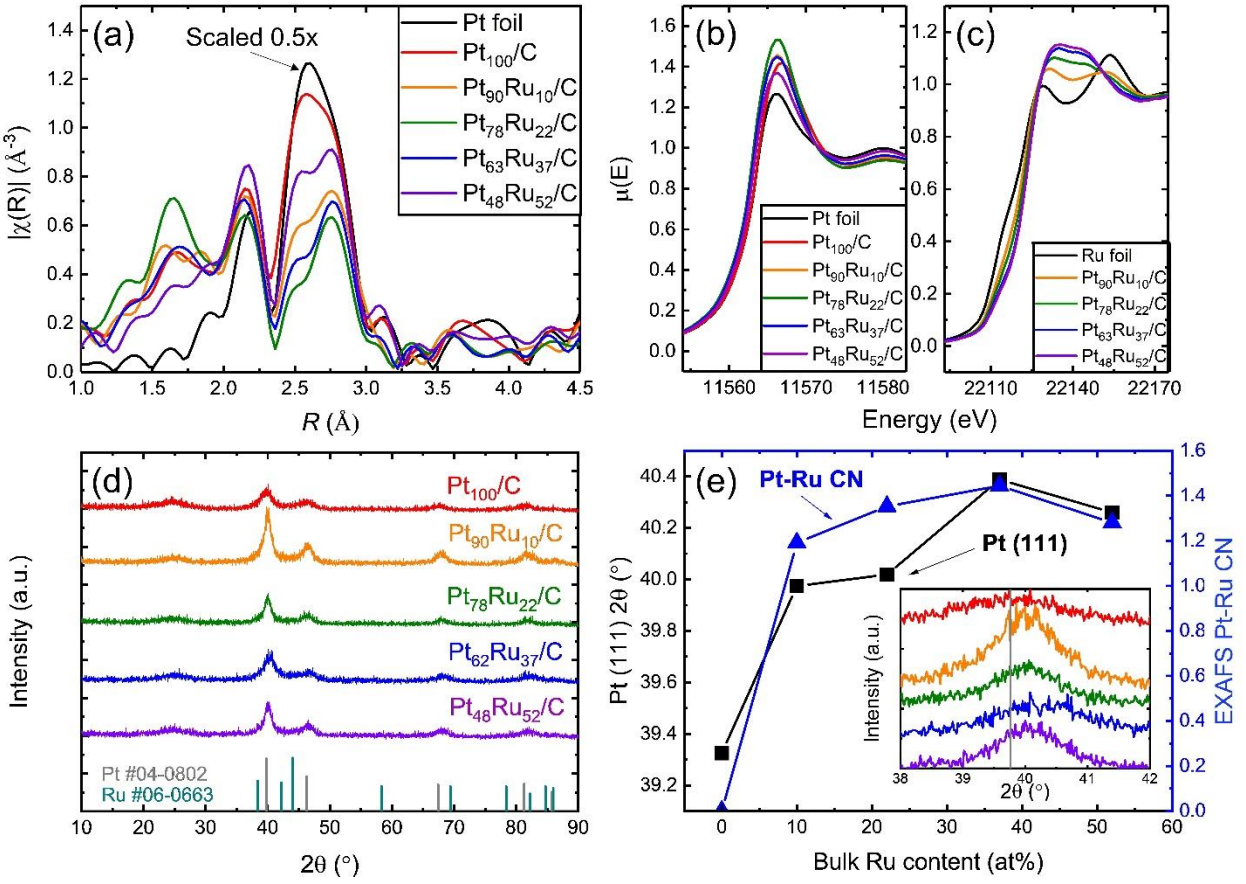

Figure 4.1. (a) *k*-weighted |χ(R)| spectra of ex-situ Pt_xRu_y/C catalysts in real space (unadjusted). The signal of the Pt foil in the EXAFS is rescaled by 0.5× to aid comparison against the synthesized Pt_xRu_y/C catalysts. XANES spectra for catalysts at **(b)** Pt L_3-edge and **(c)** Ru K-edge showing partial oxidation. **(d)** XRD spectra of Pt_xRu_y/C with Pt #04-0802 and Ru #06-0663 standards in gray and teal, respectively, and **(e)** location of the Pt(111) peak from XRD and the Pt-Ru coordination number (CN) from EXAFS shown vs. bulk Ru content. The inset provides a local magnification around the Pt(111) peak between 38 – 42°, and the gray line represents Pt #04-0802 standard. All labels for Ru content are based on actual Ru atomic percent provided in **Table 4.2**.

The XRD patterns for different compositions of the Pt_xRu_y/C display a shift in the Pt(111) diffraction patterns to higher 2θ as the Ru at% increases (**Figure 4.1d**). The shift indicates a change

in lattice constants that corresponds to alloying Ru atoms into the Pt lattice, as expected from Vegard's Law (**Figure 4.1e**). At higher atomic Ru content (> 50 at%), there is a deviation from the linear shift predicted by Vegard's Law, possibly because of a limit to the amount of Ru that can be incorporated into Pt without phase segregation.[36] The Pt-Ru coordination number determined from EXAFS and the diffraction location from XRD are correlated, **Figure 4.1e**. We do not directly compare the EXAFS and XRD distances because the EXAFS gave Pt-Pt and Pt-Ru bond distances from fitting and XRD gave an averaged shift of the metal lattice constant. Taken together, the Pt-Ru coordination from EXAFS and the lattice shift from XRD support the formation of different compositions of Pt_xRu_y/C alloys. The broadening of the four main Pt diffraction peaks between 30–90 2θ° in the XRD is also used to calculate the diameters (3–6 nm from the Scherrer equation) of the nanoparticles (**Table 4.3**). These particle sizes are consistent with the expected particle sizes from the combined coordination number of Pt-Pt and Pt-Ru from EXAFS.[44,45]

Table 4.3. Particle sizes from XRD using Scherrer equation, TEM, and EXAFS from first shell Pt-metal coordination number.

Catalyst	XRD particle size (nm)	TEM particle size (nm)	EXAFS particle size (nm)
Pt_{100}/C	3.5 ± 0.6	—	
$Pt_{90}Ru_{10}$/C	5.0 ± 1.0	4.3 ± 1.4	
$Pt_{78}Ru_{22}$/C	5.7 ± 1.0	4.0 ± 1.1	1.5–5.0 for all catalysts
$Pt_{62}Ru_{37}$/C	3.2 ± 0.7	3.9 ± 1.0	
$Pt_{48}Ru_{52}$/C	4.7 ± 1.3	3.6 ± 0.9	

The TEM images in **Figure 4.2** reveal that the synthesis resulted in Pt_xRu_y nanoparticles on the Vulcan carbon support that range from 3–5 nm in size, which agrees with XRD calculations and EXAFS analysis (**Table 4.3**). Alloying with Ru could change the fractional exposure between different Pt_xRu_y catalysts. Thus, measuring the ECSA and surface composition is important to obtain area-normalized intrinsic activities for the alloys, which we investigate in the next section.

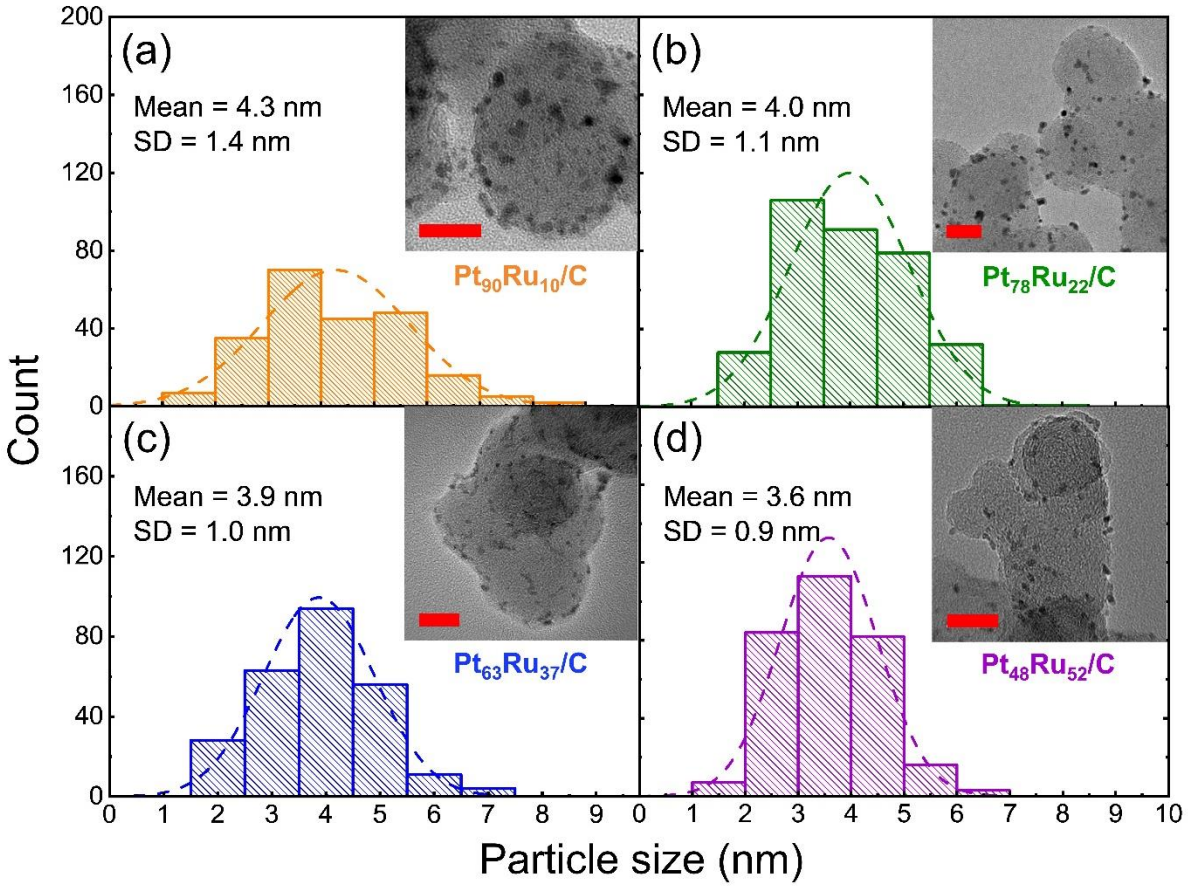

Figure 4.2. Particle size distributions from TEM for **(a)** $Pt_{90}Ru_{10}$/C, **(b)** $Pt_{78}Ru_{22}$/C, **(c)** $Pt_{63}Ru_{37}$/C, and **(d)** $Pt_{48}Ru_{52}$/C. The red scale bar indicates 20 nm in the micrograph. SD = standard deviation.

4.3.2 Surface Characterization of the Supported Pt_xRu_y Alloys

Knowledge of the Pt_xRu_y/C surface composition is important to enabling a mechanistic understanding of ENO_3RR and comparison to atomistic modeling predictions. In many Pt_xRu_y systems, changing the synthesis temperature or support can drastically alter the level of Pt-surface enrichment.[46] Thus, alloys with the same bulk composition may have different levels of activity depending on the composition of the metals on the surface that catalyze the reaction. Consequently, it is essential to determine the surface compositions and number of active sites to compare intrinsic activities among different alloys.

Accurately determining the ECSA allows us to count the number of surface Pt and Ru sites, which serves to both normalize measured activity for qualitative comparison to theory and quantify

the surface composition. Because each surface Pt atom adsorbs approximately one hydrogen atom, the charge associated with hydrogen adsorption and desorption is often used to calculate the ECSA.[47,48] However, this well-known H_{upd} technique is unsuitable for Ru-based materials due to overlapping hydrogen and ruthenium oxidation currents.[49] Additionally, more than one monolayer of hydrogen may adsorb onto Ru sites. To overcome this challenge for Pt_xRu_y/C alloys, copper underpotential deposition (Cu_{upd}) is used because there is roughly one Cu atom electrodeposited per surface Pt or Ru site (**Figure 4.3a**).[50] We ensured that no Cu adsorbed to the surface of the carbon support (**Figure 4.3b**), and determined that a single monolayer of Cu adsorbs on Pt_{100}/C at 0.42 V vs. RHE based on a charge ratio of Cu:H = 2 (**Figure 4.3c**). Cu_{upd} was also performed at different scan rates to ensure there was no significant impact on the measured ECSA (**Figure 4.3d**).

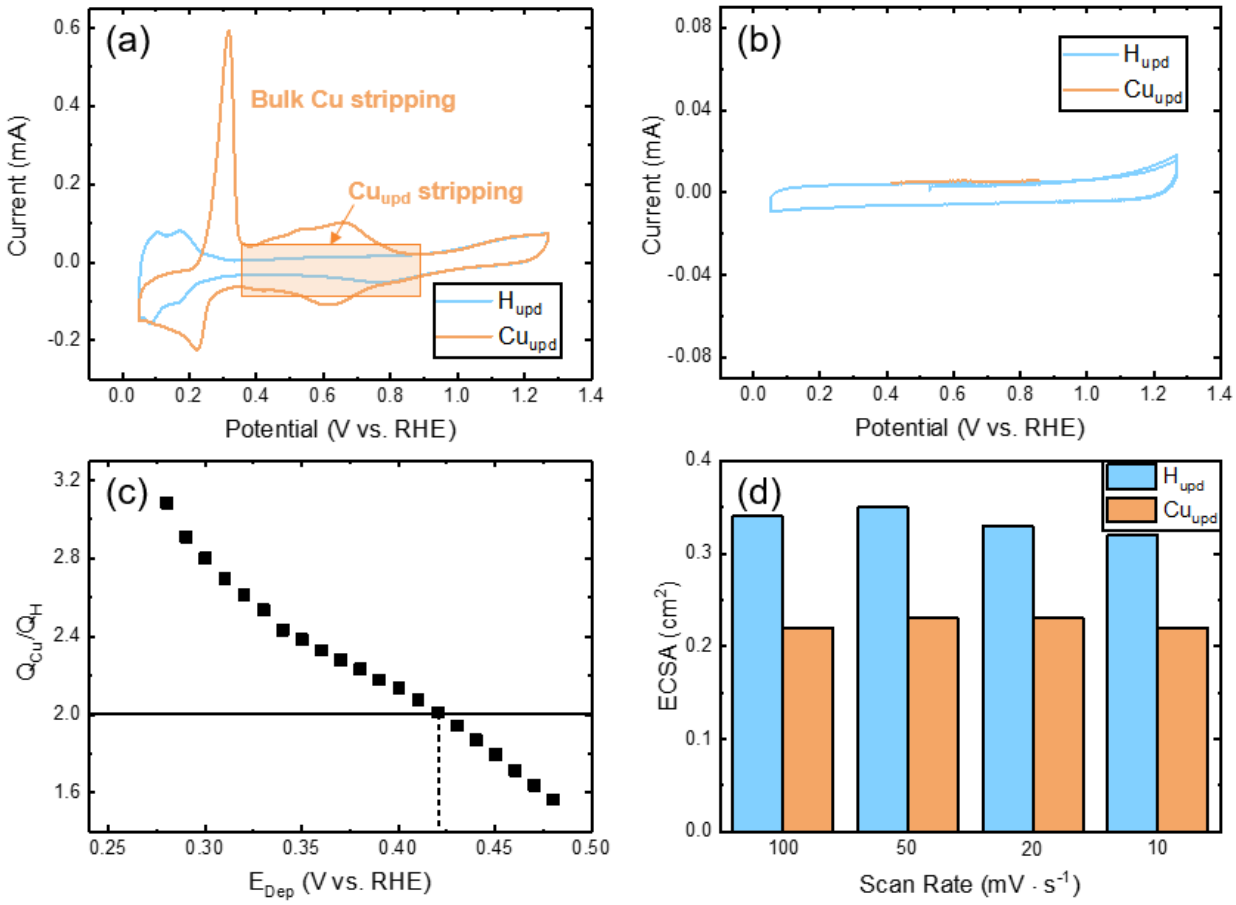

Figure 4.3. Electrochemical surface area measurements. All H_{upd} and Cu_{upd} experiments are performed in 0.1 M H_2SO_4 and 0.1 M H_2SO_4 + 2 mM $CuSO_4$, respectively. **(a)** H_{upd} (blue) and Cu_{upd} (orange) experiments of Pt_{100}/C at 100 mV s^{-1} scan rate. The peak at 0.3 V vs. RHE represent bulk Cu stripping, whereas the smaller peaks from ~0.4–0.8 V vs. RHE is the Cu_{upd} region (highlighted box). **(b)** H_{upd} CV and Cu_{upd} LSV baseline on Vulcan carbon at 100 mV s^{-1} scan rate. **(c)** A ratio of copper underpotential deposition desorption charge (Q_{Cu}) and hydrogen underpotential desorption charge (Q_H) on Pt_{100}/C was used to the find the deposition potential for a monolayer of adsorbed Cu. E_{Dep} is the applied deposition potential for 120 seconds. **(d)** H_{upd} and Cu_{upd} ECSAs at varying scan rates for commercial PtRu/C.

We selected 0.42 V vs. RHE as the deposition potential for all Pt_xRu_y/C catalysts. This choice seems reasonable based on close agreement between the ECSA results using Cu_{upd} and H_{upd} at low Ru%. Even though the selected deposition potential may slightly change the ECSA (Δ10 mV in deposition potential is ± 0.014 cm^2 in ECSA), we do not believe it would significantly impact the changes observed in the measured activities of the alloy. After measuring the charge of

the Cu_{upd} peak, the ECSA is calculated by assuming that a single Cu atom will bind to Pt or Ru with a 1:1 ratio and that two electrons are transferred from Cu^{2+}.

The Cu_{upd} values used to normalize the current activity are determined prior to kinetic experiments performed in fresh electrolyte solution. Due to the small differences in the amount of catalyst deposited on the glassy carbon electrode and contact with the electrolyte solution, the ECSA may vary up to 30% from run to run, so we report activities normalized to the ECSA from a particular run. The normalized current densities for each catalyst were reproducible when normalizing to the ECSA for that deposition.

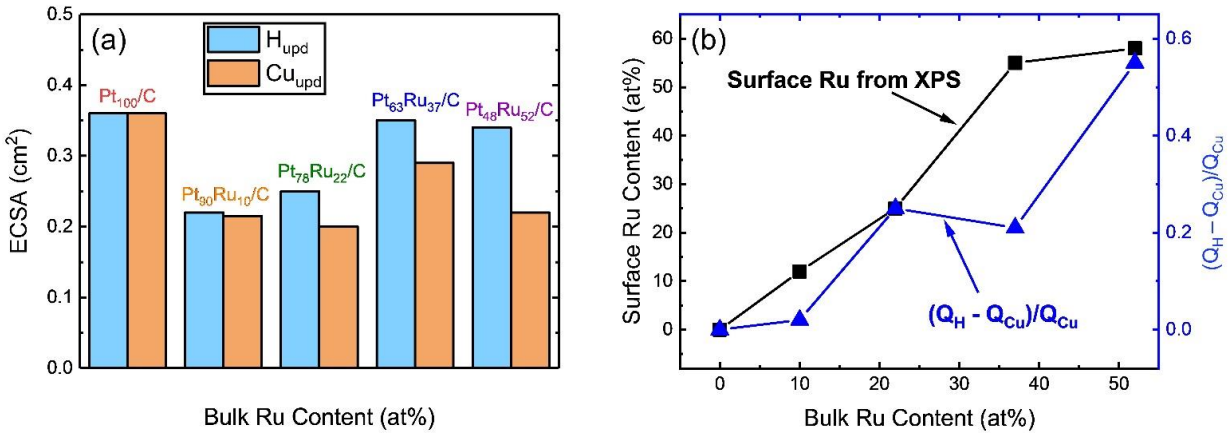

Figure 4.4. (a) Electrochemically active surface areas (ECSAs) of Pt_xRu_y/C catalyst glassy carbon electrode determined using hydrogen underpotential deposition (H_{upd}) and copper underpotential deposition (Cu_{upd}). **(b)** Ru surface at% from XPS measurements and discrepancy between the copper underpotential deposition charge (Q_{Cu}) and hydrogen underpotential deposition charge (Q_H) normalized to Q_{Cu} as a function of bulk Ru composition.

The measured ECSAs from both H_{upd} and Cu_{upd} are shown in **Figure 4.4a**. Regardless of the measurement technique, the ECSA for the five different compositions of Pt_xRu_y/C catalysts ranges between 0.20−0.35 cm^2, which is lower than the ECSA for commercial Pt/C and PtRu/C catalysts. The H_{upd} and Cu_{upd} ECSA measurements increasingly disagree as the bulk Ru at% increased. This phenomenon is attributed to more than one hydrogen adsorbing per Ru site, such that H_{upd} overcounts the ECSA when Ru is present on the surface, causing a disagreement between

H_{upd} and Cu_{upd} that increases with increasing surface Ru. The increasing discrepancy between H_{upd} and Cu_{upd} charge $((Q_H - Q_{Cu})/Q_{Cu})$ is shown in **Figure 4.4b**, which correlates with increased surface Ru at% as the bulk Ru at% increases. Likewise, the surface composition from ex-situ XPS shows a similar trend as bulk Ru at% increases. The qualitative agreement between the ex-situ XPS Ru surface composition and the Ru surface composition in electrolyte implies minimal restructuring of the surface upon exposure to the supporting electrolyte. The Cu_{upd} ECSAs measured here were used to normalize the activity of the catalysts reported in the next section unless specified otherwise.

4.3.3 Effect of Ru Alloying on Intrinsic Nitrate Reduction Activity

The data in **Figure 4.5a** shows the steady-state nitrate reduction current densities normalized to the ECSA from Cu_{upd} for five different compositions of Pt_xRu_y/C catalysts at 0.05 to 0.4 V vs. RHE in 1 M H_2SO_4 + 1 M $NaNO_3$. These measurements are made by drop-casting the catalyst onto a glassy carbon disk electrode with a Nafion binder and operating under rotation rates sufficient to eliminate external mass transfer limitations. The objective of this work is to study electrocatalytic nitrate reduction, so current densities for potentials less than 0.05 V vs. RHE are not considered due to possible interference with current from hydrogen evolution. There is no observable reduction current at the potentials specified in **Figure 4.5a** in the absence of nitrate. Therefore, the current density reported here is attributed solely to nitrate reduction. Pt_{100}/C and $Pt_{48}Ru_{52}/C$ are compared to commercial catalysts of the same composition (**Figure 4.6**) to confirm that our synthesized materials have similar intrinsic activities as their commercial counterparts when the rates are normalized to the number of available surface sites.

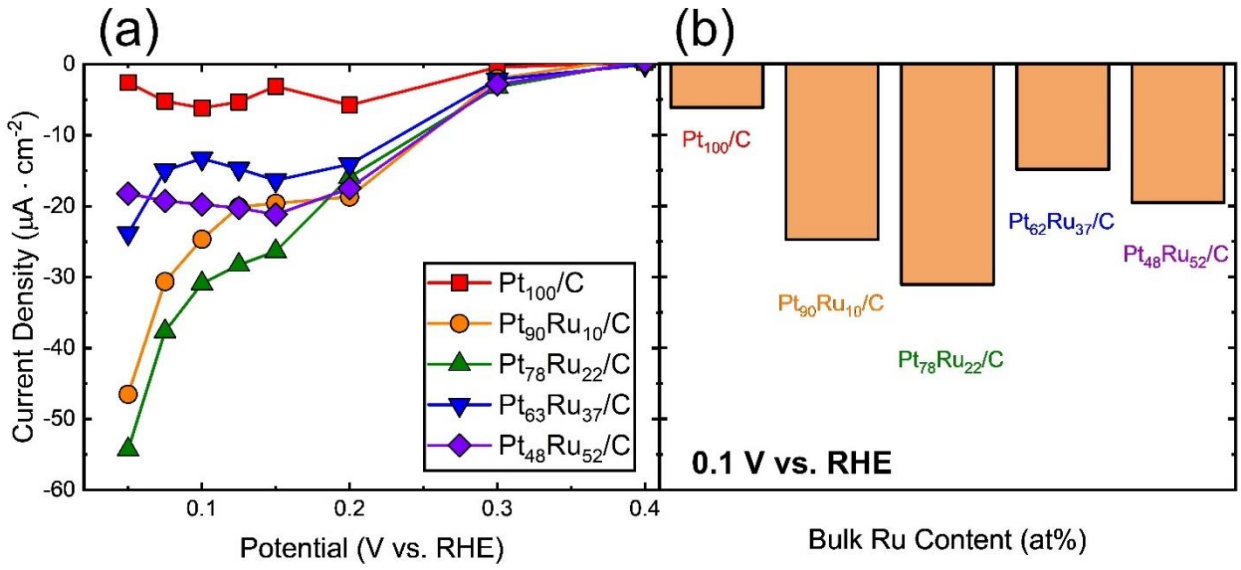

Figure 4.5. (a) Steady-state nitrate reduction current densities in 1 M $NaNO_3$ and 1 M H_2SO_4 at eight operating potentials between 0.05 to 0.4 V vs. RHE for Pt_xRu_y/C catalysts, as normalized by Cu_{upd}. **(b)** Reduction current density at 0.1 V vs. RHE for five compositions of Pt_xRu_y/C alloys with Cu_{upd} normalization.

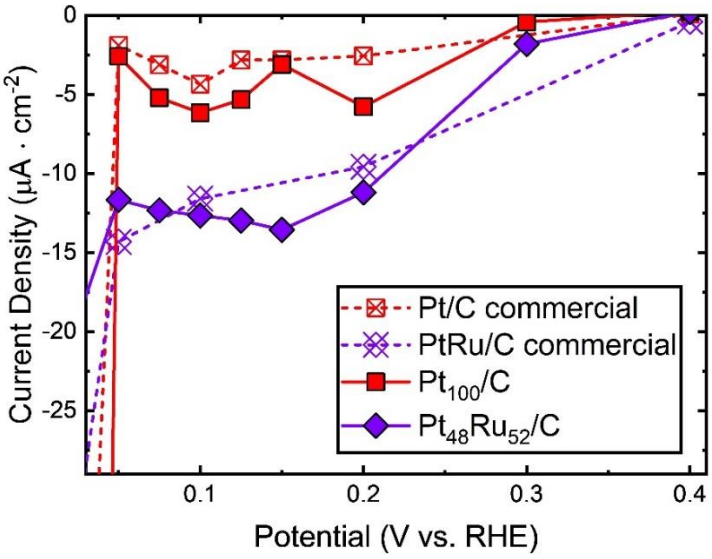

Figure 4.6. Comparison of current densities between synthesized catalysts and their commercial counterparts. The activities were tested in 1 M H_2SO_4 + 1 M $NaNO_3$ and currents were normalized by H_{upd}.

The steady-state current densities for Pt_{100}/C are comparable with other Pt/C reports and reach a maximum activity at 0.1 V vs. RHE.[24,25] This maximum in activity arises from the competition between adsorbed nitrate and hydrogen, with 0.1 V vs. RHE being the potential when

both species are considerably present on the surface.[51] Below 0.1 V, the reaction rate decreases because there is a low coverage of nitrate on the Pt, and surface sites are blocked by adsorbed hydrogen. Above 0.1 V, the reaction rate decreases because there is not enough hydrogen available on the surface. Unlike the Pt_{100}/C, none of the Pt_xRu_y/C alloys exhibit a maximum activity at 0.1 V vs. RHE. We hypothesize this is because, similar to Rh, these Pt_xRu_y alloys bind nitrate more strongly than pure Pt, which shifts the maximum activity to a more negative potential.[52] The stronger adsorption of nitrate and shift in potential of maximum activity of the Pt_xRu_y alloys is expected because Ru is less noble than Pt and is supported by our DFT calculations (discussed below). Importantly, the Pt_xRu_y/C alloys are more active than Pt_{100}/C at all eight applied potentials, confirming our previous DFT modeling predictions that Pt_3Ru would be more active than Pt for ENO_3RR.[25]

In **Figure 4.5b**, the current density for the alloys at 0.1 V vs. RHE, normalized to ECSA from Cu_{upd}, is shown as a function of Ru content. The general trends of the intrinsic activity of the alloys indicate a maximum ("volcano") behavior where $Pt_{78}Ru_{22}$/C has six times the activity than that of Pt_{100}/C when normalized by the ECSA from Cu_{upd} (discussed below). The activities of $Pt_{48}Ru_{52}$ and $Pt_{62}Ru_{37}$ are similar because the two materials displayed comparable surface compositions from XPS. However, we can more accurately extract bulk Ru at% from ICP-MS than surface Ru at% from XPS. Thus, the bulk at% was used as the naming convention of the alloys. Ru/C was also tested, but Ru leached into the acidic electrolyte solution throughout the experiment, making it impossible to accurately obtain steady-state measurements or determine active surface areas. Cyclic voltammograms of the alloy catalysts remained consistent after multiple cycles, suggesting that the alloy catalysts were stable prior to steady-state measurements.

Rh/C, the most active pure metal standard, is four times more active than $Pt_{78}Ru_{22}$/C (**Figure 4.7a**) at 0.1 V vs. RHE. However, because Rh is currently the most expensive noble metal, the catalyst cost is twice as much to convert one mole of nitrate in an hour using Rh/C compared with $Pt_{78}Ru_{22}$/C (**Figure 4.7b**). Pt/C on the other hand would be the most expensive of the considered catalysts, costing almost three times more than Rh/C to have the same total ENO_3RR conversion. This high cost is largely due to the low ENO_3RR activity of Pt/C.

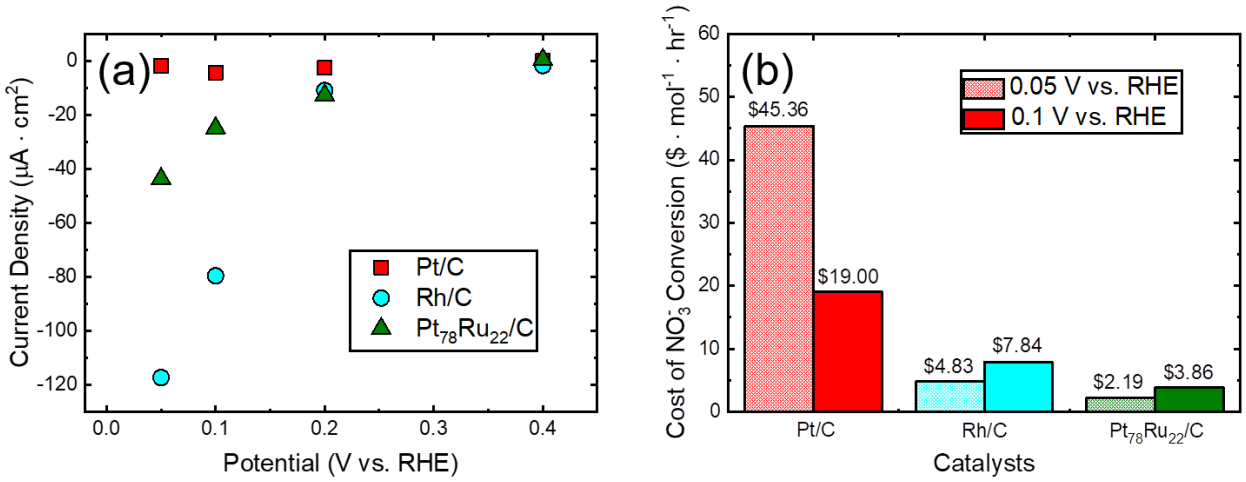

Figure 4.7. Technoeconomic comparison of Pt/C, Rh/C, and $Pt_{78}Ru_{22}$/C. **(a)** The current densities for commercial Pt/C, Rh/C, and synthesized $Pt_{78}Ru_{22}$/C catalysts reported at four different applied potentials. The electrolyte solution consisted of 1 M H_2SO_4 + 1 M $NaNO_3$. The measured currents were all normalized via H_{upd} of the active sites. **(b)** Metal cost to purchase sufficient catalyst to convert 1 mole of NO_3^- per hour based on activity of catalysts at 0.05 V vs. RHE and 0.1 V vs. RHE. To perform this analysis, a fractional exposure of 0.5 was assumed.

Another major component of evaluating the economics of different ENO_3RR electrocatalysts is the cost of electricity, which will depend on the overvoltage required and the FE of a given electrocatalyst. At an industrial electricity price of $0.07/kWh, a 0.1 V increase in overvoltage is equivalent to between 1 to 5 cents of additional cost per kilogram product.[19] Additionally, running the reaction at potentials more negative than 0 V vs. RHE results in hydrogen evolution, decreasing the amount of ENO_3RR product formed. The electricity cost per ton of producing NH_4NO_3 from ENO_3RR on both the Pt/CF and $Pt_{78}Ru_{22}$/CF (assuming oxygen evolution

as the oxidation reaction) is less than that of a recently published Ti catalyst, due to the lower overpotential required on the Pt-based catalysts (**Table 4.4**). The electricity cost using any of these electrocatalysts and the specified conditions is less than the current commercial price of NH_4NO_3.[53] However, Ti is much cheaper than platinum group metals, and therefore a full technoeconomic analysis must be performed to determine which systems are more economically viable.

Table 4.4. Electricity cost of converting NO_3^- to NH_4NO_3 using different electrocatalysts. This analysis assumes the cost of industrial electricity to be \$0.07/kWh. Overpotential refers to the ENO_3RR overpotential and counter reaction is assumed to be oxygen evolution with 0.4 V overpotential. No resistance or mass transport overpotentials are assumed.

Catalyst	Overpotential (V)	Faradaic Efficiency (%)	Electricity Cost (\$/ton NH_4NO_3)
Pt/CF	0.72	98	\$293
$Pt_{78}Ru_{22}$/CF	0.72	94	\$305
Ti – McEnaney et al.[21]	1.82	82	\$600
Current cost from USDA data[53]	—	—	\$511

4.3.4 Rationalizing Activity Rrends with DFT and Microkinetic Modeling

On pure transition metals, linear adsorbate scaling relations (among N, O, and other reaction intermediates) and Brønsted-Evans-Polanyi relations (between adsorption and activation energies) exist for the ENO_3RR.[25] Consequently, a microkinetic model for ENO_3RR can predict trends in the reaction rates, steady-state coverages, and degrees of rate control given only the N and O binding energies and an applied potential.[54] Additional computational methods and results are provided in **Appendix B**.

We show that N and O binding energies also serve as ENO_3RR activity descriptors on Pt_xRu_y alloys because similar free energy scaling relations hold on our model Pt_xRu_y surfaces. Examining the sites of strongest binding energy, we find that Pt_xRu_y alloys approximately follow the same (i) linear adsorbate scaling relations among O, N, NO_3^-, and H and (ii) Brønsted–Evans–

Polanyi relations for nitrate-to-nitrite dissociation when compared to the pure-metal relations.[25] We specifically studied the nitrate dissociation step ($NO_3^* + * \rightleftarrows NO_2^* + O^*$), as this step is hypothesized to be rate-determining for ENO_3RR on pure transition metal surfaces under most conditions.[18] Geometries and energetics for the initial state, transition state, and final state configurations for nitrate dissociation on each alloy are provided in **Appendix B**. These findings suggest we can qualitatively use the volcano plot derived for pure metals to rationalize the activity of Pt_xRu_y alloys.

4.3.4.1 *Binding Energy Trends of O and N on Pt_xRu_y*

We use DFT modeling to examine how adsorption strength of O and N depends on Pt_xRu_y surface alloy composition. Understanding N and O adsorption trends is important to determine whether N and O binding energies serve as ENO_3RR activity trend descriptors on Pt_xRu_y alloys. The atomic distribution of Pt and Ru in each alloy's surface is generated using random assignment. DFT-predicted adsorption geometries for N*, O*, H*, and NO_3* are shown in **Appendix B**. We also studied H^+ and NO_3^- adsorption to show scaling relations between N and O. For each Pt_xRu_y alloy (as well as Ru(211) and Rh(211)), we sampled binding energies on all unique atop sites for N, O, and H and for all unique third-ridge atop bidentate sites for NO_3^-.

As the Ru content of the computational model alloy catalyst (denoted "s-Pt_xRu_y") increases, both N and O bind more strongly (**Figure 4.8a**). For example, s-$Pt_{75}Ru_{25}$ binds N and O more strongly than Rh(211) by ~0.15 and ~0.20 eV, respectively. The effect of Pt_xRu_y alloy composition on binding energies can be rationalized by the Nørskov-Hammer *d*-band model, which correlates an adsorbate's binding energy to the catalyst's *d*-band center.[55] The *d*-band model predicts that a catalyst with higher *d*-band center energy relative to the Fermi level will result in adsorbate antibonding states that are also higher in energy, which increases the chemisorption

binding energy. The *d*-band center of Ru is higher in energy than that of Pt. Consequently, alloying Pt with Ru is expected to increase the prevalence of sites that adsorb reactants and intermediates stronger than pure Pt. Ru(211) binds N and O more strongly than any of the Pt_xRu_y alloys. The stronger adsorption on Ru(211) is consistent with its higher-energy *d*-band center.

In a related way, the O and N binding energies for Pt_xRu_y alloys of intermediate compositions can also be rationalized by ensemble effects at the surface of each model slab. N, O, H, and NO_3^- usually prefer bridge binding positions between two atoms in the highest FCC(211) ridge or a hollow position inside three atoms on the catalyst surface. The pair or trio of surface atoms locally bound to the adsorbate largely dictates the binding energy. For NO_3^-, binding is weakest when bound to a Pt-Pt ensemble, significantly stronger for Pt-Ru ensembles, and strongest for Ru-Ru ensembles. As expected, binding energy varies more with the type of ensemble locally bound to NO_3^- than to nonlocal changes in surface composition. The same trends hold for the other adsorbates. As the surface composition of Ru increases, the probability of finding a Pt-Ru, Ru-Ru, Pt-Ru-Ru, Ru-Ru-Ru, or other Ru-rich ensemble increases. Thus, Pt_xRu_y alloys of intermediate macroscopic Ru compositions are likely to have many microscopic coordination environments that bind N and O with intermediate adsorption strengths. Based on the linear adsorbate and BEP relationships, we thus predict that these same surfaces will also bind NO_3^- and H^+ with an intermediate strength that maximizes ENO_3RR activity.

4.3.4.2 *Rationalizing Activity Rrends with Alloy Composition by Microkinetic Modeling*

We rationalize the ENO_3RR activity as a function of surface composition (**Figure 4.8a**) using a theoretical volcano plot at 0.1 V vs. RHE in **Figure 4.8b** based on our previous work.[25] Microkinetic modeling details to generate the theoretical volcano plot are provided in **Appendix B**. The contours in **Figure 4.8b** indicate predicted catalyst turnover frequency (TOF) with respect

to NO_3^- consumption as a function of N and O binding energy. Overlaid points indicate the O and N binding energies of the model catalysts considered. The points labeled "s-Pt_xRu_y" represent the simulated random surface alloy model catalysts, and Rh(211), Ru(211), and Pt_3Ru(211) values are shown for comparison. The predictions in **Figure 4.8b** suggest that ENO_3RR activity should go through a maximum as Ru content is increased and the O and N adsorption strength is increased. s-Pt_{100} corresponds to a relatively low turnover frequency (TOF), which initially increases as more Ru is added to the surface. The TOF reaches a maximum for s-$Pt_{75}Ru_{25}$ and drops as the Ru fraction increases further. The nitrate reduction current density on our synthesized Pt_xRu_y/C alloys at 0.1 V vs. RHE increases with Ru content at low Ru compositions but decreases when more than 22 at% Ru is incorporated into the alloy. The qualitative agreement of the computed TOF trend with the trend in steady-state current measurements (from **Figure 4.5b**) is shown in **Figure 4.8c**.

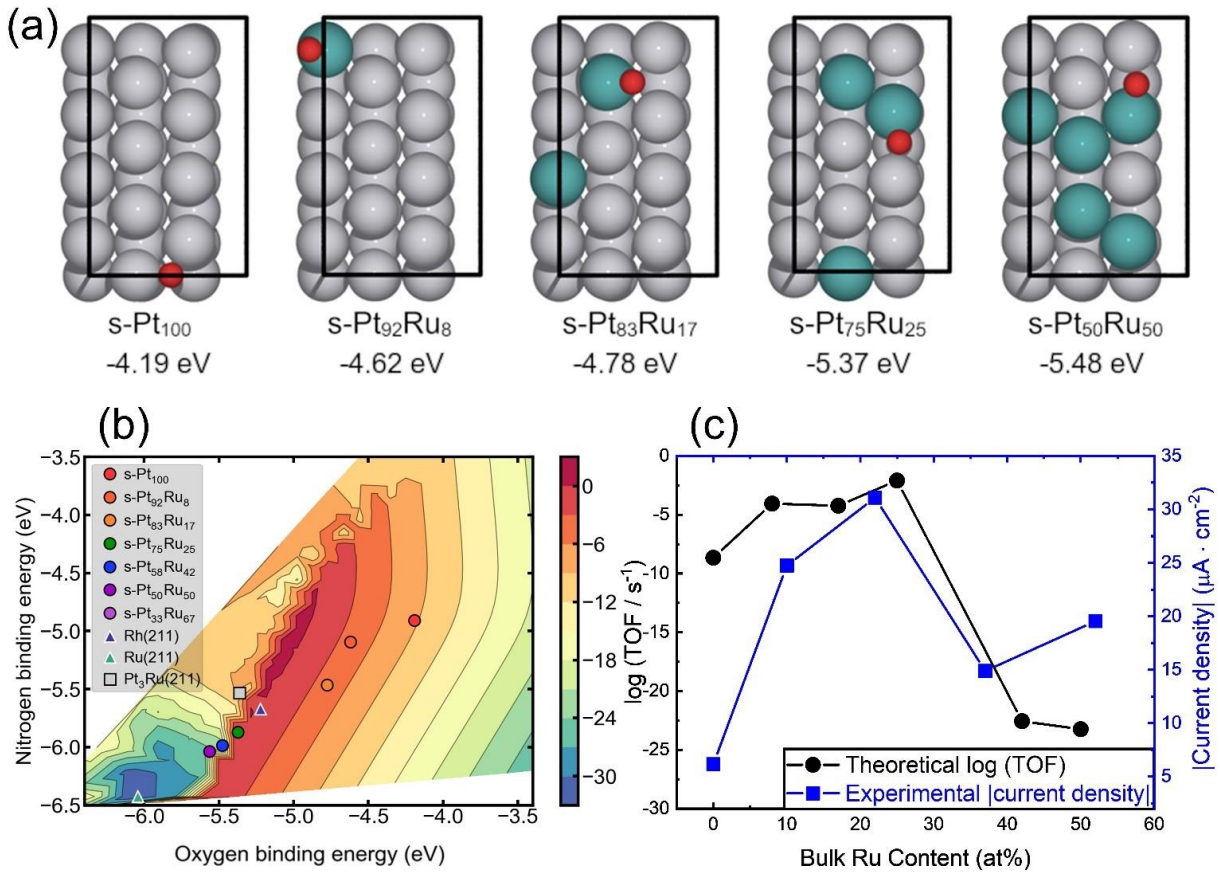

Figure 4.8. (a) Binding energies and geometry of the strongest-binding adsorbed O positions for (211) Pt_xRu_y surface slab models (denoted "s-Pt_xRu_y") with Ru content up to 50 at%. Solid black line denotes the supercell. Atom color legend: gray = Pt and teal = Ru. **(b)** ENO_3RR volcano plot contours are at 0.1 V vs. RHE and are reproduced based on data from ref. [25]. Each point represents the strongest predicted binding energy on a specified Pt_xRu_y random surface alloy or pure metal surface, for Ru surface compositions up to 50 at% (the same range as in experiment). **(c)** Comparison between the log (TOF / s^{-1}) values calculated from DFT and the magnitude of the current densities obtained via experimental results at 0.1 V vs. RHE as a function of bulk Ru at%. Similar comparison as a function of surface Ru at% is shown in **Appendix A, Section A7**. Active sites were detected and normalized by Cu_{upd}.

A volcano in activity with alloy composition occurs because alloying tunes the binding energies of reactants and key intermediates, and these binding energies are related to the barriers of individual elementary steps through free energy relations. The activity is maximized at some intermediate binding energy of O and N (**Figure 4.8b**). This is an expression of the Sabatier principle, which posits that the most active Pt_xRu_y alloy should adsorb NO_3^- and H^+ neither too strongly nor too weakly. Regions of the volcano plot with lower TOFs usually imply that some elementary step in the reaction mechanism limits the total rate. Where the TOF is maximized (at

the "peak" of the volcano), no single step limits the overall rate. The transition from one side of the volcano peak to the other often indicates where different elementary steps in the mechanism become rate-determining. For Pt, where nitrate binds weakly, the hypothesized rate-limiting step is nitrate dissociation ($NO_3^* + * \rightarrow NO_2^* + O^*$). Increasing the nitrate adsorption strength (described by the N and O binding energy) by alloying Pt with Ru increases the rate of overall reaction by increasing nitrate coverage and accelerating nitrate dissociation up to some maximum. We would expect that beyond the volcano peak, the adsorbed species start to bind too strongly, and another elementary step would become rate-determining. This new rate-determining step's rate would decrease as N and O adsorption strengths continue to increase. It is also possible that multiple steps have high degree of rate control as Ru content increases, including desorption or reaction of intermediates.

The degree to which any elementary step in the reaction mechanism determines the total activity can be estimated by computing the degree of rate control (DRC) for that reaction.[56] Our DRC analysis in this work at 0.1 V vs. RHE predicts that for surfaces with low Ru content, nitrate dissociation is rate-limiting ($DRC \approx 1$), and increasing the adsorption strength of nitrate increases the rate. But at higher Ru content, when the O and N (and consequently nitrate) binding energies are strong, the nitrate dissociation step is sufficiently fast, and increasing the rate of that elementary step no longer increases the overall rate. For Ru content greater than 25 at%, our DRC analysis predicts that the association of surface-bound N^* ($2\ N^* \rightleftarrows N_2^*$) becomes the new rate-determining step. Under these conditions, further strengthening the nitrate binding energy (as described by N and O binding energies) reduces activity.

Although the computational results predict that N_2 is the dominant species forming at high Ru contents and strong O and N adsorption, our experimental selectivity results discussed in the

following section show that NH_3 is the dominant product for all the alloy catalysts tested. Therefore, it is unlikely that the new rate-determining step is the association of nitrogen, but rather another step on the ammonia production reaction pathway. We observe that $NH_2^* + H^+ + e^- \rightleftarrows NH_3^*$ is also rate-determining for surfaces with similar adsorption energies to s-$Pt_{75}Ru_{25}$, which is in line with our experimental observations and previous reports of this step being rate controlling for CuNi alloys.[33] We attribute this DRC discrepancy to uncertainties in the linear scaling relationships for alloys and to the fact that activity trends are easier to predict with microkinetic modeling compared to selectivity trends. Nevertheless, the switch from one rate-limiting step to another at the binding energies of s-$Pt_{75}Ru_{25}$ rationalizes the experimentally observed local maximum in activity at that composition.

4.3.5 Nitrate Reduction Selectivity of Pt_xRu_y alloys

To determine selectivity for the catalysts, we increase the catalyst loading on the electrodes by depositing the alloys on high surface area carbon felts. The higher ECSA enables sufficiently high currents to produce detectable concentrations of ENO_3RR products in the aqueous electrolyte solution. **Figure 4.9a** displays the catalyst FE towards nitrite, ammonia, and other potential gas-phase products after applying a potential of 0.1 V vs. RHE for seven hours. At this operating potential, hydrogen is not thermodynamically favorable to form, and there was no significant change in the concentration of nitrate due to the large volume of the electrolyte solution.

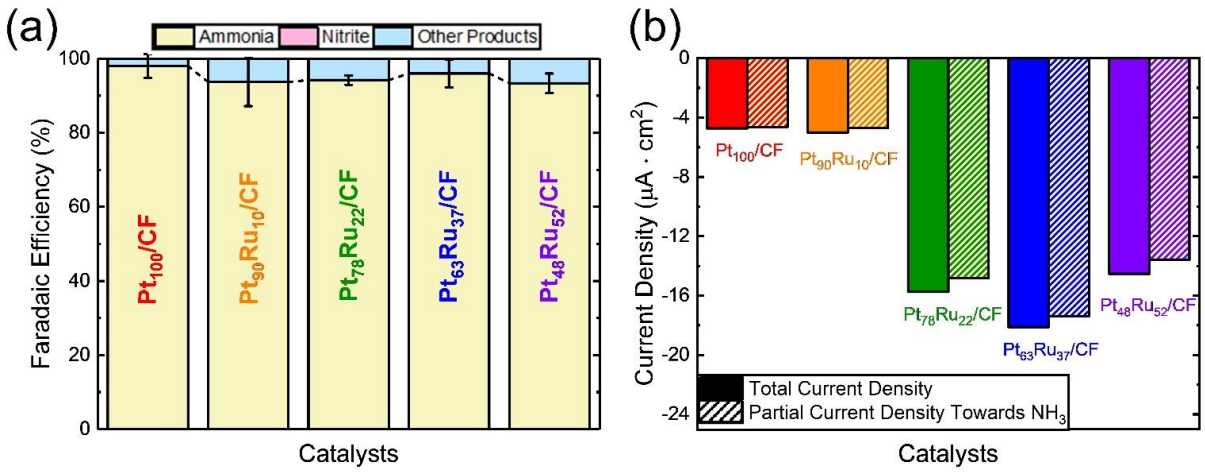

Figure 4.9. (a) The faradaic efficiency (FE) towards ammonia production for five different Pt_xRu_y compositions supported on carbon felt (CF) after applying 0.1 V vs. RHE for seven hours in 0.1 M HNO_3. No nitrite was detected using ion chromatography and "Other Products" make up the potential gas-phase products that were not examined. **(b)** Total (solid bars) and partial (striped bars) current densities towards ammonia production with Pt_xRu_y/CF. Normalized to the ECSA from Cu_{upd}.

The FE towards NH_3 production was calculated by averaging the last three time points (**Figure 4.10**). Most of the current is attributed to NH_3 production and nitrite is not detected, though it is possible that nitrite in the solution has formed NO on the surface of the electrode.[57,58] The pure Pt has nearly 100% FE to NH_3, as has been previously reported at low overpotentials,[59] and the alloy materials all display above 93% FE towards NH_3.

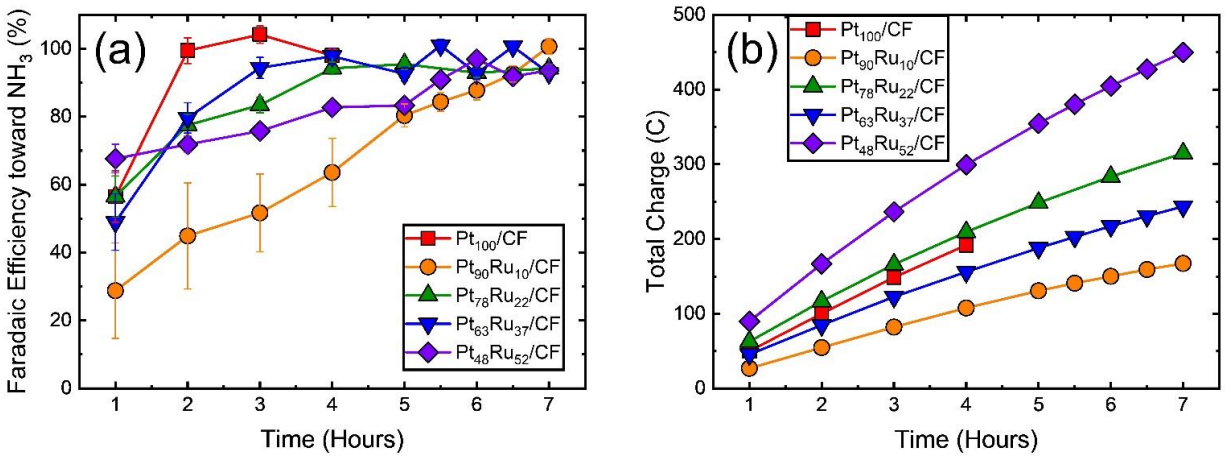

Figure 4.10. Performance of Pt_xRu_y/CF over a seven-hour reaction. **(a)** Faradaic efficiency of Pt_xRu_y/CF towards NH_3 over seven hours at applied potential of 0.1 V vs. RHE. **(b)** Total charge of Pt_xRu_y/CF during the reaction.

The total current density for the Pt_xRu_y/CF shown in **Figure 4.9b** follows a similar trend in Ru content as observed on the RDE (**Figure 4.5**). The partial current density towards ammonia is also depicted, with the alloy catalysts containing Ru having greater activity towards ammonia production than pure Pt. The rates on catalysts on the carbon felts may be limited by internal diffusion because of the porosity and greater thickness of the carbon felt compared to the RDE, which would explain the slight differences between the activity trends of the two setups. Regardless, the inclusion of Ru into the Pt catalyst increases the rate of nitrate reduction up to a certain composition, after which further addition of Ru decreases the normalized catalytic activity.

4.4 Conclusions

Using predictions of electrocatalyst activity from a theoretical volcano plot, we synthesize and report a set of Pt_xRu_y/C alloys that are more intrinsically active than pure Pt for the electrocatalytic reduction of nitrate to ammonia in acidic conditions. The binding energy of ENO_3RR intermediates increases with the inclusion of Ru such that the most active Pt_xRu_y/C alloy binds the intermediates neither too strongly nor too weakly. Our findings suggest that alloy activity

for ENO_3RR can be qualitatively understood by the effect of alloying on the binding energies of nitrate and hydrogen. The best performing composition, $Pt_{78}Ru_{22}/C$, is six times more active than pure Pt while maintaining high FE towards ammonia (> 93%). The lower cost of Pt and Ru compared to Rh makes $Pt_{78}Ru_{22}/C$ a more cost-effective catalyst for ENO_3RR. By experimentally confirming the use of N and O thermodynamic descriptors and theoretical volcano plot to find active alloys, these findings provide a blueprint to rationally select alloy compositions to find more active and less expensive/more earth-abundant materials for ENO_3RR.

4.5 References

(1) Garcia-Segura, S.; Lanzarini-Lopes, M.; Hristovski, K.; Westerhoff, P. Electrocatalytic Reduction of Nitrate: Fundamentals to Full-Scale Water Treatment Applications. *Applied Catalysis B: Environmental* **2018**, *236*, 546–568. https://doi.org/10.1016/j.apcatb.2018.05.041.

(2) Lehnert, N.; Dong, H. T.; Harland, J. B.; Hunt, A. P.; White, C. J. Reversing Nitrogen Fixation. *Nature Reviews Chemistry* **2018**, *2* (10), 278–289. https://doi.org/10.1038/s41570-018-0041-7.

(3) Schoeman, J. J.; Steyn, A. Nitrate Removal with Reverse Osmosis in a Rural Area in South Africa. *Desalination* **2003**, *155* (1), 15–26. https://doi.org/10.1016/S0011-9164(03)00235-2.

(4) Primo, O.; Rivero, M. J.; Urtiaga, A. M.; Ortiz, I. Nitrate Removal from Electro-Oxidized Landfill Leachate by Ion Exchange. *Journal of Hazardous Materials* **2009**, *164* (1), 389–393. https://doi.org/10.1016/j.jhazmat.2008.08.012.

(5) Chen, H.; Wang, D.; Li, X.; Yang, Q.; Zeng, G. Enhancement of Post-Anoxic Denitrification for Biological Nutrient Removal: Effect of Different Carbon Sources. *Environmental Science and Pollution Research* **2015**, *22* (8), 5887–5894. https://doi.org/10.1007/s11356-014-3755-1.

(6) Zhong, Y.; Li, X.; Yang, Q.; Wang, D.; Yao, F.; Li, X.; Zhao, J.; Xu, Q.; Zhang, C.; Zeng, G. Complete Bromate and Nitrate Reduction Using Hydrogen as the Sole Electron Donor in a Rotating Biofilm-Electrode Reactor. *Journal of Hazardous Materials* **2016**, *307*, 82–90. https://doi.org/10.1016/j.jhazmat.2015.12.053.

(7) Li, X.; Chen, H.; Yang, Q.; Wang, D.; Luo, K.; Zeng, G. Biological Nutrient Removal in a Sequencing Batch Reactor Operated as Oxic/Anoxic/Extended-Idle Regime. *Chemosphere* **2014**, *105*, 75–81. https://doi.org/10.1016/j.chemosphere.2013.12.043.

(8) Bao, Z.; Hu, Q.; Qi, W.; Tang, Y.; Wang, W.; Wan, P.; Chao, J.; Yang, X. J. Nitrate Reduction in Water by Aluminum Alloys Particles. *Journal of Environmental Management* **2017**, *196*, 666–673. https://doi.org/10.1016/j.jenvman.2017.03.080.

(9) Durkin, D. P.; Ye, T.; Choi, J.; Livi, K. J. T.; Long, H. C. D.; Trulove, P. C.; Fairbrother, D. H.; Haverhals, L. M.; Shuai, D. Sustainable and Scalable Natural Fiber Welded Palladium-Indium Catalysts for Nitrate Reduction. *Applied Catalysis B: Environmental* **2018**, *221*, 290–301. https://doi.org/10.1016/j.apcatb.2017.09.029.

(10) Ye, T.; Durkin, D. P.; Banek, N. A.; Wagner, M. J.; Shuai, D. Graphitic Carbon Nitride Supported Ultrafine Pd and Pd–Cu Catalysts: Enhanced Reactivity, Selectivity, and Longevity for Nitrite and Nitrate Hydrogenation. *ACS Applied Materials & Interfaces* **2017**, *9* (33), 27421–27426. https://doi.org/10.1021/acsami.7b09192.

(11) Su, L.; Li, K.; Zhang, H.; Fan, M.; Ying, D.; Sun, T.; Wang, Y.; Jia, J. Electrochemical Nitrate Reduction by Using a Novel Co3O4/Ti Cathode. *Water Research* **2017**, *120*, 1–11. https://doi.org/10.1016/j.watres.2017.04.069.

(12) Shimazu, K.; Goto, R.; Tada, K. Electrochemical Reduction of Nitrate Ions on Tin-Modified Platinum and Palladium Electrodes. *Chemistry Letters* **2002**, *31* (2), 204–205. https://doi.org/10.1246/cl.2002.204.

(13) Ghafari, S.; Hasan, M.; Aroua, M. K. Bio-Electrochemical Removal of Nitrate from Water and Wastewater—A Review. *Bioresource Technology* **2008**, *99* (10), 3965–3974. https://doi.org/10.1016/j.biortech.2007.05.026.

(14) Rezvani, F.; Sarrafzadeh, M.-H.; Ebrahimi, S.; Oh, H.-M. Nitrate Removal from Drinking Water with a Focus on Biological Methods: A Review. *Environmental Science and Pollution Research* **2019**, *26* (2), 1124–1141. https://doi.org/10.1007/s11356-017-9185-0.
(15) Osaka, T.; Shirotani, K.; Yoshie, S.; Tsuneda, S. Effects of Carbon Source on Denitrification Efficiency and Microbial Community Structure in a Saline Wastewater Treatment Process. *Water Research* **2008**, *42* (14), 3709–3718. https://doi.org/10.1016/j.watres.2008.06.007.
(16) Xu, D.; Li, Y.; Yin, L.; Ji, Y.; Niu, J.; Yu, Y. Electrochemical Removal of Nitrate in Industrial Wastewater. *Frontiers of Environmental Science & Engineering* **2018**, *12* (1), 9. https://doi.org/10.1007/s11783-018-1033-z.
(17) Yao, F.; Yang, Q.; Zhong, Y.; Shu, X.; Chen, F.; Sun, J.; Ma, Y.; Fu, Z.; Wang, D.; Li, X. Indirect Electrochemical Reduction of Nitrate in Water Using Zero-Valent Titanium Anode: Factors, Kinetics, and Mechanism. *Water Research* **2019**, *157*, 191–200. https://doi.org/10.1016/j.watres.2019.03.078.
(18) Duca, M.; Koper, M. T. M. Powering Denitrification: The Perspectives of Electrocatalytic Nitrate Reduction. *Energy & Environmental Science* **2012**, *5* (12), 9726–9742. https://doi.org/10.1039/C2EE23062C.
(19) Singh, N.; Goldsmith, B. R. Role of Electrocatalysis in the Remediation of Water Pollutants. *ACS Catalysis* **2020**, 3365–3371. https://doi.org/10.1021/acscatal.9b04167.
(20) Sanjuán, I.; García-Cruz, L.; Solla-Gullón, J.; Expósito, E.; Montiel, V. Bi–Sn Nanoparticles for Electrochemical Denitrification: Activity and Selectivity towards N2 Formation. *Electrochimica Acta* **2020**, *340*, 135914. https://doi.org/10.1016/j.electacta.2020.135914.
(21) McEnaney, J. M.; Blair, S. J.; Nielander, A. C.; Schwalbe, J. A.; Koshy, D. M.; Cargnello, M.; Jaramillo, T. F. Electrolyte Engineering for Efficient Electrochemical Nitrate Reduction to Ammonia on a Titanium Electrode. *ACS Sustainable Chem. Eng.* **2020**, *8* (7), 2672–2681. https://doi.org/10.1021/acssuschemeng.9b05983.
(22) Li, J.; Zhan, G.; Yang, J.; Quan, F.; Mao, C.; Liu, Y.; Wang, B.; Lei, F.; Li, L.; Chan, A. W. M.; Xu, L.; Shi, Y.; Du, Y.; Hao, W.; Wong, P. K.; Wang, J.; Dou, S.-X.; Zhang, L.; Yu, J. C. Efficient Ammonia Electrosynthesis from Nitrate on Strained Ruthenium Nanoclusters. *Journal of the American Chemical Society* **2020**, jacs.0c00418. https://doi.org/10.1021/jacs.0c00418.
(23) Fajardo, A. S.; Westerhoff, P.; Sanchez-Sanchez, C. M.; Garcia-Segura, S. Earth-Abundant Elements a Sustainable Solution for Electrocatalytic Reduction of Nitrate. *Applied Catalysis B: Environmental* **2021**, *281*, 119465. https://doi.org/10.1016/j.apcatb.2020.119465.
(24) Dima, G. E.; de Vooys, A. C. A.; Koper, M. T. M. Electrocatalytic Reduction of Nitrate at Low Concentration on Coinage and Transition-Metal Electrodes in Acid Solutions. *Journal of Electroanalytical Chemistry* **2003**, *554–555*, 15–23. https://doi.org/10.1016/S0022-0728(02)01443-2.
(25) Liu, J.-X.; Richards, D.; Singh, N.; Goldsmith, B. R. Activity and Selectivity Trends in Electrocatalytic Nitrate Reduction on Transition Metals. *ACS Catalysis* **2019**, *9* (8), 7052–7064. https://doi.org/10.1021/acscatal.9b02179.
(26) 1 Year Rhodium Prices and Price Charts http://www.infomine.com/investment/metal-prices/rhodium/1-year/ (accessed Jan 14, 2020).
(27) Fuller, T. F.; Harb, J. N. *Electrochemical Engineering*; John Wiley & Sons, 2018.

(28) Hossain, Md. M.; Kawaguchi, T.; Shimazu, K.; Nakata, K. Reduction of Nitrate on Tin-Modified Palladium-Platinum Electrodes. *Journal of Electroanalytical Chemistry* **2020**, 114041. https://doi.org/10.1016/j.jelechem.2020.114041.

(29) Shih, Y.-J.; Wu, Z.-L.; Huang, Y.-H.; Huang, C.-P. Electrochemical Nitrate Reduction as Affected by the Crystal Morphology and Facet of Copper Nanoparticles Supported on Nickel Foam Electrodes (Cu/Ni). *Chemical Engineering Journal* **2020**, *383*, 123157. https://doi.org/10.1016/j.cej.2019.123157.

(30) Jia, R.; Wang, Y.; Wang, C.; Ling, Y.; Yu, Y.; Zhang, B. Boosting Selective Nitrate Electroreduction to Ammonium by Constructing Oxygen Vacancies in TiO2. *ACS Catalysis* **2020**. https://doi.org/10.1021/acscatal.9b05260.

(31) Jonoush, Z. A.; Rezaee, A.; Ghaffarinejad, A. Electrocatalytic Nitrate Reduction Using Fe0/Fe3O4 Nanoparticles Immobilized on Nickel Foam: Selectivity and Energy Consumption Studies. *Journal of Cleaner Production* **2020**, *242*, 118569. https://doi.org/10.1016/j.jclepro.2019.118569.

(32) Shen, Z.; Liu, D.; Peng, G.; Ma, Y.; Li, J.; Shi, J.; Peng, J.; Ding, L. Electrocatalytic Reduction of Nitrate in Water Using Cu/Pd Modified Ni Foam Cathode: High Nitrate Removal Efficiency and N2-Selectivity. *Separation and Purification Technology* **2020**, *241*, 116743. https://doi.org/10.1016/j.seppur.2020.116743.

(33) Wang, Y.; Xu, A.; Wang, Z.; Huang, L.; Li, J.; Li, F.; Wicks, J.; Luo, M.; Nam, D.-H.; Tan, C.-S.; Ding, Y.; Wu, J.; Lum, Y.; Dinh, C.-T.; Sinton, D.; Zheng, G.; Sargent, E. H. Enhanced Nitrate-to-Ammonia Activity on Copper–Nickel Alloys via Tuning of Intermediate Adsorption. *Journal of the American Chemical Society* **2020**, *142* (12), 5702–5708. https://doi.org/10.1021/jacs.9b13347.

(34) Yang, J.; Kwon, Y.; Duca, M.; Koper, M. T. M. Combining Voltammetry and Ion Chromatography: Application to the Selective Reduction of Nitrate on Pt and PtSn Electrodes. *Analytical Chemistry* **2013**, *85* (16), 7645–7649. https://doi.org/10.1021/ac401571w.

(35) Garcia-Segura, S.; Qu, X.; Alvarez, P. J. J.; Chaplin, B. P.; Chen, W.; Crittenden, J. C.; Feng, Y.; Gao, G.; He, Z.; Hou, C.-H.; Hu, X.; Jiang, G.; Kim, J.-H.; Li, J.; Li, Q.; Ma, J.; Ma, J.; Nienhauser, A. B.; Niu, J.; Pan, B.; Quan, X.; Ronzani, F.; Villagran, D.; Waite, T. D.; Walker, W. S.; Wang, C.; Wong, M. S.; Westerhoff, P. Opportunities for Nanotechnology to Enhance Electrochemical Treatment of Pollutants in Potable Water and Industrial Wastewater – a Perspective. *Environ. Sci.: Nano* **2020**, *7* (8), 2178–2194. https://doi.org/10.1039/D0EN00194E.

(36) Aricò, A. S.; Antonucci, P. L.; Modica, E.; Baglio, V.; Kim, H.; Antonucci, V. Effect of PtRu Alloy Composition on High-Temperature Methanol Electro-Oxidation. *Electrochimica Acta* **2002**, *47* (22), 3723–3732. https://doi.org/10.1016/S0013-4686(02)00342-0.

(37) Ravel, B.; Newville, M. ATHENA, ARTEMIS, HEPHAESTUS: Data Analysis for X-Ray Absorption Spectroscopy Using IFEFFIT. *Journal of Synchrotron Radiation* **2005**, *12* (4), 537–541. https://doi.org/10.1107/S0909049505012719.

(38) J. Rehr, J.; J. Kas, J.; D. Vila, F.; P. Prange, M.; Jorissen, K. Parameter-Free Calculations of X-Ray Spectra with FEFF9. *Physical Chemistry Chemical Physics* **2010**, *12* (21), 5503–5513. https://doi.org/10.1039/B926434E.

(39) Newville, M. IFEFFIT : Interactive XAFS Analysis and FEFF Fitting. *Journal of Synchrotron Radiation* **2001**, *8* (2), 322–324. https://doi.org/10.1107/S0909049500016964.
(40) Végh, J. The Analytical Form of the Shirley-Type Background. *Journal of Electron Spectroscopy and Related Phenomena* **1988**, *46* (2), 411–417. https://doi.org/10.1016/0368-2048(88)85038-2.
(41) Moniri, S.; Van Cleve, T.; Linic, S. Pitfalls and Best Practices in Measurements of the Electrochemical Surface Area of Platinum-Based Nanostructured Electro-Catalysts. *Journal of Catalysis* **2017**, *345*, 1–10. https://doi.org/10.1016/j.jcat.2016.11.018.
(42) Zhu, D.; Zhang, L.; Ruther, R. E.; Hamers, R. J. Photo-Illuminated Diamond as a Solid-State Source of Solvated Electrons in Water for Nitrogen Reduction. *Nature Materials* **2013**, *12* (9), 836–841. https://doi.org/10.1038/nmat3696.
(43) Deivaraj, T. C.; Lee, J. Y. Preparation of Carbon-Supported PtRu Nanoparticles for Direct Methanol Fuel Cell Applications – a Comparative Study. *Journal of Power Sources* **2005**, *142* (1–2), 43–49. https://doi.org/10.1016/j.jpowsour.2004.10.010.
(44) Jentys, A. Estimation of Mean Size and Shape of Small Metal Particles by EXAFS. *Physical Chemistry Chemical Physics* **1999**, *1* (17), 4059–4063. https://doi.org/10.1039/A904654B.
(45) Frenkel, A. I.; Hills, C. W.; Nuzzo, R. G. A View from the Inside: Complexity in the Atomic Scale Ordering of Supported Metal Nanoparticles. *The Journal of Physical Chemistry B* **2001**, *105* (51), 12689–12703. https://doi.org/10.1021/jp012769j.
(46) Gasteiger, H. A.; Ross, P. N.; Cairns, E. J. LEIS and AES on Sputtered and Annealed Polycrystalline Pt-Ru Bulk Alloys. *Surface Science* **1993**, *293* (1), 67–80. https://doi.org/10.1016/0039-6028(93)90244-E.
(47) Schmidt, T. J.; Gasteiger, H. A.; Stäb, G. D.; Urban, P. M.; Kolb, D. M.; Behm, R. J. Characterization of High-Surface-Area Electrocatalysts Using a Rotating Disk Electrode Configuration. *Journal of The Electrochemical Society* **1998**, *145* (7), 2354. https://doi.org/10.1149/1.1838642.
(48) Weber, R. S. Normalizing Hetereogeneous Electrocatalytic and Photocatalytic Rates. *ACS Omega* **2019**, *4* (2), 4109–4112. https://doi.org/10.1021/acsomega.8b03377.
(49) Kinoshita, K.; Ross, P. N. Oxide Stability and Chemisorption Properties of Supported Ruthenium Electrocatalysts. *J. of Electroanalytical Chemistry* **1977**, *78*, 313. https://doi.org/10.1016/S0022-0728(77)80125-3.
(50) Green, C. L.; Kucernak, A. Determination of the Platinum and Ruthenium Surface Areas in Platinum−Ruthenium Alloy Electrocatalysts by Underpotential Deposition of Copper. I. Unsupported Catalysts. *The Journal of Physical Chemistry B* **2002**, *106* (5), 1036–1047. https://doi.org/10.1021/jp0131931.
(51) Dima, G. E.; Beltramo, G. L.; Koper, M. T. M. Nitrate Reduction on Single-Crystal Platinum Electrodes. *Electrochimica Acta* **2005**, *50* (21), 4318–4326. https://doi.org/10.1016/j.electacta.2005.02.093.
(52) Petrii, O. A.; Safonova, T. Ya. Electroreduction of Nitrate and Nitrite Anions on Platinum Metals: A Model Process for Elucidating the Nature of the Passivation by Hydrogen Adsorption. *Journal of Electroanalytical Chemistry* **1992**, *331* (1), 897–912. https://doi.org/10.1016/0022-0728(92)85013-S.
(53) USDA ERS - Fertilizer Use and Price https://www.ers.usda.gov/data-products/fertilizer-use-and-price.aspx (accessed Jul 20, 2020).

(54) Exner, K. S. Does a Thermoneutral Electrocatalyst Correspond to the Apex of a Volcano Plot for a Simple Two-Electron Process? *Angewandte Chemie International Edition* **2020**, *59* (26), 10236–10240. https://doi.org/10.1002/anie.202003688.
(55) Hammer, B.; Norskov, J. K. Why Gold Is the Noblest of All the Metals. *Nature* **1995**, *376* (6537), 238–240. https://doi.org/10.1038/376238a0.
(56) Campbell, C. T. The Degree of Rate Control: A Powerful Tool for Catalysis Research. *ACS Catalysis* **2017**, *7* (4), 2770–2779. https://doi.org/10.1021/acscatal.7b00115.
(57) Su, J. F.; Ruzybayev, I.; Shah, I.; Huang, C. P. The Electrochemical Reduction of Nitrate over Micro-Architectured Metal Electrodes with Stainless Steel Scaffold. *Applied Catalysis B: Environmental* **2016**, *180*, 199–209. https://doi.org/10.1016/j.apcatb.2015.06.028.
(58) Yoshioka, T.; Iwase, K.; Nakanishi, S.; Hashimoto, K.; Kamiya, K. Electrocatalytic Reduction of Nitrate to Nitrous Oxide by a Copper-Modified Covalent Triazine Framework. *J. Phys. Chem. C* **2016**, *120* (29), 15729–15734. https://doi.org/10.1021/acs.jpcc.5b10962.
(59) de Groot, M. T.; Koper, M. T. M. The Influence of Nitrate Concentration and Acidity on the Electrocatalytic Reduction of Nitrate on Platinum. *Journal of Electroanalytical Chemistry* **2004**, *562* (1), 81–94. https://doi.org/10.1016/j.jelechem.2003.08.011.

Chapter 5

Comparing Electrocatalytic and Thermocatalytic Conversion of Nitrate on Platinum-Ruthenium Alloys

5.1 Introduction

Modern agricultural processes release excess nitrate (NO_3^-),[1] polluting fresh water sources and posing a considerable threat to human[2,3] and ecological health.[4] Current physical nitrate removal techniques in use at water treatment plants include ion exchange and reverse osmosis. Although both options are efficient, they produce a concentrated nitrate waste stream that incurs a high financial cost for disposal.[5] Biological nitrate treatment is a more sustainable alternative to convert nitrate to nitrogen (N_2) or ammonia (NH_3); however, this process is slow, requires organic nutrients, and cannot treat streams with cellular toxins.[6] Thermocatalytic nitrate reduction (TNO_3RR) and electrocatalytic nitrate reduction (ENO_3RR) can address many of the concerns and limitations in current processes and promote the rapid conversion of nitrate to either N_2 or NH_3.[7–11] Many studies in this field have focused on closing the nitrogen cycle by exploring catalysts that are selective for N_2 production. However, recent works emphasize the high economic utility of recycling nitrate to value-added NH_3.[12–14] Producing NH_3 from nitrogen species in water could supply ~25% of NH_3 produced by the Haber-Bosch process, potentially offsetting ~1.5×10^6 TJ of energy consumption and ~60 Mt equivalent CO_2 emissions.[15,16] The market price of NH_4NO_3 from nitrate conversion was estimated to be comparable to that from the Haber-Bosch process, assuming

a low-cost, selective, and active catalyst exists.[9] However, most catalysts do not meet all of these criteria, making it difficult to implement TNO_3RR or ENO_3RR industrially.

There are no reports directly comparing the same catalysts under similar operating conditions for TNO_3RR and ENO_3RR to understand the similarities and differences between both reactions. It is essential to evaluate both systems to understand their capability to remediate nitrate while generating ammonia. Renewable electricity can either indirectly provide H_2 from water splitting that dissolve into an aqueous solution to convert nitrate over a catalyst in TNO_3RR or directly drive ENO_3RR by electrochemically reducing nitrate with protons over an electrocatalyst (**Scheme 5.1**). Most studies of TNO_3RR have used Pd-based catalysts that are effective for converting nitrite to N_2.[17–20] However, Pd is an expensive platinum group metal and requires a promoter metal to initiate nitrate reduction to nitrite. Non-precious metals have been explored for TNO_3RR to reduce catalyst costs, but are selective towards undesirable products such as nitrite, NO, or N_2O.[10,21] Additionally, TNO_3RR requires materials that can dissociate H_2. In contrast to TNO_3RR, the ENO_3RR can use materials that are less active toward H_2 dissociation by tuning the applied potential. In both TNO_3RR and ENO_3RR, there is no consensus for the best catalyst for nitrate conversion to ammonia.

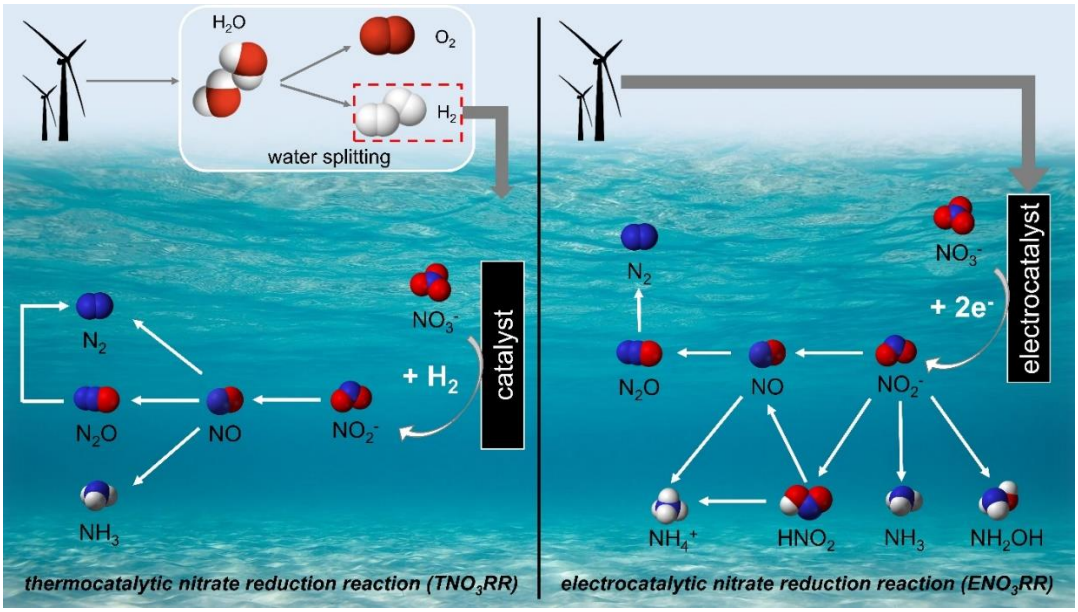

Scheme 5.1. Simplified reaction mechanism for thermocatalytic nitrate reduction reaction (TNO_3RR)[10] and electrocatalytic nitrate reduction reaction (ENO_3RR).[22] The major products and intermediates are shown for each reaction. The proposed rate-determining step is the reduction of nitrate to nitrite for both reactions. Renewable electricity can provide H_2 gas from water splitting in TNO_3RR or directly drive ENO_3RR. Color legend: O atom = red; N atom = blue; H atom = white. Oxidation reactions at the ENO_3RR counter electrode are not included.

Studying catalysts for TNO_3RR and ENO_3RR on a comparable basis would identify critical mechanistic similarities and differences. **Scheme 5.1** gives a comparative overview of the simplified reaction mechanisms for TNO_3RR[10] and ENO_3RR.[22] The rate-determining step (RDS) for both TNO_3RR and ENO_3RR is often the reduction of nitrate to nitrite.[10,23–27] Additionally, under judicious control of the operating conditions and catalyst, both reactions produce N_2 and NH_3 as the major products and nitrogen oxide compounds as less abundant products. However, the effects of the driving chemical potential for reduction (H_2 for TNO_3RR and applied potential for ENO_3RR), pH, nitrate concentration, and catalyst on both reactions have not been compared. Comparing thermocatalytic and electrocatalytic reactions has been valuable to improve the understanding of bio-oil hydrogenation,[28–30] H_2O_2 production,[31] and CO_2 reduction,[32] and can provide further insight into nitrate reduction.

We recently used density functional theory (DFT) and microkinetic modeling to generate theoretical activity volcano plots as a function of the N and O atomic adsorption energies as descriptors for the ENO_3RR activity.[25] The N and O adsorption energies are descriptors of activity because they scale with the adsorption strengths of nitrate reduction intermediates and associated activation barriers through adsorbate scaling and Brønsted-Evans-Polanyi relationships. Using these volcano plots, we identified Pt_3Ru as a promising electrocatalyst and experimentally validated this prediction for ENO_3RR on a series of Pt_xRu_y/C alloys. Results showed that $Pt_{78}Ru_{22}/C$ was greater than 10 times more active than Pt/C at pH = 0 and 0.05 V vs. RHE.[33] The kinetic enhancement resulted from $Pt_{78}Ru_{22}$ having high nitrate and hydrogen coverage on the surface. We hypothesize that if the catalytic mechanisms and RDS on Pt_xRu_y/C alloys for ENO_3RR and TNO_3RR are similar, then a similar rate enhancement should be observed for TNO_3RR.

In this work, we study Pt/C, PtRu/C, and $Pt_{75}Ru_{25}/C$ for TNO_3RR and ENO_3RR under various operating conditions (i.e., pH, hydrogen partial pressure, nitrate concentration, applied potential) to compare thermocatalytic and electrocatalytic approaches for nitrate reduction. We find that increasing the hydrogen driving force (0.1 to 1 atm H_2 and 0.15 to 0.05 V vs. RHE) increases the rate of nitrate conversion and that the ranking of catalyst activity is the same for ENO_3RR and TNO_3RR, that is, Pt/C << PtRu/C < $Pt_{75}Ru_{25}/C$. This change in activity from increasing Ru content in the alloy is attributed to increasing the adsorption strength of nitrate, hydrogen, and intermediates. Similarly, increasing the nitrate concentration increases reaction rates in ENO_3RR and TNO_3RR for PtRu/C. However, at concentrations above 0.5 M NO_3^-, ENO_3RR activity decreases due to surface poisoning by nitrate. Unlike hydrogen driving force and nitrate concentration, which similarly affect catalyst activity, the effect of the pH and the apparent activation energies were different for ENO_3RR and TNO_3RR on the PtRu/C catalyst. This finding

implies that pH has a more complex role in the nitrate reduction mechanism than previously developed microkinetic models based on Langmuir-Hinshelwood surface reactions might suggest, and that there are fundamental differences between the two reactions. Despite these differences, certain catalyst properties (such as stronger nitrate adsorption) or reaction conditions (more available adsorbed hydrogen) increase the TNO_3RR and ENO_3RR rates in a way that is qualitatively captured by the existing theoretical volcano plot.[25,33] We compare the TNO_3RR and ENO_3RR performance on PtRu/C to rates and operating costs for industrial ammonia synthesis to evaluate the feasibility of both systems. Our results show that TNO_3RR on PtRu/C at pH 1 produces NH_3 at comparable rates to the Haber-Bosch process and, depending on the regional cost of H_2, can have lower operational costs than the USDA standard cost per tonne of NH_4NO_3. Ultimately, this work clarifies mechanistic similarities and differences between TNO_3RR and ENO_3RR and serves as a model for evaluating catalytic systems for industrial implementation of nitrate reduction technology.

5.2 Methods

5.2.1 Material Synthesis and Characterization

A $NaBH_4$ reduction synthesis was used to synthesize $Pt_{75}Ru_{25}/C$.[33] The carbon black (Vulcan XC 72; Fuel Cell Store) was pretreated at 400 °C for 2 hrs to remove surface impurities. Afterwards, the support was suspended and sonicated in Millipore water (18.2 MΩcm, Millipore MilliQ system) for 15 min. Measured concentrations of $RuCl_3$ (38% Ru; Alfa Aesar) and H_2PtCl_6 (38–40% Pt; Sigma Aldrich) in Millipore water were added to the solution and stirred for another 15 min before 40 mg of $NaBH_4$ (Sigma Aldrich) dissolved in 25 mL of Millipore water were added to accelerate the reaction. The final solution was stirred for 2 hrs before centrifuging three times at 3000 rpm for 8 min each and washed with Millipore water. The recovered solid was dried

overnight in an oven at 80 °C in air. All commercial catalysts (Pt/C and PtRu/C) were purchased from Fuel Cell Store. For the nitrate concentration and pH effect studies, we used the commercial PtRu/C instead of the most active synthesized $Pt_{75}Ru_{25}$/C because a single batch of commercial PtRu/C was sufficient to perform all studies. Using $Pt_{75}Ru_{25}$/C for these studies would require multiple batch syntheses and introduce batch-to-batch variations in the measurements.

The final metal loadings were determined by using thermogravimetric analysis (TGA) on a Shimadzu TGA-50H in a quartz pan. All catalyst samples were pretreated under He at 100 °C for 30 min to remove surface contaminants and adsorbed water. Samples were heated to 700 °C at 10 °C/min in air to oxidize all the carbon.[34,35] The metal weight loading was determined by dividing the final weight by the initial weight prior to the temperature ramp. X-ray diffraction (XRD) analysis was conducted using a Rigaku Miniflex XRD with Cu Kα radiation and a Ni filter (λ = 1.5418 Å). The 2θ range ($10° < 2\theta < 90°$) was scanned at 5°/min with a 0.02° step size. Crystallite sizes were estimated using the Scherrer equation and the Pt and Ru peaks were referenced to #04-0802 and #06-0663, respectively, from JADE XRD processing software. Imaging and chemical characterization of the catalysts were performed with scanning electron microscopy (Nova 200 Nanolab; Thermo Fisher) coupled with energy-dispersive X-ray spectroscopy (SEM/EDX).

5.2.2 Thermal Catalytic Nitrate Reduction Experiments

Thermocatalytic nitrate reduction activity was measured in a 125 mL 3-neck jacketed flask (ChemGlass) at atmospheric pressure. For all experiments, 10 mg of catalyst was suspended in 100 mL of Millipore water and stirred at 500 rpm. The solution was sparged with H_2 (Cryogenic Gases) for at least 30 min to remove dissolved oxygen and reduce the catalyst. The H_2 partial pressure (0.1–1 atm) was adjusted accordingly by co-feeding Ar (Cryogenic Gases) while keeping

the total flow rate consistent at 250 mL/min. The temperature (20–50 °C) of the reactor was controlled via a refrigerated/heated bath circulator (Fisher Scientific). Desired concentrations of nitrate (1–100 mM $NaNO_3$) were added to the reactor at the beginning of the reaction after H_2 pretreatment. For lower concentrations of nitrate (≤10 mM $NaNO_3$), a sample was collected every 3 min for the first 15 min. At higher nitrate concentrations (>10 mM $NaNO_3$), a sample was collected every 15 min to ensure accurate rate quantifications under differential conditions. In all cases, a 1 mL syringe was used to extract the sample from the reactor before centrifuging at 3000 rpm for 5 min to separate the aliquot solution and catalyst particles. Nitrate, nitrite, and ammonia concentrations were measured using a UV-Vis spectrometer (Thermo Fischer, Evolution 350) (discussed in **Sec. 2.5**). The activity is reported as a turnover frequency (TOF) in moles of aqueous products (e.g., ammonia, nitrite) per mole of surface metal per minute.

5.2.3 Electrocatalytic Reduction Experiments

A single-compartment, 3-electrode, glass electrochemical cell (Pine Research) was used for electrochemical measurements with a clean graphite rod (Alfa Aesar, Ultra "F" purity) as the counter electrode. A single junction reference electrode (Pine Research, in 4 M KCl) was used in solutions with pH less than or equal to 7, and a double-junction reference electrode (Pine Research, in 10% KNO_3) was used in pH 10. Both reference electrodes were calibrated at 1 atm of H_2 (Cryogenic Gases) in different pH solutions. The cell initially contained 100 mL of electrolyte solution (pH 0: 1 M sulfuric acid; pH 1: 0.1 M sulfuric acid; pH 3: 0.1 M sodium citrate + 0.1 M citric acid; pH 5: 0.2 M sodium acetate + 0.2 M acetic acid; pH 7: 0.2 M sodium phosphate + 0.1 M citric acid; pH 10: 0.1 M sodium carbonate + 0.1 M sodium bicarbonate; Sigma Aldrich). Prior to electrochemical experiments, N_2 (Cryogenic Gases) was sparged through the solution with a stir bar for at least 45 min to remove traces of dissolved O_2. Cyclic voltammogram (CV) scans after

sparging confirmed the absence of dissolved O_2 from the solution and stability of the working electrode.

The working electrode was prepared and tested as described previously.[33] Briefly, a catalyst ink was prepared with a Nafion binder and deposited onto a glassy carbon rotating disk insert (Pine Research) to result in a total loading of 9.6 μg of catalyst, including carbon. The prepared electrodes were cleaned by cycling 50 times between hydrogen evolution and oxidation potentials (from –0.1 to 1.2 V vs. RHE) at 100 mV s^{-1}. Both hydrogen underpotential deposition (H_{upd}) and copper underpotential deposition (Cu_{upd}) were used to accurately evaluate the electrochemically active surface area (ECSA) of the catalysts as described previously.[33] After an 85% compensation for internal solution resistance as measured by electrochemical impedance spectroscopy, H_{upd} was determined by cycling between the onset of HER to Pt oxidation (pH 0: 0.06–1.3, pH 1: 0.07–1.3, pH 3: 0.05–1.3, pH 5: 0.05–0.8, pH 7: 0.06–1.3, and pH 10: 0.04–1.3 V vs. RHE), at a scan rate of 100 mV s^{-1} until the cyclic voltammograms were stable. The background-corrected hydrogen desorption charge and the average charge density of Pt (210 μC cm^{-2}) were used to determine the ECSA.

All chronoamperometry measurements were taken after an 85% compensation for internal solution resistance as measured by electrochemical impedance spectroscopy. The rotating disk electrode (RDE) was held at a rotation rate of 2500 rpm to eliminate mass transfer limitations. Currents were measured at four different applied potentials (0.05, 0.075, 0.1, 0.15 V vs. RHE) and recorded as the average current in the final 20 s. A baseline current was recorded in the electrolyte solution at each applied potential without the presence of nitrate. For ENO_3RR experiments, 20 mL of dissolved sodium nitrate in electrolyte solution was added to reach the desired concentration (0.01, 0.03, 0.1, 0.5, 1 M $NaNO_3$) before measuring the current at each applied potential.

5.2.4 Apparent Activation Energy Measurements

For ENO_3RR measurements, reduction currents were recorded for 10 min at two applied potentials (0.05 V and 0.1 V vs. RHE) and four different temperatures (T = 10, 20, 25, 30 °C) after compensating for 85% of the internal solution resistance. The TNO_3RR experiments were prepared using similar methods as described in **Sec. 5.2.2** and operated at four different temperatures (T = 20, 30, 40, 50 °C). A heating/cooling jacket was used with a refrigerated/heated bath circulator (Fischer Scientific) to maintain the desired temperature. The difference in the temperature ranges selected were due to limitations of the experimental setup. For ENO_3RR experiments above 30 °C, thermal expansion caused the glassy carbon electrode to pop out of the Teflon holder. A wider range of temperatures was used for thermocatalytic measurements to reduce the influence of experimental error on the results. The apparent activation energy (E_a) was evaluated from an Arrhenius plot of the current density or TOF.

5.2.5 Selectivity Measurements

ENO_3RR measurements from depositing catalysts onto glassy carbon did not generate high enough currents to allow for product quantification. Thus, 10 mg of powder Pt_xRu_y/C catalysts were directly deposited on 2.5×2.5 cm^2 pieces of carbon felt (6.35 mm thick, 99.0%, Alfa Aesar) in 40 mL of 1 M H_2SO_4. To ensure all of the catalyst was deposited onto the carbon felt, the solution was mixed for 30 min with bubbling H_2 at 80 °C. In a two-compartment electrochemical cell separated by Nafion 117 membrane, these carbon felts (CFs) were attached to a graphite rod (AGKSP grade, ultra "F" purity, Alfa Aesar) for use as the working electrode for ENO_3RR selectivity experiments as previously described.[33]

Nitrate and select liquid-phase products (i.e., NO_2^- and NH_3) were measured using UV-vis spectrometer (Thermo Fischer, Evolution 350). Nitrate was quantified using standard spectrometry

techniques. 10 μL from the sample aliquot was acquired and diluted to 2 mL using Millipore water. 1 mL of this resulting, well-mixed solution was further diluted to 3 mL in a quartz cuvette (Fisher Scientific, Azzota Corp 10 mm). UV-Vis measurements were taken between 190–300 nm, and the nitrate concentrations were calculated via the adsorption peak at 220 nm.[36] Millipore water was used as the background and subtracted from the sample spectra, and a calibration curve was created using known concentrations of $NaNO_3$ in solution.

Nitrite (NO_2^-) was quantified via a modified Griess diazotization reaction.[36,37] 0.3 mL of the extracted sample aliquot was diluted to 1 mL and neutralized with 1 M NaOH. 40 μL of the Griess color reagent, which consisted of 2% sulfanilamide (Fischer Scientific, ≥98%) and 0.2% *N*-(1-napthyl)-ethylenediamine (Sigma Aldrich, ≥98%) in phosphoric acid (Acros Organics; 85%) diluted to 0.1 M, was added. The resulting solution was left in the dark for 30 min before measuring absorbances at 543 nm. Known concentration of calibration standards were made from $NaNO_2$ (>99.0%, Sigma Aldrich).

Ammonia was quantified by using the indophenol blue test[13,38] with 1 mL of the sample aliquot. 1 M NaOH (Sigma Aldrich, 99.99%) was added to the electrolyte solution to neutralize the acid to a pH of 12. This was followed by sequentially adding 122 μL of sodium salicylate (Sigma Aldrich, >99.5%), 27.3 μL of sodium nitroprusside dihydrate (Sigma Aldrich, >99%), and 40 μL of sodium hypochlorite solution (Sigma Aldrich, 4.00–4.99%) to the electrolyte solution and manually stirred together. The solution was covered and left for 40 min. The indophenol peak was identified as the maximum absorbance between 600–700 nm. A fresh 0.1 M HNO_3 electrolyte solution prepared with the indophenol blue method was used as the background and subtracted from the sample spectra. If the concentration of NH_3 was too high and oversaturated the detector, the solution was diluted and retested. A calibration curve was created using known concentrations

of NH_4Cl (99.99%, Sigma Aldrich) and unknown NH_3 concentrations were calculated using the Beer-Lambert law.

The faradaic efficiency (FE) for ENO_3RR was calculated by dividing the charge required to form the total NH_3 measured by the total charge passed during the steady-state experiments. The total charge passed was calculated by integrating the reduction current over the duration of the experiment and the charge required from NH_3 was calculated by assuming that eight electrons are required to form one molecule of NH_3 from one molecule of nitrate.

5.3 Results and Discussion

5.3.1 Applied Potential vs. H_2 Partial Pressure on Pt_xRu_y/C Performance for Nitrate Conversion

Here we study TNO_3RR and ENO_3RR on Pt/C, PtRu/C, and $Pt_{75}Ru_{25}/C$ to compare the effect of hydrogen driving force. The weight loading of the catalysts was determined by TGA, and corresponding crystallite sizes were calculated by applying the Scherrer equation to the XRD results. The average nanoparticle sizes of Pt/C, PtRu/C and $Pt_{75}Ru_{25}/C$ were 2.6, 2.4, and 3.7 nm, respectively. SEM images of the Pt_xRu_y/C catalysts are provided in **Figure C.3**, and subsequent elemental analysis from EDX is shown in **Figure C.4**. No change in ammonia production rates is observed at rotation rates beyond 500 rpm. As a result, a 500-rpm stir rate was used throughout TNO_3RR experiments to ensure no external mass transport limitations. Without the presence of metals on the Vulcan carbon support, no catalytic activity is recorded. Additional details on material characterization and baseline measurements are provided in **Appendix C**.

We study the nitrate conversion TOF (for TNO_3RR) and current density (for ENO_3RR) as a function of H_2 pressure and applied potential, respectively, for the Pt/C, PtRu/C, and $Pt_{75}Ru_{25}/C$

materials in **Figure 5.1**. For all catalysts that showed activity, increasing the hydrogen driving force for reduction increases the rate of nitrate conversion. For TNO_3RR, the TOF on $Pt_{75}Ru_{25}/C$ and PtRu/C increases as H_2 partial pressure increases. Likewise, the current density magnitudes from ENO_3RR for all Pt_xRu_y/C catalysts increase as the applied potential becomes more negative and approaches 0 V vs. RHE (the standard thermodynamic potential for 1 bar H_2). This finding implies that the driving force to form adsorbed hydrogen plays a similar and important role in both TNO_3RR and ENO_3RR, which is corroborated by prior studies.[11,22] This observation also supports the method of using the computational hydrogen electrode (where applied potential is equated to the chemical potential of hydrogen) to qualitatively model ENO_3RR.[25,33]

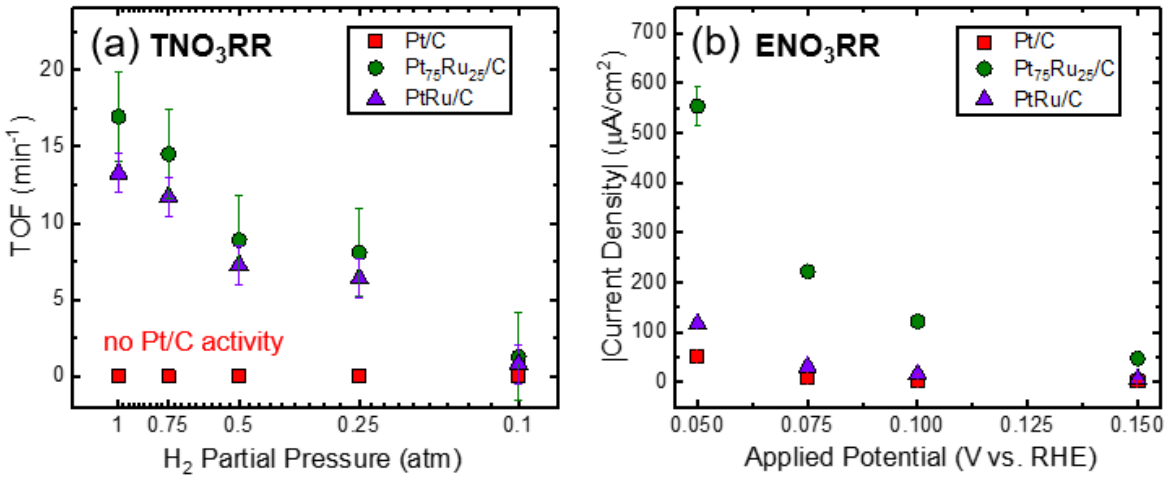

Figure 5.1. Comparison of Pt_xRu_y/C activity for nitrate conversion at **(a)** different hydrogen partial pressures in thermocatalytic nitrate reduction reaction (TNO_3RR) based on ammonia production rate and **(b)** different applied potentials in electrocatalytic nitrate reduction reaction (ENO_3RR). All measurements were performed in pH 7 solution with 0.1 M $NaNO_3$. Assuming all electrons for ENO_3RR go to ammonia, a current density of 1 $\mu A \cdot cm^{-2}$ is equivalent to a TOF of 31 min^{-1} on Pt/C. Note that we show hydrogen pressure increasing right to left in **Figure 5.1a** to match the convention for less positive applied potential increasing the driving force for proton reduction in **Figure 5.1b**.

The activity of the catalysts follows the order $Pt_{75}Ru_{25}/C$ > PtRu/C > Pt/C for both TNO_3RR (**Figure 5.1a**) and ENO_3RR (**Figure 5.1b**) at pH 7. These measurements demonstrate that the enhancement previously reported,[33] where PtRu/C and $Pt_{75}Ru_{25}/C$ were more active than Pt for

ENO_3RR at pH 0, also holds at pH 7. We previously attributed the higher ENO_3RR activity of Pt_xRu_y compared with pure Pt to increased adsorption strength of nitrate.[33] Pt_xRu_y alloys have ensembles of sites (e.g., Pt-Ru-Ru, Pt-Pt-Ru) that adsorb reactants and intermediates stronger than Pt. Our results here show similar activity trends hold for Pt_xRu_y/C towards TNO_3RR, suggesting that catalyst design metrics, such as the nitrate adsorption energy, are related for TNO_3RR and ENO_3RR under this set of conditions. The reason that PtRu/C is less active than $Pt_{75}Ru_{25}$/C, despite having more Ru and thus more sites with stronger adsorption, is rationalized by a theoretical volcano plot, where the nitrate adsorption is too strong and decreases the rate.[33] The decrease in activity for PtRu/C compared to $Pt_{75}Ru_{25}$/C is also observed for TNO_3RR, but to a lesser extent.

While the behavior of TNO_3RR and ENO_3RR with hydrogen pressure/applied potential and catalyst alloying are qualitatively the same, there are differences in the reactions when considering the quantitative activity of the catalysts. One difference in the behavior is that for Pt/C there was no measured activity during TNO_3RR, even with increasing the amount of catalyst in the reactor, whereas some catalytic activity was observed for ENO_3RR. More specifically, while Pt/C was entirely inactive for TNO_3RR compared to PtRu/C or $Pt_{75}Ru_{25}$/C (**Figure 5.1a**), a current density of 52 $\mu A\ cm^{-2}$ was recorded for Pt/C at 0.05 V vs. RHE during ENO_3RR (only 55% lower than PtRu/C, **Figure 5.1b**). Our results agree with previous studies that show no activity for Pt in TNO_3RR.[39] However, the Pt catalyst has been demonstrated to be active for the thermocatalytic hydrogenation of nitrite.[40] The inactivity of pure Pt relative to that of Pt_xRu_y/C leads us to postulate that Ru is responsible for hydrogenation of nitrate to nitrite and both Ru and Pt sites participate in further hydrogenation of nitrite to ammonia. These results point to potential differences in the hydrogenation mechanism between electrocatalytic and thermocatalytic reduction on the surface of Pt.

5.3.2 Nitrate Concentration on PtRu/C

The data in **Figure 5.2** shows that both TNO_3RR and ENO_3RR have a positive rate order in nitrate on PtRu/C at low concentrations (<0.5 M $NaNO_3$) and a negative rate order in nitrate at higher concentrations (>0.5 M $NaNO_3$) for ENO_3RR. A positive rate order at low nitrate concentrations for TNO_3RR has been previously observed for kinetic studies on PdCu alloys.[41] For all applied potentials, ENO_3RR on PtRu/C follows the same qualitative trend and is the most active at 0.5 M NO_3^- in pH 7 solution. The trends observed for ENO_3RR show the RDS is a surface reaction, which qualitatively agrees with a prior report that explores nitrate concentration effects on Pt.[42] A simple rate law for this reaction is:

$$rate = k\theta_H\theta_N \tag{5.1}$$

where k is the rate constant of the surface reaction and θ_H and θ_N represent the hydrogen and nitrate coverages, respectively, and are controlled by their corresponding equilibrium adsorption constants and concentrations for those species (see SI for more details). At low nitrate concentrations, both θ_N and the current densities are directly proportional to the concentration of nitrate in solution. There is a decrease in reaction rate at high nitrate concentrations for ENO_3RR, suggesting that the nitrate is blocking surface sites for H^+ adsorption and inhibiting reduction. This hypothesis is supported by previous X-ray absorption near edge spectra measurements on Pt/C, where addition of nitrate to solution caused a decrease in hydrogen coverage, implying competitive adsorption between nitrate and hydrogen.[25] We were unable to accurately quantify TNO_3RR ammonia production rates using UV-Vis spectroscopy for nitrate concentrations greater than 0.1 M NO_3^-, so activities above that concentration are not included in **Figure 5.2**. The ENO_3RR rates were measurable at these concentrations because the activity is based on the current density, rather than direct quantification of ammonia at short time scales.

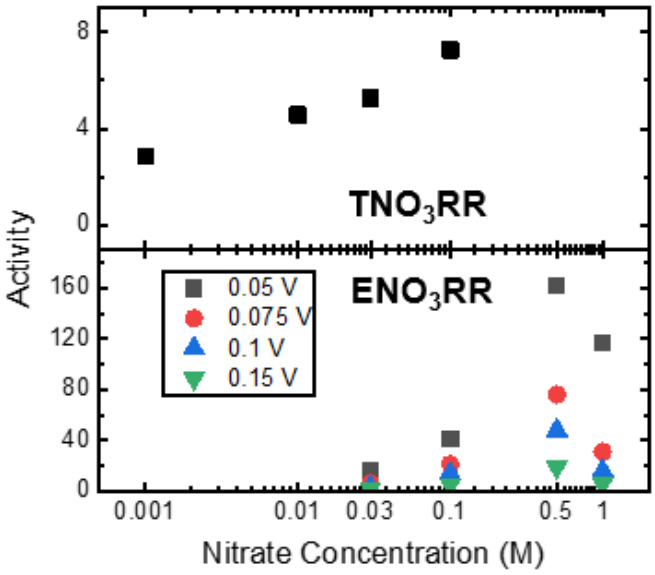

Figure 5.2. The activity of PtRu/C as a function of nitrate concentration in pH 7 solution. The activity of the TNO_3RR and ENO_3RR is defined in TOF (min^{-1}) and |Current Density| ($\mu A \cdot cm^{-2}$), respectively. All experiments were performed at room temperature (23.3 °C), and the hydrogen partial pressure for TNO_3RR was set at 0.5 atm.

The ENO_3RR activity as a function of nitrate concentration is rationalized using the Langmuir-Hinshelwood model used to generate the rate law in **Equation 5.1** (**Appendix C**). The fitted rate law captures that the activity for PtRu/C in pH 7 increases with nitrate concentration up to 0.4 M, but decreases at higher nitrate concentrations. For a surface reaction involving adsorbed hydrogen and adsorbed nitrate, increasing the nitrate concentration has a similar effect as increasing the nitrate adsorption strength, as both lead to higher nitrate coverages. The model provides a qualitative description of the relationship between ENO_3RR activity, nitrate adsorption energy, and nitrate concentration. Although, as discussed above, there is the possibility of a bifunctional (multi-site) mechanism on alloys, we do not see conclusive evidence that this is the case from our kinetic modeling and thus postulate only the simplest model that qualitatively describes the data. Further understanding the reaction chemistry and incorporating additional reaction steps would improve model fitting.

The results in **Figure 5.1** and **Figure 5.2** imply that the computational volcano plots[25,33] and a simple Langmuir-Hinshelwood model apply qualitatively to both TNO_3RR and ENO_3RR, where the rate is related to the amount of available hydrogen and the coverage of nitrate on the surface. This similarity may be due to the two reactions sharing a common RDS or catalyst properties that control their respective RDS. However, as observed for the contrast between activity for Pt/C in ENO_3RR and TNO_3RR, there are quantitative differences in TNO_3RR and ENO_3RR, which we explore in the following section.

5.3.3 pH Effects on Rate and Apparent Activation Energy of PtRu/C

Despite the similar effect of hydrogen chemical potential, alloying, and nitrate concentration between TNO_3RR and ENO_3RR, there are distinct differences when considering the effect of pH and apparent activation energies (E_a), **Figure 5.3**. TNO_3RR shows higher activity at pH 1 than pH 7 (**Figure 5.3a**). In contrast, the ENO_3RR rates are higher at pH 7 than pH 1. These rates are consistent with the order of the E_a for TNO_3RR and ENO_3RR, where the E_a for TNO_3RR is lower at pH 1 and the E_a for ENO_3RR is lower at pH 7 (**Figure 5.3b**). The previously used volcano plots[25,33] and our Langmuir-Hinshelwood models do not incorporate the effect of pH (all calculations implicitly assume pH = 0). However, the large effect of pH and opposite trends for TNO_3RR and ENO_3RR reveal that a more complex mechanistic model than previously proposed is needed to understand this reaction. We will first discuss potential causes of the effect of pH on TNO_3RR and then discuss the influence on ENO_3RR in greater detail. Note that all measurements for ENO_3RR are at the same potential vs. RHE, so the thermodynamic effect of changing the pH has been considered, and the pH effects observed in **Figure 5.3** are non-Nernstian.

We propose that the higher activity and lower E_a observed for TNO_3RR at lower pH is most likely because it is easier for nitrite to either decompose or hydrogenate to other products in

acidic conditions.[43] At low pH, literature has indicated higher nitrite hydrogenation TOF rates through increased surface coverage of reaction intermediates, such as *NO and *HNO.[44] The E_a for TNO_3RR at pH 7 is 45 kJ mol^{-1}, similar to that of measurements of Pt group metals in neutral solution.[45,46] The lower E_a at pH 1 than pH 7 may arise from more favorable intermediate conversion to ammonia at low pH. It is also possible that the pH (and corresponding changes in the electrochemical double layer) affects the adsorption of nitrate, which would influence the rate.

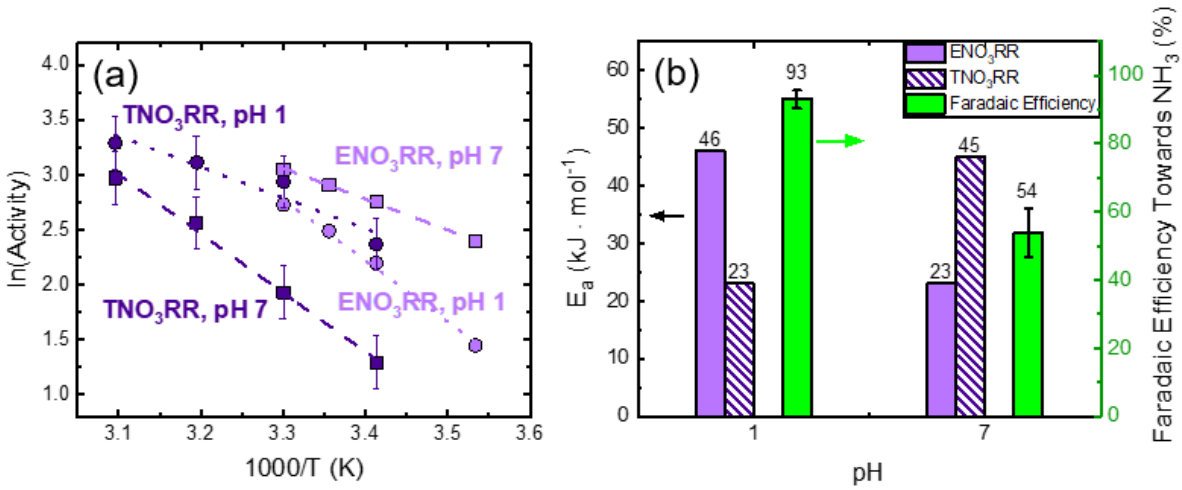

Figure 5.3. (a) Arrhenius plots of PtRu/C for thermocatalytic nitrate reduction reaction (TNO_3RR) and electrocatalytic nitrate reduction reaction (ENO_3RR) at pH 1 and pH 7. Temperatures for TNO_3RR experiments range from 20–50 °C and 10–30 °C for ENO_3RR. The activity of the TNO_3RR and ENO_3RR is defined in TOF (min^{-1}) and |Current Density| ($\mu A \cdot cm^{-2}$), respectively. **(b)** Comparison of apparent activation energy (E_a) and faradaic efficiency (FE) towards NH_3 across different solution pH and reaction systems. The light-purple solid bars denote E_a from ENO_3RR and dark-purple striped bars denote E_a from TNO_3RR. H_2 partial pressure was set at 0.5 atm and FE experiments were performed at 0.1 V vs. RHE.

The shift in activity and E_a for ENO_3RR with pH is more challenging to deconvolute than for TNO_3RR. This change in activity may either be due to a different RDS entirely at the different pH values or the same RDS, but with different coverages of the intermediates. Although the pH may affect nitrate adsorption energy and thus the reaction rate, because the effect of pH is opposite for TNO_3RR than ENO_3RR, other pH effects likely play a role in the reaction. Similarly, the

conversion of nitrite being faster at lower pH values (as described above for TNO_3RR) does not explain the trend in pH for ENO_3RR.

Previous reports hypothesize a mechanistic shift occurs with an increase in the pH of the electrolyte solution for ENO_3RR.[45,46] In acidic media, the concentration of H^+ correlates to the nitrate reduction activity.[45,46] As the pH increases, the reaction stops being dependent on H^+, and the hydrogen source is provided from H_2O. Similarly, in our results the FE for ENO_3RR changes from 93% at pH 1 to 54% at pH 7 (**Figure 5.3b** and **Figure C.9**). This change is likely due to the reaction favoring an ammonia production mechanism at pH 1 and favoring a nitrogen production mechanism at more basic pH.[8] We note that gaseous products such as nitrogen are not measured in this study and future works to understand product distribution changes as a function of pH are needed to understand the mechanism.

To investigate the role protons and water play in the ENO_3RR in more detail, the PtRu/C current densities for ENO_3RR for pH 0–10 at four different operating potentials vs. RHE are shown in **Figure 5.4**. These results show that as the electrolyte pH increases, the ENO_3RR activity of PtRu/C increases, with a slight decrease or plateau at pH 7, which may be due to effects from the reaction environment or changes in the catalyst structure due to pH. For example, at pH 10, where the current densities are the highest, the catalyst may be forming Ru oxides above pH 9 that are artificially inflating the reduction currents.[47] It is also possible that the high activity results from favorable Ru lattice strains from subsurface oxide formation.[12] A previous study of ENO_3RR on Rh and Pt reported that the reduction rate decreases with the concentration of hydronium ions decreasing from pH 0 to 4,[48] which is opposite to what we observe for PtRu/C. In that work, NaCl was added as the pH increased to maintain a constant ionic strength of the electrolyte. Because chloride is known to inhibit both Pt[49] and Rh[50,51] for ENO_3RR, the previously reported decrease in

activity may be due to increasing chloride inhibition of catalyst sites, not the change in pH. It is possible that the ionic strength of the solution in our results is affecting the reduction currents and needs to be accounted for to obtain an accurate pH effect analysis. **Figure C.10** provides the ionic strength of the buffer solutions at each pH, ranging from 0.25 (pH 1) up to 2.5 M (pH 0). The ionic strengths vary from different pH solutions, but do not match the activity trends observed in **Figure 5.4**, and so are not the sole cause of the pH effect.

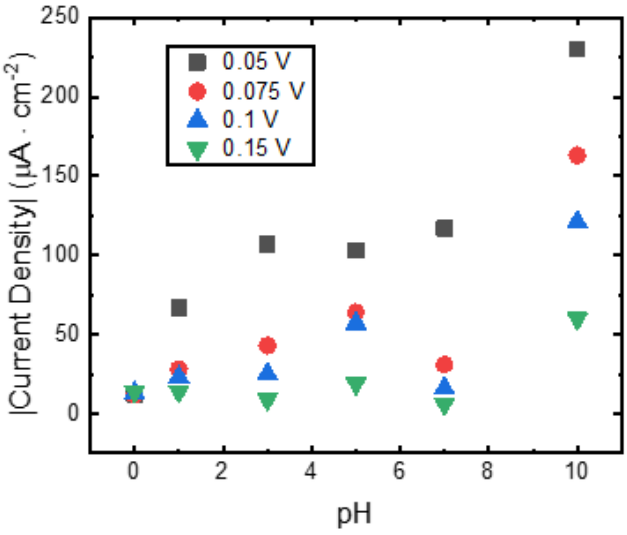

Figure 5.4. Absolute current densities for pH 0–10 in 1 M $NaNO_3$ using PtRu/C at different applied potentials vs. RHE. The electrolyte solution at each pH is: pH 0 – 1 M H_2SO_4, pH 1 – 0.1 M H_2SO_4, pH 3 – 0.1 M sodium citrate + 0.1 M citric acid, pH 5 – 0.2 M sodium acetate + 0.2 M acetic acid, pH 7 – 0.2 M sodium phosphate + 0.1 M citric acid, pH 10 – 0.1 M sodium carbonate + 0.1 M sodium bicarbonate.

The effect of pH on other electrocatalytic reactions has been studied extensively, and some of the findings for other reactions may be applied to ENO_3RR. Hydrogen binding energy is one proposed factor in which pH influences catalytic activity,[52,53] but other effects, such as the ionic strength of the buffer,[48,54] hydrogen equilibrium potential,[55] point of zero free charge (pzfc),[56–58] and water orientation and reorganization energy,[59–61] can also influence the activity. For hydrogen evolution, the activities for Pt group metals are much higher at lower pH values, but the reason is debated in several recent reviews and publications.[62–66] This enhancement is the opposite direction

of what we observe for ENO_3RR. Oxygen reduction reaction (ORR) is more complicated, with ORR activity on Pt(111) increasing as the pH increases from 1 to 6 and decreasing with increasing pH past 11 and a predicted maximum at pH 9.[67] This trend is attributed to the ORR onset potential being positive and negative with respect to the pzfc of the electrode in acidic and basic solution, respectively, causing the switch in pH dependence. For ENO_3RR on PtRu/C, there seems to be a maximum with pH similar to ORR, but the ENO_3RR maximum occurs at pH 5 (excluding potential oxide effects at pH 10). Thus, one possible cause of the pH dependence of ENO_3RR could be differences in the surface charge of the electrode.

Although a Langmuir-Hinshelwood model describes some of the reaction data, it does not adequately capture the effects of pH and the buffer solutions on the activity (**Figure C.8**), indicating a lack of mechanistic understanding of these effects. Therefore, future experimental kinetic studies with controlled ionic strength and benign supporting electrolytes are needed, as well as studies testing the kinetic isotope effect of H. In addition, in-situ spectroscopy to detect surface intermediates and computational simulations that include the influence of pH are necessary to understand this reaction better. Particularly, electrochemical-specific considerations need to be addressed to accurately model the effect of pH for ENO_3RR, as the effect of pH is different from what is observed for TNO_3RR.

5.3.4 Economic Evaluation of TNO_3RR and ENO_3RR for Ammonia Production

We evaluate the costs of electricity for ENO_3RR catalysts and hydrogen costs for TNO_3RR catalysts to produce NH_4NO_3 and the rate of NH_3 production as a simple metric to compare different catalyst under multiple operating conditions (**Figure 5.5**). The ideal catalytic system must have lower NH_4NO_3 costs than the USDA standard to be feasibly implemented and maintain

similar or higher NH_3 production rates than the current Haber-Bosch processes (0.2 mol g^{-1} hr^{-1}).[68,69] In our analysis, PtRu/C in pH 1 and 7 solutions for ENO_3RR have electricity costs at or lower than USDA standards for NH_4NO_3.[70] However, the NH_3 production rates are 1 to 2 orders of magnitude lower than needed to meet the current industrial NH_3 synthesis process in our limited scope of using carbon felts in a batch reactor system, which is lower than the RDE values (more discussion in the SI). Further analysis in a flow reactor that removes mass transfer limitations should be used to assess more accurate ammonia production rates. For comparison, we also evaluate the $/tonne of NH_4NO_3 production for a strained Ru catalyst, which was reported to have among the highest electrochemical NH_3 production rates.[12] Strained Ru also achieves nearly 100% FE toward NH_3 at −0.2 V vs. RHE at basic conditions, which results in lower electricity cost per tonne of NH_4NO_3 than the current USDA standard price.

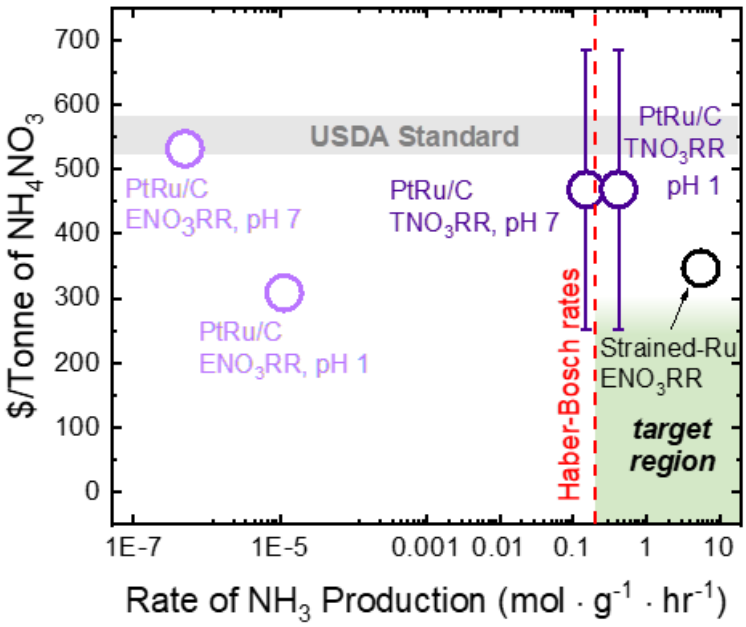

Figure 5.5. Comparative electricity (ENO_3RR) and H_2 (TNO_3RR) cost per tonne of NH_4NO_3 vs. the rate of NH_3 production for TNO_3RR and ENO_3RR PtRu/C at pH 1 and 7 per gram of metal. For TNO_3RR (dark purple), the cost of H_2 was ranged from $2.50/kg to $6.80 /kg (error bars), which is the current standard for H_2 production from PEM cells with $0.07/kWh.[71,72] For ENO_3RR, the electricity cost was assumed to be $0.07/kWh with experimentally measured FE towards ammonia (93% for pH 1 and 54% for pH 7) and a

total cell voltage of 1.53 V. The large light purple arrows indicate potential increase in ammonia production rates in flow system without mass transfer limitations. The value for the strained Ru catalyst for ENO_3RR is from Ref. [12] and corresponds to a FE of 99% and total cell voltage of 1.83 V. The gray area represents the USDA standard cost per tonne of NH_4NO_3,[70] and the dashed red line represents the current NH_3 production rate from the industrial Haber-Bosch process with Ru catalysts. The green block indicates the range for an ideal catalyst based on cost factors and production capabilities.

The hydrogen cost and rate of NH_3 production is also provided for PtRu/C for TNO_3RR in pH 1 and 7. In this reaction system, the primary cost for the production of NH_4NO_3 is H_2, which ranges from \$2.50/kg to \$6.80/kg based on electrolysis of water in proton exchange membrane cells assuming electricity costs to be \$0.07/kWh.[71,72] Assuming all unused H_2 in the reactor will be recycled, the H_2 cost per tonne of NH_4NO_3 at both pH values is the same. Depending on the regional cost of H_2, the cost of NH_4NO_3 varies between \$252/tonne up to \$685/tonne. However, the rate of NH_3 production for PtRu/C at pH 1 is three times higher than the rate at pH 7 and two times higher than the current NH_3 rates from the Haber-Bosch process, making TNO_3RR in acidic conditions on PtRu/C a sustainable alternative process. We note that electricity and hydrogen costs are only a portion of the total operating costs of this process, and a full detailed technoeconomic study would be needed to accurately identify the cost of this process. However, the economic analysis presented here can be used as an initial benchmark to evaluate promising catalysts and target improvements for implementation of sustainable ammonia in place of the Haber-Bosch process.

5.4 Conclusions

This study presents a series of kinetic comparisons between thermocatalytic and electrocatalytic nitrate reduction by Pt/C, PtRu/C, and $Pt_{75}Ru_{25}$/C that reveals details in the mechanisms for both reactions. These findings are valuable to understand the mechanism of nitrate reduction and highlight the utility of comparing thermocatalytic and electrocatalytic reactions to clarify catalytic mechanisms. We identify similarities between the TNO_3RR and ENO_3RR

showing that the hydrogen driving force and nitrate concentration increases the reaction activity. We show that changing the alloy composition of Pt_xRu_y/C lead to similar activity trends for both TNO_3RR and ENO_3RR. This finding shows that catalysts can be screened by considering the material properties that result in high activity for both TNO_3RR and ENO_3RR, namely nitrate and hydrogen adsorption strength, supporting the use of volcano plots for these reactions. However, we also identify major differences between the two reactions such as the apparent activation energy and effect of pH on activity, indicating that there are reaction effects and changes to the mechanism related to electrochemical processes that are unique to ENO_3RR. This finding is consistent with the growing body of literature emphasizing the importance of considering pH for electrocatalytic reactions. To isolate pH effects and further elucidate the nitrate reduction mechanism, additional ENO_3RR tests that account for the ionic strength and point of zero free charge of the buffer solution and product quantification at different pH values are needed. The study here highlights the value in comparing thermocatalytic and electrocatalytic reactions for the same catalysts for both mechanistic insight and identifying the practicality of implementation.

5.5 References

(1) Pennino, M. J.; Compton, J. E.; Leibowitz, S. G. Trends in Drinking Water Nitrate Violations across the United States. *Environmental science & technology* **2017**, *51* (22), 13450–13460.

(2) The Health Effects of Nitrate, Nitrite, and N-Nitroso Compounds: Part 1 of a 2-Part Study, 1981, 531.

(3) Ward, M. H.; Jones, R. R.; Brender, J. D.; de Kok, T. M.; Weyer, P. J.; Nolan, B. T.; Villanueva, C. M.; van Breda, S. G. Drinking Water Nitrate and Human Health: An Updated Review. *Int J Environ Res Public Health* **2018**, *15* (7).

(4) *National Academy of Engineering Grand Challenges For Engineers*; National Academy of Engineering, 2017; pp 19–22.

(5) Werth, C. J.; Yan, C.; Troutman, J. P. Factors Impeding Replacement of Ion Exchange with (Electro)Catalytic Treatment for Nitrate Removal from Drinking Water. *ACS EST Eng.* **2021**, *1* (1), 6–20. https://doi.org/10.1021/acsestengg.0c00076.

(6) Rezvani, F.; Sarrafzadeh, M.-H.; Ebrahimi, S.; Oh, H.-M. Nitrate Removal from Drinking Water with a Focus on Biological Methods: A Review. *Environmental Science and Pollution Research* **2019**, *26* (2), 1124–1141. https://doi.org/10.1007/s11356-017-9185-0.

(7) Singh, N.; Goldsmith, B. R. Role of Electrocatalysis in the Remediation of Water Pollutants. *ACS Catal.* **2020**, *10* (5), 3365–3371. https://doi.org/10.1021/acscatal.9b04167.

(8) Wang, Z.; Richards, D.; Singh, N. Recent Discoveries in the Reaction Mechanism of Heterogeneous Electrocatalytic Nitrate Reduction. *Catal. Sci. Technol.* **2021**, *11* (3), 705–725. https://doi.org/10.1039/D0CY02025G.

(9) van Langevelde, P. H.; Katsounaros, I.; Koper, M. T. M. Electrocatalytic Nitrate Reduction for Sustainable Ammonia Production. *Joule* **2021**, *5* (2), 290–294. https://doi.org/10.1016/j.joule.2020.12.025.

(10) Barrabés, N.; Sá, J. Catalytic Nitrate Removal from Water, Past, Present and Future Perspectives. *Applied Catalysis B: Environmental* **2011**, *104* (1–2), 1–5. https://doi.org/10.1016/j.apcatb.2011.03.011.

(11) Tokazhanov, G.; Ramazanova, E.; Hamid, S.; Bae, S.; Lee, W. Advances in the Catalytic Reduction of Nitrate by Metallic Catalysts for High Efficiency and N2 Selectivity: A Review. *Chemical Engineering Journal* **2020**, *384*, 123252. https://doi.org/10.1016/j.cej.2019.123252.

(12) Li, J.; Zhan, G.; Yang, J.; Quan, F.; Mao, C.; Liu, Y.; Wang, B.; Lei, F.; Li, L.; Chan, A. W. M.; Xu, L.; Shi, Y.; Du, Y.; Hao, W.; Wong, P. K.; Wang, J.; Dou, S.-X.; Zhang, L.; Yu, J. C. Efficient Ammonia Electrosynthesis from Nitrate on Strained Ruthenium Nanoclusters. *J. Am. Chem. Soc.* **2020**, *142* (15), 7036–7046. https://doi.org/10.1021/jacs.0c00418.

(13) McEnaney, J. M.; Blair, S. J.; Nielander, A. C.; Schwalbe, J. A.; Koshy, D. M.; Cargnello, M.; Jaramillo, T. F. Electrolyte Engineering for Efficient Electrochemical Nitrate Reduction to Ammonia on a Titanium Electrode. *ACS Sustainable Chem. Eng.* **2020**, *8* (7), 2672–2681. https://doi.org/10.1021/acssuschemeng.9b05983.

(14) Wang, Y.; Xu, A.; Wang, Z.; Huang, L.; Li, J.; Li, F.; Wicks, J.; Luo, M.; Nam, D.-H.; Tan, C.-S.; Ding, Y.; Wu, J.; Lum, Y.; Dinh, C.-T.; Sinton, D.; Zheng, G.; Sargent, E. H. Enhanced Nitrate-to-Ammonia Activity on Copper–Nickel Alloys via Tuning of

Intermediate Adsorption. *Journal of the American Chemical Society* **2020**, *142* (12), 5702–5708. https://doi.org/10.1021/jacs.9b13347.

(15) Tarpeh, W. A.; Chen, X. Making Wastewater Obsolete: Selective Separations to Enable Circular Water Treatment. *Environmental Science and Ecotechnology* **2021**, *5*, 100078.

(16) Nørskov, J.; Chen, J.; Miranda, R.; Fitzsimmons, T.; Stack, R. *Sustainable Ammonia Synthesis–Exploring the Scientific Challenges Associated with Discovering Alternative, Sustainable Processes for Ammonia Production*; US DOE Office of Science, 2016.

(17) Jung, S.; Bae, S.; Lee, W. Development of Pd–Cu/Hematite Catalyst for Selective Nitrate Reduction. *Environ. Sci. Technol.* **2014**, *48* (16), 9651–9658. https://doi.org/10.1021/es502263p.

(18) Wang, Q.; Wang, W.; Yan, B.; Shi, W.; Cui, F.; Wang, C. Well-Dispersed Pd-Cu Bimetals in TiO2 Nanofiber Matrix with Enhanced Activity and Selectivity for Nitrate Catalytic Reduction. *Chemical Engineering Journal* **2017**, *326*, 182–191. https://doi.org/10.1016/j.cej.2017.05.110.

(19) Ye, T.; Durkin, D. P.; Banek, N. A.; Wagner, M. J.; Shuai, D. Graphitic Carbon Nitride Supported Ultrafine Pd and Pd–Cu Catalysts: Enhanced Reactivity, Selectivity, and Longevity for Nitrite and Nitrate Hydrogenation. *ACS Applied Materials & Interfaces* **2017**, *9* (33), 27421–27426. https://doi.org/10.1021/acsami.7b09192.

(20) Sun, W.; Yang, W.; Gao, S.; Xu, Z.; Du, Q.; Chen, L.; Li, Q. Elevated N2 Selectivity in Catalytic Denitrification by Amino Group-Assisted in-Situ Buffering Effect of NH2-SiO2 Supported PdCu Bimetallic Nanocatalyst. *Chemical Engineering Journal* **2020**, *390*, 124617. https://doi.org/10.1016/j.cej.2020.124617.

(21) Martínez, J.; Ortiz, A.; Ortiz, I. State-of-the-Art and Perspectives of the Catalytic and Electrocatalytic Reduction of Aqueous Nitrates. *Applied Catalysis B: Environmental* **2017**, *207*, 42–59. https://doi.org/10.1016/j.apcatb.2017.02.016.

(22) Duca, M.; Koper, M. T. M. Powering Denitrification: The Perspectives of Electrocatalytic Nitrate Reduction. *Energy & Environmental Science* **2012**, *5* (12), 9726–9742. https://doi.org/10.1039/C2EE23062C.

(23) Dima, G. E.; de Vooys, A. C. A.; Koper, M. T. M. Electrocatalytic Reduction of Nitrate at Low Concentration on Coinage and Transition-Metal Electrodes in Acid Solutions. *Journal of Electroanalytical Chemistry* **2003**, *554–555*, 15–23. https://doi.org/10.1016/S0022-0728(02)01443-2.

(24) Shimazu, K.; Goto, R.; Tada, K. Electrochemical Reduction of Nitrate Ions on Tin-Modified Platinum and Palladium Electrodes. *Chemistry Letters* **2002**, *31* (2), 204–205. https://doi.org/10.1246/cl.2002.204.

(25) Liu, J.-X.; Richards, D.; Singh, N.; Goldsmith, B. R. Activity and Selectivity Trends in Electrocatalytic Nitrate Reduction on Transition Metals. *ACS Catalysis* **2019**, *9* (8), 7052–7064. https://doi.org/10.1021/acscatal.9b02179.

(26) Hörold, S.; Vorlop, K.-D.; Tacke, T.; Sell, M. Development of Catalysts for a Selective Nitrate and Nitrite Removal from Drinking Water. *Catalysis Today* **1993**, *17* (1–2), 21–30. https://doi.org/10.1016/0920-5861(93)80004-K.

(27) Vorlop, K.-D.; Tacke, T. Erste Schritte Auf Dem Weg Zur Edelmetallkatalysierten Nitrat-Und Nitrit-Entfernung Aus Trinkwasser. *Chemie Ingenieur Technik* **1989**, *61* (10), 836–837. https://doi.org/10.1002/cite.330611023.

(28) Song, Y.; Gutiérrez, O. Y.; Herranz, J.; Lercher, J. A. Aqueous Phase Electrocatalysis and Thermal Catalysis for the Hydrogenation of Phenol at Mild Conditions. *Applied Catalysis B: Environmental* **2016**, *182*, 236–246. https://doi.org/10.1016/j.apcatb.2015.09.027.
(29) Song, Y.; Sanyal, U.; Pangotra, D.; Holladay, J. D.; Camaioni, D. M.; Gutiérrez, O. Y.; Lercher, J. A. Hydrogenation of Benzaldehyde via Electrocatalysis and Thermal Catalysis on Carbon-Supported Metals. *Journal of Catalysis* **2018**, *359*, 68–75. https://doi.org/10.1016/j.jcat.2017.12.026.
(30) Bababrik, R.; Santhanaraj, D.; Resasco, D. E.; Wang, B. A Comparative Study of Thermal- and Electrocatalytic Conversion of Furfural: Methylfuran as a Primary and Major Product. *J Appl Electrochem* **2021**, *51* (1), 19–26. https://doi.org/10.1007/s10800-020-01427-y.
(31) Adams, J. S.; Kromer, M. L.; Rodríguez-López, J.; Flaherty, D. W. Unifying Concepts in Electro- and Thermocatalysis toward Hydrogen Peroxide Production. *J. Am. Chem. Soc.* **2021**, *143* (21), 7940–7957. https://doi.org/10.1021/jacs.0c13399.
(32) Koshy, D.; Nathan, S.; Asundi, A.; Abdellah, A.; Dull, S.; Cullen, D.; Higgins, D.; Bao, Z.; Bent, S.; Jaramillo, T. Bridging Thermal Catalysis and Electrocatalysis: Catalyzing CO2 Conversion with Carbon-Based Materials. *Angewandte Chemie International Edition* **2020**, *n/a* (n/a). https://doi.org/10.1002/anie.202101326.
(33) Wang, Z.; Young, S. D.; Goldsmith, B. R.; Singh, N. Increasing Electrocatalytic Nitrate Reduction Activity by Controlling Adsorption through PtRu Alloying. *Journal of Catalysis* **2021**, *395*, 143–154. https://doi.org/10.1016/j.jcat.2020.12.031.
(34) Baturina, O. A.; Aubuchon, S. R.; Wynne, K. J. Thermal Stability in Air of Pt/C Catalysts and PEM Fuel Cell Catalyst Layers. *Chem. Mater.* **2006**, *18* (6), 1498–1504. https://doi.org/10.1021/cm052660e.
(35) Pinchuk, O. A.; Aubuchon, S. R.; Marks, C.; Dominey, R.; Dundar, F.; Deniz, O. F.; Ata, A.; Wynne, K. J. Thermally Pretreated 46% Pt/Vulcan XC72: Characterisation by TGA/DSC/TEM and Cyclic Voltammetry. *Fuel Cells* **2009**, *9* (5), 554–561. https://doi.org/10.1002/fuce.200800183.
(36) Singh, P.; Singh, M. K.; Beg, Y. R.; Nishad, G. R. A Review on Spectroscopic Methods for Determination of Nitrite and Nitrate in Environmental Samples. *Talanta* **2019**, *191*, 364–381. https://doi.org/10.1016/j.talanta.2018.08.028.
(37) Kurniawati, P.; Gusrianti, R.; Dwisiwi, B. B.; Purbaningtias, T. E.; Wiyantoko, B. Verification of Spectrophotometric Method for Nitrate Analysis in Water Samples. *AIP Conference Proceedings* **2017**, *1911*, 020012. https://doi.org/10.1063/1.5016005.
(38) Zhu, D.; Zhang, L.; Ruther, R. E.; Hamers, R. J. Photo-Illuminated Diamond as a Solid-State Source of Solvated Electrons in Water for Nitrogen Reduction. *Nature Materials* **2013**, *12* (9), 836–841. https://doi.org/10.1038/nmat3696.
(39) Epron, F.; Gauthard, F.; Pinéda, C.; Barbier, J. Catalytic Reduction of Nitrate and Nitrite on Pt–Cu/Al2O3 Catalysts in Aqueous Solution: Role of the Interaction between Copper and Platinum in the Reaction. *Journal of Catalysis* **2001**, *198* (2), 309–318. https://doi.org/10.1006/jcat.2000.3138.
(40) Hirayama, J.; Yasuda, K.; Misu, S.; Otomo, R.; Kamiya, Y. Drastic Change in Selectivity Caused by Addition of Oxygen to the Hydrogen Stream for the Hydrogenation of Nitrite in Water over a Supported Platinum Catalyst. *Catal. Sci. Technol.* **2019**, *9* (15), 4017–4022. https://doi.org/10.1039/C9CY00999J.
(41) Mikami, I.; Sakamoto, Y.; Yoshinaga, Y.; Okuhara, T. Kinetic and Adsorption Studies on the Hydrogenation of Nitrate and Nitrite in Water Using Pd-Cu on Active Carbon Support.

Applied Catalysis B: Environmental **2003**, *44* (1), 79–86. https://doi.org/10.1016/S0926-3373(03)00021-3.

(42) de Groot, M. T.; Koper, M. T. M. The Influence of Nitrate Concentration and Acidity on the Electrocatalytic Reduction of Nitrate on Platinum. *Journal of Electroanalytical Chemistry* **2004**, *562* (1), 81–94. https://doi.org/10.1016/j.jelechem.2003.08.011.

(43) Yang, J.; Kwon, Y.; Duca, M.; Koper, M. T. M. Combining Voltammetry and Ion Chromatography: Application to the Selective Reduction of Nitrate on Pt and PtSn Electrodes. *Analytical Chemistry* **2013**, *85* (16), 7645–7649. https://doi.org/10.1021/ac401571w.

(44) Ebbesen, S. D.; Mojet, B. L.; Lefferts, L. Effect of PH on the Nitrite Hydrogenation Mechanism over Pd/Al2O3 and Pt/Al2O3: Details Obtained with ATR-IR Spectroscopy. *J. Phys. Chem. C* **2011**, *115* (4), 1186–1194. https://doi.org/10.1021/jp106521t.

(45) Pintar, A.; Batista, J.; Levec, J.; Kajiuchi, T. Kinetics of the Catalytic Liquid-Phase Hydrogenation of Aqueous Nitrate Solutions. *Applied Catalysis B: Environmental* **1996**, *11* (1), 81–98. https://doi.org/10.1016/S0926-3373(96)00036-7.

(46) Witońska, I.; Karski, S.; Gołuchowska, J. Kinetic Studies on the Hydrogenation of Nitrate in Water Using Rh/Al2O3 and Rh-Cu/Al2O3 Catalysts. *Kinet Catal* **2007**, *48* (6), 823–828. https://doi.org/10.1134/S0023158407060109.

(47) Povar, I.; Spinu, O. Ruthenium Redox Equilibria: 3. Pourbaix Diagrams for the Systems Ru-H2O and Ru-Cl--H2O. *Journal of Electrochemical Science and Engineering* **2016**, *6* (1), 145–153. https://doi.org/10.5599/jese.229.

(48) Yang, J.; Sebastian, P.; Duca, M.; Hoogenboom, T.; M. Koper, M. T. PH Dependence of the Electroreduction of Nitrate on Rh and Pt Polycrystalline Electrodes. *Chemical Communications* **2014**, *50* (17), 2148–2151. https://doi.org/10.1039/C3CC49224A.

(49) Horányi, G.; Rizmayer, E. M. Role of Adsorption Phenomena in the Electrocatalytic Reduction of Nitric Acid at a Platinized Platinum Electrode. *Journal of Electroanalytical Chemistry* **1982**, *140*, 347–366.

(50) Horányi, G.; Wasberg, M. Polarization Behaviour of Nitric Acid at Rhodized Electrodes Partially Blocked by Chemisorbed Species. *Electrochimica Acta* **1997**, *42* (2), 261–265. https://doi.org/10.1016/0013-4686(96)00157-0.

(51) Wasberg, M.; Horányi, G. Electrocatalytic Reduction of Nitric Acid at Rhodized Electrodes and Its Inhibition by Chloride Ions. *Electrochimica Acta* **1995**, *40* (5), 615–623. https://doi.org/10.1016/0013-4686(94)00338-2.

(52) Qin, X.; Zhang, L.; Xu, G.-L.; Zhu, S.; Wang, Q.; Gu, M.; Zhang, X.; Sun, C.; Balbuena, P. B.; Amine, K.; Shao, M. The Role of Ru in Improving the Activity of Pd toward Hydrogen Evolution and Oxidation Reactions in Alkaline Solutions. *ACS Catal.* **2019**, *9* (10), 9614–9621. https://doi.org/10.1021/acscatal.9b01744.

(53) Singh, N.; Lee, M.-S.; Akhade, S. A.; Cheng, G.; Camaioni, D. M.; Gutiérrez, O. Y.; Glezakou, V.-A.; Rousseau, R.; Lercher, J. A.; Campbell, C. T. Impact of PH on Aqueous-Phase Phenol Hydrogenation Catalyzed by Carbon-Supported Pt and Rh. *ACS Catal.* **2019**, *9* (2), 1120–1128. https://doi.org/10.1021/acscatal.8b04039.

(54) Wiesner, A. D.; Katz, L. E.; Chen, C.-C. The Impact of Ionic Strength and Background Electrolyte on PH Measurements in Metal Ion Adsorption Experiments. *Journal of Colloid and Interface Science* **2006**, *301* (1), 329–332. https://doi.org/10.1016/j.jcis.2006.05.011.

(55) Jerkiewicz, G. Standard and Reversible Hydrogen Electrodes: Theory, Design, Operation, and Applications. *ACS Catal.* **2020**, *10* (15), 8409–8417. https://doi.org/10.1021/acscatal.0c02046.

(56) Silva, F.; Sottomayor, M. J.; Hamelin, A. The Temperature Coefficient of the Potential of Zero Charge of the Gold Single-Crystal Electrode/Aqueous Solution Interface: Possible Relevance to Gold-Water Interactions. *Journal of Electroanalytical Chemistry and Interfacial Electrochemistry* **1990**, *294* (1), 239–251. https://doi.org/10.1016/0022-0728(90)87148-D.

(57) Rizo, R.; Sitta, E.; Herrero, E.; Climent, V.; Feliu, J. M. Towards the Understanding of the Interfacial PH Scale at Pt(111) Electrodes. *Electrochimica Acta* **2015**, *162*, 138–145. https://doi.org/10.1016/j.electacta.2015.01.069.

(58) Ganassin, A.; Sebastián, P.; Climent, V.; Schuhmann, W.; Bandarenka, A. S.; Feliu, J. On the PH Dependence of the Potential of Maximum Entropy of Ir(111) Electrodes. *Scientific Reports* **2017**, *7* (1), 1246. https://doi.org/10.1038/s41598-017-01295-1.

(59) García-Aráez, N.; Climent, V.; Feliu, J. M. Evidence of Water Reorientation on Model Electrocatalytic Surfaces from Nanosecond-Laser-Pulsed Experiments. *J. Am. Chem. Soc.* **2008**, *130* (12), 3824–3833. https://doi.org/10.1021/ja0761481.

(60) Ledezma-Yanez, I.; Wallace, W. D. Z.; Sebastián-Pascual, P.; Climent, V.; Feliu, J. M.; Koper, M. T. M. Interfacial Water Reorganization as a PH-Dependent Descriptor of the Hydrogen Evolution Rate on Platinum Electrodes. *Nature Energy* **2017**, *2* (4), 1–7. https://doi.org/10.1038/nenergy.2017.31.

(61) Sarabia, F. J.; Sebastián-Pascual, P.; Koper, M. T. M.; Climent, V.; Feliu, J. M. Effect of the Interfacial Water Structure on the Hydrogen Evolution Reaction on Pt(111) Modified with Different Nickel Hydroxide Coverages in Alkaline Media. *ACS Appl. Mater. Interfaces* **2019**, *11* (1), 613–623. https://doi.org/10.1021/acsami.8b15003.

(62) Zheng, J.; Zhuang, Z.; Xu, B.; Yan, Y. Correlating Hydrogen Oxidation/Evolution Reaction Activity with the Minority Weak Hydrogen-Binding Sites on Ir/C Catalysts. *ACS Catal.* **2015**, *5* (7), 4449–4455. https://doi.org/10.1021/acscatal.5b00247.

(63) McCrum, I. T.; Janik, M. J. PH and Alkali Cation Effects on the Pt Cyclic Voltammogram Explained Using Density Functional Theory. *J. Phys. Chem. C* **2016**, *120* (1), 457–471. https://doi.org/10.1021/acs.jpcc.5b10979.

(64) Zheng, J.; Nash, J.; Xu, B.; Yan, Y. Perspective—Towards Establishing Apparent Hydrogen Binding Energy as the Descriptor for Hydrogen Oxidation/Evolution Reactions. *J. Electrochem. Soc.* **2018**, *165* (2), H27. https://doi.org/10.1149/2.0881802jes.

(65) Cheng, T.; Wang, L.; Merinov, B. V.; Goddard, W. A. Explanation of Dramatic PH-Dependence of Hydrogen Binding on Noble Metal Electrode: Greatly Weakened Water Adsorption at High PH. *J. Am. Chem. Soc.* **2018**, *140* (25), 7787–7790. https://doi.org/10.1021/jacs.8b04006.

(66) Rebollar, L.; Intikhab, S.; Oliveira, N. J.; Yan, Y.; Xu, B.; McCrum, I. T.; Snyder, J. D.; Tang, M. H. "Beyond Adsorption" Descriptors in Hydrogen Electrocatalysis. *ACS Catal.* **2020**, *10* (24), 14747–14762. https://doi.org/10.1021/acscatal.0c03801.

(67) Briega-Martos, V.; Herrero, E.; Feliu, J. M. Effect of PH and Water Structure on the Oxygen Reduction Reaction on Platinum Electrodes. *Electrochimica Acta* **2017**, *241*, 497–509. https://doi.org/10.1016/j.electacta.2017.04.162.

(68) Haber, F.; Rossignol, R. L. Über Die Technische Darstellung von Ammoniak Aus Den Elementen. *Zeitschrift für Elektrochemie und angewandte physikalische Chemie* **1913**, *19* (2), 53–72. https://doi.org/10.1002/bbpc.19130190201.
(69) Kandemir, T.; Schuster, M. E.; Senyshyn, A.; Behrens, M.; Schlögl, R. The Haber–Bosch Process Revisited: On the Real Structure and Stability of "Ammonia Iron" under Working Conditions. *Angewandte Chemie International Edition* **2013**, *52* (48), 12723–12726. https://doi.org/10.1002/anie.201305812.
(70) USDA ERS - Fertilizer Use and Price https://www.ers.usda.gov/data-products/fertilizer-use-and-price.aspx (accessed 2020 -07 -20).
(71) Mayyas, A. T.; Ruth, M. F.; Pivovar, B. S.; Bender, G.; Wipke, K. B. *Manufacturing Cost Analysis for Proton Exchange Membrane Water Electrolyzers*; NREL/TP-6A20-72740, 1557965; 2019; p NREL/TP-6A20-72740, 1557965. https://doi.org/10.2172/1557965.
(72) Vickers, J.; Peterson, D.; Randolph, K. *Cost of Electrolytic Hydrogen Production with Existing Technology*; 20004; Department of Energy, 2021; p 5.

Chapter 6

Conclusions, Future Recommended Works, and Outlook

6.1 Summary and Overall Conclusions

The goal of the research described in this dissertation was to develop catalysts and investigate alternative catalytic systems for sustainable ammonia synthesis. Even though the Haber-Bosch process is widely used and continues to support the growing global population, the Haber-Bosch process is extremely energy-intensive and emits excess CO_2 that is detrimental to the environment.[1] Additionally, anthropogenic nitrogen fixation creates excess nitrate contaminants from the oxidation of ammonia. Thus, regulating and rebalancing excess nitrate in water sources is important to maintain overall environmental health. This dissertation investigated three different methods of solving these problems:

1. Improve the Haber-Bosch process by exploring catalysts that are feasible for this reaction at ambient pressures to reduce energy consumption during operations.
2. Develop and design new catalysts for electrocatalytic nitrate reduction reaction (ENO_3RR), and verify applications of computational models for optimizing alloys.
3. Compare ENO_3RR to thermal catalytic nitrate reduction reaction (TNO_3RR) to gain mechanistic insights for both reactions and evaluate both systems for commercial operations and industrial upscaling.

In **Chapter 3**, we explored a series of metal-supported molybdenum carbides (Mo_2C) and nitrides (Mo_2N) that have previously been shown to be active for ammonia synthesis at ambient atmospheric pressure.[2] By supporting metals (e.g., Fe, Co, and Ru) on the surface of the carbide or nitride support, we hypothesized that metal sites will activate N_2 bond dissociation and support sites will perform the hydrogenation step to improve ammonia synthesis activity. A series of metal-supported Mo_2C and Mo_2N were synthesized, characterized, and tested at 400 °C and 1 atm. Even though there was little to no catalytic improvement with the addition of metals on the supports, further in situ work is recommended to understand the role of nitrogen atoms from the nitride participating in the ammonia synthesis reaction via a Mars-van Krevelen mechanism.[3]

The work in **Chapters 4** and **5** focus on using nitrate as the primary reactant to produce ammonia. Because excess nitrate is a water pollutant, reducing and recycling nitrate to ammonia is a promising approach to help balance the nitrogen cycle.[4] Previous research from the Goldsmith Group used first-principles microkinetic modeling to predict that a Pt_3Ru alloy could be active for ENO_3RR.[5] In **Chapter 4**, we experimentally confirm these calculations by synthesizing different compositions of Pt_xRu_y/C (x = 48–100%) and characterizing their activity and selectivity for nitrate reduction at different operating potentials. The Pt_xRu_y/C alloys are more active than Pt/C, with $Pt_{78}Ru_{22}/C$ being six times more active than Pt/C at 0.1 V vs. RHE, and ammonia faradaic efficiencies between 93–98%. Experimental and computational results show increasing Pt_xRu_y activity as Ru content increases to ~25 at% followed by a decrease in activity at higher Ru content. By tuning the amount of Ru in the alloy, an optimum in nitrate and hydrogen binding energies occurs, which maximizes the electrocatalytic activity. This maximum is due to a transition from nitrate dissociation as the rate determining step to a new rate determining step at higher Ru content. This work demonstrates how electrocatalyst activity can be tuned by changing the adsorption

strength of reacting species through alloying. Ultimately, this study provides insights for characterizing and designing alloys for optimal nitrate reduction and ammonium production.

In **Chapter 5**, we compared the ENO_3RR with TNO_3RR on Pt_xRu_y/C to obtain additional mechanistic insights for both reactions and evaluate the same catalysts under similar operating conditions (e.g., hydrogen partial pressure, applied potential, nitrate concentration, and pH). Although both catalytic systems are promising for converting nitrate to ammonia, there are no studies that directly compare the two catalytic reactions due to different experimental conditions and applications. Our results show that increasing the driving force of hydrogen increases the rate of nitrate reduction for both ENO_3RR and TNO_3RR while the order of catalyst activity remains the same ($Pt/C << PtRu/C < Pt_{75}Ru_{25}/C$). Additionally, increasing the nitrate concentration nitrate reduction rates in both reactions for PtRu/C. However, at concentrations beyond 0.5 M NO_3^-, ENO_3RR activity decreases due to poisoning of active sites by excess nitrate in the solution. Despite these similarities, pH has a different effect on PtRu/C for TNO_3RR and ENO_3RR activity and results in a change in the apparent activation energy E_a from acidic to neutral pH. For TNO_3RR, E_a is lower in acidic conditions due to faster conversion of nitrite to ammonia. However, it is more difficult to deconvolute pH effects on ENO_3RR. The FE shifts from 93% to 54% from pH 1 to 7, suggesting a possible mechanism shift that favors nitrogen production instead of ammonia. Many other factors, including the ionic strength of the electrolyte solution, hydrogen equilibrium potential, the point of zero free charge, and water orientation and reorganization energy can also affect the measured reduction currents. Finally, this work evaluates the practicality of TNO_3RR and ENO_3RR on PtRu/C for industrial processes based on the cost per tonne of NH_4NO_3 and ammonia production rates. Ultimately, this work provides a comparative insight into

the similarities and differences between TNO_3RR and ENO_3RR mechanism and serves as a model for evaluating systems for industrial implementation of nitrate reduction technology.

6.2 Extension of Current Research

The work in this dissertation establishes a foundation for investigating catalysts for different ammonia production reactions. Suggested areas for further examination can further elucidate reaction mechanisms and improve system designs for increased activity and selectivity towards ammonia. These future works are broken down into the three distinct catalytic systems: **Section 6.2.1** will provide an overview of future improvements on the carbide and nitride supports for ammonia synthesis, and **Sections 6.2.2** and **6.2.3** will explore options to improve the understanding of ENO_3RR and TNO_3RR mechanisms, respectively.

6.2.1 Metal Carbides and Nitrides for Ammonia Synthesis at Ambient Pressure

The results presented in **Chapter 3** show that the pretreatment conditions greatly effect the rate of ammonia production. These measurements suggest that under reaction conditions, lattice N from Mo_2N might be reacting with H_2 to form NH_3 via the Mars-van Krevelen mechanism.[3] Therefore, it is recommended to use isotopic nitrogen labeling to perform product quantification for supported Mo_2N materials. This technique is especially useful for determining the source of product nitrogen species, and distinguish if the product is from the reactant (detected as ^{15}N) or from decomposition of the catalyst (detected as ^{14}N).[6,7] Additionally, in situ XAFS can be used to provide insights on how lattice nitrogen reacts with H_2 under reaction conditions and provide further mechanistic understanding of the reaction. To understand the stability of these materials, supported Mo_2N should be tested for an extended time to see if N_2 reactant can replenish the nitrogen sites in the nitrides for ammonia production under reaction conditions.

Because there is little to no enhancement from the addition of transition metals on the Mo_2C and Mo_2N supports, it is recommended to alter the synthesis process to increase the activity of the supports at ambient pressure. Previous studies show improvement of catalyst activity by first alloying the metals before carbonization and nitridation.[8,9] Additionally, adding promoters such as Cs or K to the metal supported catalysts can further improve ammonia synthesis activity Cs and K sites function as electronic promoters to accelerate the nitrogen dissociation step.[10,11]

6.2.2 Improve Understanding of pH Effects on Electrocatalysts for ENO_3RR

Results and discussion presented in **Chapter 5** indicate that there limited studies that provide a mechanistic understanding of the role of hydronium ions in ENO_3RR from changing the pH of the electrolyte solution. Many different factors and inconsistencies make it difficult to measure the effect of pH on the reaction. For example, buffer solutions are required to maintain a wide range of pH conditions, but these solutions have different ionic strengths that ultimately may affect the measured nitrate reduction currents. To eliminate the influence of ionic strength in the electrolyte buffer solutions, previous studies have balanced the solution by adding NaCl.[12,13] However, many studies also show that anions such as sulfate[14] or chloride[15–17] inhibits catalyst active sites, thus is unclear whether the decrease in activity observed is due to change in pH or catalyst poisoning from added NaCl.

To improve the understanding of pH on ENO_3RR, it is recommended to continue using a variety of buffer solutions to span a wider range of testing conditions, while balancing the ionic strength of the solution by adding benign salts. It is also recommended to improve experimental designs when measuring the selectivity of electrocatalysts at different pH. Studies claim that ammonia is the favored product at low pH and shifts to nitrogen at neutral and basic conditions.[12,13,18] But many of these studies operate in a single-compartment cell with added NaCl

to balance the ionic strength. Chloride has been cited to increase ENO_3RR selectivity from ammonia towards N_2[19] through the production of oxidized chlorine species (ClO^-) at the anode that then oxidizes ammonia to N_2 in the bulk solution. Thus, in a single-compartment cell, it is unclear whether the mechanistic shift with increasing pH is due to an actual change in the selectivity or due to the oxidation of ammonia at the anode. Future experiments in this area must be conducted in a two-compartment cell to garner better understanding of the system and isolate pH effects on selectivity.

By improving our understanding of pH effects on ENO_3RR, we can develop a better mechanistic understanding of how hydronium ions influence the activity and selectivity of the reaction. For practical purposes, these findings can also aid the modeling and designing of catalysts for different types of wastewater treatment applications.

6.2.3 Designing Alloy Systems for TNO_3RR

A majority of TNO_3RR literature focuses on using bimetallic catalysts that use an active promoter metal that converts nitrate to nitrite before a selective noble metal drives the reaction to desired products. Previous studies show that the proximity of the noble metal is essential to stabilize the promoter metal via hydrogen spill-over effect. In the example of a PdCu catalytic system, the phase-segregated (non-alloy) metals had higher selectivity towards nitrogen production while phase-pure alloys had higher overall activity for nitrate reduction.[20] The results in **Chapter 5** show that Pt_xRu_y alloys might function in a similar bifunctional mechanism where Ru initiates the reaction from nitrate to nitrite and both metals function to reduce nitrite to ammonia. Our study primarily focused on exploring the activity of different surface compositions of Pt and Ru and comparison to ENO_3RR, but the next steps should focus on synthesizing, testing, and modeling the activity and selectivity of phase-pure and phase-segregated PtRu/C alloys. Since

the hydrogen spill-over effect is related to the proximity of the two metals, it is also important to consider how the particle size of the alloys influences the activity and selectivity.

Furthermore, if there is a significant difference between the phase-pure and phase-segregated alloys, it would also be interesting to consider optimizing the reaction with multiple reactors in series. For example, the first system would operate at low pH to accelerate the conversion of nitrate to nitrite while the second reactor would function at optimal conditions for nitrite reduction to ammonia or nitrogen, depending on intended application.[21] A two-reactor system might increase capital and operating costs but provide more precise and controlled reaction conditions for optimal product selectivity.

Given comparable ammonia production rates as the Haber-Bosch process, it is also important to test TNO_3RR catalysts under simulated wastewater conditions before upscaling industrially. Similar to how anions in solutions can affect the reactivity of ENO_3RR catalysts, increasing the hardness and salinity of tap water decreases the activity of catalysts for TNO_3RR.[22] Thus, it is important to further understand catalyst deactivation mechanisms and sources of site poisoning.

6.3 Research in New Areas

The work in this dissertation has primarily focused on investigating specific carbides and nitrides for ammonia synthesis and PtRu alloy systems for TNO_3RR and ENO_3RR, and serves as a guide for investigating catalytic system for ammonia production. Further expansion upon this work includes new material designs to improve catalytic activity and selectivity. The theoretical volcano plots developed by the Goldsmith Group predicted Fe_3Ru, Fe_3Ni, and Fe_3Cu to be active for nitrate reduction reaction in addition to Pt_3Ru.[5] Future experimental work into these materials can further evaluate the feasibility of using nitrogen and oxygen binding energies as descriptors

for nitrate reduction activity. Additionally, transitional metals such as Fe, Ni, and Cu are cheaper than platinum group metals traditionally used for nitrate reduction, and can provide a more cost-effective approach to this catalytic system.

Aside from improving nitrate conversion to ammonia from alloying, it would be important to investigate straining effects of materials on the reactivity and selectivity. In the example of the strained Ru nanocluster for ENO_3RR, the subsurface Ru–O coordination generates hydrogen radicals that hydrogenates intermediates and lowers the kinetic barriers of the rate-limiting steps.[23] This catalytic design maintains above 99% selectivity towards ammonia production and enables high rates of ammonia production (5.56 mol g^{-1} h^{-1}) for 12 hrs. Using this proposed mechanism, similar approaches can be used to investigate catalyst strain effects on other reducible oxides such as CeO_2, TiO_2, Al_2O_3, and MgO, and find relationships between the oxidation state of different material and the nitrate reduction reactivity and selectivity.

Machine learning can accelerate the process of discovering catalysts that are most active and selective for TNO_3RR and ENO_3RR by correlating descriptors, such as chemical and physical properties, to their performance.[24] Machine learning methods can help identify patterns in catalysis data and provide fundamental insights on key descriptors that influence stability, activity, and selectivity. Ultimately, machine learning techniques may guide future experimental designs by searching for optimal catalysts for both TNO_3RR and ENO_3RR in large combinatorial spaces, such as binary and ternary alloys.

6.4 Outlooks

Over the past decades, there has been a substantial increase in studies that focus on sustainable ammonia production, ranging from discovering new catalysts for traditional ammonia synthesis to elucidating the electrochemical nitrate reduction mechanism. Currently, the global

production of ammonia is increasing at 2.3% every year,[25] and industrial Haber-Bosch synthesis with methane-fed H_2 production is not environmentally sustainable. Additionally, nitrate concentrations in water sources continue to rise as fertilizer consumption increases, making problems with the nitrogen cycle an immediate engineering challenge.[26] Current research for Haber-Bosch ammonia synthesis has shifted to focus more on electrocatalytic reduction of nitrogen to ammonia, which will not be included in this section. **Section 6.4.1** provides an overview of how to improve current research in the nitrate reduction reaction, and **Section 6.4.2** provides policy recommendations that can enable the implementation of this technology in the future.

6.4.1 Improvements upon Current Research

Despite the multitude of research in catalytic systems for ammonia production, there lacks a general evaluation standard for nitrate reduction catalysts. For TNO_3RR, PdCu bimetallic system is identified as the best catalyst for the conversion of nitrate to nitrogen.[27–32] Until recently, there has been limited research for active materials to reduce nitrate to ammonia.[33] Similarly, works in ENO_3RR have predominantly focused on nitrogen selectivity, and there is no consensus for the most active and selective catalyst. To overcome these challenges, we need to develop a better mechanistic understanding of materials for heterogeneous thermocatalytic and electrocatalytic nitrate reduction to ammonia. This would provide insight into catalyst properties that would allow for more active and selective material towards the desired products.

Despite the understanding of the reaction mechanism for ENO_3RR, few studies report steady-state electrocatalytic performance at a controlled potential. This becomes a problem for measuring long-term stability, activity, and selectivity in applied systems for nitrate remediation. Many reports show the rate of conversion of nitrate, but less frequently with reported current

densities and applied potentials that are needed for evaluating scale-up potential and economic viability. Additionally, more studies with controlled potentials and measured current densities normalized to the electrochemically active surface area will make comparisons between labs and to ab initio simulations, such as DFT, much easier. These normalized rates would also help to test hypothesized reaction mechanisms, rate-determining steps, and selectivity determining steps.

To explore the possibility of both TNO_3RR and ENO_3RR in real wastewater streams, we need to test material under different operating conditions and understand how other contaminants in water can poison and deactivate catalyst performance. For TNO_3RR, there are limited studies conducted outside of neutral pH water with low nitrate concentrations and no recent studies that address the concerns of catalyst poisoning. There is a wide range of materials that have been explored for ENO_3RR, including alloys, metal oxides, sulfides, and phosphides, that may be capable of addressing the problem of electrocatalyst poisoning. However, many of these materials have not been evaluated for capabilities of converting nitrate to ammonia under simulated wastewater conditions. A detailed understanding of the interaction between nitrate, contaminant ions, and other reaction conditions on the catalyst surface may lead to discovery of new materials that can achieve the activity, selectivity, and stability necessary for a commercial nitrate reduction system.

6.4.2 Future Policy Recommendations

The research in this dissertation addresses two fundamental problems in the nitrogen cycle: sustainable ammonia production and effective wastewater treatment and management. The policy recommendations in this section will provide short-term and long-term objectives to enable the use of promising catalytic technology and have broader impacts on water pollutant management.

6.4.2.1 *Sustainable ammonia production systems*

Current catalytic technology can operate at levels comparable to the Haber-Bosch process,[23,34] but are limited due to the cost of renewable energy sources and a lack of hydrogen infrastructure. *Federal institutions should provide additional research funding to improve the efficiency of renewable energy sources, reduce the cost of production without compromising environmental regulations, and explore methods for disposing massive volumes of electronic waste.*[35] Currently, over 77% of Americans support investigating alternative energy sources[36] and renewable energy is projected to represent 42% of the electricity grid by 2050.[37] However, there are limited policies involving end-of-life solar panels, which will become a source of hazardous waste. To reduce carbon footprint of renewable technology waste, the most environmentally friendly option is to offer financial incentives for users to recycle old panels to manufacturers.[38] This recommendation will reduce the cost of renewable electricity, which in turn makes electrocatalytic systems more cost-effective to implement industrially.

Likewise, *federal and state governments should increase research funding to upscale hydrogen infrastructure.* Current research has predominately focused on building smaller hydrogen infrastructure to improve large-scale transportation. However, creating industrial-level hydrogen from electricity can break the barrier for implementing TNO_3RR or Haber-Bosch ammonia synthesis with H_2 produced from renewable electricity. The U.S. is currently on track to reducing the cost of renewable H_2 sources to \$1/kg of H_2 by 2030,[39] which will significantly cut operating costs for thermal catalytic hydrogenation systems.

6.4.2.2 *Water contamination and management*

The Environmental Protection Agency establishes the national limit on pollutants while state agencies are responsible for developing and implementing a state compliance plan. These

national limits are set based on a pollutant-by-pollutant basis. For example, under the Safe Drinking Water Act, the federal maximum contaminant level for nitrate has been set at 10 mg/L since 1992.[40] However, these limits do not take into consideration the cumulative impact of mixed pollutants, despite growing evidence that interactions of different chemicals can expose people to greater health risks.[41] Thus, *federal and state governments should investigate and limit the excretion of water pollutants based on cumulative effects in addition to point-source effects*. By amending current policies, this recommendation will improve the overall health and well-being through a more holistic analysis of how water pollutants affect public health.

Additionally, it is important to consider environmental justice when regulating water and air quality. In many cases, poor air and water qualities are typical problems for marginalized communities dominated by people of color. For example, researchers evaluated national databases from 1966 – 1995 to determine that hazardous waste site permits were more likely to be approved in areas with growing demographics among people of color.[42] Beyond regulation limits established by the federal government, *state and local governments need to fund and push policies that target collective participatory democracy that addresses the concerns of citizens that suffer from a lack of clean water and air*. California, one of the states with the most progressive environmental regulations, passed AB 617 in 2006, which addresses local pollution hotspots and empowers communities to work directly with regulators to address environmental issues.[43] Since then, these efforts have garnered support for policies that address historic disparities in local environmental exposure among marginalized communities, and created a form of accountability where the public can provide input on where they believe public agencies are falling short. Continued implementation of model legislation such as AB 617 would improve participatory democracy among marginalized communities and address local concerns of environmental pollutants.

6.5 References

(1) Smith, C.; Hill, A. K.; Torrente-Murciano, L. Current and Future Role of Haber–Bosch Ammonia in a Carbon-Free Energy Landscape. *Energy Environ. Sci.* **2020**, *13* (2), 331–344. https://doi.org/10.1039/C9EE02873K.

(2) Kojima, R.; Aika, K. Molybdenum Nitride and Carbide Catalysts for Ammonia Synthesis. *Applied Catalysis A: General* **2001**, *219* (1), 141–147. https://doi.org/10.1016/S0926-860X(01)00676-7.

(3) Zeinalipour-Yazdi, C. D.; Hargreaves, J. S. J.; Catlow, C. R. A. Nitrogen Activation in a Mars–van Krevelen Mechanism for Ammonia Synthesis on Co3Mo3N. *J. Phys. Chem. C* **2015**, *119* (51), 28368–28376. https://doi.org/10.1021/acs.jpcc.5b06811.

(4) Zeng, Y.; Priest, C.; Wang, G.; Wu, G. Restoring the Nitrogen Cycle by Electrochemical Reduction of Nitrate: Progress and Prospects. *Small Methods n/a* (n/a), 2000672. https://doi.org/10.1002/smtd.202000672.

(5) Liu, J.-X.; Richards, D.; Singh, N.; Goldsmith, B. R. Activity and Selectivity Trends in Electrocatalytic Nitrate Reduction on Transition Metals. *ACS Catalysis* **2019**, *9* (8), 7052–7064. https://doi.org/10.1021/acscatal.9b02179.

(6) Andersen, S. Z.; Čolić, V.; Yang, S.; Schwalbe, J. A.; Nielander, A. C.; McEnaney, J. M.; Enemark-Rasmussen, K.; Baker, J. G.; Singh, A. R.; Rohr, B. A.; Statt, M. J.; Blair, S. J.; Mezzavilla, S.; Kibsgaard, J.; Vesborg, P. C. K.; Cargnello, M.; Bent, S. F.; Jaramillo, T. F.; Stephens, I. E. L.; Nørskov, J. K.; Chorkendorff, I. A Rigorous Electrochemical Ammonia Synthesis Protocol with Quantitative Isotope Measurements. *Nature* **2019**, *570* (7762), 504–508. https://doi.org/10.1038/s41586-019-1260-x.

(7) Song, Y.; Johnson, D.; Peng, R.; Hensley, D. K.; Bonnesen, P. V.; Liang, L.; Huang, J.; Yang, F.; Zhang, F.; Qiao, R.; Baddorf, A. P.; Tschaplinski, T. J.; Engle, N. L.; Hatzell, M. C.; Wu, Z.; Cullen, D. A.; Meyer, H. M.; Sumpter, B. G.; Rondinone, A. J. A Physical Catalyst for the Electrolysis of Nitrogen to Ammonia. *Science Advances* **2018**, *4* (4), e1700336. https://doi.org/10.1126/sciadv.1700336.

(8) AlShibane, I.; Daisley, A.; Hargreaves, J. S. J.; Hector, A. L.; Laassiri, S.; Rico, J. L.; Smith, R. I. The Role of Composition for Cobalt Molybdenum Carbide in Ammonia Synthesis. **2017**, 9.

(9) Kojima, R.; Aika, K. Cobalt Molybdenum Bimetallic Nitride Catalysts for Ammonia Synthesis: Part 3. Reactant Gas Treatment. *Applied Catalysis A: General* **2001**, *219* (1), 157–170. https://doi.org/10.1016/S0926-860X(01)00678-0.

(10) Ertl, G.; Thiele, N. XPS Studies with Ammonia Synthesis Catalysts. *Applications of Surface Science* **1979**, *3* (1), 99–112. https://doi.org/10.1016/0378-5963(79)90064-3.

(11) Ertl, G. Surface Science and Catalysis—Studies on the Mechanism of Ammonia Synthesis: The P. H. Emmett Award Address. *Catalysis Reviews* **1980**, *21* (2), 201–223. https://doi.org/10.1080/03602458008067533.

(12) Dortsiou, M.; Katsounaros, I.; Polatides, C.; Kyriacou, G. Influence of the Electrode and the PH on the Rate and the Product Distribution of the Electrochemical Removal of Nitrate. *Environmental Technology* **2013**, *34* (3), 373–381. https://doi.org/10.1080/09593330.2012.696722.

(13) Yang, J.; Sebastian, P.; Duca, M.; Hoogenboom, T.; M. Koper, M. T. PH Dependence of the Electroreduction of Nitrate on Rh and Pt Polycrystalline Electrodes. *Chemical Communications* **2014**, *50* (17), 2148–2151. https://doi.org/10.1039/C3CC49224A.

(14) Horányi, G.; Rizmayer, E. M. Role of Adsorption Phenomena in the Electrocatalytic Reduction of Nitric Acid at a Platinized Platinum Electrode. *Journal of Electroanalytical Chemistry* **1982**, *140*, 347–366.
(15) Horányi, G.; Rizmayer, E. M. Role of Adsorption Phenomena in the Electrocatalytic Reduction of Nitric Acid at a Platinized Platinum Electrode. *Journal of Electroanalytical Chemistry and Interfacial Electrochemistry* **1982**, *140* (2), 347–366. https://doi.org/10.1016/0022-0728(82)85178-4.
(16) Wasberg, M.; Horányi, G. Electrocatalytic Reduction of Nitric Acid at Rhodized Electrodes and Its Inhibition by Chloride Ions. *Electrochimica Acta* **1995**, *40* (5), 615–623. https://doi.org/10.1016/0013-4686(94)00338-2.
(17) Horányi, G.; Wasberg, M. Polarization Behaviour of Nitric Acid at Rhodized Electrodes Partially Blocked by Chemisorbed Species. *Electrochimica Acta* **1997**, *42* (2), 261–265. https://doi.org/10.1016/0013-4686(96)00157-0.
(18) Wang, Z.; Richards, D.; Singh, N. Recent Discoveries in the Reaction Mechanism of Heterogeneous Electrocatalytic Nitrate Reduction. *Catal. Sci. Technol.* **2021**, *11* (3), 705–725. https://doi.org/10.1039/D0CY02025G.
(19) Garcia-Segura, S.; Lanzarini-Lopes, M.; Hristovski, K.; Westerhoff, P. Electrocatalytic Reduction of Nitrate: Fundamentals to Full-Scale Water Treatment Applications. *Applied Catalysis B: Environmental* **2018**, *236*, 546–568. https://doi.org/10.1016/j.apcatb.2018.05.041.
(20) Deganello, F.; Liotta, L. F.; Macaluso, A.; Venezia, A. M.; Deganello, G. Catalytic Reduction of Nitrates and Nitrites in Water Solution on Pumice-Supported Pd–Cu Catalysts. *Applied Catalysis B: Environmental* **2000**, *24* (3), 265–273. https://doi.org/10.1016/S0926-3373(99)00109-5.
(21) Pintar, A.; Batista, J. Catalytic Stepwise Nitrate Hydrogenation in Batch-Recycle Fixed-Bed Reactors. *Journal of Hazardous Materials* **2007**, *149* (2), 387–398. https://doi.org/10.1016/j.jhazmat.2007.04.004.
(22) Pintar, A.; \v{S}etinc, M.; Levec, J. Hardness and Salt Effects on Catalytic Hydrogenation of Aqueous Nitrate Solutions. *Journal of Catalysis* **1998**, *174* (1), 72–87. https://doi.org/10.1006/jcat.1997.1960.
(23) Li, J.; Zhan, G.; Yang, J.; Quan, F.; Mao, C.; Liu, Y.; Wang, B.; Lei, F.; Li, L.; Chan, A. W. M.; Xu, L.; Shi, Y.; Du, Y.; Hao, W.; Wong, P. K.; Wang, J.; Dou, S.-X.; Zhang, L.; Yu, J. C. Efficient Ammonia Electrosynthesis from Nitrate on Strained Ruthenium Nanoclusters. *Journal of the American Chemical Society* **2020**, jacs.0c00418. https://doi.org/10.1021/jacs.0c00418.
(24) Goldsmith, B. R.; Esterhuizen, J.; Liu, J.-X.; Bartel, C. J.; Sutton, C. Machine Learning for Heterogeneous Catalyst Design and Discovery. *AIChE Journal* **2018**, *64* (7), 2311–2323. https://doi.org/10.1002/aic.16198.
(25) Food and Agriculture Organization of the United Nations. *World Fertilizer Trends and Outlook to 2022.*; Food & Agriculture Org: S.l., 2019.
(26) Wang, Z.; Richards, D.; Singh, N. Recent Discoveries in the Reaction Mechanism of Heterogeneous Electrocatalytic Nitrate Reduction. *Catal. Sci. Technol.* **2021**, 10.1039.D0CY02025G. https://doi.org/10.1039/D0CY02025G.
(27) Barrabés, N.; Sá, J. Catalytic Nitrate Removal from Water, Past, Present and Future Perspectives. *Applied Catalysis B: Environmental* **2011**, *104* (1–2), 1–5. https://doi.org/10.1016/j.apcatb.2011.03.011.

(28) Jung, S.; Bae, S.; Lee, W. Development of Pd–Cu/Hematite Catalyst for Selective Nitrate Reduction. *Environ. Sci. Technol.* **2014**, *48* (16), 9651–9658. https://doi.org/10.1021/es502263p.
(29) Wang, Q.; Wang, W.; Yan, B.; Shi, W.; Cui, F.; Wang, C. Well-Dispersed Pd-Cu Bimetals in TiO2 Nanofiber Matrix with Enhanced Activity and Selectivity for Nitrate Catalytic Reduction. *Chemical Engineering Journal* **2017**, *326*, 182–191. https://doi.org/10.1016/j.cej.2017.05.110.
(30) Ye, T.; Durkin, D. P.; Banek, N. A.; Wagner, M. J.; Shuai, D. Graphitic Carbon Nitride Supported Ultrafine Pd and Pd–Cu Catalysts: Enhanced Reactivity, Selectivity, and Longevity for Nitrite and Nitrate Hydrogenation. *ACS Applied Materials & Interfaces* **2017**, *9* (33), 27421–27426. https://doi.org/10.1021/acsami.7b09192.
(31) Sun, W.; Yang, W.; Gao, S.; Xu, Z.; Du, Q.; Chen, L.; Li, Q. Elevated N2 Selectivity in Catalytic Denitrification by Amino Group-Assisted in-Situ Buffering Effect of NH2-SiO2 Supported PdCu Bimetallic Nanocatalyst. *Chemical Engineering Journal* **2020**, *390*, 124617. https://doi.org/10.1016/j.cej.2020.124617.
(32) Tokazhanov, G.; Ramazanova, E.; Hamid, S.; Bae, S.; Lee, W. Advances in the Catalytic Reduction of Nitrate by Metallic Catalysts for High Efficiency and N2 Selectivity: A Review. *Chemical Engineering Journal* **2020**, *384*, 123252. https://doi.org/10.1016/j.cej.2019.123252.
(33) Wei, L.; Liu, D.-J.; Rosales, B. A.; Evans, J. W.; Vela, J. Mild and Selective Hydrogenation of Nitrate to Ammonia in the Absence of Noble Metals. *ACS Catal.* **2020**, *10* (6), 3618–3628. https://doi.org/10.1021/acscatal.9b05338.
(34) McEnaney, J. M.; Blair, S. J.; Nielander, A. C.; Schwalbe, J. A.; Koshy, D. M.; Cargnello, M.; Jaramillo, T. F. Electrolyte Engineering for Efficient Electrochemical Nitrate Reduction to Ammonia on a Titanium Electrode. *ACS Sustainable Chem. Eng.* **2020**, *8* (7), 2672–2681. https://doi.org/10.1021/acssuschemeng.9b05983.
(35) Mulvaney, D. *Solar Power: Innovation, Sustinability, and Environmental Justice*; University of California Press, 2019.
(36) Desilver, D. Renewable Energy Is Growing Fast in the U.S., but Fossil Fuels Still Dominate. *Pew Research Center*, 2020.
(37) Annual Energy Outlook 2021 https://www.eia.gov/outlooks/aeo/ (accessed May 26, 2021).
(38) Chowdhury, Md. S.; Rahman, K. S.; Chowdhury, T.; Nuthammachot, N.; Techato, K.; Akhtaruzzaman, Md.; Tiong, S. K.; Sopian, K.; Amin, N. An Overview of Solar Photovoltaic Panels' End-of-Life Material Recycling. *Energy Strategy Reviews* **2020**, *27*, 100431. https://doi.org/10.1016/j.esr.2019.100431.
(39) *Hydrogen Economy Outlook*; BloombergNEF, 2020.
(40) US EPA, O. National Primary Drinking Water Regulations https://www.epa.gov/ground-water-and-drinking-water/national-primary-drinking-water-regulations (accessed May 24, 2021).
(41) Dominici, F.; Peng, R. D.; Barr, C. D.; Bell, M. L. Protecting Human Health from Air Pollution: Shifting from a Single-Pollutant to a Multipollutant Approach. *Epidemiology* **2010**, *21* (2), 187–194. https://doi.org/10.1097/EDE.0b013e3181cc86e8.
(42) Mohai, P.; Saha, R. Which Came First, People or Pollution? Assessing the Disparate Siting and Post-Siting Demographic Change Hypotheses of Environmental Injustice. *Environ. Res. Lett.* **2015**, *10* (11), 115008. https://doi.org/10.1088/1748-9326/10/11/115008.

(43) Fowlie, M.; Walker, R.; Wooley, D. Climate Policy, Environmental Justice, and Local Air Pollution. **2020**, 27.

Appendices

Appendix A

Catalyst Characterization and Evaluation

This Appendix contains additional processing work for catalyst characterization work in **Chapter 4**.

XAFS Measurements and data processing

The raw data obtained at the Pt L_3-edge is presented in **Figure A.1**. Because the raw signal of the bulk Pt foil was much higher, the actual values have been scaled by a factor of 0.5 in the *R* and *k* space to aid visual comparison. Based on the XANES spectra at the Pt L_3-edge in **Figure A.1a**, the white line intensity for the Pt_xRu_y/C catalysts compared to the bulk metallic Pt foil show that these samples were slightly oxidized. These surface oxides were expected and were reduced under electrochemical pretreatment conditions prior to catalyst use.

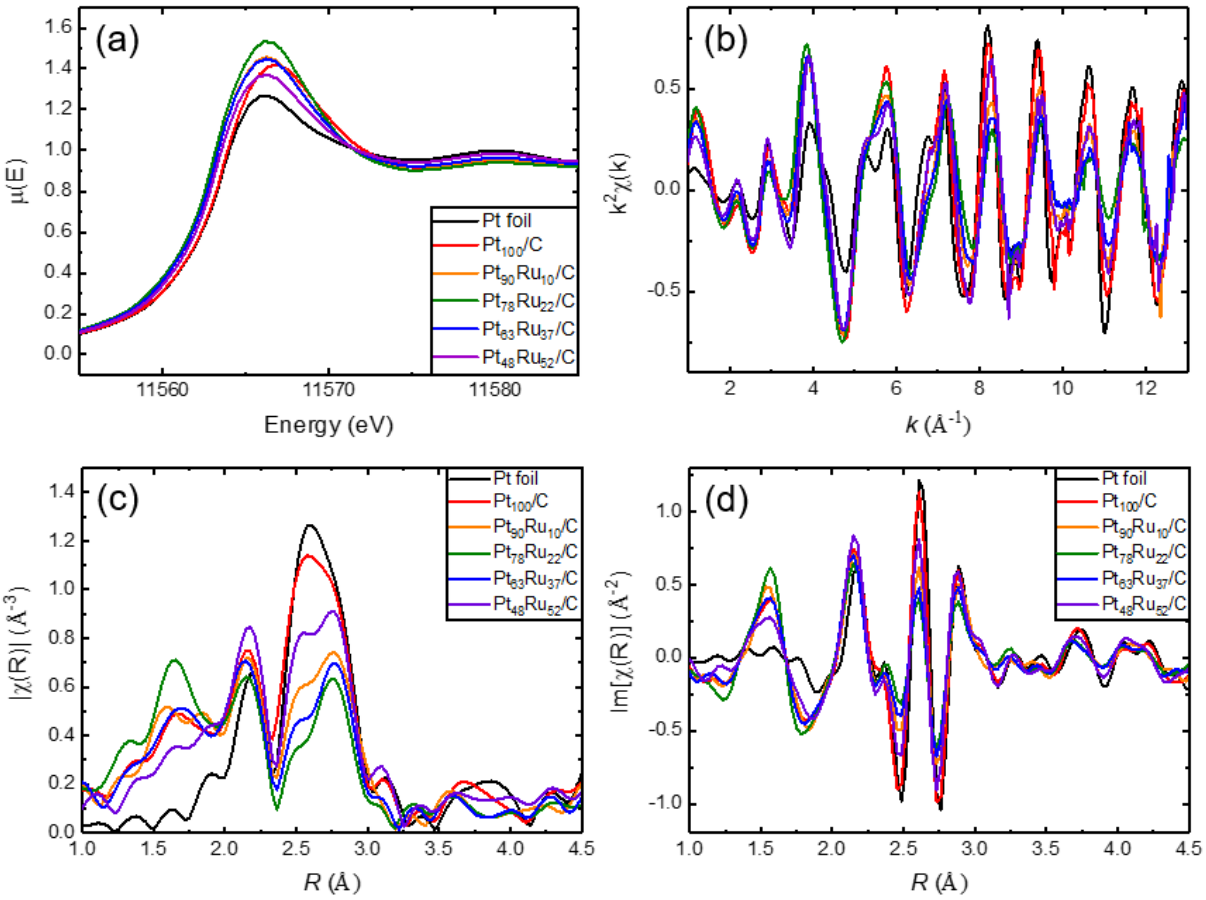

Figure A.1. Unadjusted raw XAFS spectra for Pt_xRu_y/C catalysts at the Pt L_3-edge as **(a)** normalized XANES spectra (also shown in **Figure 1b** of the main text), **(b)** EXAFS in the *k*-space, **(c)** magnitude of the *R*-space (also shown in **Figure 1a** of the main text), and **(d)** the imaginary *R*-space. The black lines represent the measured spectra for the Pt foil, which has been rescaled by 0.5× in the *k*- and *R*-space. Each of the colors represent different compositional ratios of Pt and Ru catalyst.

The measured spectra and fittings for the Pt foil and each of the five compositions of the Pt_xRu_y/C are shown in **Figure A.2** and **Figure A.3**.

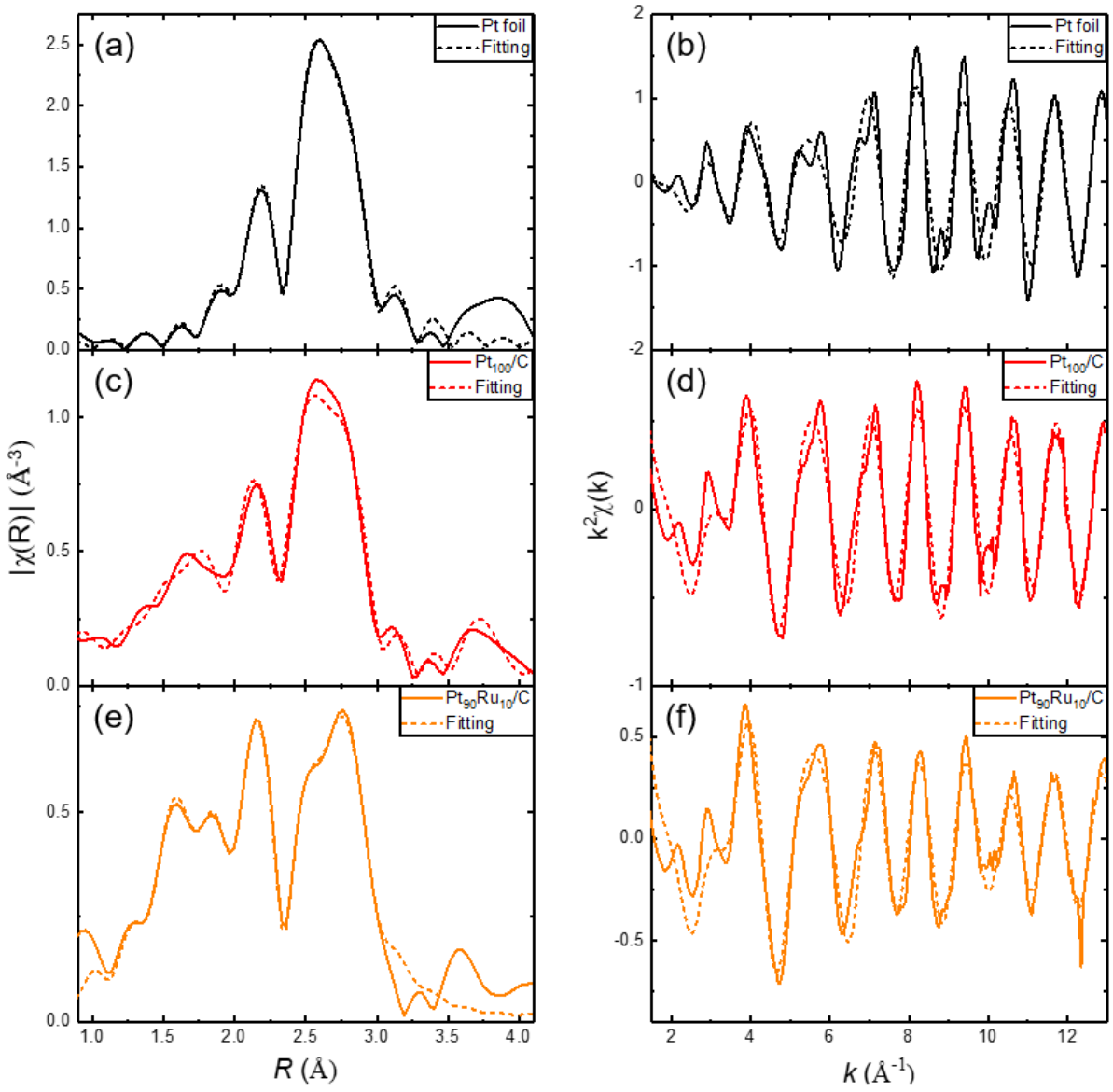

Figure A.2. Measured and fitted EXAFS spectra for **(a, b)** Pt foil, **(c, d)** Pt_{100}/C, and **(e, f)** $Pt_{90}Ru_{10}$/C in *R*- and *k*-space, respectively. The experimental data is presented as the solid lines, whereas the dashed lines represent the fits. Paths for the Pt foil only include Pt-Pt, whereas the Pt_xRu_y/C include Pt-Pt, Pt-O, and Pt-Ru fitted with R-range = 1 to 3 Å and k-range = 3 to 15 $Å^{-1}$.

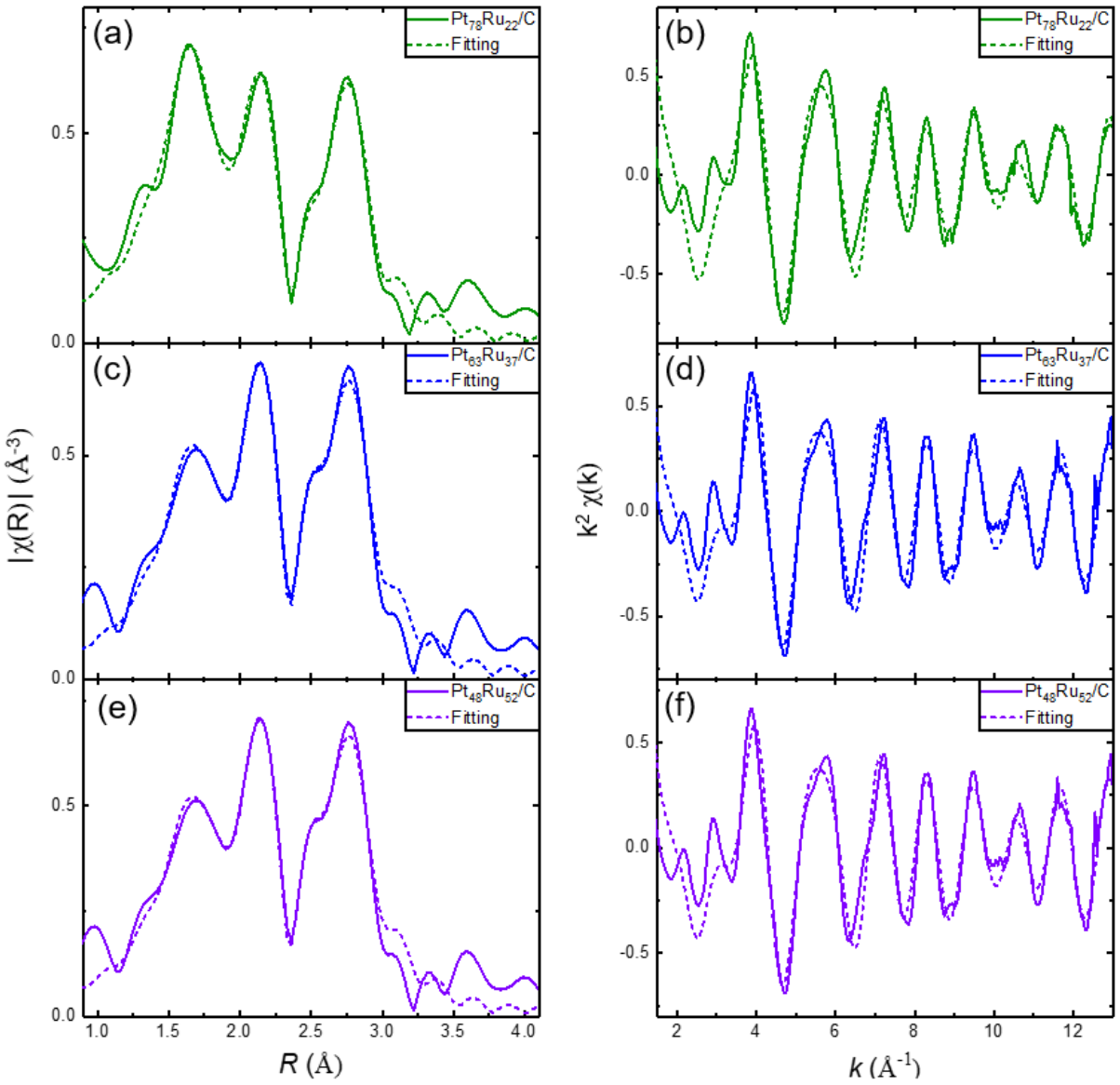

Figure A.3. Measured and fitted EXAFS spectra for **(a, b)** $Pt_{78}Ru_{22}$/C, **(c, d)** $Pt_{63}Ru_{37}$/C, and **(e, f)** $Pt_{48}Ru_{52}$/C in the *R*- and *k*-space, respectively. The experimental data is presented in the solid lines, whereas the dashed lines represent the FEFF fits. Paths include Pt-Pt, Pt-O, and Pt-Ru fitted with R-range = 1 to 3 Å and k-range = 3 to 15 $Å^{-1}$.

EXAFS fittings were conducted with Pt-Pt, Pt-O, and Pt-Ru paths generated in FEFF9. First, the Pt foil was fitted by setting the coordination number to 12, which is the expected value of bulk Pt. The set amplitude and E_0 were found to be 0.915 ± 0.02 and 5.55 ± 0.2 eV, respectively. Tabulated fittings and errors for the bond distance, coordination number, and σ^2 values are presented in **Table A.1**. For comparison, Pt_{100}/C was fitted with and without the Pt-Ru path.

Although the coordination number of the Pt-Ru path on Pt_{100}/C was ~0.5, it increased the χ error compared to fitting Pt_{100}/C without the Pt-Ru path.

The total coordination number (CN) from the Pt-Pt and Pt-Ru paths ranges from 6–9 for all the samples. From established relationships between metal nanoparticle size and first shell CN [1,2], these values correspond to nanoparticles between 1.5–5 nm, which is within the range of XRD calculations and TEM imaging (**Table A.1**). Nanoparticle sizes estimated from CN are lower than sizes extracted from TEM images, which may arise because the CN from EXAFS fittings estimates of size exclude the oxide layer around each nanoparticle, as only the metal-metal bonds of the metallic core are counted.

Table A.1. Tabulated fitting results for Pt foil and Pt_xRu_y/C catalysts. When fitting the Pt foil, the Pt coordination number was set to 12 (bolded) to obtain the set amplitude and E_0 values that are used in the Pt_xRu_y/C fittings. The results of the fittings and errors for *R*, CN, and σ^2 are given in the table. The 3rd cumulant had no effect on the fit, and thus the results are not reported in the table.

	Material	**Pt foil**	**Pt_{100}/C**	**$Pt_{90}Ru_{10}$/C**	**$Pt_{78}Ru_{22}$/C**	**$Pt_{63}Ru_{37}$/C**	**$Pt_{48}Ru_{52}$/C**
Pt-Pt Path	*R* (Å)	2.756 ± 0.01	2.743 ± 0.03	2.740 ± 0.03	2.735 ± 0.04	2.738 ± 0.04	2.745 ± 0.03
	CN	**12**	7.5 ± 0.5	5.8 ± 0.6	4.4 ± 0.6	5.6 ± 0.1	7.3 ± 0.6
	σ^2 (Å^2)	0.005 ± 0.0001	0.006 ± 0.0004	0.007 ± 0.0007	0.006 ± 0.0010	0.007 ± 0.0007	0.006 ± 0.0006
Pt-O Path	*R* (Å)		1.995 ± 0.04	1.995 ± 0.03	1.992 ± 0.05	1.987 ± 0.05	1.983 ± 0.05
	CN		1.28 ± 0.18	1.34 ± 0.20	1.77 ± 0.21	1.22 ± 0.18	0.79 ± 0.19
	σ^2 (Å^2)		0.006 ± 0.0026	0.005 ± 0.0026	0.004 ± 0.0020	0.004 ± 0.0024	0.005 ± 0.0043
Pt-Ru Path	*R* (Å)			2.792 ± 0.03	2.785 ± 0.03	2.776 ± 0.02	2.758 ± 0.00
	CN			1.19 ± 0.51	1.35 ± 0.55	1.44 ± 0.44	1.28 ± 0.42
	σ^2 (Å^2)			0.009 ± 0.0038	0.008 ± 0.0034	0.008 ± 0.0025	0.007 ± 0.0028

The raw data obtained at the Ru K-edge is presented in **Figure A.4**. Because the raw signal of the Ru foil is much higher than that of the alloy catalysts, the values have been scaled by a factor of 0.5 in the *R*-space to aid visual comparison. The spectral measurements taken at the Ru K-edge have low signal, thus we did not extract Ru-Ru and Ru-O information from ARTEMIS. Based on the XANES spectra at the Ru K-edge in **Figure A.4a**, the white line intensity of the Pt_xRu_y/C catalysts suggests oxidation compared with the bulk Ru foil. These surface oxides are expected for metallic nanoparticles because the experiment was conducted ex-situ. The amount of oxidation increases as the bulk Ru alloy content increases, which we attribute to Ru being more easily oxidized than Pt.

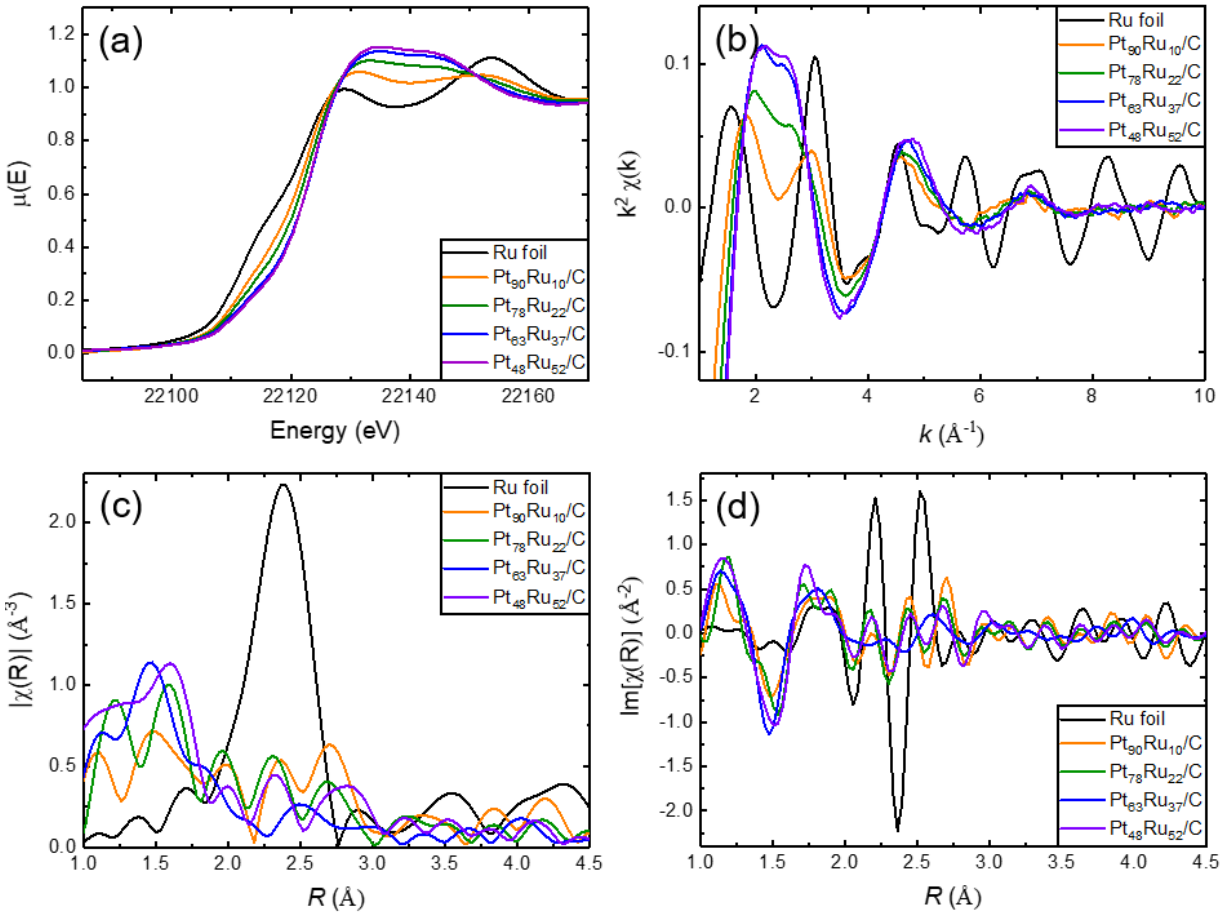

Figure A.4. Unadjusted raw XAFS spectra for Pt_xRu_y/C catalysts at the Ru K-edge as **(a)** normalized XANES spectra, **(b)** in the *k*-space, **(c)** magnitude of the *R*-space, and **(d)** the imaginary *R*-space. The black

lines represent the measured spectra for the Ru foil, which has been rescaled by 0.5× in the *k*- and *R*-space. Each of the colors represent different compositional ratios of Pt and Ru catalyst.

Additional TEM imaging

Under 1.5 million times magnification, the crystal lattice of the nanoparticles in $Pt_{78}Ru_{22}/C$ is observed (**Figure A.5**). The amorphous gray shape in the lower half of the image is the carbon support and the lighter gray top half is the Cu grid used for the microscopy experiment. The black spheres and ovals are the alloy nanoparticles, ranging from 3–5 nm in diameter.

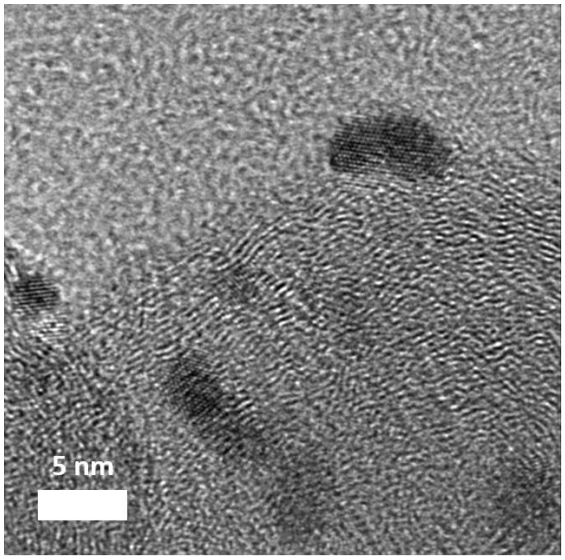

Figure A.5. TEM image of $Pt_{78}Ru_{22}/C$ at 1.5 million magnification.

Additional details on H_{upd} and Cu_{upd} experiments

Under the assumption that copper atoms adsorb on the electrode surface at the same sites as the hydrogen atoms, the ratio of copper and hydrogen charge was expected to be two on the Pt nanoparticles. 0.42 V vs. RHE was determined as the potential for adequate formation of a Cu_{upd} monolayer without interference from bulk Cu. At deposition potentials lower than 0.42 V vs. RHE, the charge ratio is greater than two, meaning that bulk Cu could still be adsorbed to the surface. There was a loss in charge above 0.42 V vs. RHE, indicating that the underpotential monolayer is

not fully formed. This deposition potential of 0.42 V was used to measure the Cu_{upd} of all Pt_xRu_y/C materials (**Figure A.6a-e**).

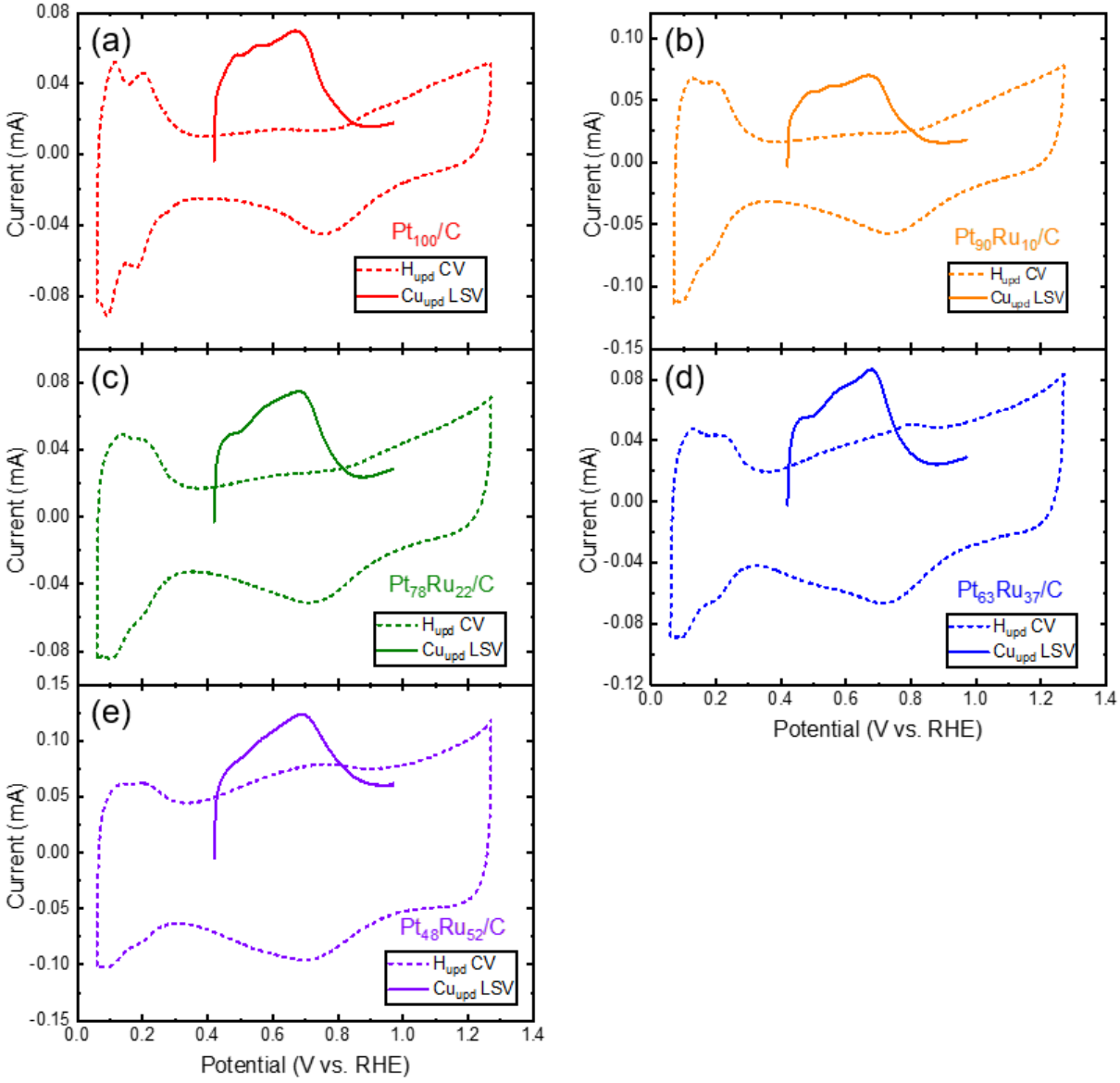

Figure A.6. Baseline H_{upd} CVs in 0.1 M H_2SO_4 and corresponding Cu_{upd} LSV in 0.1 M H_2SO_4 and 2 mM $CuSO_4$ at 100 mV $\cdot s^{-1}$ for **(a)** Pt_{100}/C, **(b)** $Pt_{90}Ru_{10}/C$, **(c)** $Pt_{78}Ru_{22}/C$, **(d)** $Pt_{63}Ru_{37}/C$, **(e)** $Pt_{48}Ru_{52}/C$.

The measured ECSA from H_{upd} and Cu_{upd} techniques are presented in **Table A.2**. The commercial Pt/C and PtRu/C both had higher ECSA compared to the synthesized materials despite having the same metal loading. This may arise because the commercial catalysts had higher dispersion, therefore a smaller average particle size calculated from XRD. The ECSA of

synthesized Pt_xRu_y/C ranged from 0.2–0.4 cm, regardless of measurement technique. The difference between the ECSAs of H_{upd} and Cu_{upd} increases as the Ru content increases because more than one hydrogen binds to Ru active sites. The Cu_{upd} approach eliminates the over counted sites because only one Cu atom adsorbs per Ru site.

Table A.2. Measured electrochemical active surface area from H_{upd} and Cu_{upd} technique for commercial and synthesized Pt_xRu_y/C catalysts.

Catalysts	H_{upd} (cm^2)	Cu_{upd} (cm^2)
Pt/C – commercial	0.94	0.94
PtRu/C – commercial	0.71	0.51
Pt_{100}/C	0.36	0.36
$Pt_{90}Ru_{10}/C$	0.22	0.22
$Pt_{78}Ru_{22}/C$	0.25	0.20
$Pt_{63}Ru_{37}/C$	0.35	0.29
$Pt_{48}Ru_{52}/C$	0.34	0.22

XPS data processing

The data from **Table A.3** shows that the surface Ru at% from XPS correlates with the bulk Ru at% obtained from ICP-MS. At lower Ru loading, the bulk and surface concentrations are more similar than that at higher Ru loading.

Table A.3. Comparison between bulk Ru at% determined from ICP-MS and surface Ru at% determined from Ru XPS intensity. The naming convention of the catalysts are based on the bulk at% of the metals.

Catalysts	Bulk Ru at%	Surface Ru at%	Ru XPS Intensity
Pt_{100}/C	0	0	0
$Pt_{90}Ru_{10}/C$	10	12	2932.6
$Pt_{78}Ru_{22}/C$	22	25	6221.5
$Pt_{63}Ru_{37}/C$	37	55	17172.6
$Pt_{48}Ru_{52}/C$	52	58	18634.2

Stability of Ru/C

We evaluated the activity of commercial Ru/C under the same conditions as that of the Pt_xRu_y/C catalysts. The CV scans did not show Ru redox peaks due to the low loading of Ru on the support. Instead, there was substantial Ru leaching into the solution during pretreatment in 1 M H_2SO_4. From **Figure A.7a**, the onset potential for oxygen evolution occurs at ~1.4 V vs. RHE in the first cycle. Continued cycling slowly strips away Ru from the catalyst into the acidic electrolyte solution leading to an increase in the oxidation onset potential. Unlike the Pt/C (**Figure A.7b**), which displays H_{upd} peaks that are indicative of hydrogen adsorbing and desorbing from the surface of the metal after 50 pretreatment cycles, Ru/C displays no metal peaks and all of the current is attributed to the carbon support.

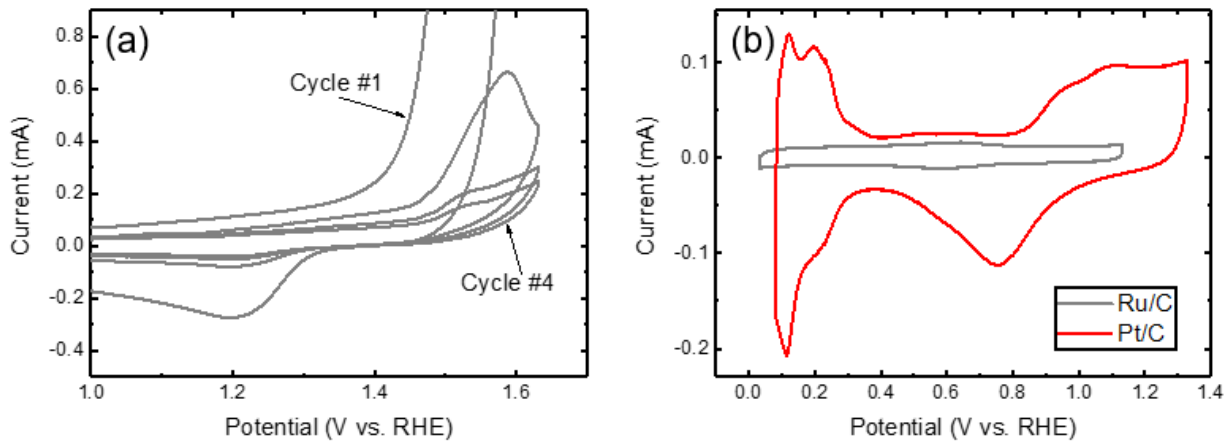

Figure A.7. Cyclic voltammetry of commercial Ru/C in 1 M H_2SO_4 for **(a)** Scanning at 100 mV/s, cycles in the oxidation region over time shows an increase in oxidation onset potential. **(b)** Comparison of Ru/C with Pt/C after 50 electrochemical pretreatment cycles showing little to no faradaic activity for Ru/C, which is attributed to Ru leaching into the electrolyte solution.

For comparison, the last three H_{upd} CVs of Pt_xRu_y/C catalyst after 50 cycles of pretreatment are included in **Figure A.8**, which show the stability of the material before steady-state

experiments. No CVs were performed after the experiment because the presence of nitrate in the solution alters the CV scans.

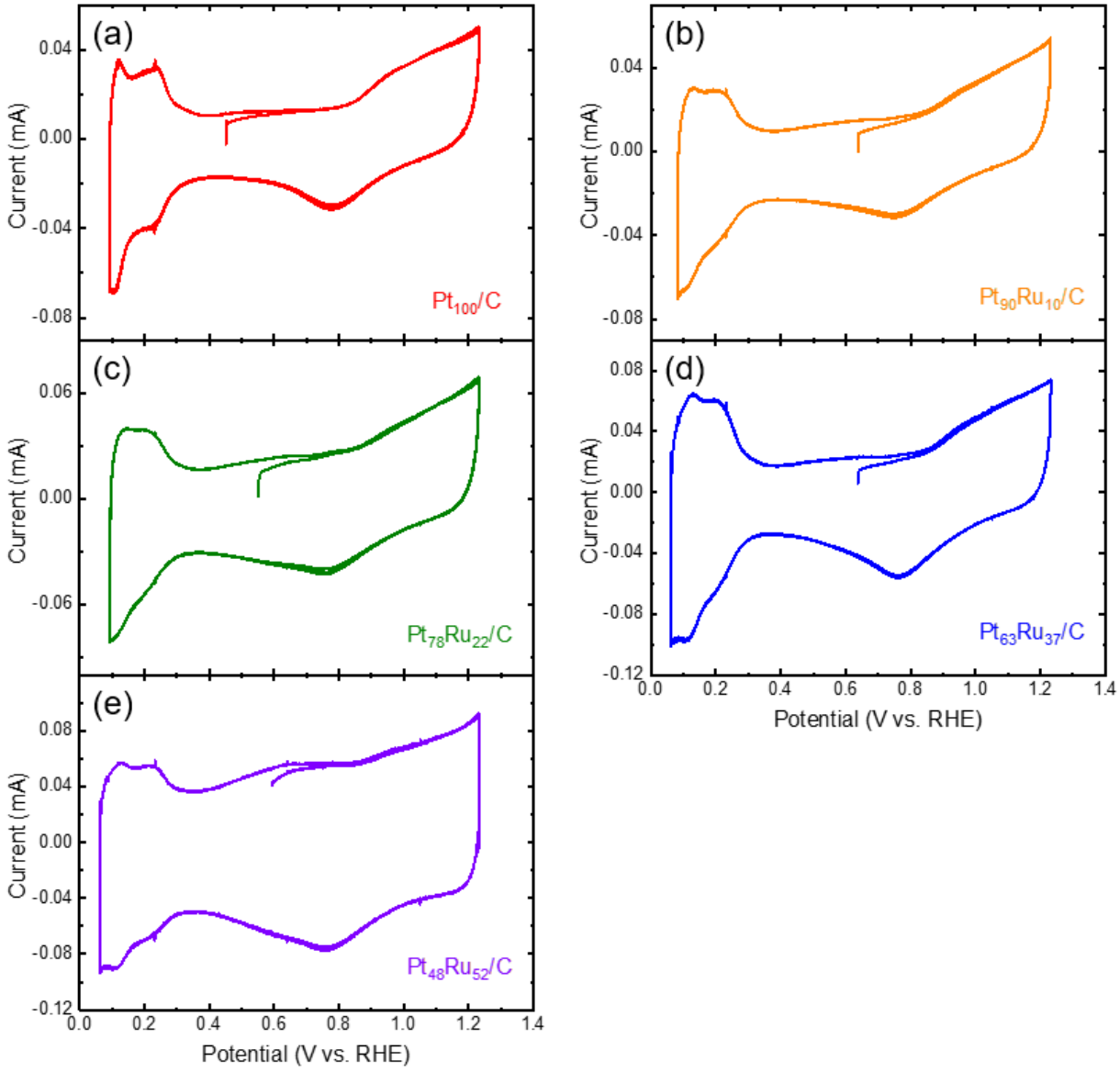

Figure A.8. Last three cycles of H_{upd} CVs in 1 M H_2SO_4 before steady-state measurements for **(a)** Pt_{100}/C, **(b)** $Pt_{90}Ru_{10}$/C, **(c)** $Pt_{78}Ru_{22}$/C, **(d)** $Pt_{63}Ru_{37}$/C, and **(e)** $Pt_{63}Ru_{37}$/C.

ENO_3RR activity at different applied potentials

The current densities normalized by H_{upd} and Cu_{upd} at 0.05, 0.075, and 0.1 V vs. RHE are presented in **Figure A.9a–c**, respectively. Catalysts tend to have higher current densities with more

negative applied potentials, with 0.05 V vs. RHE showing the greatest reduction currents for $Pt_{78}Ru_{22}/C$ at −55 μA/cm^2 when normalizing intrinsic activity by the ECSA from Cu_{upd}. This current density is ~20 times greater than the activity of Pt_{100}/C.

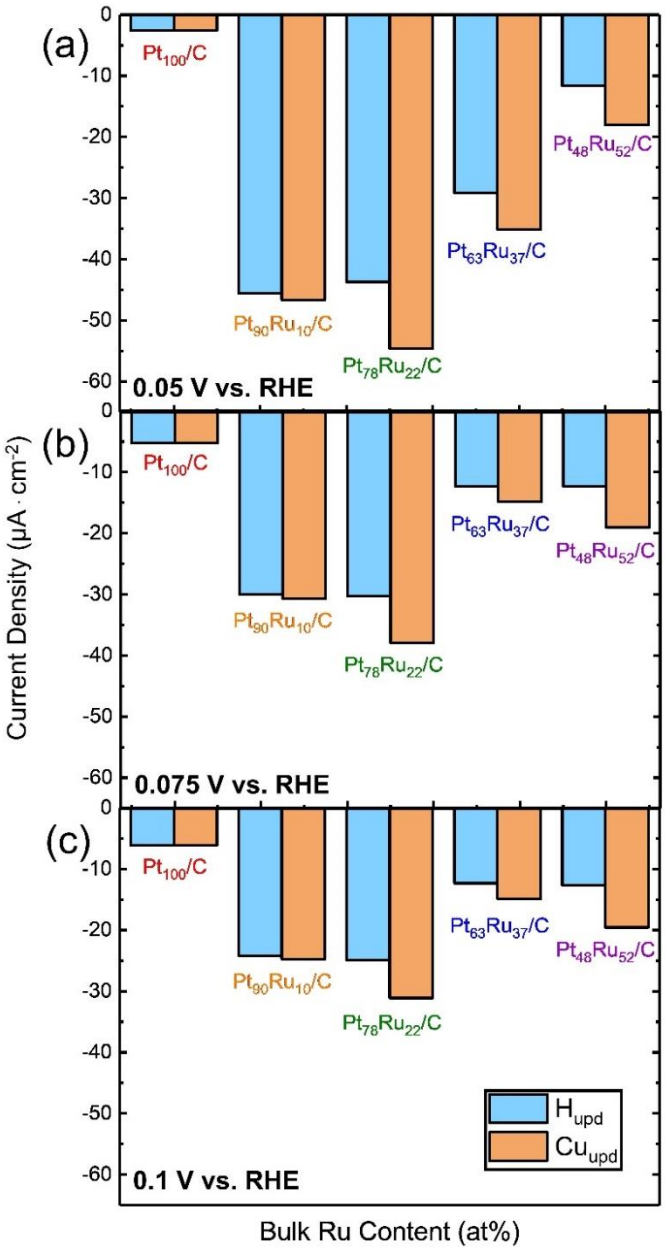

Figure A.9. Measured current densities for Pt_xRu_y/C at **(a)** 0.05 V, **(b)** 0.075 V, and **(c)** 0.1 V vs. RHE as normalized to both H_{upd} and Cu_{upd} active sites. Steady-state measurements were conducted in 1 M H_2SO_4 + 1 M $NaNO_3$. Each potential is applied for 5 min with RDE rotation of 2500 rpm.

Activity comparison

The magnitude of the current density from **Figure 4.8b** is replotted as a function of the surface Ru at%. Since the theoretical calculations only explored the change in surface composition of Pt and Ru, the experimental current densities from RDE measurements as a function of surface Ru at% aligns closer to the predicted TOFs. However, we can more accurately extract bulk Ru at% from ICP-MS than surface Ru at% from XPS. Thus, the bulk at% was used as the naming convention and compositional structure of the alloys.

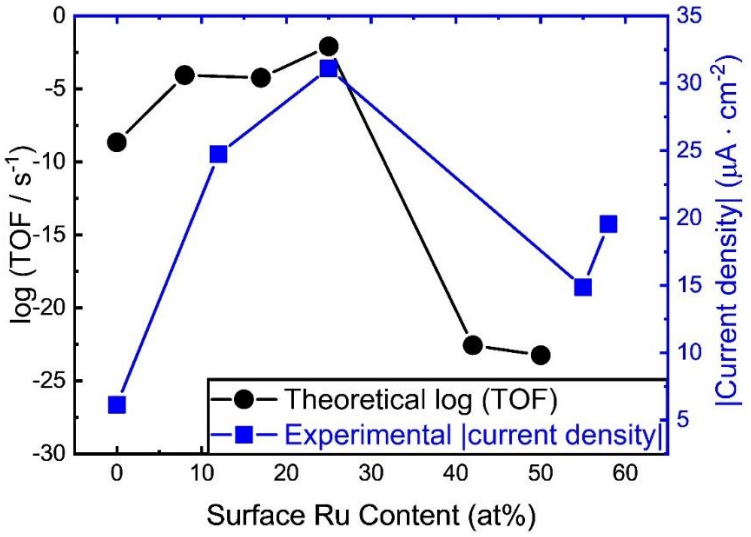

Figure A.10. Comparison between the log (TOF / s^{-1}) values calculated from microkinetic modeling and the magnitude of the current densities obtained via RDE experiments at 0.1 V vs. RHE as a function of surface Ru at%. Active sites are detected and normalized by Cu_{upd}.

Selectivity measurements

Ion chromatography measurements do not show significant changes in the nitrate concentration over the course of four hours for Pt_xRu_y/C (**Figure A.11**). Pt_{100}/CF shows the largest decrease in nitrate concentrations over time, which can be attributed to higher metal loading during the catalyst preparation on the carbon felts, resulting in a higher ECSA.

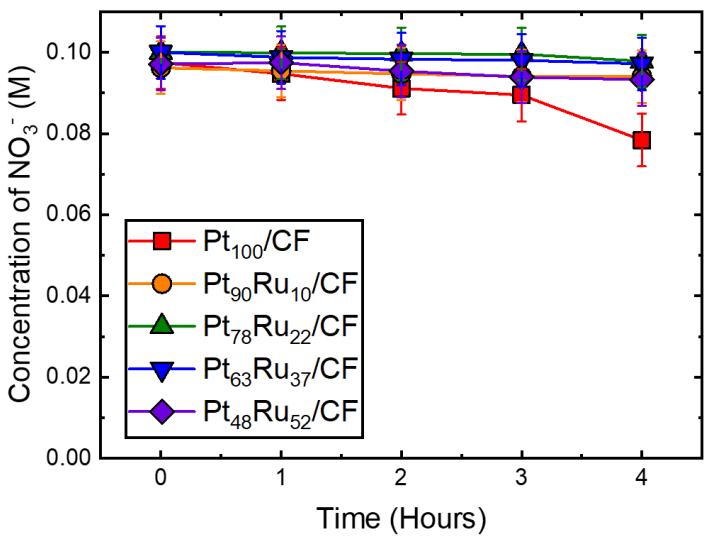

Figure A.11. Concentration of nitrate as a function of time during electrolysis at applied potential of 0.1 V vs. RHE in 0.1 M HNO_3 for the five synthesized catalysts. The error bars indicate the propagated error obtained from measurement and sampling variability.

References

(1) Jentys, A. Estimation of Mean Size and Shape of Small Metal Particles by EXAFS. *Physical Chemistry Chemical Physics* **1999**, *1* (17), 4059–4063. https://doi.org/10.1039/A904654B.

(2) Frenkel, A. I.; Hills, C. W.; Nuzzo, R. G. A View from the Inside: Complexity in the Atomic Scale Ordering of Supported Metal Nanoparticles. *The Journal of Physical Chemistry B* **2001**, *105* (51), 12689–12703. https://doi.org/10.1021/jp012769j.

Appendix B

Computational Modeling

This Appendix contains the detailed methodology and additional results for the density functional theory modeling work in **Chapter 4**. The computational work in this section is performed by Samuel D. Young from the Goldsmith Group and included in this dissertation for complete comprehension of the work.

Density functional theory modeling methodology

All DFT calculations used the Vienna Ab Initio Simulation Package, version 5.4.4.[1,2] Calculations used the projector-augmented wave method[1,3] with an energy cutoff of 400 eV, the PBE functional,[4] and Gaussian smearing of 0.2 eV. For surface calculations, the Brillouin zone was sampled with a 6×6×1 Monkhorst-Pack *k*-point grid.[5] Self-consistent electronic calculations used a between-iteration tolerance of 10^{-4} eV and ionic relaxation proceeded until all forces on atoms were less than 0.02 eV/Å.

The alloy catalysts were constructed using the Atomic Simulation Environment software package, version 3.17.0.[6] Nine random surface alloys were created based on a 3×4×4 supercell of Pt(211), using a Pt lattice constant which was optimized (3.97677 Å) with the PBE functional on a 16×16×16 *k*-point grid. For all simulations, the surface slab contained four layers of atoms, where the bottom two layers were constrained to their bulk positions and the top two layers could relax.

Surface alloy models were prepared by randomly assigning each of the 12 atoms in the top surface layer as either Pt or Ru, resulting in surface compositions ranging from 0 at% Ru to 50 at% Ru. Surfaces were then geometry-optimized with a vacuum of at least 15 Å in the *z* direction.

The Pymatgen software package[7] was used to locate unique adsorption sites. The electronic binding energy ΔE_A of species *A* was calculated with respect to the bare surface and the electronic energy of species *A* in the gas phase. Aqueous-phase NO_3^- adsorption Gibbs free energies were obtained at 298.15 K and 0 V vs. RHE using a thermodynamic cycle.[8] Adsorption sites with the strongest binding energy are reported in the main text, and the energetics and geometries of all sampled sites are provided here.

The catalyst activity was predicted by relating the gas-phase electronic binding energies of atomic O and N (ΔE_{O} and ΔE_{N}) to the overall mean-field kinetics of the nitrate reduction reaction. This task was accomplished by using a theoretical volcano plot developed in our previous work [9]. The PBE functional and face-centered cubic (FCC) (211) facet were chosen for the current work to match our prior work and enable the comparison of our results with its theoretical volcano plot. We also consider this an appropriate comparison to our synthesized Pt_xRu_y particles because we considered only Ru compositions for which Pt_xRu_y particles form in an FCC lattice.

The nitrate-to-nitrite dissociation barrier ($NO_3^* + * \rightleftarrows NO_2^* + O^*$) for each random surface alloy slab was computed using the climbing-image nudged elastic band (CI-NEB) method.[10] The band was formed with five interior images linearly interpolated between the initial and final endpoint geometry. CI-NEB relaxation used spring forces of 5 eV $Å^{-1}$ between images and the same electronic and force tolerance parameters as the adsorption calculations. Illustrations of alloy configurations, adsorbate binding locations, and CI-NEB calculations for nitrate dissociation are given here.

All DFT-predicted energetics (adsorption energies, reaction energies, and activation energies) are done at low coverages (i.e., 1/12 ML for H, N, and O and 1/6 ML for NO_3^-) and neglect lateral adsorbate-adsorbate interactions due to high coverage of a single species or the presence of co-adsorbed species (e.g., co-adsorbed H affecting the adsorption strength of NO_3^-, which weakens adsorption strength of nitrate by ~0.25 eV at 1/12 ML H coverage). Such shifts are typical of co-adsorption of H with small molecular adsorbates on metal surfaces.[11] We stress that this effect would also similarly weaken adsorption energies for other ENO_3RR species, and thus would likely not qualitatively change trends. Neglecting co-adsorbate interactions on adsorption free energies is a common approximation when studying complex reaction networks such as electrocatalytic nitrate reduction because of the large computational expense to treat coverage-dependent interactions for all species in the model.

Additional computational results

Generating the model Pt_xRu_y random surface alloys

Experimental surface composition analysis of the Pt_xRu_y catalysts reveal that Ru surface concentrations are close to the target bulk compositions for each catalyst. To model the effect of Pt_xRu_y surface composition on nitrate reduction, a random surface alloying approach was used to generate Pt_xRu_y surfaces. This approach begins with a 3×4×4 supercell of the Pt(211) lattice and randomly assigns each atom in the topmost layer to be either Pt or Ru. The decision to use random surface layer alloys supported on Pt(211) instead of searching the optimal Pt_xRu_y structure for each composition using methods such as cluster expansion[12,13] is motivated by computational tractability and simplicity, because here we are only seeking qualitative trends in binding energies and activation barriers. The Ru atoms deep within the Pt subsurface will contribute far weaker ligand and strain effects to the catalyst properties than surface Ru atoms do. As shown herein,

these random surface alloy models capture qualitative activity trends compared with experiment measurements. The random assignment creates atomic compositions of the top layers ranging from 0 to 50 at% Ru, which corresponds approximately to the five Pt_xRu_y experimental catalysts. Surface alloy models up to 100 at% Ru at the surface and a Ru(211) slab were also created for further study, although such alloy catalysts may not be stable under reaction conditions due to Ru phase segregation and leaching.

Linear adsorbate scaling relationships

Linear adsorbate scaling relationships between adsorbates are predicted to exist on Pt_xRu_y alloys. The data in **Figure B.1** shows six linear adsorbate scaling relationships found between N, O, H^+, and NO_3^- binding energies on Pt_xRu_y random surface alloys. N and O binding energies correlate highly with each other, and each correlate well with NO_3^- binding energy. In general, N, O, and NO_3^- follow poorer scaling relationships with H^+ than with each other, as shown previously.[14] These linear scaling relations on Pt_xRu_y are similar to those used to construct the volcano plot from Ref.[14] using pure metals.

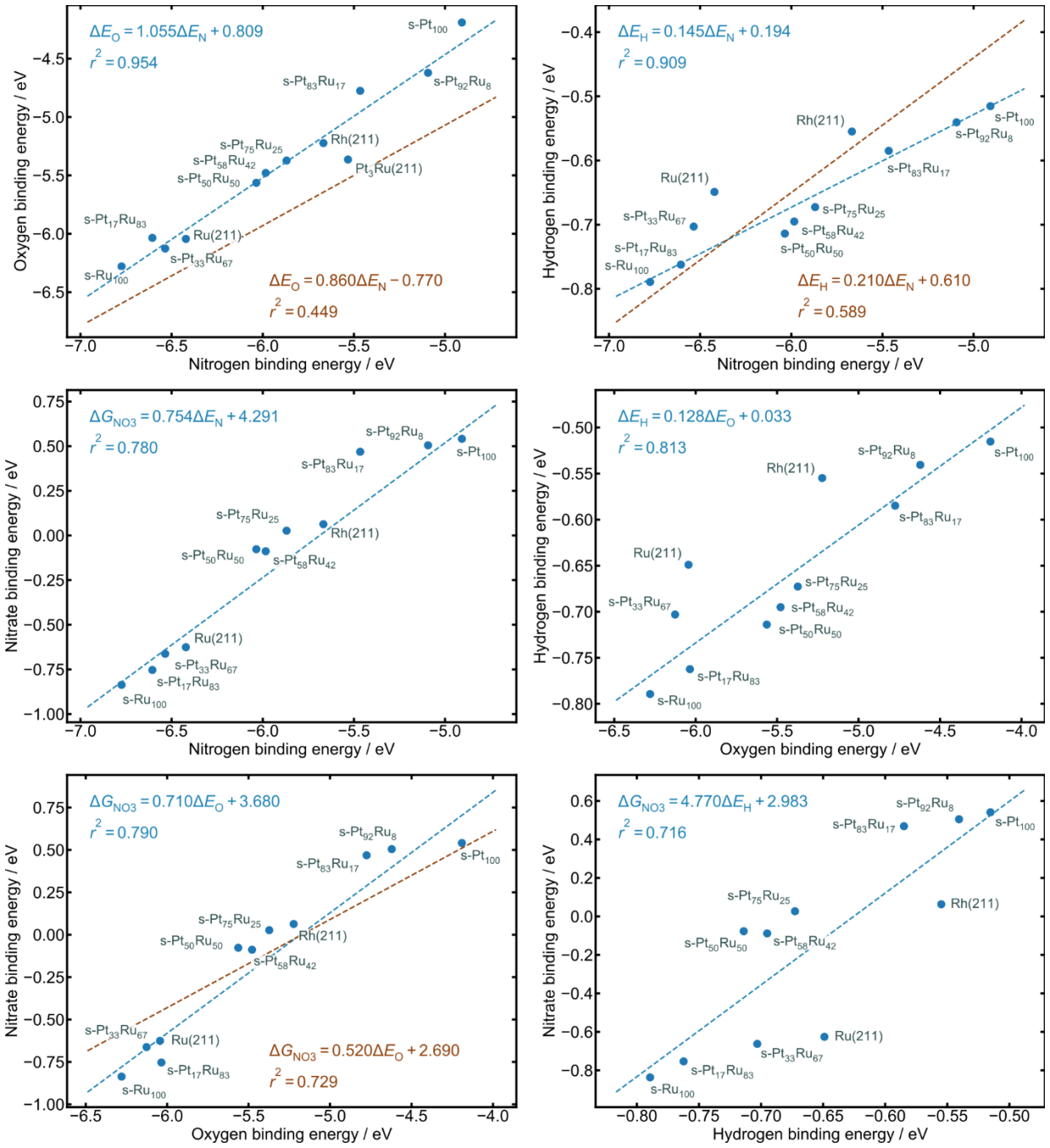

Figure B.1. Linear adsorbate scaling relationships between N, O, H^+, and NO_3^- on Pt_xRu_y alloys. Dashed lines are linear least-squares fits, and r^2 is the coefficient of determination. Where available, lines and regression equations in brown were taken from our previous study on pure metals,[14] and those in blue are calculated from the data in this study, including the Pt_xRu_y alloys. Electronic binding energies are reported at 0 K and 0 V vs. RHE, and Gibbs binding energies are at 298.15 K and 0 V vs. RHE.

Brønsted-Evans-Polanyi relation for nitrate to nitrite dissociation

To use the volcano plot that was derived for pure metals for our alloy systems, it is important to check if the Brønsted-Evans-Polayni (BEP) relations are similar for the key steps. Because nitrate to nitrite dissociation ($NO_3^* \rightarrow NO_2^* + O^*$) is often rate-limiting, we specifically examine this elementary step in detail. **Figure B.2** shows the BEP plot for this elementary step, which relates reaction energies and dissociation barriers. The alloy BEP relationship appears to have a maximum error of ~0.2 eV compared to the pure metal BEP relationship, suggesting we can qualitatively use the volcano plot derived for pure metals to rationalize the activity of our alloy systems.

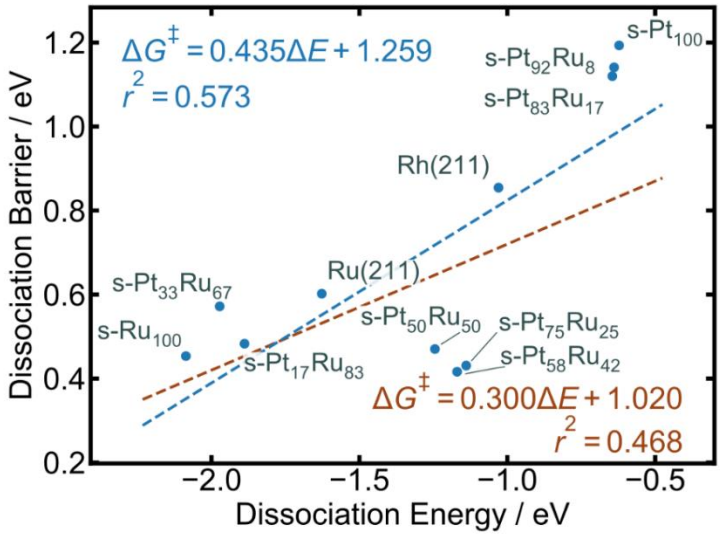

Figure B.2. Brønsted-Evans-Polanyi plot for the $NO_3^* \rightarrow NO_2^* + O^*$ dissociation on Pt_xRu_y surfaces, along with Rh(211) and Ru(211). The blue line and equation are the BEP relation for the alloyed surfaces; the corresponding line and equation in brown are taken from our previous study on pure metals.[14]

Initial, transition state, and final geometries for CI-NEB calculations

For each NEB calculation, the initial image was the relaxed geometry of NO_3^* at its optimal [O–O]-chelating binding position on the third ridge of each FCC(211) material. The final endpoint was formed by assuming an elementary step in which one of the basal O atoms migrates to a neighboring bridge site up or down the third ridge, following which the remaining NO_2 fragment rotates downward into a [N–O]-chelating position. **Figure B.3** shows the initial, transition state, and final images for each CI-NEB calculation performed to calculate the activation barrier for nitrate-to-nitrite dissociation.

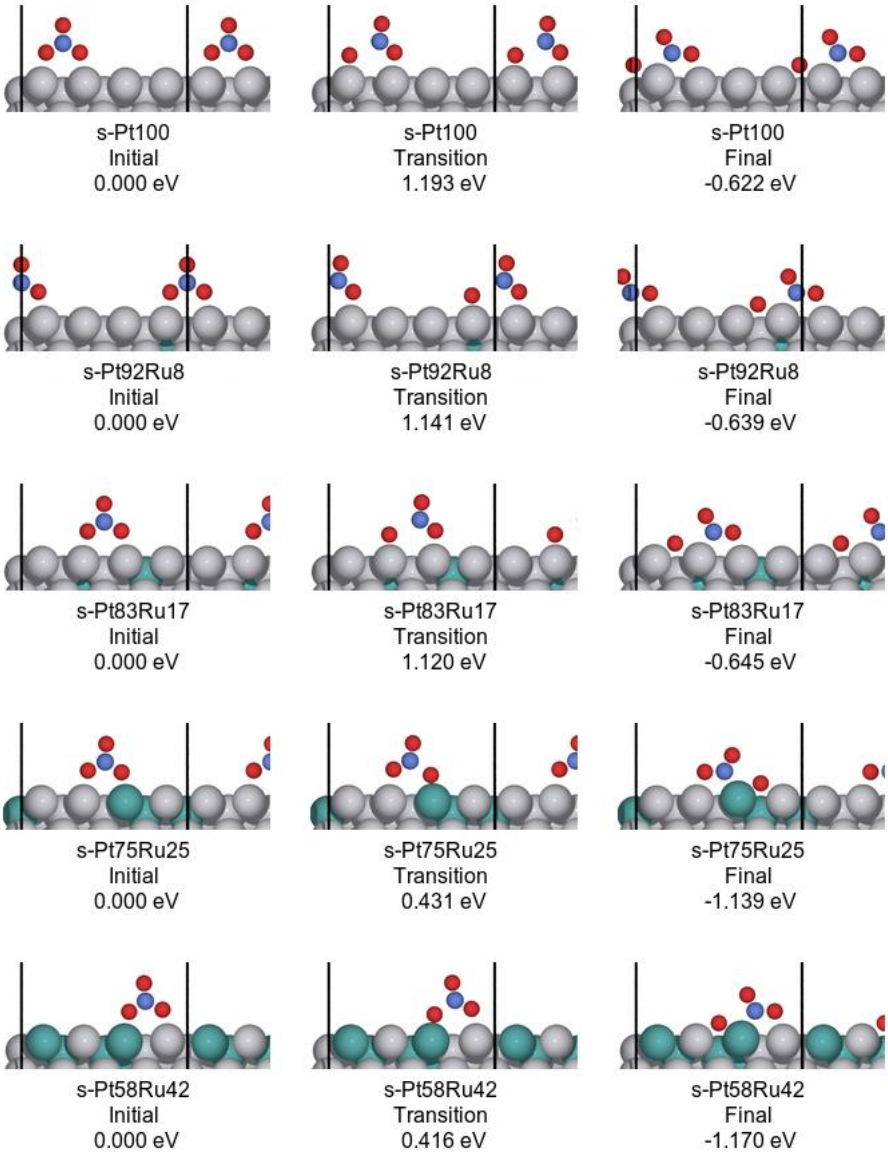
s-Pt100
Initial
0.000 eV
s-Pt100
Transition
1.193 eV
s-Pt100
Final
-0.622 eV
s-Pt92Ru8
Initial
0.000 eV
s-Pt92Ru8
Transition
1.141 eV
s-Pt92Ru8
Final
-0.639 eV
s-Pt83Ru17
Initial
0.000 eV
s-Pt83Ru17
Transition
1.120 eV
s-Pt83Ru17
Final
-0.645 eV
s-Pt75Ru25
Initial
0.000 eV
s-Pt75Ru25
Transition
0.431 eV
s-Pt75Ru25
Final
-1.139 eV
s-Pt58Ru42
Initial
0.000 eV
s-Pt58Ru42
Transition
0.416 eV
s-Pt58Ru42
Final
-1.170 eV

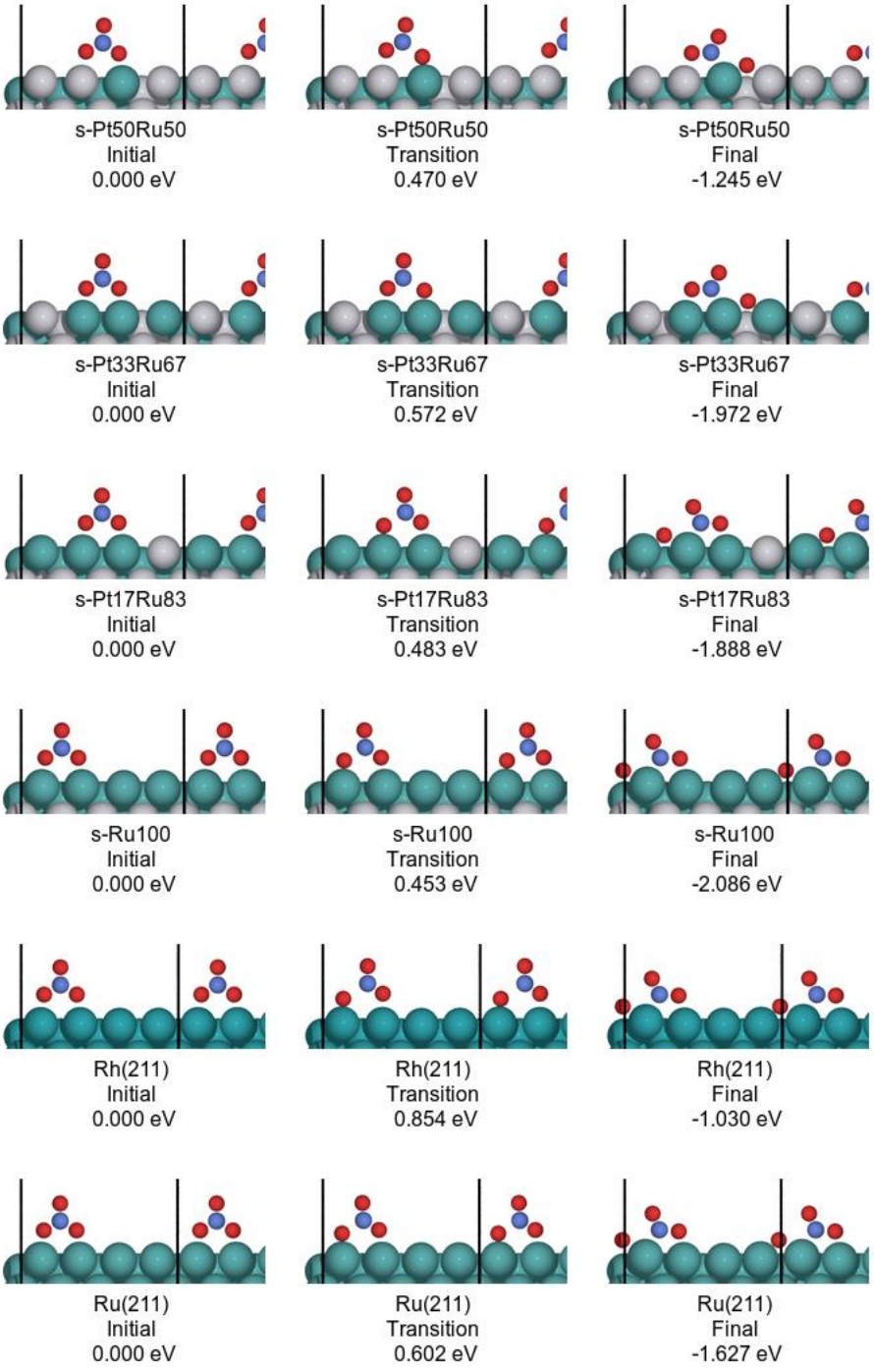

Figure B.3. Initial, transition state, and final geometries for CI-NEB calculations for each surface model. Electronic energies are relative to the initial state. Solid black lines denote the boundary of the periodic supercell.

Models of the random surface alloys

The random surface alloy (s-Pt_xRu_y) models, as well as Rh(211) and Ru(211) are shown in **Figure B.4**.

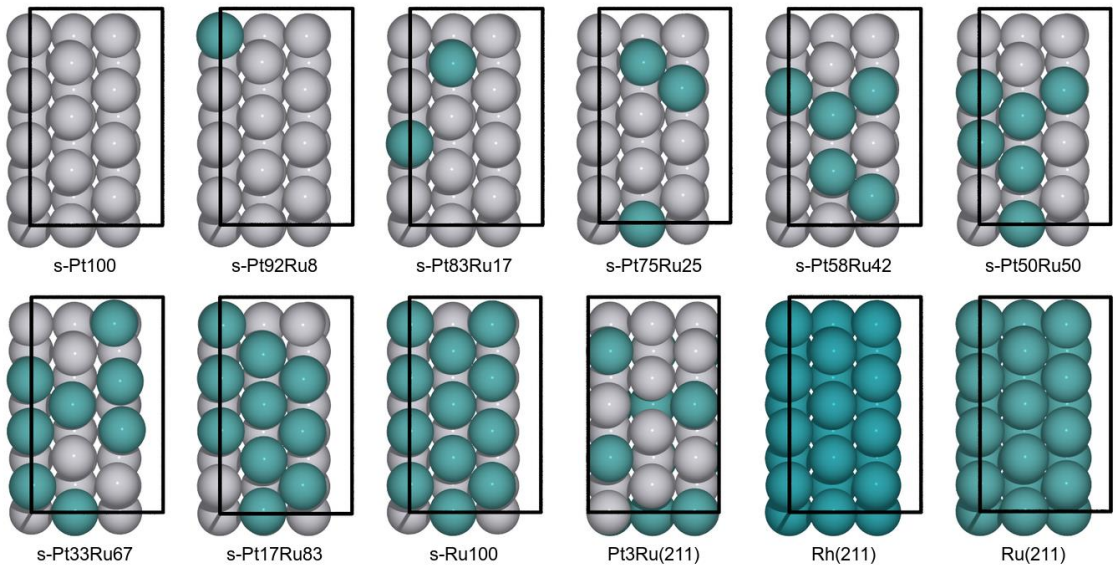

Figure B.4. Top views of the supercells of the Pt_xRu_y(211) surfaces, as well as Rh(211) and Ru(211) for comparison. Each surface is FCC(211), so that the rightmost column of atoms is the highest in the *z* direction (normal to the surface). Teal = Ru, grey = Pt, dark teal = Rh.

Renderings of adsorption on the model Pt_xRu_y alloys

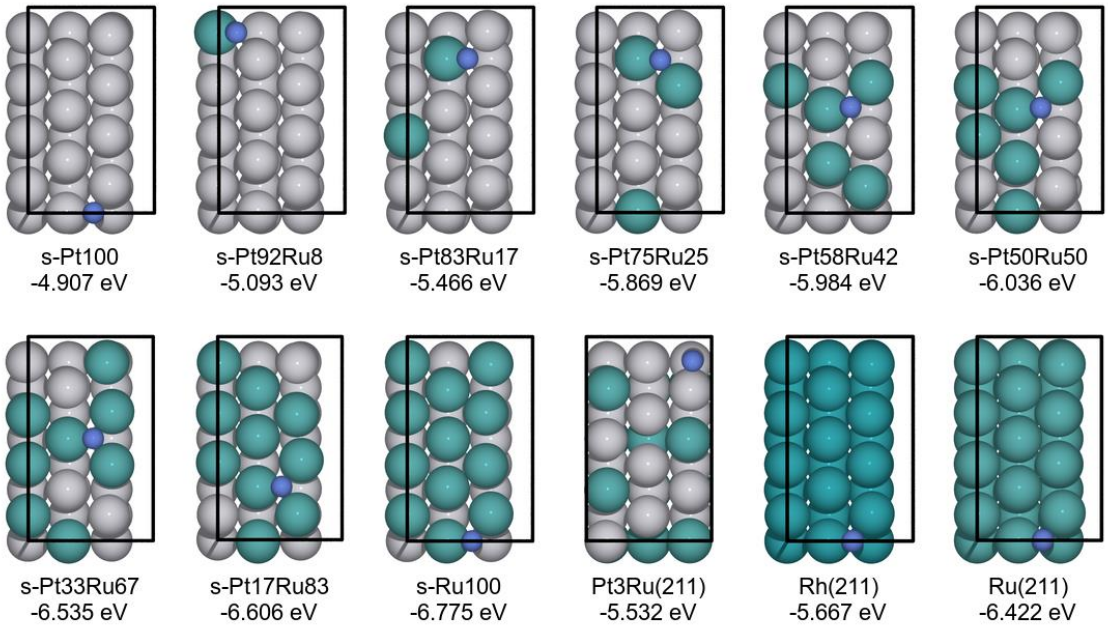

Figure B.5. Nitrogen atom adsorption on the Pt_xRu_y alloys. The strongest N binding energy is reported for each Pt_xRu_y composition in eV, as well as Rh(211) and Ru(211) for comparison. Black solid lines denote the supercell. Teal = Ru, grey = Pt, blue = N, dark teal = Rh.

The N atom prefers to adsorb in hollow sites, but also in locations that maximize its coordination with surface Ru atoms (**Figure B.5**). N prefers a FCC or HCP hollow site between the middle and rightmost ridges of the FCC(211) surface, but will also adsorb strongly in a hollow site between the left and middle ridges if that is the only location where a Ru atom is available (e.g., see s-$Pt_{92}Ru_8$).

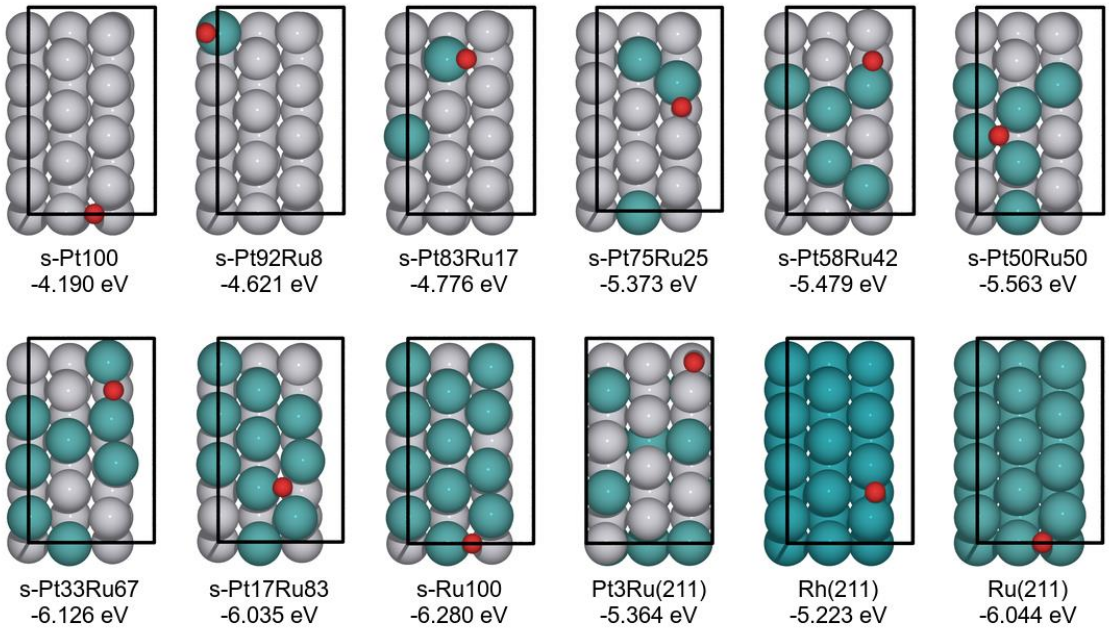

Figure B.6. Oxygen atom adsorption on the Pt_xRu_y alloys. The strongest O binding energy is reported for each Pt_xRu_y composition in eV, as well as Rh(211) and Ru(211) for comparison. Teal = Ru, grey = Pt, red = O, dark teal = Rh.

Like N, the O atom prefers adsorption locations that maximize its coordination with surface Ru atoms (**Figure B.6**). Atomic O also prefers bridge and hollow sites on the rightmost ridge for many but not all surface compositions. However, O will also adsorb strongly in a hollow site if this site increases its coordination to Ru atoms.

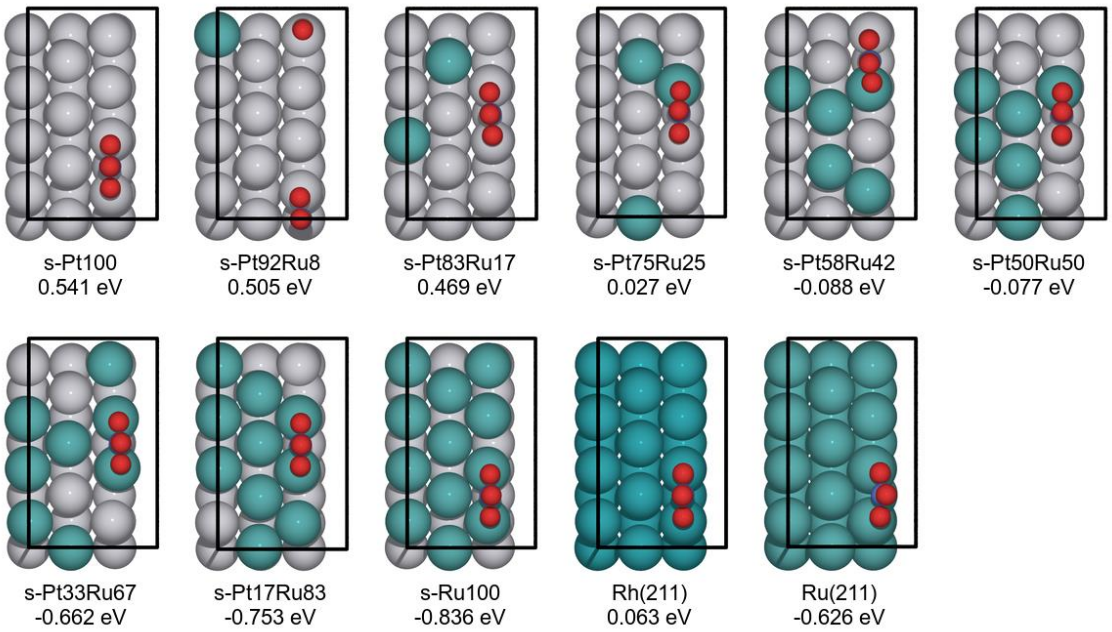

Figure B.7. NO_3^- adsorption on Pt_xRu_y alloys. The strongest NO_3^- binding energy is reported for each Pt_xRu_y composition in eV, as well as Rh(211) and Ru(211) for comparison. Teal = Ru, grey = Pt, blue = N, red = O, dark teal = Rh.

NO_3^- adsorption free energies were predicted at 298.15 K using a thermodynamic cycle[15] to avoid error in predicting ion energies using periodic DFT calculations. For NO_3^- binding, only sites in which NO_3^- binds in an O,O-bidentate chelating fashion to two consecutive atoms on the same vertical FCC(211) ridge were considered. We tested such binding positions only for the middle and rightmost ridges, as our preliminary studies indicated that binding on the leftmost (lowest) ridge is unfavorable. For all surfaces, NO_3^- prefers to bind on the rightmost (highest) ridge and to as many Ru atoms on that ridge as possible at once (**Figure B.7**). For example, for s-$Pt_{75}Ru_{25}$, NO_3^- binds to a Pt-Ru pair of surface atoms even though a Pt-Pt pair of surface atoms is available. Similarly, for s-$Pt_{33}Ru_{67}$ and s-$Pt_{17}Ru_{83}$, NO_3^- binds to a Ru-Ru pair even though a Ru-Pt ensemble is available.

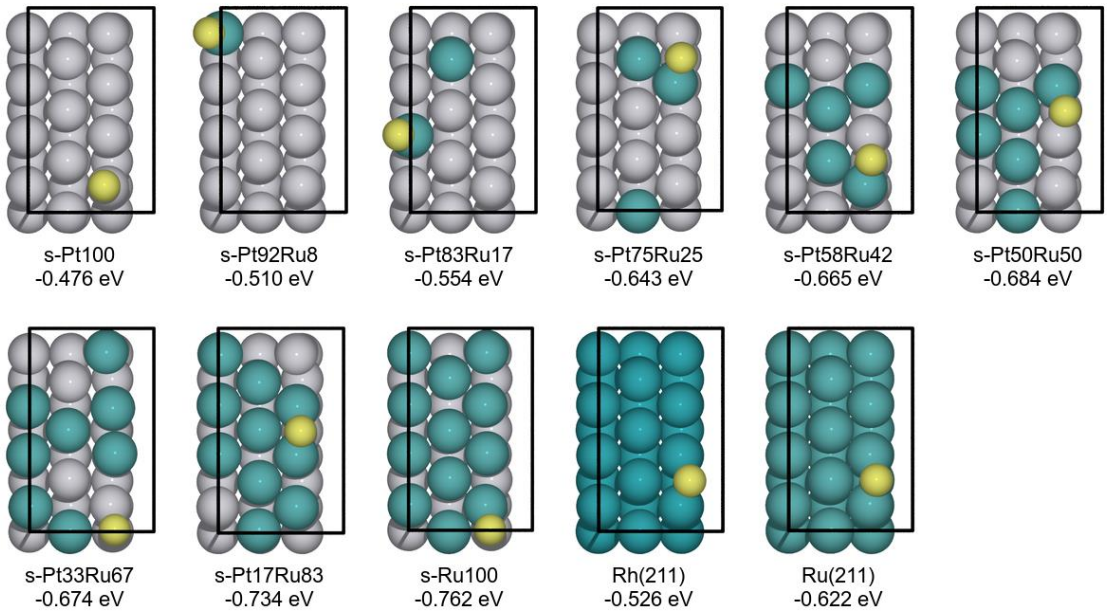

Figure B.8. Hydrogen adsorption on Pt_xRu_y alloys. The strongest H binding energy is reported for each Pt_xRu_y composition in eV, as well as Rh(211) and Ru(211) for comparison. Teal = Ru, grey = Pt, yellow = H, dark teal = Rh.

On pure Pt(211) facets (denoted as s-Pt_{100}), H prefers an atop site at the top ridge (**Figure B.8**). As Ru surface atoms become available, H prefers to adsorb at sites near the top ridge and which increase the coordination of H with Ru. For most sites, H adsorbs at a bridge position in the top ridge with at least one Ru atom in its first coordination sphere. For surfaces where Ru is available only in the bottom ridge (e.g., s-$Pt_{92}Ru_8$ and s-$Pt_{83}Ru_{17}$), H adsorbs at a position between the top ridge and the bottom ridge immediately next to it, such that it is as close to a Ru atom as possible.

Sampling of adsorbate binding energies

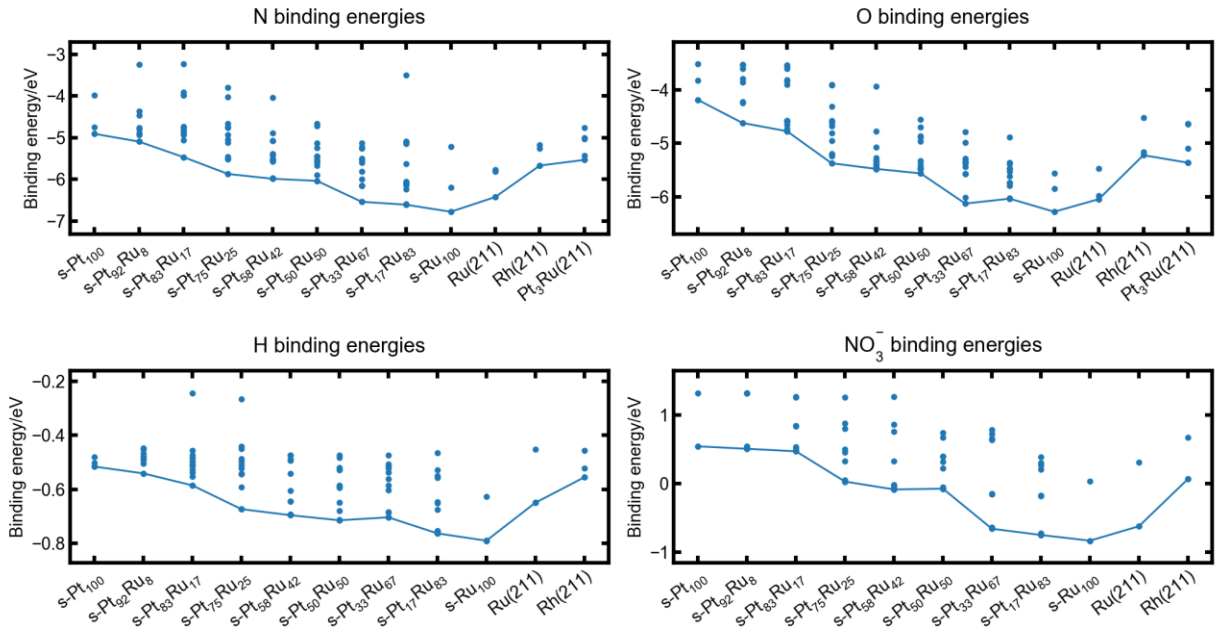

Figure B.9. N, O, H, and NO_3^- binding energies sampled on the Pt_xRu_y alloys, Ru(211), and Rh(211). Each point represents an adsorption calculation, and the solid lines track the strongest binding energies as a function of alloy composition. Electronic binding energies are reported at 0 K (except for NO_3^- binding free energies, which are reported at 298.15 K using a thermodynamic cycle as discussed above).

Binding energies of NO_3^- on Pt_xRu_y surface alloys, Rh(211), and Ru(211)

The data in **Figure B.10** shows the strongest binding free energies for NO_3^- found on each $Pt_xRu_y(211)$ surface, as well as Rh(211) and Ru(211). For the Pt_xRu_y alloys, the sites with strongest nitrate binding energies cluster into three groups based on how nitrate is bound: Group 1 containing s-Pt_{100}, s-$Pt_{92}Ru_8$, and s-$Pt_{83}Ru_{17}$ where nitrate binds to Pt-Pt sites; Group 2 containing s-$Pt_{75}Ru_{25}$, s-$Pt_{58}Ru_{42}$, and s-$Pt_{50}Ru_{50}$ where nitrate binds to Pt-Ru sites; and Group 3 containing s-$Pt_{33}Ru_{67}$, s-$Pt_{17}Ru_{83}$, and s-Ru_{100} where nitrate binds to Ru-Ru sites. Although this grouping is artificial because in reality a distribution of Pt-Pt, Pt-Ru, and Ru-Ru sites are present on alloy surfaces, it displays the general trend that nitrate adsorption strength increases as the number of Ru atoms bound to nitrate increases. The Pt-Pt sites are most abundant at low Ru concentrations, whereas as

Ru concentration increases the number of Ru-Pt and Ru-Ru sites on the surface is expected to increase. Thus, Pt_xRu_y surfaces with more Ru should have stronger nitrate binding energies, on average.

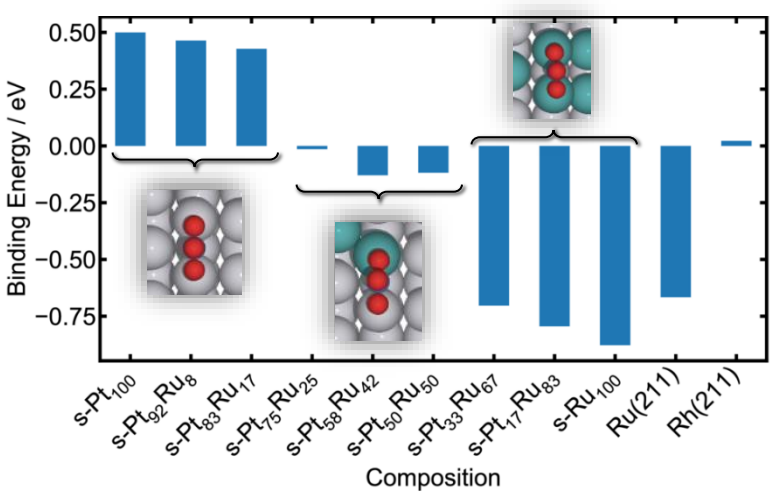

Figure B.10. Strongest DFT-predicted binding free energies of NO_3^- on Pt_xRu_y surface alloys, Ru(211), and Rh(211). Each inset shows a representative example of the adsorption motif for each cluster of binding energies. Color Legend: Teal = Ru, grey = Pt, red = O, blue = N. Binding free energies are reported at 298 K and 0 V vs. RHE.

Some of the model alloys (s-$Pt_{17}Ru_{83}$ and s-Ru_{100}) adsorb nitrate more strongly than Ru(211). Here, the Ru(211) surface was generated by optimizing the lattice constant of FCC Ru, whereas all the model alloys surfaces (including s-$Pt_{17}Ru_{83}$ and s-Ru_{100}) are FCC(211) surfaces constrained to the Pt lattice constant, which is slightly larger than that of Ru. Thus, the alloy surface atoms are under a slight biaxial tensile strain, which raises the average *d*-band center of the surface with respect to the Fermi level,[16] increasing the overall adsorbate-surface bonding interaction. In reality, an alloyed surface would have a different lattice constant between that of its constituent metals. Nonetheless, strain effects have a much smaller perturbation on the nitrate binding energy than change in adsorption site (i.e., from interacting directly with a Pt atom to a Ru atom) and the qualitative trends match with experiment.

Mean-field microkinetic modeling

To study the competition between surface reactions and rationalize the experimentally observed composition dependence of the observed ENO_3RR rate, we performed mean-field microkinetic modeling with degree of rate control fitting. We used the MKMCXX software package[17] (version 2.7.0) with a modeling protocol similar to that used in our previous study.[14] Specifically, we calculated the overall turnover frequency with respect to nitrate ion consumption and the degree of rate control factor for all elementary steps 0.1 V vs. RHE. **Table B.1** shows the 19 elementary steps considered in the microkinetic model. These steps were taken from our prior study,[14] where the effects of applied potential on the reaction thermodynamics and activation barriers were modeled using the computational hydrogen electrode[18] and Butler-Volmer formalism,[19] respectively.

Table B.1. Elementary reactions considered in the mean-field microkinetic model.

Reaction	ID	Reaction	ID
$NO_3^-{}_{(aq)} + * \leftrightarrows NO_3* + e^-$	(r_1)	$H_2O* \leftrightarrows H_2O_{(l)} + *$	(r_{12})
$H^+_{(aq)} + e^- + * \leftrightarrows H*$	(r_2)	$NO* \leftrightarrows NO_{(g)} + *$	(r_{13})
$2H* \leftrightarrows H_{2(g)} + 2*$	(r_3)	$N_2* \leftrightarrows N_{2(g)} + *$	(r_{14})
$NO_3* + * \leftrightarrows NO_2* + O*$	(r_4)	$N_2O* \leftrightarrows N_2O_{(g)} + *$	(r_{15})
$NO_2* + * \leftrightarrows NO* + O*$	(r_5)	$N* + H^+_{(aq)} + e^- \leftrightarrows NH*$	(r_{16})
$NO* + * \leftrightarrows N* + O*$	(r_6)	$NH* + H^+_{(aq)} + e^- \leftrightarrows NH_2*$	(r_{17})
$N* + N* \leftrightarrows N_2* + *$	(r_7)	$NH_2* + H^+_{(aq)} + e^- \leftrightarrows NH_3*$	(r_{18})
$NO* + NO* \leftrightarrows N_2O* + O*$	(r_8)	$NH_3* \leftrightarrows NH_{3(g)} + *$	(r_{19})
$N_2O* + * \leftrightarrows N_2* + O*$	(r_9)		
$O* + H^+_{(aq)} + e^- \leftrightarrows OH*$	(r_{10})		
$OH* + H^+_{(aq)} + e^- \leftrightarrows H_2O*$	(r_{11})		

For the adsorption and desorption reactions of NO, N_2, N_2O, and H_2O, and NH_3, rate constants were estimated by the Hertz-Knudsen (HK) equation. For HK reactions, the binding energy of each component was calculated from N and O binding energies through the adsorbate

scaling relations. All other reactions were modeled using the Arrhenius equation. For Arrhenius reactions, forward and backward pre-exponential factors were assumed to be 10^{13} s^{-1} and the forward and backward barriers were calculated from N and O binding energies using BEP relations. See the MKMCXX input files in our GitHub repository (https://github.com/goldsmith-lab/ptru-alloy-no3rr-activity) for more information.

The simulations were constructed over a grid of O and N binding energies, each ranging from –700 kJ mol^{-1} to –200 kJ mol^{-1} in increments of 10 kJ mol^{-1}. For each pair of O and N binding energies (i.e., each grid point in the simulation), a microkinetic model was constructed by calculated HK and Arrhenius parameters for that pair of binding energies, and the rate equations were integrated to a simulation time of 10^{12} s, until the calculation diverged, or until each surface coverage changed by an absolute value of no more than 10^{-12}. Any points for which at least one activation barrier was predicted to be unphysical (e.g., negative) were excluded from calculation. The remaining points form the roughly triangle-shaped envelope seen in **Figure B.11** and in the other microkinetics plots.

Figure 4.5a in **Chapter 4** shows the volcano plot (where the turnover frequency is defined as the *consumption* rate of $NO_3^-{}_{(aq)}$ normalized by site count) for random surface alloys with surface compositions of up to 50 at% Ru for comparison with experiment. The same figure is reproduced in **Figure B.11**, but with additional surface alloys at higher Ru compositions shown. The calculated points for s-Ru_{100}, s-$Pt_{17}Ru_{83}$, and s-$Pt_{33}Ru_{67}$ fall outside the envelope for the volcano contours. This issue occurs because volcano contours are drawn only within the envelope of N and O binding energies for which adsorbate scaling and BEP relationships predict positive activation energies. The fact that some points fall outside of this envelope shows limitations[14] of the adsorbate scaling and BEP relationships at very exothermic N and O binding energies.

However, the trend shows that there is a certain level of Ru content in the surface that correlates to a high TOF, and levels of surface Ru that are too high or too low correspond to lower activities. Future studies that include more metals and alloys and more detailed microkinetic modeling of ENO_3RR are needed to refine the theoretical volcano plot.

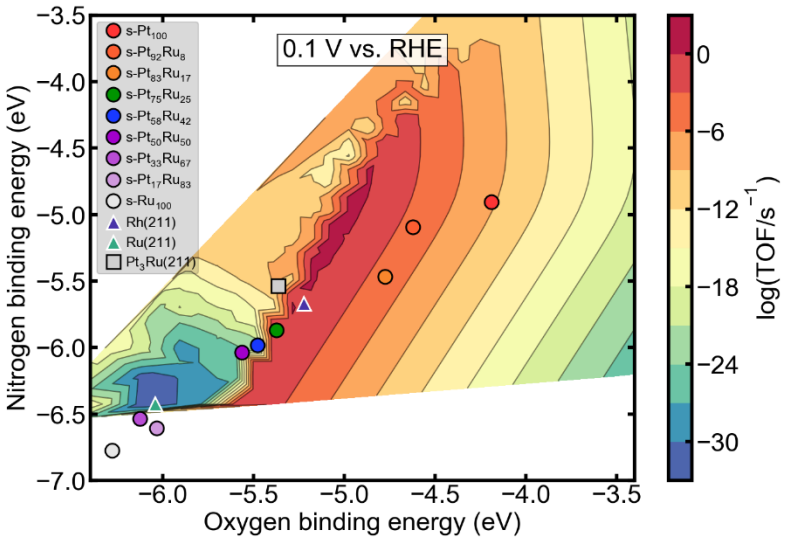

Figure B.11. Theoretical volcano plot at 0.1 V vs. RHE showing nitrate reduction activity of Pt_xRu_y, Pt(211), Ru(211), and the $Pt_3Ru(211)$ point from our previous study.[14] The predicted N and O binding energies from this work are overlaid on a map of catalyst turnover frequency (TOF) as a function of N and O binding energies from previous work.[14]

The degree-of-rate-control factor[20] (DRC) was calculated for each elementary reaction for each grid point. $|\mathrm{DRC}| \approx 0$ typically indicates that a reaction has weak control over the overall rate; $|\mathrm{DRC}| \gtrsim 1$ indicates strong control. For our study, DRC values were clipped to the range $[-2, 2]$ and non-numeric DRC values (e.g., NaNs, infinite values) were excluded from the results. These results appear in **Figure B.12**.

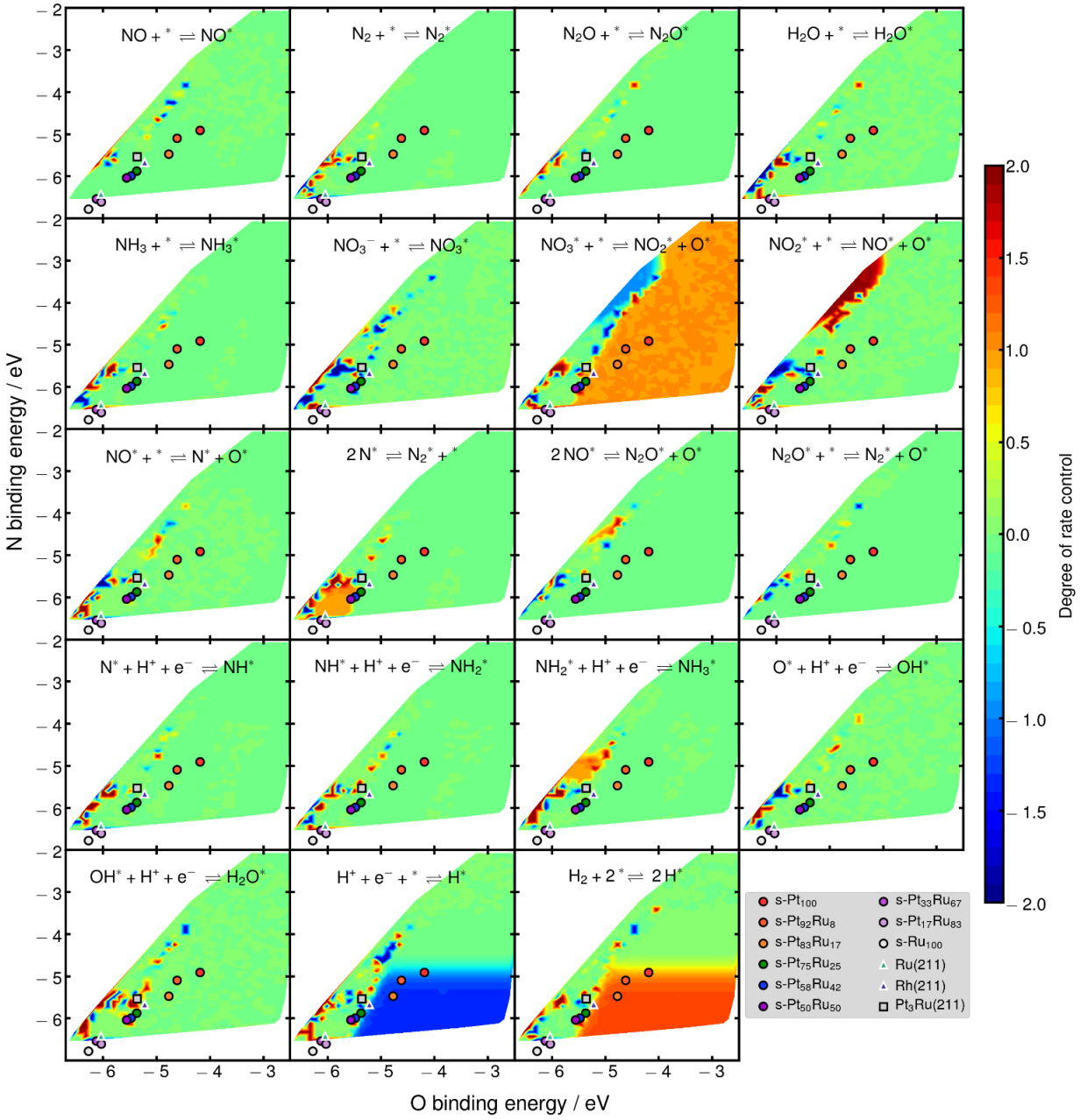

Figure B.12. Campbell degree of rate control factor for all elementary steps as a function of O and N binding energies at 0.1 V vs. RHE. The $Pt_3Ru(211)$ point from our previous work[14] is shown for comparison. All computed DRC values were clipped to the range $[-2.0, 2.0]$. White regions outside each envelope indicate O and N binding energies for which at least one surface reaction barrier is unphysical (negative).

Figure B.12 suggests that nitrate dissociation tends to dominate the overall reaction rate when O and N binding energies are both more positive than –4.5 eV. When O and N binding energies are both very negative, interconversion of N_2^* and N^* are predicted to control the overall

rate. In another region, with very strong O binding energy but moderate N binding energy, NH_2^* hydrogenation is predicted to control the overall rate. Although only the modeled bulk $Pt_3Ru(211)$ alloy falls close to the boundary of this region, this step being rate-determining is more consistent with the ammonia production we observe experimentally at higher Ru alloy content. At regions of very negative N binding energy and moderate or more positive O binding energy, the adsorption and desorption of aqueous H^+ and gaseous H_2 dominate the rate. There also is a region in which NO_2^* dissociation strongly controls the overall rate along the upper left edge of the contour envelope (high N binding energies at moderate O binding energies), but no modeled catalyst falls within this region.

Experiments show that maximum ENO_3RR current density is achieved at 0.1 V vs. RHE when using a $Pt_{75}Ru_{25}/C$ catalyst. Our DRC results in **Figure B.12** help rationalize this observation. For the five regions mentioned above in which a single elementary step controls the overall reaction rate, the s-$Pt_{75}Ru_{25}$ point lies at or very close to the boundary of each region. DRC analysis also predicts that none of the other elementary steps becomes rate-limiting at the N and O binding energies of s-$Pt_{75}Ru_{25}$. These results suggest that s-$Pt_{75}Ru_{25}$ exhibits near-optimal N and O binding energies for which no single elementary step in the mechanism is rate-limiting. Under these conditions, one would expect the overall reaction rate to reach a local maximum, which rationalizes the observation that $Pt_{75}Ru_{25}/C$ produces the highest ENO_3RR current density of all the Pt_xRu_y catalysts.

References

(1) Kresse, G.; Hafner, J. Ab Initio Molecular-Dynamics Simulation of the Liquid-Metal-Amorphous-Semiconductor Transition in Germanium. *Physical Review B* **1994**, *49* (20), 14251–14269. https://doi.org/10.1103/PhysRevB.49.14251.

(2) Kresse, G.; Furthmüller, J. Efficient Iterative Schemes for Ab Initio Total-Energy Calculations Using a Plane-Wave Basis Set. *Physical Review B* **1996**, *54* (16), 11169–11186. https://doi.org/10.1103/PhysRevB.54.11169.

(3) Kresse, G.; Joubert, D. From Ultrasoft Pseudopotentials to the Projector Augmented-Wave Method. *Physical Review B* **1999**, *59* (3), 1758–1775. https://doi.org/10.1103/PhysRevB.59.1758.

(4) Perdew, J. P.; Burke, K.; Ernzerhof, M. Generalized Gradient Approximation Made Simple. *Physical Review Letters* **1996**, *77* (18), 3865–3868. https://doi.org/10.1103/PhysRevLett.77.3865.

(5) Monkhorst, H. J.; Pack, J. D. Special Points for Brillouin-Zone Integrations. *Physical Review B* **1976**, *13* (12), 5188–5192. https://doi.org/10.1103/PhysRevB.13.5188.

(6) Hjorth Larsen, A.; Jørgen Mortensen, J.; Blomqvist, J.; Castelli, I. E.; Christensen, R.; Dułak, M.; Friis, J.; Groves, M. N.; Hammer, B.; Hargus, C.; Hermes, E. D.; Jennings, P. C.; Bjerre Jensen, P.; Kermode, J.; Kitchin, J. R.; Leonhard Kolsbjerg, E.; Kubal, J.; Kaasbjerg, K.; Lysgaard, S.; Bergmann Maronsson, J.; Maxson, T.; Olsen, T.; Pastewka, L.; Peterson, A.; Rostgaard, C.; Schiøtz, J.; Schütt, O.; Strange, M.; Thygesen, K. S.; Vegge, T.; Vilhelmsen, L.; Walter, M.; Zeng, Z.; Jacobsen, K. W. The Atomic Simulation Environment-a Python Library for Working with Atoms. *Journal of Physics. Condensed Matter: An Institute of Physics Journal* **2017**, *29* (27), 273002. https://doi.org/10.1088/1361-648X/aa680e.

(7) Ong, S. P.; Richards, W. D.; Jain, A.; Hautier, G.; Kocher, M.; Cholia, S.; Gunter, D.; Chevrier, V. L.; Persson, K. A.; Ceder, G. Python Materials Genomics (Pymatgen): A Robust, Open-Source Python Library for Materials Analysis. *Computational Materials Science* **2012**, *68*, 314–319.

(8) Calle-Vallejo, F.; Huang, M.; Henry, J. B.; Koper, M. T. M.; Bandarenka, A. S. Theoretical Design and Experimental Implementation of Ag/Au Electrodes for the Electrochemical Reduction of Nitrate. *Physical Chemistry Chemical Physics* **2013**, *15* (9), 3196–3202. https://doi.org/10.1039/C2CP44620K.

(9) Liu, J.-X.; Richards, D.; Singh, N.; Goldsmith, B. R. Activity and Selectivity Trends in Electrocatalytic Nitrate Reduction on Transition Metals. *ACS Catalysis* **2019**, *9* (8), 7052–7064. https://doi.org/10.1021/acscatal.9b02179.

(10) Henkelman, G.; Uberuaga, B. P.; Jónsson, H. A Climbing Image Nudged Elastic Band Method for Finding Saddle Points and Minimum Energy Paths. *The Journal of Chemical Physics* **2000**, *113* (22), 9901–9904. https://doi.org/10.1063/1.1329672.

(11) Xu, L.; Xiao, H. Y.; Zu, X. T. First-Principles Study on the Geometry and Stability of CO and Hydrogen Coadsorption on the Ni(111)2×2 Surface. *Chemical Physics* **2006**, *323* (2), 334–340. https://doi.org/10.1016/j.chemphys.2005.09.041.

(12) Sanchez, J. M.; Ducastelle, F.; Gratias, D. Generalized Cluster Description of Multicomponent Systems. *Physica A: Statistical Mechanics and its Applications* **1984**, *128* (1), 334–350. https://doi.org/10.1016/0378-4371(84)90096-7.

(13) Lerch, D.; Wieckhorst, O.; Hart, G. L. W.; Forcade, R. W.; Müller, S. UNCLE: A Code for Constructing Cluster Expansions for Arbitrary Lattices with Minimal User-Input. *Modelling Simul. Mater. Sci. Eng.* **2009**, *17* (5), 055003. https://doi.org/10.1088/0965-0393/17/5/055003.

(14) Liu, J.-X.; Richards, D.; Singh, N.; Goldsmith, B. R. Activity and Selectivity Trends in Electrocatalytic Nitrate Reduction on Transition Metals. *ACS Catal.* **2019**, *9* (8), 7052–7064. https://doi.org/10.1021/acscatal.9b02179.

(15) Calle-Vallejo, F.; Huang, M.; Henry, J. B.; Koper, M. T. M.; Bandarenka, A. S. Theoretical Design and Experimental Implementation of Ag/Au Electrodes for the Electrochemical Reduction of Nitrate. *Physical Chemistry Chemical Physics* **2013**, *15* (9), 3196. https://doi.org/10.1039/c2cp44620k.

(16) Kitchin, J. R.; Nørskov, J. K.; Barteau, M. A.; Chen, J. G. Role of Strain and Ligand Effects in the Modification of the Electronic and Chemical Properties of Bimetallic Surfaces. *Phys. Rev. Lett.* **2004**, *93* (15), 156801. https://doi.org/10.1103/PhysRevLett.93.156801.

(17) Filot, I. A. W.; van Santen, R. A.; Hensen, E. J. M. The Optimally Performing Fischer–Tropsch Catalyst. *Angewandte Chemie International Edition* **2014**, *53* (47), 12746–12750. https://doi.org/10.1002/anie.201406521.

(18) Nørskov, J. K.; Rossmeisl, J.; Logadottir, A.; Lindqvist, L.; Kitchin, J. R.; Bligaard, T.; Jónsson, H. Origin of the Overpotential for Oxygen Reduction at a Fuel-Cell Cathode. *J. Phys. Chem. B* **2004**, *108* (46), 17886–17892. https://doi.org/10.1021/jp047349j.

(19) Bessarabov, D.; Millet, P. Chapter 3 - Fundamentals of Water Electrolysis. In *PEM Water Electrolysis*; Bessarabov, D., Millet, P., Eds.; Hydrogen Energy and Fuel Cells Primers; Academic Press, 2018; pp 43–73. https://doi.org/10.1016/B978-0-12-811145-1.00003-4.

(20) Campbell, C. T. The Degree of Rate Control: A Powerful Tool for Catalysis Research. *ACS Catalysis* **2017**, *7* (4), 2770–2779. https://doi.org/10.1021/acscatal.7b00115.

Appendix C

Characterization, Baseline, and Kinetic Modeling

This appendix provides additional characterization and baseline results for the measurements conducted in **Chapter 5**. Additionally, it provides the procedure and results from kinetic models.

Additional Synthesis and Characterization Results

A standard set of characterization experiments were performed on Pt/C, PtRu/C, $Pt_{75}Ru_{25}$/C, and Ru/C. Due to the instability of Ru/C for electrochemical experiments for comparison, this material was omitted from kinetic measurements and major results presented. **Figure C.1** shows the results from thermal gravimetric analysis (TGA) of the Vulcan carbon supported catalysts. Both the Pt/C and PtRu/C showed total metal loading around 30 wt%, as expected. The synthesized $Pt_{75}Ru_{25}$/C had 5 wt% lower loading than targeted, indicating that not all the precursor was deposited on the supported during synthesis. The manufacturing company claimed a 20 wt% loading for Ru/C, but the TGA results show loadings closer to 30 wt%.

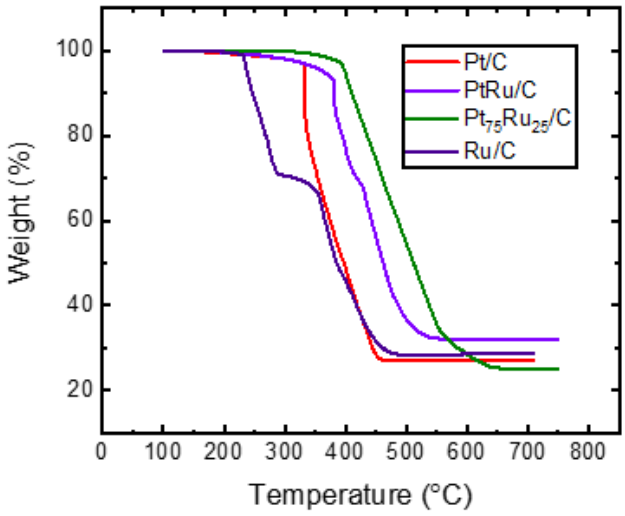

Figure C.1. Thermal gravimetric analysis data of the Vulcan carbon based catalysts in air. Treatments were conducted by first degassing the samples in He at 100 °C before ramping at 10 °C/min.

X-ray diffraction (XRD) spectra for Pt_xRu_y/C catalysts and the corresponding Pt and Ru powder diffraction files are provided in **Figure C.2**. Similar to the trends observed in our prior work on Pt_xRu_y/C,[3] increasing Ru composition in the material increases the 2θ angle of the Pt peaks. There are no separate Pt and Ru peaks present in the alloys, indicating no phase segregation in the material.

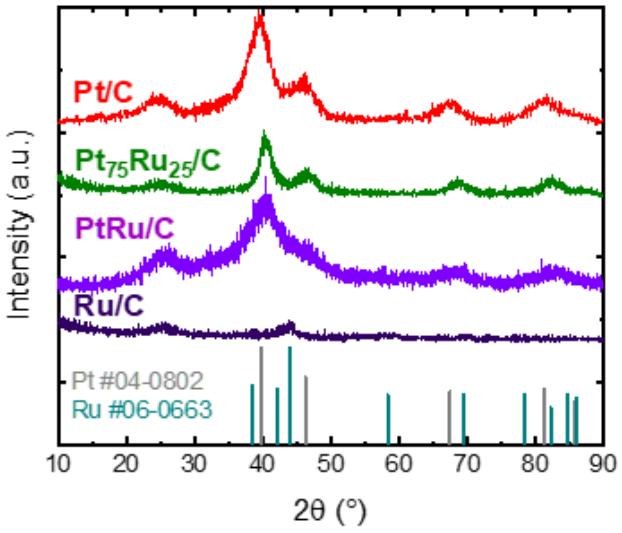

Figure C.2. X-ray diffraction spectra of Pt_xRu_y/C catalysts with Cu Kα radiation and a Ni filter (λ = 1.5418 Å) from 10° to 90° 2θ range. Crystallite sizes were estimated using the Scherrer equation and the Pt and Ru peaks are referenced to #04-0802 and #06-0663, respectively.

The crystallite sizes and weight loading of the catalysts were calculated by applying the Scherrer equation (**Table C.1**). The different catalysts have roughly the same average particle sizes. Additionally, we confirm that the particle size of $Pt_{75}Ru_{25}$/C matched previously synthesized materials.[3]

Table C.1. Crystallite sizes and metal weight percent loading for platinum-ruthenium catalysts. The crystallite sizes are calculated from the Scherrer equation while the metal weight loadings are obtained from TGA experiments. The error is calculated from the deviation from each individual metal peaks in the XRD spectra.

Catalysts	Crystallite Size (nm)	Weight Loading (%)
Pt/C	2.6 ± 0.6	27.3
PtRu/C	2.4 ± 0.3	32.2
$Pt_{75}Ru_{25}$/C	3.7 ± 1.0	25.1
Ru/C	2.9 ± 0.5	28.7

Scanning electron microscopy (SEM) images and elemental analysis from energy dispersive spectroscopy (EDX) are shown in **Figure C.3** and **Figure C.4**, respectively. EDX analysis reveal that the metal nanoparticles are dispersed on the surface of the support and confirms that the Ru at% increases as the Ru content in the alloy increases. Also, the at% of the metal

averaged over three different areas in the EDX analysis shows that the surface composition of metals is similar to the target composition from synthesis.

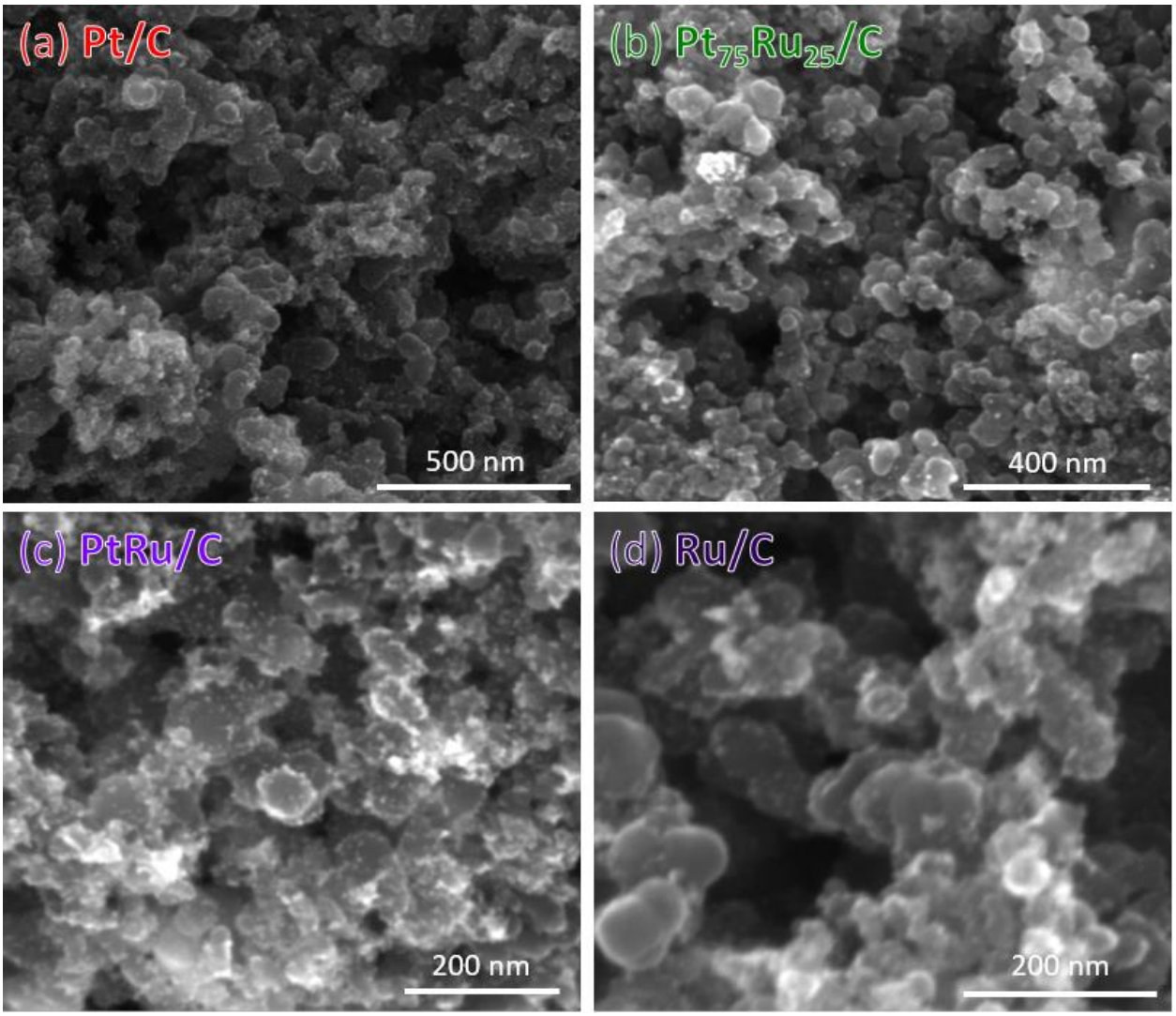

Figure C.3. Scanning electron microscopy images of **(a)** Pt/C, **(b)** $Pt_{75}Ru_{25}$/C, **(c)** PtRu/C, and **(d)** Ru/C. The accelerating voltage is set at 10 kV with 5 mm working distance.

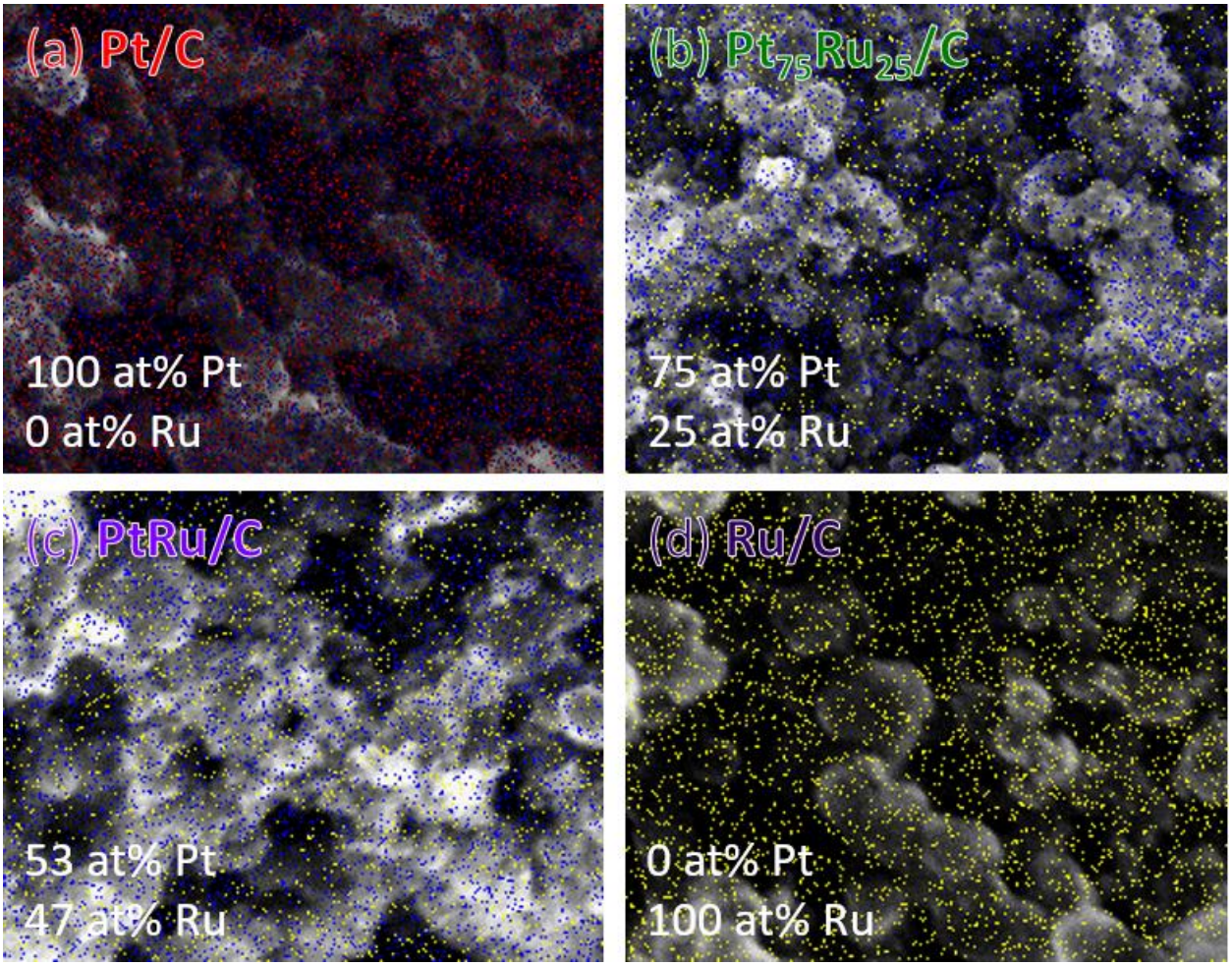

Figure C.4. Overlay of elemental analysis from energy-dispersive X-ray spectroscopy on SEM images for **(a)** Pt/C, **(b)** $Pt_{75}Ru_{25}$/C, **(c)** PtRu/C, and **(d)** Ru/C. Color legend: carbon = red; platinum = blue; ruthenium = yellow.

Additional Thermocatalytic Experimental Results

To ensure that no mass diffusion limitations occurred throughout TNO_3RR experiments, the ammonia production rate throughout the course of the reaction was measured for PtRu/C at three different stir rates (**Figure C.5**). As the catalysts are non-porous (and thus there are no internal diffusion limitations), these results indicate a lack of transport limitations here.

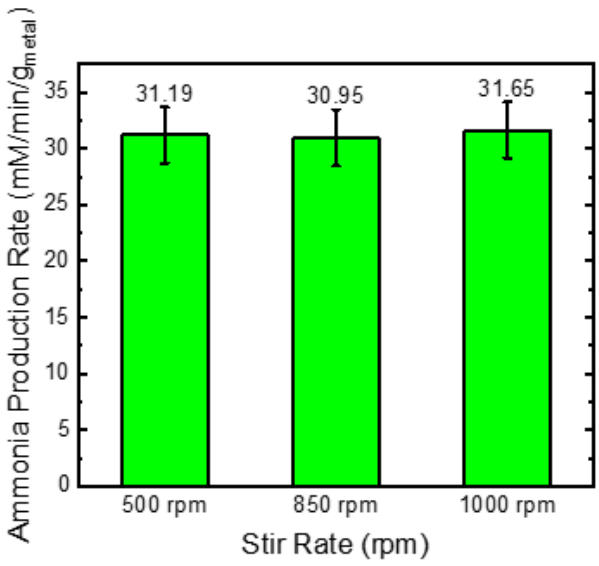

Figure C.5. Measured ammonia production rate for TNO_3RR on PtRu/C at pH 2 and 0.01 M $NaNO_3$ at stir rates from 500–1000 rpm. Average ammonia production rates are written inset. Experiments were performed at room temperature (23.3 °C) and the partial pressure of H_2 was 0.5 atm.

Additional baseline experiments were performed to ensure that the catalytic effects observed are due to the metal alloy. **Figure C.6a** and **Figure C.6b** display the nitrate and product (i.e., ammonia, nitrite) concentrations over the course of a standard 90 min reaction using no catalyst and Vulcan carbon, respectively. Without the presence of metals on the Vulcan carbon support, no catalytic activity is recorded. The miniscule amount of ammonia shown in these figures (~0.02 mM) is subtracted as a baseline for analysis. A known concentration of ammonia is recorded over the course of the reaction in **Figure C.6c**. The consistent level of ammonia concentration indicates that aqueous ammonia does not evaporate with continuous H_2 bubbling through the system.

For TNO_3RR measurements for Pt/C, there was no observed nitrate conversion and ammonia production activity. To ensure that this result is due to a catalytic effect rather than experimental design issue, we increased the amount of Pt/C in the reactor from 10 mg to 50 mg. **Figure C.6d** shows no significant change in catalytic activity with increasing the amount of

catalyst in the reactor. For comparison, the nitrate concentration for PtRu/C is provided, where a drastic drop in nitrate is recorded over the course of 90 min.

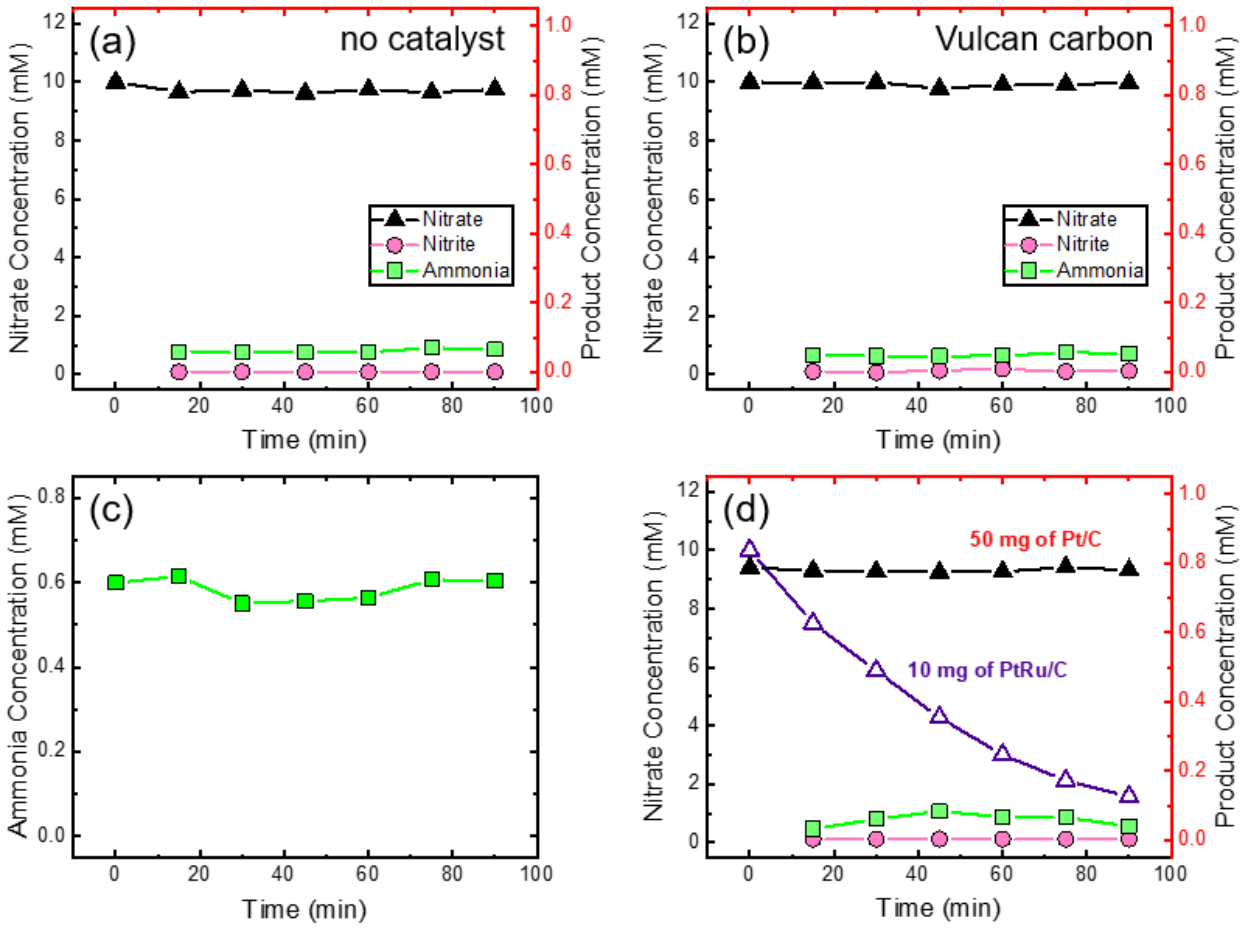

Figure C.6. Initial baseline measurements for TNO_3RR measurements. Nitrate, nitrite, and ammonia concentration under reaction conditions (pH 2, 0.01 M $NaNO_3$) **(a)** with no catalyst and **(b)** with Vulcan carbon support. **(c)** Known concentration of ammonia over 90 min of reaction to ensure no ammonia evaporation from H_2 bubbling into the system. **(d)** Comparison of the nitrate concentration of reaction with 50 mg of Pt/C and 10 mg of PtRu/C. Ammonia and nitrite concentrations throughout the reaction from Pt/C. Color legend: nitrate = black, ammonia = green, nitrite = pink.

Additional Kinetic ENO_3RR Modeling Procedures and Results

Kinetic Model Procedure

Assuming ENO_3RR follows a Langmuir-Hinshelwood model, both a single site model (SSM) and multisite model (MSM) were considered to model the reaction. SSM assumes a

homogeneous electrode surface, the rate r can be derived as shown is **Equation C.1** by inserting expressions for the coverages into **Equation 5.1**. Both nitrate and H^+ adsorb onto this single site and competitively inhibit the other species. The adsorption equilibrium constants K_N and K_H refer to the adsorption of nitrate and H^+, respectively; C_i refers to the bulk concentration of species i; k_{SSM} denotes the rate constant of the surface reaction between adsorbed nitrate and hydrogen for the SSM.

$$r = k_{SSM} \frac{K_{\mathrm{N}} K_{\mathrm{H}} C_{\mathrm{N}} \mathrm{C}_{\mathrm{H}}}{(1 + K_{\mathrm{N}} C_{\mathrm{N}} + K_{\mathrm{H}} \mathrm{C}_{\mathrm{H}})^2} \; [M\, s^{-1}\, m^{-2}] \tag{C.1}$$

If TNO_3RR follows a surface reaction RDS, it will obey the same rate equation.

The main assumptions of the proposed multisite kinetic model (MSM) are as follows: 1) There are two adsorption sites on the catalyst surface, $*_1$,$*_2$; 2) The reaction only occurs between NO_3*_1 and $H*_2$ and thus each species competitively inhibits the other on the opposite site. Adsorption equilibrium constants K_1, K_2, K_3, K_4, refer to **Equations C.2**–**5**, respectively.

$$NO_3^- + *_1 \rightleftharpoons NO_3^{*1} + e^- \tag{C.2}$$

$$NO_3^- + *_2 \rightleftharpoons NO_3^{*2} + e^- \tag{C.3}$$

$$H^+ + *_1 + e^- \rightleftharpoons H^{*1} \tag{C.4}$$

$$H^+ + *_2 + e^- \rightleftharpoons H^{*2} \tag{C.5}$$

The rate determining step is seen in **Equation C.6**, resulting in the corresponding rate law shown in **Equation C.7**.

$$NO_3^{*1} + H^{*2} \rightarrow NO_2^* + OH^* \tag{C.6}$$

$$r = k_{MSM} \theta_{N^{*1}} \theta_{H^{*2}} \tag{C.7}$$

In **Equation C.7**, θ_{i^*j} refers to the surface coverage of the species *i* on site *j*. From these assumptions, and assuming quasi-equilibrium in the adsorption reactions in **Equations C.2–5**, a rate law (**Equation C.8**) is derived relating reaction rate with bulk concentration of nitrate (C_N) and H^+ (C_H), a constant of proportionality k_{MSM} $[M\ s^{-1}\ m^{-2}]$, and using a site balance in **Equation C.9**.

$$r = k_{MSM}\frac{C_N C_H}{K_1 K_4\left(\frac{C_N}{K_1}+\frac{C_H}{K_3}+1\right)\left(\frac{C_N}{K_2}+\frac{C_H}{K_4}+1\right)} \tag{C.8}$$

$$1 = \theta_{N^*1} + \theta_{H^*1} + \theta_{*1} = \theta_{N^*2} + \theta_{H^*2} + \theta_{*2} \tag{C.9}$$

θ_{*1} and θ_{*2} are the coverage of open sites on site 1 and 2, respectively. This MSM rate law is compared to that of the SSM for accuracy in predicting the nitrate reduction reaction rate. A nonlinear least-square regression was performed on MATLAB version R2020b, relating current density to concentration of H^+. The SSM can be reduced to a two-parameter fit (**Equations C.10, C.11**), and the MSM to a three-parameter fit (**Equations C.12, C.13**). The independent variable, *x*, may refer to C_H, or $10^{-\mathrm{pH}}$ depending on context.

$$r = \frac{\alpha x}{(\beta + x)^2} \tag{C.10}$$

$$\alpha = k_{SSM}\frac{K_N C_N}{K_H}\ [M^2\ s^{-1} m^{-2}], \beta = \frac{1}{K_H} + \frac{K_N C_H}{K_H}\ [M] \tag{C.11}$$

$$r = \frac{\mathrm{Ax}}{(\mathrm{x}+\mathrm{B})(\mathrm{x}+\mathrm{C})} \tag{C.12}$$

$$A = k_{MSM}\frac{C_N K_3}{K_1}\ [M^2\ s^{-1} m^{-2}], B\ = \frac{C_N K_3}{K_1} + K_4\ [M], C = \frac{C_N K_4}{K_2} + K_4\ [M] \tag{C.13}$$

Kinetic Model Results

When fitting the LH models to nitrate concentration and experimental data, the *B* and *C* fit parameters become equivalent, rendering the MSM mathematically identical to the SSM. The data in **Figure C.7** shows the fit of this LH model to the experimental ENO_3RR activity at pH 1 and 7 for the considered catalysts. The nitrate concentration has little effect on the activity of Pt/C. The rate of reaction on Pt_xRu_y/C at pH 1 and pH 7 has a positive order with respect to nitrate concentration until 0.5 M, where it becomes negative order. $Pt_{75}Ru_{25}/C$ in pH 7 is the exception to this trend. The model qualitatively agrees with the experimental data, and helps to explain that increasing in nitrate concentration is associated with increasing nitrate reduction activity up until concentrations between 0.2–0.4 M NO_3^- as the nitrate coverage increases, whereas at higher nitrate coverages the surface sites are blocked by nitrate and cause the rate to decrease.

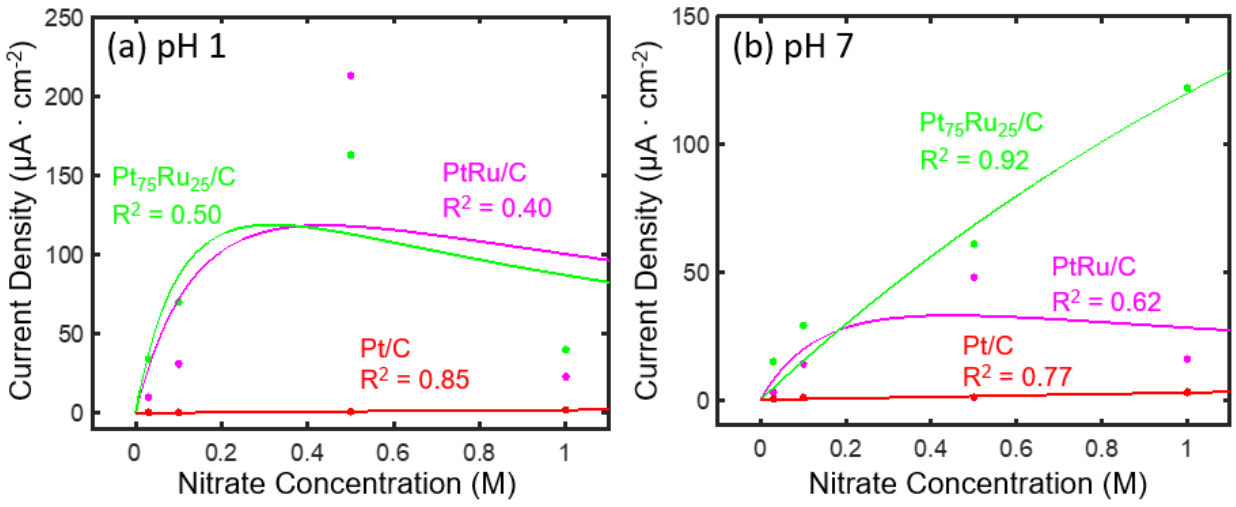

Figure C.7. Langmuir-Hinshelwood model of ENO_3RR activity for Pt_xRu_y/C catalysts as a function of nitrate concentration at **(a)** pH 1 and **(b)** pH 7. All experimental data points are collected at 0.1 V vs. RHE. Coefficient of determination R^2 is written inset.

Initially, both the SSM and MSM were fit to a pH range of 0–7 to describe the C_H effect on rate (**Figure C.8a**). Similar to fitting the data to nitrate concentration, *B* and *C* fit parameters become equivalent, rendering the MSM mathematically identical to the SSM. In this analysis, pH 10 data was omitted due to potential oxide formation skewing the measured reduction currents.

Results of the fitting show negative R^2 values, which indicate that a simple Langmuir-Hinshelwood model does not capture all the pH effects on nitrate reduction activity. Previous experiments show that catalyst activity is dependent on C_H at pH < 4.[4,5] Thus, additional fittings were conducted between pH 0–4 for the SSM (**Figure C.8b**) and MSM (**Figure C.8c**). Although there are only three data points for each catalyst at this pH range, the MSM shows a superior fit over the SSM fit.

The kinetic models explored are simplistic and only capture direct effects of C_H and C_N, and thus cannot provide a comprehensive understanding for the effect of pH on reaction rate. For example, pH affects the adsorption equilibria of both nitrate and protons while the model assumes these equilibria to be fixed. Future works should focus on improving these models by incorporating expressions that account for pH effects on the system.

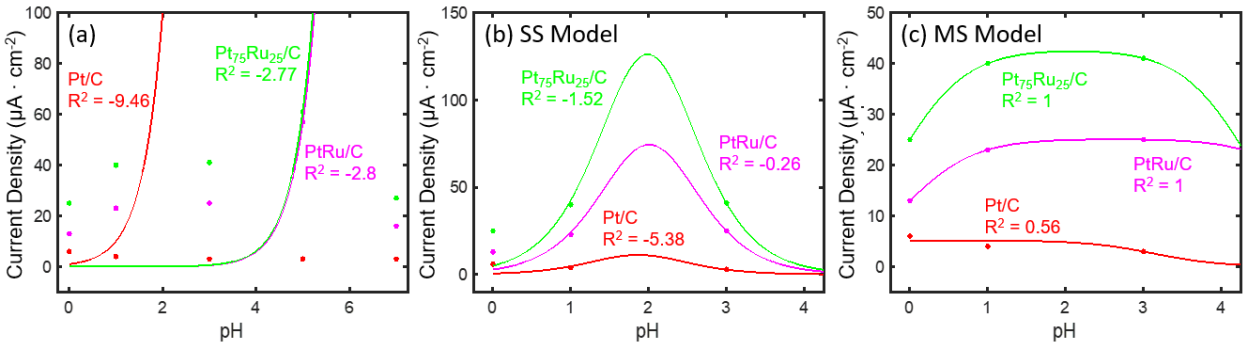

Figure C.8. SSM and MSM Langmuir-Hinshelwood models of ENO_3RR activity for Pt_xRu_y/C catalysts as a function of pH. **(a)** LH fitting for data collected between pH 0–7. **(b)** SSM for pH 0–3, and **(c)** MSM for pH 0–3. All experimental data points are collected at 0.1 V vs. RHE.

Additional Electrocatalytic Experimental Results

The FE of PtRu/C towards NH_3 at pH 1 and pH 7 are shown in **Figure C.9**. The reactions were performed at 0.1 V vs. RHE for at least 6 hrs. The FE reaches ~ 93% at pH 1 after 5.5 hrs, whereas the FE reaches ~54% at pH 7 after 3 hrs. The increase in the measured FE over time can be attributed to many factors. Because the measurements are performed in a batch reactor on a porous carbon felt, diffusion limitations may delay the transport of the products to the bulk solution. It is also possible that some intermediates are forming on the surface of the felt but reacting slowing, which results in high FE towards ammonia once the intermediates react. The reported FE in the main text is the averaged last four timepoints in each experiment.

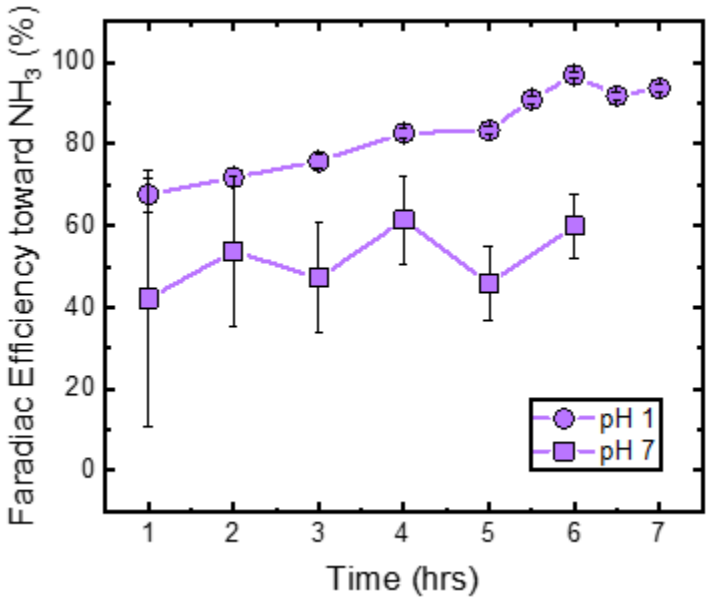

Figure C.9. Comparison between the faradaic efficiency of 10 mg of PtRu/C deposited on carbon felts in pH 1 (0.1 M HNO_3) and pH 7 (0.2 M sodium phosphate + 0.1 citric acid) electrolyte solution. Both experiments are conducted with 0.1 M nitrate at 0.1 V vs. RHE for at least 6 hrs.

For all the ENO_3RR measurements in different pH, different buffer solutions were prepared to ensure that the pH of the solution remains constant throughout the reaction. However, the ionic strength of the solution can also influence the reduction currents.[4,5] **Figure C.10** displays the

calculated ionic strength of all the buffer solutions prepared for the pH experiments, and shows a large variation between 0.25–2.5 M for different electrolytes. However, the pH trends do not match the ionic strengths of the solution, implying that other effects, such as hydrogen equilibrium potential,[6] the point of zero free charge (pzfc),[7–9] and water orientation and reorganization energy,[10–12] may also influence the current measurements with varying pH.

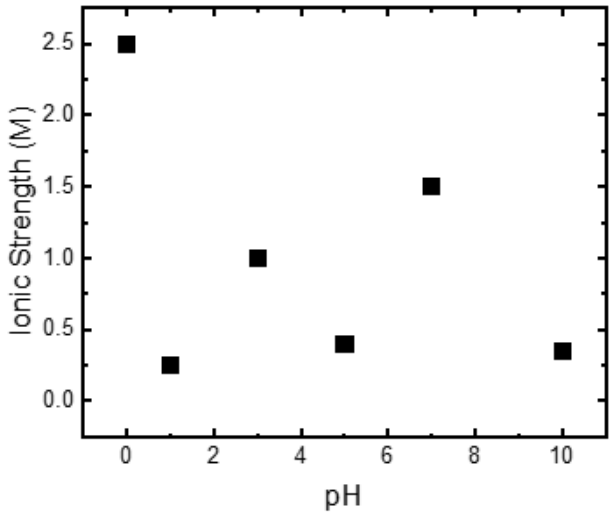

Figure C.10. Calculated ionic strength of all pH solutions for ENO_3RR experiments. The electrolyte solution at each pH is listed: pH 0: 1 M H_2SO_4, pH 1: 0.1 M H_2SO_4, pH 3: 0.1 M sodium citrate + 0.1 M citric acid, pH 5: 0.2 M sodium acetate + 0.2 M acetic acid, pH 7: 0.2 M sodium phosphate + 0.1 M citric acid, pH 10: 0.1 M sodium carbonate + 0.1 M sodium bicarbonate.

References

(1) Baturina, O. A.; Aubuchon, S. R.; Wynne, K. J. Thermal Stability in Air of Pt/C Catalysts and PEM Fuel Cell Catalyst Layers. *Chem. Mater.* **2006**, *18* (6), 1498–1504. https://doi.org/10.1021/cm052660e.

(2) Pinchuk, O. A.; Aubuchon, S. R.; Marks, C.; Dominey, R.; Dundar, F.; Deniz, O. F.; Ata, A.; Wynne, K. J. Thermally Pretreated 46% Pt/Vulcan XC72: Characterisation by TGA/DSC/TEM and Cyclic Voltammetry. *Fuel Cells* **2009**, *9* (5), 554–561. https://doi.org/10.1002/fuce.200800183.

(3) Wang, Z.; Young, S. D.; Goldsmith, B. R.; Singh, N. Increasing Electrocatalytic Nitrate Reduction Activity by Controlling Adsorption through PtRu Alloying. *Journal of Catalysis* **2021**, *395*, 143–154. https://doi.org/10.1016/j.jcat.2020.12.031.

(4) Dortsiou, M.; Katsounaros, I.; Polatides, C.; Kyriacou, G. Influence of the Electrode and the PH on the Rate and the Product Distribution of the Electrochemical Removal of Nitrate. *Environmental Technology* **2013**, *34* (3), 373–381. https://doi.org/10.1080/09593330.2012.696722.

(5) Yang, J.; Sebastian, P.; Duca, M.; Hoogenboom, T.; M. Koper, M. T. PH Dependence of the Electroreduction of Nitrate on Rh and Pt Polycrystalline Electrodes. *Chemical Communications* **2014**, *50* (17), 2148–2151. https://doi.org/10.1039/C3CC49224A.

(6) Jerkiewicz, G. Standard and Reversible Hydrogen Electrodes: Theory, Design, Operation, and Applications. *ACS Catal.* **2020**, *10* (15), 8409–8417. https://doi.org/10.1021/acscatal.0c02046.

(7) Silva, F.; Sottomayor, M. J.; Hamelin, A. The Temperature Coefficient of the Potential of Zero Charge of the Gold Single-Crystal Electrode/Aqueous Solution Interface: Possible Relevance to Gold-Water Interactions. *Journal of Electroanalytical Chemistry and Interfacial Electrochemistry* **1990**, *294* (1), 239–251. https://doi.org/10.1016/0022-0728(90)87148-D.

(8) Rizo, R.; Sitta, E.; Herrero, E.; Climent, V.; Feliu, J. M. Towards the Understanding of the Interfacial PH Scale at Pt(111) Electrodes. *Electrochimica Acta* **2015**, *162*, 138–145. https://doi.org/10.1016/j.electacta.2015.01.069.

(9) Ganassin, A.; Sebastián, P.; Climent, V.; Schuhmann, W.; Bandarenka, A. S.; Feliu, J. On the PH Dependence of the Potential of Maximum Entropy of Ir(111) Electrodes. *Scientific Reports* **2017**, *7* (1), 1246. https://doi.org/10.1038/s41598-017-01295-1.

(10) García-Aráez, N.; Climent, V.; Feliu, J. M. Evidence of Water Reorientation on Model Electrocatalytic Surfaces from Nanosecond-Laser-Pulsed Experiments. *J. Am. Chem. Soc.* **2008**, *130* (12), 3824–3833. https://doi.org/10.1021/ja0761481.

(11) Ledezma-Yanez, I.; Wallace, W. D. Z.; Sebastián-Pascual, P.; Climent, V.; Feliu, J. M.; Koper, M. T. M. Interfacial Water Reorganization as a PH-Dependent Descriptor of the Hydrogen Evolution Rate on Platinum Electrodes. *Nature Energy* **2017**, *2* (4), 1–7. https://doi.org/10.1038/nenergy.2017.31.

(12) Sarabia, F. J.; Sebastián-Pascual, P.; Koper, M. T. M.; Climent, V.; Feliu, J. M. Effect of the Interfacial Water Structure on the Hydrogen Evolution Reaction on Pt(111) Modified with Different Nickel Hydroxide Coverages in Alkaline Media. *ACS Appl. Mater. Interfaces* **2019**, *11* (1), 613–623. https://doi.org/10.1021/acsami.8b15003.